UNIVERSITY OF SOUTHAMPTON

Observational constraints on the evolution of cataclysmic variable stars

Magaretha Le Riche Pretorius

Submitted for the degree Doctor of Philosophy
SCHOOL OF PHYSICS AND ASTRONOMY
FACULTY OF SCIENCE

22 February 2008

UNIVERSITY OF SOUTHAMPTON

ABSTRACT

FACULTY OF SCIENCE
SCHOOL OF PHYSICS AND ASTRONOMY

Doctor of Philosophy

Observational constraints on the evolution of cataclysmic variable stars

by Magaretha Le Riche Pretorius

I provide observational constraints on the size and period distribution of the Galactic cataclysmic variable (CV) population, and derive the implications that these constraints have for the theory of CV evolution. The results are based on quantitative modelling applied to three observational CV samples, two of which are newly constructed here.

Large differences between the size and other properties of the known sample of CVs and the predictions of the theory of binary star evolution have long been recognized. However, because all existing observational CV samples suffer from strong selection effects, observational biases must be taken into account before it is possible to tell whether there are real inconsistencies. In order to address this, I implement a Monte Carlo method to model selection effects in observed CV samples, and make a new measurement of the space density of CVs.

I illustrate the effects of the biases that are introduced by several of the most common observational strategies for identifying CVs. Also, by simulating the selection criteria of the Palomar–Green (PG) Survey, I show that selection effects cannot reconcile the relative sizes of the long- and short-period CV populations predicted by standard CV evolution theory with the observed sample.

The selection criteria used to define most CV samples (including the PG sample) discriminate heavily against the discovery of intrinsically faint, short-period systems. The situation can be improved by selecting systems for the presence of emission lines; I have therefore constructed a homogeneous new sample of 17 CVs, selected on the basis of Hα emission from the AAO/UKST SuperCOSMOS Hα Survey (SHS). I present observations of the CVs discovered in this search, and use the sample to constrain the properties of the intrinsic CV population. I show that even very generous allowance for selection effects is not sufficient to reconcile the ratio of short- to long-period CVs predicted by standard CV evolution theory with the observed sample, confirming the result based on the PG survey. The most likely implication is that short-period systems evolve faster than predicted by the disrupted magnetic braking model. This would require that an angular momentum loss mechanism besides gravitational radiation acts on CVs with orbital periods below the period gap. To bring the model into agreement with observations, the rate of angular momentum loss below the period gap must be increased by a factor of at least 3, unless the model also overestimates the angular momentum loss rate of long-period CVs.

In order to constrain the size of the Galactic CV population, I construct a small, but purely X-ray flux-limited sample of CVs, using the *ROSAT* North Ecliptic Pole (NEP) survey. The sample includes only 4 systems, 2 of which are new discoveries. Orbital periods are measured for both these systems from time-resolved spectroscopy, and the distances of all the CVs in this sample are estimated. The space density of the CV population represented by the sample is $1.1^{+2.3}_{-0.7} \times 10^{-5}\,\mathrm{pc}^{-3}$. I also place upper limits on the space density of any population of CVs too faint to be included in the NEP survey—if the overall space density of CVs is as high as $2 \times 10^{-4}\,\mathrm{pc}^{-3}$ (as has been predicted theoretically), the vast majority of CVs must have X-ray luminosities below $\simeq 2 \times 10^{29}\,\mathrm{erg\,s}^{-1}$.

Opgedra aan die herinnering van my vader, Adrian Stephanus Pretorius, met dankbaarheid en liefde

Acknowledgments

It is a pleasure to acknowledge and thank my supervisor, Christian Knigge, first for suggesting this project and for the steadfastness that saw it to completion, but also for more patience than I could claim to deserve. I can't express how highly I value my education, and I now owe most of it to Christian. He is the kind of scientist I hope to become.

I have benefited greatly over the past six years from Darragh O'Donoghue's knowledge and kindness. My thanks for unfaltering support, and for agreeing to co-supervise my PhD work.

Some of the work presented here relies heavily on an accretion disc model written by Romuald Tylenda, and on the results of a population synthesis model written by Ulrich Kolb. Pat Henry and Isabella Gioia provided information on the optical identification of stellar sources detected in the *ROSAT* North Ecliptic Pole Survey, and made the identification spectra of these objects available to me. Fred Ringwald kindly provided an updated list of CVs included in the Palomar–Green survey. I thank Tom Marsh for the use of his software package MOLLY, and Giusi Micela, John Thorstensen and Daisaku Nogami for communicating the results of unpublished observations to me. Several people have taken the time to answer my questions; specifically, Brian Warner, Simon Harris, Andrew Witham, Tom Maccarone, Dave Kilkenny, Joe Patterson, Boris Gänsicke, and Elmar Körding. I am also indebted to night assistants and support astronomers at La Silla and Calar Alto, and to service observers at Cerro Tololo.

Many members of the Astronomy Group played some or other part in making my time in Southampton enjoyable. In particular, I thank Dave Russell, Katrine Rogers, Vanessa McBride, and Omar Jamil for their friendship.

Financial support for my studies came from the South African National Research Foundation and the University of Southampton, in the form of a Stobie-SALT scholarship.

Throughout my rather long years at university, my brothers provided guidance, financial support, and places in two hemispheres where I could go to be home. My mother spared no personal sacrifice to give me the opportunity to study, and has delighted more than anyone else in what success I have had.

Retha Pretorius

Declaration of authorship

This thesis presents results of research I performed while enrolled as a student at the University of Southampton, between October 2004 and February 2008.

I reduced and analysed all observations presented here. Observations from the European Southern Observatory, the South African Astronomical Observatory, and Calar Alto Observatory were also taken by me, while data from the Cerro Tololo Inter-American Observatory were obtained for me by service observers. I used standard data reduction software as noted in the text. The Monte Carlo codes used in Chapter 3, 4, and 5 were written by me. One figure is reproduced from the work of others; the source is credited in the caption.

Most of the content of Chapters 3 through 5 has appeared in the the following publications.

1. Pretorius M.L., Knigge C., Kolb U., *The influence of selection effects on the observed cataclysmic variable population: modelling and application to the Palomar–Green sample*, 2007, MNRAS, 374, 149
2. Pretorius M.L., Knigge C., O'Donoghue D., Henry J.P., Gioia I.M., Mullis C.R., *The space density of cataclysmic variables: constraints from the* ROSAT *North Ecliptic Pole Survey*, 2007, MNRAS, 382, 1279
3. Pretorius M.L., Knigge C., *An Hα-selected sample of cataclysmic variables – I. Observations of newly discovered systems*, 2008, MNRAS, in press (arXiv:0801.1065)
4. Pretorius M.L., Knigge C., *An Hα-selected sample of cataclysmic variables – II. Implications for CV evolution*, 2008, MNRAS, in press (arXiv:0801.1070)

I benefited from the help of my coauthors in many technical aspects, as well as in interpreting the results and presenting the work.

Magaretha Le Riche Pretorius
Southampton, 22 February 2008

Contents

Chapter 1

Introduction

Cataclysmic variable stars (CVs) are amongst the most dramatically and frequently variable objects in the sky. Their variability fueled early interest in these stars, and this has been sustained for well over a century now. CVs have been detected at all wavelengths from radio to γ-rays, and they vary on time-scales ranging from seconds to millions of years, as the result of several distinct physical mechanisms. It was realized several decades ago that CVs are binary stars and almost immediately suspected that the rich phenomenology is related to binarity (e.g. Joy 1954; Walker 1954; Kraft 1964).

Most stars are believed to occur in binary or multiple systems (but see Lada 2006), and in a significant fraction of these systems the stars interact by exchanging mass. This changes the evolution of the stellar components from that of isolated stars, and also has implications for several very diverse areas of study. For example, nova eruptions, which result from the accretion of hydrogen-rich material onto the surface of a white dwarf, influence the properties of the interstellar medium and the chemical evolution of galaxies (e.g. Amari et al. 1990; Shara & Prialnik 1994; Kolb & Politano 1997; Gehrz et al. 1998); CVs are important in the study of Galactic X-ray and γ-ray source populations (e.g. Muno et al. 2003; Barlow et al. 2006; Heinke et al. 2008); and binary stars are probably responsible for the far-UV excess in elliptical galaxies (Han et al. 2007). Another strong motivation for the study of accreting white dwarfs in binary systems is that they are the likely progenitors of Type Ia supernovae (e.g. Whelan & Iben 1973; King et al. 2003; Starrfield et al. 2004).

Despite its importance, the evolution of binary stars is not nearly as well understood as stellar evolution, and the development of more successful binary evolution models requires observational constraints. CVs provide a useful testing ground for theories of binary star evolution. This is because (i) CVs are a frequent outcome of common envelope evolution (a phase that many other types of close binaries pass through), (ii) there is a known sample of CVs large enough to be indicative of the general properties of the population, and (iii) the angular momentum loss mechanisms driving the evolution of CVs also play an important role in the evolution of many other types of binaries. Processes controlling the evolution of CVs depend almost entirely on the properties of the red dwarf, and likely determine the

evolution of all close binary systems containing a late-type component. CV evolution thus has very wide applicability, which includes specifically the evolution of low-mass X-ray binaries (a review of low-mass X-ray binary evolution may be found in Verbunt & van den Heuvel 1995; see also Pfahl et al. 2003, Kiel & Hurley 2006, and Yungelson et al. 2006 for more recent results). In fact, it is likely that supersoft X-ray sources (objects with very soft X-ray spectra and luminosities near the Eddington limit, believed to be powered by steady nuclear burning of accreting material on the surface of a white dwarf; e.g. Kahabka & van den Heuvel 1997) are essentially CVs in a peculiar evolutionary phase (e.g. Schenker et al. 2002).

The evolution of CVs sets the boundary conditions for the accretion processes in these objects. Accretion is the most efficient source of energy in the universe, and a very important astrophysical process, but is still poorly understood. In many cases accretion takes place via a thin disc of material orbiting a compact object at its centre. Such accretion discs are very commonly occurring structures and therefore relevant in many branches of astronomy. Gravitational potential energy released by the infall of material from an accretion disc is known to be the principal source of energy in several types of close binary systems, and many more binary stars form discs at some stage of their evolution. Accretion discs around young stellar objects allow for gravitational collapse while conserving angular momentum and are the structures out of which planets form. Active galactic nuclei are amongst the most energetic objects in the universe and are believed to be powered by accretion of matter from the inner galactic disc onto a supermassive black hole. Astrophysical jets (collimated, bipolar outflows) are commonly associated with accreting compact objects and represent an important power output mechanism in such systems. The key to understanding all these exotic objects is the study of accretion, and the best opportunity to observe and understand accretion is offered by CVs.

With the increase in the number of CVs with orbital period measurements came the realization that the period distribution is very structured (Warner 1976 first pointed out that the distribution is bimodal). It was recognized early that mass transfer in CVs requires steady loss of angular momentum from the binary orbit (e.g. Kraft et al. 1962; Paczyński 1981), which leads to orbital period evolution. This means that the orbital period of a CV gives an indication of its evolutionary state, and that it should be possible to use the period distribution of the observed CV population to study the evolution of CVs.

Guided mainly by the observed period distribution, a model for CV evolution has been developed, but many challenges concerning the evolution of CVs remain. The standard model of CV evolution at least crudely matches many of the properties of the observed CV population, but fails in several details. Specifically, the observed period distribution differs markedly from that of the predicted intrinsic population. However, existing observational CV samples suffer from strong, complicated selection effects, and these must be taken into account before theory can be confronted with observations in a meaningful way. The most important shortcoming of comparisons between the predicted and observed properties

of the CV population has to date been the treatment of selection effects. Also, almost all usefully large CV samples suffer from the same selection effects, because they were constructed in similar ways. These biases produce large systematic errors in the inferences that are observationally made.

Another fundamental prediction of CV formation and evolution scenarios is the overall space density of CVs. Even this differs by an order of magnitude between various theoretical studies, in part because of uncertainties concerning the lifetime of CVs, and our understanding of the formation of CVs. Much of the theoretical difficulty results from the lack of quantitative observational constraints—observational measurements of the space density of CVs spanning more than two orders of magnitude have been reported.

It is therefore at present not clear whether theory really is inconsistent with observations, and, if so, how the standard theory should be adjusted, or whether it has to be discarded.

The evolution of CVs is the subject of this thesis. I provide observational constraints on the orbital period distribution and size of the Galactic CV population, and examine the implications that these constraints have for CV evolution theory.

A computational method for quantitatively assessing the impact of selection effects on observational CV samples is presented in Chapter 3, and applied to quantify the selection effects in the Palomar–Green Survey. I also construct a new CV sample, free from some of the most common observational biases, by selecting emission line objects from the AAO/UKST SuperCOSMOS Hα Survey. The selection procedure and observations, as well the implications of the resulting Hα-selected CV sample for CV evolution, are presented in Chapter 4. The Hα-selected and Palomar–Green CV samples, together with the modelling of selection effects, provide constraints on the period distribution of CVs, and have implications for the rate at which CVs evolve. In Chapter 5, the *ROSAT* North Ecliptic Pole Survey is used to place constraints on the space density of CVs. The results and implications of these separate studies are reviewed together in Chapter 6, and the conclusions are summarized in Chapter 7. First, however, I introduce some of the necessary background on CVs, and review our knowledge of the evolution of CVs (Chapter 2).

Chapter 2

An overview of cataclysmic variables and their evolution

This chapter provides an outline of the phenomenology of CVs, as well as of our understanding of these systems, and their formation and evolution. I start by introducing CVs in terms of Roche geometry, and then give a brief overview of some important aspects of accretion, as well as of the structure, spectral energy distribution (SED), and classification of CVs. The standard theoretical picture of the formation and evolution of CVs is described in slightly more detail, together with some properties of the observed CV population. Finally, I discuss several alternative evolutionary scenarios.

The most comprehensive review of CVs may be found in Warner (1995). Another useful, but much less complete, review is given by Hellier (2001).

2.1 Roche geometry

In a binary star system where the orbits are circular, the orbital angular velocity in an inertial frame is given by Newton's generalization of Kepler's third law,

$$\boldsymbol{\Omega}_{orb} = \sqrt{\frac{G(M_1 + M_2)}{a^3}}\ \hat{\boldsymbol{z}}, \tag{2.1}$$

where $\hat{\boldsymbol{z}}$ is a unit vector perpendicular to the orbital plane, a is the orbital separation, and M_1 and M_2 are the masses of the stars (M_1 will be used to denote the mass of the accreting star, and M_2 the mass of its companion, throughout). The orbital period is $P_{orb} = 2\pi/\Omega_{orb}$. Assuming that both stars can be approximated as point masses, the sum of the gravitational and centrifugal potential in a reference frame rotating with the binary is

$$\boldsymbol{\Phi}_R(\boldsymbol{r}) = -\frac{GM_1}{|\boldsymbol{r} - \boldsymbol{r}_1|} - \frac{GM_2}{|\boldsymbol{r} - \boldsymbol{r}_2|} - \frac{1}{2}(\boldsymbol{\Omega}_{orb} \times \boldsymbol{r})^2 \tag{2.2}$$

(e.g. Frank et al. 1985), where $\boldsymbol{r}_1$ and $\boldsymbol{r}_2$ are the position vectors of the centres of the stars. $\boldsymbol{\Phi}_R(\boldsymbol{r})$ is called the Roche potential. It can be shown (e.g. Warner 1995) that

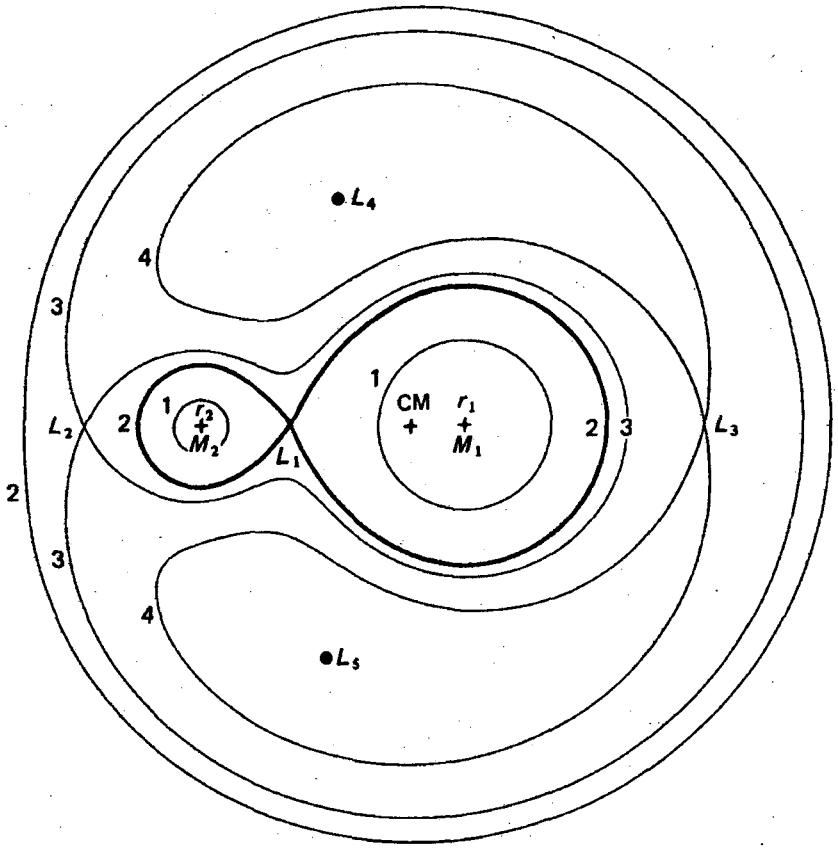

Figure 2.1: The intersection of Roche equipotential surfaces with the orbital plane for a binary with $q = 0.25$. The equipotentials are numbered 1 to 4 in order of increasing Φ_r. The centre of mass as well as the Lagrangian points are shown. Taken from Frank et al. (1985).

the shapes of the Roche equipotential surfaces $\Phi_R = const$ depend only on the mass ratio $q = M_2/M_1$, while their overall scale is a function of a only. Fig. 2.1 shows the intersection of a few equipotential surfaces, for a $q = 0.25$ binary, with the orbital plane. Φ_R has five stationary (or Lagrangian) points; these are indicated in Fig. 2.1. L_1, L_2, and L_3 are saddle points, while L_4 and L_5 are maxima. Of particular interest is the double-lobed equipotential surface that contains the inner Lagrangian point, L_1 (shown in Fig. 2.1 as a heavier curve). The two lobes of this equipotential surface are called the Roche lobes of the stars, and are the largest closed equipotentials that can contain the respective masses of the stars.

Since the stellar surface must coincide with an equipotential, a component of a binary system will be close to spherical if it has a radius that is small relative to its Roche lobe, while an increasingly larger star will have a more and more distorted shape, until it fills its Roche lobe. A binary system is called detached if both stars lie within their Roche lobes, a contact binary if both stars fill or exceed their Roche lobes, and a semi-detached binary if only one star fills its Roche lobe. In a semi-detached binary, any outward perturbation of the envelope of the Roche lobe filling star in the region of the L_1 point causes mass to be

transferred into the Roche lobe of the other component, where it ultimately accretes onto that star. Accretion by this process is called Roche lobe overflow. CVs are semi-detached binary stars, consisting of a white dwarf (the primary star) accreting from a lower mass secondary (usually a late-type, approximately main-sequence star) through Roche lobe overflow.

The assumption that the stars can be approximated as point masses holds for a CV because the mass of the secondary is sufficiently centrally condensed, and the primary is very small compared to the size of its Roche lobe. Furthermore, tidal interaction in a CV locks the rotation of the secondary to its orbital motion, and removes any eccentricity that may initially exist in the orbit. This happens on a time-scale that is short compared to the lifetime of a CV (e.g. Tassoul 1988; Abt & Boonyarak 2004), and means that equations 2.1 and 2.2 are valid[1].

2.2 The structure and spectral energy distribution of CVs

In this section, I describe the structure of CVs, together with their emission, focusing on non-magnetic systems. The structure of magnetic CVs differs from that of non-magnetic CVs mainly in the geometry of the accretion flow, which is altered by a strong white dwarf magnetic field (see Section 2.3 below). The presence of the magnetic field, and the resulting change of accretion geometry to almost radial infall, also affects the SED.

2.2.1 The accretion disc and bright spot

The reason for much of the interest in CVs is their accretion discs. Accretion discs, as well as their formation, are reviewed by Pringle (1981) and Verbunt (1982).

When mass transfer first begins, material enters the Roche lobe of the primary at the L_1 point with initial velocity (perpendicular to the orbital motion) close to the isothermal sound speed in the gas (c_s). It is then accelerated as it falls towards the primary. The Coriolis force deflects the stream so that it follows a trajectory which takes it around the primary (e.g. Flannery 1975; Lubow & Shu 1975). The stream collides with itself at supersonic speed, shocking the gas to high temperatures so that the relative kinetic energy of the collision is radiated. While only a very small fraction of the angular momentum of the stream is lost to the secondary in this process, a significant amount of energy is dissipated (e.g. Lubow & Shu 1975; Pringle 1981). Therefore, since a circular orbit has the lowest energy for a given angular momentum, this leads to the formation of a ring of gas orbiting the primary at the circularization radius, which is very close to the radius at which material in Keplerian orbit around the primary has the same specific angular momentum as it had at the L_1 point.

[1]The equipotential surfaces in the reference frame rotating with the binary are time-dependent for an elliptical orbit.

The Keplerian velocity of a particle in a circular orbit around the primary is

$$v_K(r) = \sqrt{\frac{GM_1}{r}}, \tag{2.3}$$

where r is the radius of the orbit. Since the ring has finite radial thickness, equation 2.3 implies that it rotates differentially. Viscosity in the gas then leads to dissipation of energy, as heat generated by the shearing flow is radiated. The loss of energy causes most of the gas particles to spiral to smaller radii through a series of approximately circular orbits. This inward drift requires a loss of angular momentum, which, in the absence of external torques[2], occurs by transfer of angular momentum between adjacent disc annuli by viscous torques. Thus the outermost particles gain angular momentum and spiral outwards; in this manner the ring spreads into a disc (see e.g. Lynden-Bell & Pringle 1974).

The disc material has momentum primarily in the orbital plane. The thickness of the disc perpendicular to this plane is therefore determined by hydrostatic equilibrium (radiation pressure and self gravitation are not important in CV discs; e.g. Frank et al. 1985). Assuming that the disc is isothermal in the direction perpendicular to the orbital plane, the scale height is given by $H(r) = rc_s/v_K$; i.e. the disc is geometrically thin if and only if the local Keplerian velocity is highly supersonic. This is the case in CV discs, as demonstrated by the observed line widths.

Viscosity is required to transport angular momentum and drive accretion through the disc. This cannot be provided by ordinary molecular viscosity, since discs are too tenuous (e.g. Pringle 1981). However, high observed accretion luminosities, and the fact that some CVs are able to adjust to large changes in the mass transfer rate through the disc ($\dot{M}_d$) in only days, indicate that angular momentum is efficiently transported. The most plausible cause for viscosity is magnetic turbulence (e.g. Lynden-Bell 1969). Any magnetic field present in the disc will be sheared by the differential rotation, so that radial components are transformed into azimuthal components, and amplified. The energy required to amplify the field comes from the kinetic energy of the disc material. When the magnetic pressure becomes comparable to the central disc pressure, the Parker instability leads to a dynamo action in the disc, without requiring a strong equilibrium magnetic field (Parker 1970; Balbus & Hawley 1991; Tout & Pringle 1992b). The effective kinematic viscosity of a turbulent process has the form $\nu_k \sim \ell v_t$, where ℓ is the size of the largest turbulent eddies, and v_t is their turn-over speed. The viscosity can then be parametrized as

$$\nu_k = \alpha H c_s \tag{2.4}$$

(Shakura & Sunyaev 1973), and since the largest eddies are smaller than the scale height, and the turbulence is probably subsonic, one expects $\alpha < 1$. Equation 2.4 is the α-prescription for disc viscosity.

The optical flux of most (known) CVs is dominated by emission from the disc. Models

[2]External torques may also play a role; an example of such a mechanism is a centrifugally-driven disc wind (Cannizzo & Pudritz 1988).

of the SEDs of accretion discs are expected to be most successful for high mass transfer rate ($\dot{M}$) CVs, with optically thick, steady state discs (nova-like variables—see Section 2.3.2 below). Such disc SED models are presented by, e.g., La Dous (1989) and Shaviv & Wehrse (1991), and match observations of high-$\dot{M}$ CVs reasonably well, but fail in the case of low-$\dot{M}$ systems (e.g. Shaviv & Wehrse 1991; Kiplinger 1979, 1980). Very good models of low-$\dot{M}$ discs, accounting for optically thin regions, have not yet been developed; the models of Tylenda (1981a) are arguably still the best available, and these will be used in Chapter 3 and 4. More recent work on this problem is presented by Idan et al. (2008).

The luminosity of the disc corresponds to roughly half the gravitational potential energy lost as the disc material spirals down to the white dwarf surface:

$$L_d \simeq \frac{1}{2}\frac{GM_1\dot{M}_d}{R_1} \tag{2.5}$$

(where R_1 is the radius of the white dwarf; R_2 will be used to denote the radius of the secondary). The other half is transferred into kinetic energy of the disc material's Keplerian motion, and is radiated close to the white dwarf surface.

In the absence of a strong magnetic field, the inner disc is expected to extend down to the surface of the white dwarf. Since the angular velocity of the white dwarf (Ω_1) is much lower than the Keplerian angular velocity, $\Omega_K(r) = \sqrt{GM_1/r^3}$, at its surface ($r = R_1$), the disc material must be decelerated to match Ω_1 in the innermost annulus of the disc. This 'boundary layer' is expected to have a very small radial extent ($\ll R_1$), and radiation pressure becomes significant in this region (e.g. Frank et al. 1985). The luminosity released in the boundary layer is

$$L_{BL} \simeq L_d\left(1 - \frac{\Omega_1}{\Omega_K(R_1)}\right)^2 \tag{2.6}$$

(Kley 1991). By equation 2.5 and 2.6, almost half of the accretion luminosity is radiated in the boundary layer, unless Ω_1 is close to break-up velocity. If the boundary layer is optically thick, most of the radiation is emitted at soft X-ray and EUV wavelengths; an optically thin boundary layer radiates mostly hard X-rays (e.g. Pringle 1977; Pringle & Savonije 1979; Tylenda 1981b; Patterson & Raymond 1985a,b; see also Section 2.3.1.1).

The outer disc is significantly affected by the tidal influence of the secondary (e.g. Paczyński 1977; Osaki et al. 1993). This interaction transfers the angular momentum transported outwards through the disc back into the binary orbit. The outer disc radius (r_d) is determined by tidal dissipation, as well as disc viscosity and the effects of the accretion stream. More extreme tidal interaction can also occur (see Section 2.3.1.2).

The accretion stream from the L_1 point makes a turbulent, supersonic impact with the outer rim of the disc, forming a shock front in which the energy of the impact is radiated (see e.g. Livio 1993; Warner 1995). The resulting 'bright spot' can be an important contributor to the optical flux of a system viewed at high binary inclination (i). It is possible for part of the stream to flow over the disc rim, but if the bulk of the stream

impacts in the bright spot, its luminosity is not much less than the upper limit given by

$$L_{sp} \lesssim \frac{GM_1(-\dot{M}_2)}{r_d}, \tag{2.7}$$

where $\dot{M}_2$ is the time rate of change of M_2. The bright spot is responsible for orbital humps (e.g. Krzemiński 1965), which are a prominent feature of many CV light curves.

2.2.1.1 Line emission from the accretion flow

Almost all CVs display emission lines in their optical spectra. Balmer lines are usually the strongest, followed by He I and, in some systems, He II. The detection of lines from different ionization states suggests that lines are formed in more that one site. More direct indications for this are the presence of several velocity components in radial velocity curves (this has been observed for a long time, but particularly nice trailed spectra are shown by Spruit & Rutten 1998), and the fact that not all lines are eclipsed to the same extent or for the same duration (e.g. Honeycutt et al. 1986; Young & Schneider 1980). The important sites for the formation of optical lines are the disc and bright spot, with lines from the disc dominating in most cases (e.g. Robinson 1976; Williams 1980; Tylenda 1981a; Williams & Shipman 1988; Elitzur et al. 1988; Horne & Saar 1991). While UV emission lines also form in winds from CV discs (e.g. Drew 1987; Woods et al. 1992; Knigge et al. 1995), lines from winds are rarely prominent at optical wavelengths (but see Robinson 1973; Honeycutt et al. 1986; Hoare 1994; Kafka & Honeycutt 2004).

Emission lines will form in regions of the accretion disc that are optically thin in the continuum, but optically thick in the lines. In the models of e.g. Tylenda (1981a) and Williams (1980), the inner disc is optically thick, and lines originate in a cool, optically thin outer disc. The equivalent widths (EWs) of emission lines are then expected to decrease with increasing i, since the disc is optically thick in the continuum when viewed at high i. However, strong emission lines are detected in deeply eclipsing, low-$\dot{M}$ systems, such as Z Cha and OY Car; also, in high-$\dot{M}$ systems, emission line strength increases with increasing i (e.g. Warner 1987). These observations imply that chromospheric emission also plays a role in discs (see also Marsh 1987).

The optically thin upper layer of the disc is heated, most importantly by irradiation from the inner accretion flow and the white dwarf; this photoionizes the atmosphere of the disc and creates a temperature inversion (e.g., Jameson et al. 1980; Patterson & Raymond 1985a; Ko et al. 1996). The disc chromosphere is thought to be the dominant site of line formation (e.g. Wood et al. 1992; Vrielmann et al. 2002a,b).

The strength of Balmer emission lines increases with decreasing disc luminosity, because line emission makes a significant contribution to the cooling of a low-$\dot{M}$ disc (e.g. Patterson 1984; this is discussed further in Chapter 4).

2.2.2 The white dwarf

Once a white dwarf has formed, it cools at a rate determined mainly by the energy stored in its core and the transparency of its envelope (see e.g. Dreizler & Werner 1996; Salaris et al. 2000). In a CV, however, the white dwarf will be heated again when it starts accreting, and this heating depends on the rate of accretion onto the primary, $\dot{M}_1$ (e.g. Shaviv & Starrfield 1987; Regev & Shara 1989). Most CV primaries are probably CO white dwarfs; their properties are reviewed by Sion (1999).

The eclipse of the white dwarf can be seen in optical light curves of some high-i, low-$\dot{M}$ systems (e.g. Smak 1986; Wood et al. 1989; Steeghs et al. 2003; Feline et al. 2004a,b), and Marsh et al. (1987) show the optical spectrum of the primary in one such system. Balmer absorption lines from the white dwarf are also detected in the spectra of several low-$\dot{M}$ CVs at all orbital phases; a few examples are WZ Sge, GW Lib, and SDSS J161033.64-010223.3 (Greenstein 1957; van Zyl et al. 2000; Szkody et al. 2002).

The radial velocities of emission lines in CVs do not provide reliable estimates of the velocity of the white dwarf, and therefore M_1 measurements from spectroscopy are very uncertain (e.g. Smak 1969, 1970; Stover 1981; Marsh et al. 1987; Hessman et al. 1989). Accurate mass measurements are possible for eclipsing systems, and the available values are listed by Patterson et al. (2005). Knigge (2006) uses a sample of 16 of these eclipsing CVs to show that there is no evidence of a systematic trend in M_1 with P_{orb}.

The white dwarf is expected to dominate the far-UV flux of low-$\dot{M}$ CVs (e.g. Panek & Holm 1984). The white dwarf effective temperature (T_{eff}) has been estimated in several systems using far-UV flux measurements or spectra (e.g. Smak 1984; Szkody et al. 2002; Howell et al. 2002; Gänsicke et al. 2005b). However, in the absence of a spectral feature originating from the white dwarf, T_{eff} measurements are perhaps only reliable for systems where the white dwarf flux contribution is known from eclipse photometry (e.g. Wood et al. 1995; Feline et al. 2005).

2.2.3 The secondary star

The secondary stars in CVs are important in the study of CV evolution, because their response to mass loss is one of the factors that determines the evolutionary tracks of CVs (see Section 2.4 and 2.5 below). Because CV secondaries are non-spherical, and are losing mass and rotating rapidly, their structure is expected to deviate from that of main-sequence stars.

Secondaries are detected directly in the optical and, more often, near-IR spectra of some CVs, through molecular absorption features. The spectral types of CV secondaries are discussed by, e.g., Smith & Dhillon (1998), Beuermann et al. (1998), and Knigge (2006). The data of Smith & Dhillon (1998) revealed no difference between main-sequence stars and CV secondaries in systems at $P_{orb} \lesssim 7\,\mathrm{h}$. However, when single main-sequence stars are assigned the periods that they would have in a semi-detached binary[3], Beuermann

[3]By using measured masses and radii, and equation 2.9 below.

et al. (1998) find that the majority of CVs at $P_{orb} > 3\,\mathrm{h}$ has later spectral types than main-sequence stars at those periods. Knigge (2006) finds that this is the case at all periods.

CV secondaries have larger radii, and are more luminous than main-sequence stars of the same mass (e.g. Patterson 2001; Patterson et al. 2005; Knigge 2006). However, for $M_2 \gtrsim 0.1\,\mathrm{M}_\odot$, a CV secondary is expected to have the same effective temperature (and thus spectral type) as a main-sequence star with the same mass (e.g. Verbunt 1984; Kolb, King & Baraffe 2001), and this is supported by observations (e.g. Knigge 2006).

The spectral types of secondaries as a function of P_{orb} define a clear sequence, with little scatter at $P_{orb} \lesssim 5\,\mathrm{h}$, and increased scatter at longer periods (Knigge 2006). This implies that most CVs at $P_{orb} \lesssim 5\,\mathrm{h}$ follow a single evolutionary sequence (see also Section 2.5.2 and 2.8.6 below).

Since the secondary star is cool compared to the white dwarf and disc, its relative contribution to the flux from a CV increases at longer wavelengths. The secondary is expected to be faint compared to other components in the optical bands; in fact, in most CVs, the white dwarf alone is brighter than the secondary in UBV (e.g. Knigge 2006). Even in the near-IR, the disc and white dwarf flux contributions usually dominate (e.g. Dhillon et al. 2000; Knigge 2006), but in low-$\dot{M}$ CVs with periods above $\simeq 3\,\mathrm{h}$, the secondary star often makes a large contribution to the K-band flux (e.g. Dhillon & Marsh 1995).

Some CV light curves show orbital modulations that are due to the secondary[4]. So-called ellipsoidal modulations in IR photometry are caused by the phase-dependent visible surface area of the non-spherical secondary. The ellipsoidal variation can be used to constrain i and q (see e.g. Frank et al. 1981; McClintock et al. 1983; Haug 1988; Allan et al. 1996). Because it is being irradiated by, e.g., the disc and white dwarf, the side of the secondary facing the white dwarf is brighter than the rest of the star; this can also lead to an orbital modulation, called a reflection effect, in optical and IR light curves of CVs. The amplitude of the variation caused by the reflection effect obviously depends on i, and also on the degree of irradiation—systems with particularly bright white dwarfs or inner discs (as the result of a recent nova outburst, high $\dot{M}$, or high M_1) show a larger reflection effect (e.g. Kaluzny & Chlebowski 1988; Kovetz et al. 1988; Somers & Naylor 1999; Retter et al. 1999; Woudt & Warner 2003). The irradiated face of the secondary can also be the source of some line emission (e.g. Beuermann & Thomas 1990; Rutten & Dhillon 1994; Dhillon et al. 1994; Harlaftis & Marsh 1996; Potter et al. 2004; Hartley et al. 2005).

Since CV secondaries have systematically higher rotation velocities than single late-type stars, they should be more magnetically active, and therefore have higher X-ray luminosities. However, the secondary star is expected to be much fainter than the boundary layer in X-rays, and emission from the secondaries probably does not make a significant contribution to the X-ray fluxes of known CVs (e.g. Eracleous et al. 1991).

[4]Besides eclipses, which are, of course, also caused by the secondary

2.3 Classification of CVs

CVs are classified mainly on the basis of their long-term photometric behaviour. The classes are further sub-divided by more specific photometric as well as spectroscopic criteria. There is some variation in how different authors define CV types and allow them to overlap. I will briefly outline the definition of the following classes: dwarf novae (DNe), nova-like variables (NLs), novae, polars, and intermediate polars (IPs). The DN and NL classes are mutually exclusive, as are polar and IP. IPs can be DNe, but I will not include either IPs or polars amongst the NLs. CVs of all sub-types are expected to undergo the eruptions that define novae, but a CV is only called a nova if it has been observed to have such an eruption. Once a nova is back at minimum, it can also be assigned to one (or more) of the other sub-types.

2.3.1 Dwarf novae

DNe are characterized by outbursts during which their luminosity increases by typically 2–5 magnitudes; the outburst amplitude is larger for some systems. The (normal) outbursts last for about 2 to 20 days and the recurrence interval ranges from tens of days to tens of years, but is fairly well defined for any given system. Outburst morphology divides DNe into three distinct subtypes:

(i) *SU UMa stars*, in addition to normal outbursts, also undergo superoutbursts, which last $\simeq$5 times longer than normal outbursts and have maxima $\simeq$0.7 mag brighter. Photometric modulations, called superhumps, are present in all superoutbursts.

(ii) *Z Cam stars* show rapid successions of outbursts interspersed with 'standstills', lasting tens of days to years, during which they stay at $\simeq$0.7 mag below maximum.

(iii) *U Gem stars* are DNe that do not belong to either of the two other subtypes.

Additional DN sub-types have been defined; in particular, the SU UMa stars with the longest (shortest) outburst recurrence times are sometimes referred to as WZ Sge stars (ER UMa stars).

2.3.1.1 The thermal instability

Observations of Smak (1971), Warner & Nather (1971), and Warner (1974) showed that the component of a DN that brightens during outburst is the disc. It is now generally accepted that a DN outburst results from the release of gravitational potential energy during a temporary phase of increased $\dot{M}_d$, in accordance with the thermal (or disc) instability model of Osaki (1974). Osaki (1996) presents a review of the thermal instability model, dealing also with superoutbursts (Section 2.3.1.2).

By the thermal instability model, $-\dot{M}_2$ is roughly constant, and higher than viscous interactions in the quiescent disc allow $\dot{M}_d$ to be. Matter therefore builds up in the disc until an instability triggers an outburst by making the viscosity rise sharply, so that angular momentum transport is greatly enhanced. The resulting increase in $\dot{M}_d$ increases the system luminosity and drains the disc of material until it drops back into the quiescent, low

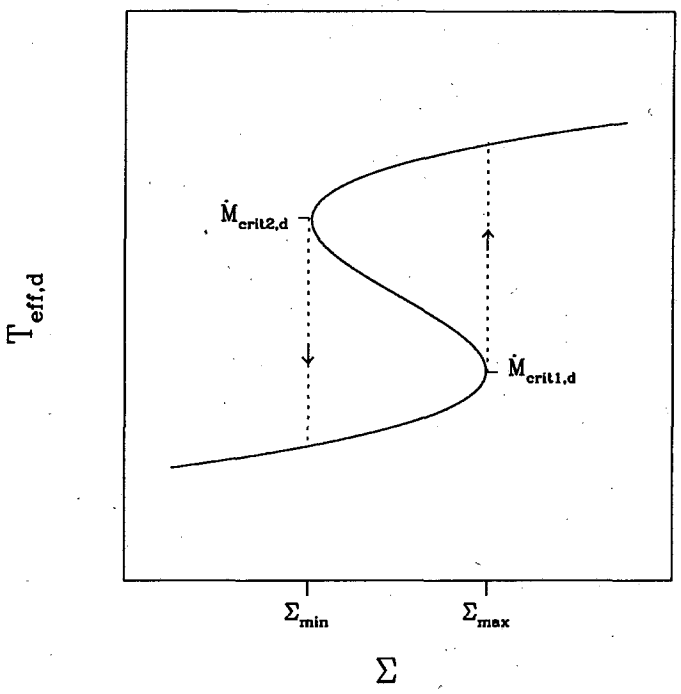

Figure 2.2: A schematic representation of the thermal equilibrium S-curve in the Σ–$T_{eff,d}$ plane. The upper (lower) branch of the curve corresponds to outburst (quiescence). An annulus on the middle branch is in unstable thermal equilibrium. In realistic models, the shape of the S-curve depends on α (e.g. Pojmanski 1986). The thermal cycle of heating and cooling is illustrated by dashed lines and arrows.

viscosity state. Hoshi (1979) discovered the physical mechanism responsible for the thermal instability; his work was further developed by, e.g., Meyer & Meyer-Hofmeister (1981), and Cannizzo et al. (1982). The ionization of hydrogen at a temperature of $T \sim 10^4$ K lies at the heart of the thermal instability. The opacity of hydrogen, as it is becoming ionized, is significantly higher than that of neutral hydrogen; furthermore, it is a very sensitive function of temperature ($\kappa \sim T^{10}$). This leads to the existence of a range of surface densities ($\Sigma = 2 \int \rho_d dz$, where ρ_d is the volume density of the disc, and z is the direction perpendicular to the orbital plane[5]) where each value of Σ corresponds to three thermal equilibrium values of the disc effective temperature ($T_{eff,d}$), in any given region of the disc, depending on its ionization state. In other words, if the locus of models for which heating through viscous interactions equals energy radiated from the surface is plotted in the Σ–$T_{eff,d}$ plane, they form an S-shaped curve. The S-curve of thermal equilibrium models is shown schematically in Fig. 2.2.

A disc annulus with $(\Sigma, T_{eff,d})$ to the left of the curve cools to the lower branch of the curve, while $(\Sigma, T_{eff,d})$ to the right of the curve will cause the annulus to heat until it reaches thermal equilibrium on the upper branch (where hydrogen is fully ionized, and κ depends less sensitively on T). A disc annulus on the middle branch of the S-curve (where $\partial T_{eff,d}/\partial \Sigma < 0$) is unstable, since, in such a region, the local $\dot{M}_d$ increases in response to a decrease in Σ, decreasing Σ even further. Therefore, the structure of a disc adjusts to place it on the upper or lower branch of the curve. The transition from low- to high-$T_{eff,d}$ structure occurs at a critical surface density, Σ_{max}; the onset of the inverse process is marked by Σ_{min}. These two values of Σ correspond to mass transfer rates $\dot{M}_{crit1,d}$ and

[5] z is used later to denote height above the Galactic plane, and r, which in this chapter denotes radius in the accretion disc, will later be used for radius in the Galactic disc, but there should be no confusion.

$\dot{M}_{crit2,d}$, and are increasing functions of radius (e.g. Mineshige & Osaki 1985; Hameury et al. 1998; relations for $\dot{M}_{crit1,d}$ and $\dot{M}_{crit2,d}$ are quoted in Section 3.2.4).

If the mass transfer rate into some annulus, with $T_{eff,d}$ on the lower branch of the S-curve, is between $\dot{M}_{crit1,d}$ and $\dot{M}_{crit2,d}$, its surface density increases until it reaches Σ_{max}. At this point the instability is triggered and the annulus heats until it enters the high state. Material spreads to adjacent annuli, pushing their surface densities over the critical value, and in this manner a heating wave propagates through the disc and switches the whole disc to outburst. The outburst rise time depends on both the distribution of material in the disc, and the radius of the first annulus to enter the high state. The larger the radius of this annulus, the faster the rise to maximum. The instability that flips the disc back to the low state is again triggered locally when the drain of material out of the disc causes the surface density of some annulus to drop below Σ_{min}. This is always an annulus in the outer disc, since Σ_{min} is highest there, explaining why, whereas outburst rise times differ, the rate of decay from maximum is similar for all outbursts. A cooling wave propagates inwards, and returns the whole disc to quiescence.

In outbursts with a fast optical rise the system brightens at longer wavelengths first, with the rise at shorter wavelengths progressively delayed (e.g. Hassall et al. 1983; Smak 1987); this is called the UV delay. An almost simultaneous rise at all wavelengths occurs for outbursts with a slow optical rise (e.g. Bailey 1980; Smak 1987). The EUV flux only rises when the heating wave reaches the inner edge of the disc, since $\dot{M}_1$ increases only at that point (e.g. Smak 1987; Cannizzo 1993).

Whereas a DN brightens also at soft X-ray and EUV wavelengths during outburst, the hard X-ray flux decreases (e.g. Patterson & Raymond 1985a; Jones & Watson 1992). A change in the vertical optical depth of the boundary layer is thought to cause this—at low accretion rates the boundary layer is optically thin and cools inefficiently, so that it reaches very high temperatures and emits hard X-rays, but when $\dot{M}_d$ increases, the boundary layer becomes optically thick, cools more efficiently, and radiates at EUV and soft X-ray wavelengths (see e.g. Pringle 1977; Pringle & Savonije 1979; Tylenda 1981b; Patterson & Raymond 1985a).

Because the temperature of the disc at maximum light is similar in all DNe, and the size of the disc is sensitive only to P_{orb}, the absolute magnitude of DNe at maximum is fairly well constrained by P_{orb} and i alone, making it possible to obtain distance estimates from outburst photometry (Warner 1987; see also Section 5.2.2).

2.3.1.2 The thermal-tidal instability

Superoutbursts, accompanied by superhumps, are the defining property of the SU UMa stars. Superhumps were first observed by Vogt (1974) and Warner (1975) in a superoutburst of VW Hyi. They have periods (P_{sh}) a few percent longer than P_{orb}, amplitudes of roughly 0.3 to 0.4 mag, and pulse profiles that are usually highly non-sinusoidal. The lack of a correlation between superhump amplitude and i implies that they represent an intrinsic flux variation, rather than a geometric effect (e.g. Warner 1995).

Superoutbursts are explained as resulting from tidal resonance between the disc and the secondary, which drives the disc into an elliptical shape (Whitehurst 1988b; the presence of an elliptical disc in superoutburst was already proposed by Vogt 1982). A superoutburst is always triggered by a normal outburst (e.g. Vogt 1982, 1983). As the disc radius expands during outburst, the outer edge of the disc can, under the right conditions, reach a region where particles in the outer disc are in a 3 : 1 tidal resonance with the secondary (i.e. the particles orbit three times per binary orbital cycle). This causes the disc to become elliptical, and strong tidal dissipation in the eccentric disc maintains the high viscosity required for a DN outburst, thereby prolonging the outburst. The elliptical disc precesses progradely, and viscous dissipation, caused by tidal stresses, produces the superhump modulation at a frequency $1/P_{sh} = 1/P_{orb} - 1/P_{prec}$, where P_{prec} is the precession period of the disc (e.g. Whitehurst 1988a). Because P_{prec} is related to q (e.g. Osaki 1985; Patterson 1998), measurements of P_{sh} and P_{orb} can be used to estimate q (and therefore M_2, since M_1 does not vary by much). The fractional superhump period excess, $\epsilon = (P_{sh} - P_{orb})/P_{orb}$, is therefore a useful indication of M_2 (e.g. Patterson 1998, 2001; Patterson et al. 2003, 2005b).

For a disc in equilibrium with the mass transfer stream, the 3 : 1 resonance radius is smaller than the tidal radius (at which the disc is truncated by the influence of the secondary) only if $q \lesssim 0.25$ (Paczyński 1977; Hirose & Osaki 1990). Since the secondary is Roche lobe-filling, q and P_{orb} are closely related for a system with a typical M_1 and M_2–R_2 relation (see equation 2.9 below). In such a system $q \lesssim 0.25$ implies $P_{orb} \lesssim 3$ h. Almost all the SU UMa stars do have P_{orb} below 3 h, and, conversely, all DNe at these periods are expected to be SU UMa stars. Patterson et al. (2005) find empirically that the fraction of CVs displaying superhumps decreases with q to 50% at $q \simeq 0.35$.

2.3.2 Nova-like variables

NLs are high-$\dot{M}$ systems which do not show any outbursts. These objects have $-\dot{M}_2 > \dot{M}_{crit2,d}$, are spectroscopically similar to DNe in outburst, and, indeed, have absolute magnitudes similar to DNe at maximum (e.g. Patterson 1984; Warner 1987).

Several NL sub-types are recognized:

(i) *UX UMa stars* have persistent broad Balmer absorption lines in addition to the emission lines usually present in NLs.

(ii) *RW Tri stars* have pure emission line spectra, sometimes with sharp absorption cores.

(iii) *VY Scl stars* are characterized by occasional photometric low states (at least 1 mag fainter than the average brightness, lasting for weeks to years).

(iv) *SW Sex stars* are NLs in which the Balmer emission lines display significant radial velocity phase shifts relative to the expected radial velocity of the white dwarf, as well as phase-dependent central absorption. These objects also have a few other fairly commonly shared properties, but the exact definition of the class is not agreed on.

There is quite a bit of overlap between these four subtypes. UX UMa stars and RW Tri

stars are distinct classes, but a VY Scl star at maximum can belong to any of the other three subtypes, and SW Sex stars are usually also RW Tri stars.

The distinction between the spectroscopically defined UX UMa and RW Tri subtypes results (at least in part) from i. In all NLs (except VY Scl stars in low state; see below) most of the disc is expected to be optically thick, so that the contribution from the absorption line spectrum decreases with increasing i. This is evident in RW Tri stars, where the relative strengths of the optical emission lines are seen to be greater for higher i systems (Warner 1995).

The photometrically defined VY Scl stars were first described by Wade & Ward (1985); most occur in the orbital period range 3 to 4 h. While faint, VY Scl stars have the spectroscopic appearance of DNe in quiescence. These low states are believed to be caused by changes in $\dot{M}_2$—in terms of the disc instability model (Section 2.3.1.1), VY Scl stars usually have $-\dot{M}_2 > \dot{M}_{crit2,d}$, but occasionally $-\dot{M}_2 < \dot{M}_{crit2,d}$ (e.g. King & Cannizzo 1998).

SW Sex stars were defined by Thorstensen et al. (1991); most of them are high-i systems (the first five were all eclipsing). Besides the Balmer line absorption events and radial velocity phase shifts, they typically have single-peaked spectral lines, 3 h $< P_{orb} <$ 4 h, and V-shaped eclipse profiles; also, the high-excitation lines are eclipsed to greater extent than the low-excitation lines (e.g. Thorstensen et al. 1991; Rutten et al. 1992; Horne 1999; Knigge et al. 2000; Rodríguez-Gil et al. 2007). It was at first thought that the SW Sex properties may result purely from very high i (e.g. Dhillon et al. 1992), but since then low-i SW Sex stars have been recognized (e.g. V442 Oph; Hoard et al. 2000). There is no satisfactory model for the behaviour of SW Sex stars, but the proposed explanations include a disc-anchored magnetic propeller; flared, self-occulting accretion discs; accretion stream overflow in combination with an accretion wind; and strong white dwarf magnetism (Horne 1999; Knigge et al. 2000; Hellier 2000; Rodríguez-Gil et al. 2001; Patterson et al. 2002b).

2.3.3 Magnetic CVs

In about 20% of CVs in the Ritter & Kolb (2003) catalogue, the white dwarf has a magnetic field sufficiently strong either to prevent the formation of a disc entirely, or at least disrupt it to a significant extent. These are the magnetic CVs, and they are divided into two sub-types:

(i) *Polars* (or AM Her stars) show strong circular and linear polarization, modulated at the orbital period.

(ii) *Intermediate polars* (or DQ Her stars) are characterized by very stable pulsations, at periods $< P_{orb}$ in their optical and X-ray light curves.

The distinction between the observational properties of polars and IPs are explained by a combination of white dwarf magnetic field strength and accretion rate, with polars having stronger fields and lower $\dot{M}$ than IPs.

The most detailed review of polars is given by Cropper (1990). Defining characteristics of the class are strong circular and linear polarization, and white dwarf rotation synchronized with the binary orbit. The strong polarization implies very large magnetic fields (measured in several polars from cyclotron harmonics or Zeeman splitting to be in the range ~ 10 to $\sim 100\,\mathrm{MG}$; e.g. Wickramasinghe & Meggitt 1982; Wickramasinghe & Martin 1985; Schmidt et al. 1996; Schwope et al. 2006) that can only originate in the white dwarf. The period of modulation of the polarized light from polars is identical to P_{orb}, implying spin-orbit synchronism. Polars do not have discs—the accretion is magnetically channelled onto small (on the order of 0.01 or 0.001 of the white dwarf surface area; e.g., Bailey & Cropper 1991; Bailey et al. 1993) accretion zones near the white dwarf magnetic poles. The optical light is dominated by cyclotron emission (hence the strong polarization), and cyclotron humps are detected in the spectra of most polars (e.g. Cropper et al. 1989; Bailey et al. 1991; Wickramasinghe et al. 1991); high excitation lines, specifically He II λ4686, are also prominent.

Accretion exerts a spin-up torque on the rotation of the white dwarf, and it is the strong interaction of the white dwarf and secondary magnetic fields that phase-locks the rotation of the white dwarf in a polar (see e.g. Lamb et al. 1983; Campbell 1989). In fact, several polars rotate slightly asynchronously (see e.g. Stockman et al. 1988; Campbell & Schwope 1999), but the degree of asynchronism in these systems is small (the white dwarf spin period and P_{orb} differ by only $\sim 1\%$), and they will attain spin-orbit synchronism on a short time-scale (e.g. Schmidt & Stockman 1991).

Patterson (1994) reviews the subject of IPs. Besides the defining short-period photometric pulsations, widely shared properties of IPs are high excitation spectra, pulsations in the He II λ4686 emission lines, circular polarization, and very hard X-ray spectra.

Magnetically channelled accretion from the inner edge of a truncated disc onto a rapidly rotating white dwarf explains most of the phenomenology of IPs. The white dwarf spin cycle produces the photometric modulation that characterizes an IP as the rotating 'beam', originating from the almost radially infalling accretion, periodically sweeps either across the line of sight, or over some structure that reprocesses it. This model was constructed to explain observations of the type star, DQ Her, and took some time to develop (see Bath et al. 1974; Lamb 1974; Katz 1975; Patterson et al. 1978; Chanan et al. 1978; Chester 1979; Petterson 1979, 1980) The most direct evidence supporting the magnetic rotator model is the detection of circular polarization in several IPs (Penning et al. 1986; Stockman et al. 1992; Buckley et al. 1995; Rodríguez-Gil & Potter 2003).

Primaries in IPs have magnetic field strengths in the range ~ 1 to $\sim 10\,\mathrm{MG}$ (e.g. Norton & Watson 1989; Wickramasinghe et al. 1991). The field strength, orbital separation, and $\dot{M}$ determine whether a disc forms. Most IPs are thought to have truncated discs (e.g. Hellier 1991; cf. Hameury et al. 1986; King 1993), but V2400 Oph is believed to be an example of a discless IP (Buckley et al. 1997).

The theory of disc-fed accretion onto a compact magnetic star was developed by Elsner & Lamb (1977) and Ghosh & Lamb (1978, 1979a,b). This early work applies to a

dipole field with its axis aligned to the white dwarf spin axis; IPs are probably all oblique rotators (in fact, if the white dwarf spin and magnetic axes are aligned, the system will not display the photometric modulation required for recognition as an IP). Three dimensional magnetohydrodynamic simulations of accretion from a disc onto an inclined dipole field are presented by Romanova et al. (2003, 2004).

2.3.4 Novae

Nova eruptions are the largest amplitude variations seen in CVs—the observed brightenings range from $\simeq 6$ to $\gtrsim 19$ magnitudes. This is the cataclysm that gives CVs their name. The rise to maximum takes days to weeks (e.g. Liller et al. 1975; della Valle 1991), and novae decay to 3 magnitudes below maximum in ~ 10 to ~ 100 d (e.g. Duerbeck 1987). Eruptions of larger amplitudes are of shorter duration, and faster novae are also intrinsically brighter at maximum (e.g. Mclaughlin 1945; Duerbeck 1987).

The physical cause of a nova eruption is a thermonuclear runaway of the hydrogen-rich material accumulating through accretion on the surface of the white dwarf (see e.g. Shara 1989 for a review). The increasing mass of the layer of accreted material causes the temperature and pressure at its base to rise to values sufficient to ignite hydrogen fusion. The energy released by fusion raises the temperature (increasing the reaction rate) but does not cause the layer to expand (because the material is degenerate; e.g. Saslaw 1968). The resulting runaway reaction only ends when the temperature is so high that electron degeneracy is lifted, and the envelope is able to expand; a 'nova shell' is then ejected (the expansion velocity can reach $\sim 4\,000\,\mathrm{km/s}$; e.g. Prialnik 1986).

The mass needed for a nova eruption obviously depends on the surface gravity of the white dwarf, but also on the rate at which it accretes (e.g. Shaviv & Starrfield 1987; Townsley & Bildsten 2004, 2005). Lower $\dot{M}$ implies that a more massive envelope must accumulate before a nova eruption results. For $\dot{M} \sim 10^{-9}\,\mathrm{M_\odot/yr}$ and $0.6\,\mathrm{M_\odot} < M_1 < 1.3\,\mathrm{M_\odot}$, the nova recurrence time-scale is estimated to range from $\sim 10^4\,\mathrm{yr}$ to $\sim 10^6\,\mathrm{yr}$ (see e.g. Fujimoto 1982). All CVs (with the possible exception of systems that form with secondaries of very low mass) are expected to undergo many nova eruptions during their lifetimes. Classical novae are defined as CVs that have had exactly one observed nova eruption, and recurrent novae are CVs that have had more than one observed eruption.

Almost all objects classified as recurrent novae contain evolved secondary stars, and the "nova" mechanism is probably different in some of them (e.g. Webbink et al. 1987). It is possible, however, for a normal CV to be a recurrent nova. Recurrence time-scales of nova eruptions will be < 100 yr for CVs with $\dot{M} \gtrsim 10^{-8}\,\mathrm{M_\odot/yr}$ and M_1 near $1.4\,\mathrm{M_\odot}$ (e.g. Livio & Truran 1992). T Pyx is the only known example of such a system (i.e., it has a short P_{orb}, and a low-mass secondary). The amplitudes and recurrence time-scales of the eruptions in recurrent novae overlap with those of some SU UMa stars, but, because of the expanding nova shell, one can spectroscopically distinguish between the two types of variability.

It is difficult to compare the mass of the ejected shell with the total mass accreted

between nova eruptions (both because of uncertainties in measuring the mass of the shell and because the long-term average $\dot{M}$ is not known). Measurements of abundances in nova ejecta suggest that roughly all mass accreted by the white dwarf is lost during nova eruptions; only very massive white dwarfs increase in mass over a complete nova cycle (e.g. Starrfield et al. 1985, 1988; Livio & Truran 1992; Townsley & Bildsten 2004).

2.4 Angular momentum loss and mass transfer

Mass transfer in a binary changes the orbital period and separation, the Roche geometry, and, eventually, the structure of the mass losing star. The secular evolution of such a systems refers mainly to the changes in P_{orb}, and is described in the rest of this chapter. Reviews of CV evolution theory are given by King (1988) and Warner (1995).

The size of the Roche lobe of the secondary can be approximated to an accuracy of 2% by

$$R_L = \frac{2}{3^{4/3}} a \left(\frac{q}{1+q}\right)^{1/3} = 0.462a \left(\frac{M_2}{M_1+M_2}\right)^{1/3} \qquad \text{for} \quad 0 < q \leq 0.8 \tag{2.8}$$

(Paczyński 1971), where R_L is the radius of a sphere with the same volume as the Roche lobe. For a semi-detached system (where $R_2 = R_L$), equation 2.8 and 2.1 then give the mean density of the secondary, $\langle \rho_2 \rangle$, in terms of the orbital period:

$$\langle \rho_2 \rangle = 110 (P_{orb}/\mathrm{h})^{-2} \, \mathrm{g/cm^3}, \tag{2.9}$$

so that, given a mass-radius relation for the secondary, its mass is determined by the orbital period[6].

The magnitude of the orbital angular momentum is

$$J = \frac{M_1 M_2}{M_1 + M_2} a^2 \Omega_{orb}. \tag{2.10}$$

Differentiating equation 2.10 and 2.1 with respect to time gives the following two relations for the rate of change of the orbital period and separation:

$$\frac{\dot{P}_{orb}}{P_{orb}} = 3\frac{\dot{J}}{J} - \left(\frac{2+3q}{1+q}\right)\frac{\dot{M}_1}{M_1} - \left(\frac{3+2q}{1+q}\right)\frac{\dot{M}_2}{M_2} \tag{2.11}$$

$$\frac{\dot{a}}{a} = 2\frac{\dot{J}}{J} - \left(\frac{1+2q}{1+q}\right)\frac{\dot{M}_1}{M_1} - \left(\frac{2+q}{1+q}\right)\frac{\dot{M}_2}{M_2}, \tag{2.12}$$

and the time derivative of equation equation 2.8, combined with equation 2.12 gives

$$\frac{\dot{R}_L}{R_L} = 2\frac{\dot{J}}{J} - \left(\frac{4/3+2q}{1+q}\right)\frac{\dot{M}_1}{M_1} - \left(\frac{5/3+q}{1+q}\right)\frac{\dot{M}_2}{M_2}. \tag{2.13}$$

[6] If an exact relation is used, instead of the approximate equation 2.8, $\langle \rho_2 \rangle$ would be a function of q, but the q-dependence is weak.

These simplify to

$$\frac{\dot{P}_{orb}}{P_{orb}} = 3(q-1)\frac{\dot{M}_2}{M_2} \tag{2.14}$$

$$\frac{\dot{a}}{a} = 2(q-1)\frac{\dot{M}_2}{M_2} \tag{2.15}$$

$$\frac{\dot{R}_L}{R_L} = 2(q-5/6)\frac{\dot{M}_2}{M_2}. \tag{2.16}$$

for conservative mass transfer (i.e., $\dot{M}_1 = -\dot{M}_2$ and $\dot{J} = 0$). Equation 2.14 and 2.15 show that conservative mass transfer from the secondary to the primary ($\dot{M}_2 < 0$) decreases the orbital separation and period only if $q > 1$ (because material then moves closer to the centre of mass). By equation 2.16, the secondary Roche lobe shrinks under these conditions for $q > 5/6$. Whether the secondary remains in contact with the Roche lobe when transferring mass depends on both its internal structure and q. For $q < 5/6$, mass loss from the secondary causes its Roche lobe to expand away from the stellar surface and cuts off mass transfer[7]. CVs are observed to be in states of sustained mass transfer, despite the fact that they typically have $q < 5/6$, so that at least one of the requirements for conservative mass transfer must be violated, and, in fact, both are. In most CVs, roughly all the mass transferred is lost from the system over a full nova cycle (see Section 2.3.4); small amounts of mass are also lost more continuously through winds (Drew 1987; Proga 2003). The angular momentum loss caused by winds and the ejection of nova shells are examples of consequential angular momentum loss and are not sufficient to account for the observationally inferred mass transfer rates (see Section 2.8.4). This implies that another mechanism whereby angular momentum is lost is required to keep the secondary in contact with its Roche lobe and hence to drive mass transfer—and, with it, the secular evolution of CVs.

The two most important angular momentum loss mechanisms in CVs are gravitational radiation and magnetic braking; they are discussed in turn in the next two sections. Magnetic braking is thought to lead to much faster angular momentum loss than gravitational radiation, and to act mainly or only in long-period ($P_{orb} \gtrsim 3$ h) systems, while in short-period CVs ($P_{orb} \lesssim 3$ h) gravitational radiation is usually assumed to dominate.

The angular momentum loss rate ($-\dot{J}$) is the crucial ingredient of CV evolution theory. In the absence of mass transfer, angular momentum loss obviously decreases a and P_{orb}, but in a CV, where M_2 is decreasing, the P_{orb} evolution depends on the structure of the secondary star and on its reaction to mass loss, which in turn depends on $\dot{M}_2$ (and thus $\dot{J}$). If the binary remains semi-detached ($R_2 = R_L$), and if the secondary has a similar internal structure to a lower main-sequence star ($R_2 \propto M_2$) then, from equation 2.13 with $\dot{M}_1 = -\dot{M}_2$, the mass loss rate is related to $\dot{J}$ by

$$\frac{-\dot{M}_2}{M_2} = -\frac{\dot{J}}{J}\left(\frac{1}{4/3-q}\right). \tag{2.17}$$

[7]Unless the star is evolving off the main-sequence, and therefore expanding. In almost all CVs, however, the secondaries are low-mass stars with main-sequence lifetimes longer than a Hubble time.

The mean density of the secondary determines P_{orb} in a semi-detached system (by equation 2.9). For a secondary near the main-sequence, $\langle \rho_2 \rangle$ increases when the star loses mass, so that a CV evolves to shorter P_{orb}, as long as its secondary is not too different from a main-sequence star.

2.4.1 Gravitational radiation

All binary stars lose angular momentum through gravitational quadrupole radiation. Assuming again that the stars can be approximated as point masses, gravitational radiation causes J to change at a rate $\dot{J}_{GR}$, related to the masses of the stars and the orbital separation by

$$\frac{\dot{J}_{GR}}{J} = -\frac{32G^3}{5c^5}\frac{M_1 M_2 (M_1 + M_2)}{a^4} \tag{2.18}$$

(Landau & Lifschitz 1958). $\dot{J}_{GR}$ is sufficient to have a significant influence on the evolution of close binaries such as CVs (e.g. Paczyński 1967; Faulkner 1971). In the case of a CV with $P_{orb} \lesssim 9$ h, this drives mass transfer from the secondary at a rate

$$\dot{M}_2 = -3.8 \times 10^{-11} \frac{(M_1/\mathrm{M}_\odot)^{2/3}(P_{orb}/\mathrm{h})^{-1/6}}{(1 - 15q/19)(1+q)^{1/3}} \ \mathrm{M}_\odot/\mathrm{yr}, \tag{2.19}$$

assuming that the secondary can be treated as a main-sequence star (Warner 1995). This gives $10^{-11}\,\mathrm{M}_\odot/\mathrm{yr} \lesssim \dot{M} \lesssim 10^{-10}\,\mathrm{M}_\odot/\mathrm{yr}$, for typical CV masses and periods, which is consistent with observational estimates for most short-period CVs (e.g. Patterson 1984).

2.4.2 Magnetic braking

In most CVs at $P_{orb} \gtrsim 3\,\mathrm{h}$, a much more efficient mechanism of angular momentum loss is required to account for the observed accretion luminosities (e.g. Patterson 1984; Warner 1987). It is widely accepted that this mechanism is magnetic braking—an ionized stellar wind from a magnetic star is forced to corotate on magnetic field lines out to the Alfvén radius, thereby exerting a braking torque on the rotation of the star. Since tidal locking keeps the secondary in synchronous rotation, angular momentum lost from its rotation drains from the orbit. Magnetic braking in CVs is discussed by e.g. Verbunt & Zwaan (1981), Rappaport et al. (1983), Mestel & Spruit (1987), and McDermott & Taam (1989). The expected mass transfer rate is given by

$$\dot{M}_2 = -2.0 \times 10^{-11} (P_{orb}/\mathrm{h})^{3.2\pm0.2}\,\mathrm{M}_\odot/\mathrm{y} \qquad \text{for } P_{orb} > 2.7\,\mathrm{h} \tag{2.20}$$

(Rappaport et al. 1983, using the braking law of Verbunt & Zwaan 1981; McDermott & Taam 1989 derive a similar rate).

There is no fundamental theory for angular momentum loss resulting from magnetic braking. Equation 2.20 assumes, amongst other things, that the form of the rotational angular momentum loss relation derived for slowly rotating single stars ($\dot{J}_{rot} \propto R_2^2 J_{rot}^3$) is valid when extrapolated to the much faster rotation of CV secondaries. Because the

acceleration of the stellar wind changes from thermally driven to centrifugally driven at large J_{rot}, the dependence of $\dot{J}_{rot}$ on J_{rot} is expected to be less sensitive in rapidly rotating stars, and magnetic braking rates differing by orders of magnitude have been proposed (e.g. Andronov et al. 2003; Ivanova & Taam 2003; Andronov & Pinsonneault 2004).

2.5 The orbital period distribution

Equation 2.11 implies that the orbital period distribution of CVs is a useful indicator in the study of their evolution—loss of angular momentum and the resulting mass transfer changes P_{orb}. In practice, P_{orb} is also the only parameter accurately measured for a large number of systems. Most studies of the evolution of CVs are therefore aimed at accounting for the observed P_{orb} distribution.

This distribution is shown in Fig. 2.3. Its most striking features are the period gap (a pronounced drop in the number of systems at 2 h $\lesssim P_{orb} \lesssim$ 3 h), and the period minimum (a sharp cut-off in the period distribution at $P_{orb} = P_{min} \simeq 76$ min). The distribution also tails off gradually towards longer periods. The standard theory of CV evolution was developed to account for these properties; they are considered in turn below.

2.5.1 The decline in frequency at long periods

The gradual drop in the number of CVs towards increasing P_{orb} leaves only 22 known systems with $P_{orb} > 12$ h. This almost complete absence of CVs at $P_{orb} > 12$ h is easily accounted for by the requirement that $q < 1$, which implies $M_2 \lesssim 1.4$, since the primary mass cannot exceed the Chandrasekhar limit[8]. Equation 2.9, together with the rough approximation $M_2/\mathrm{M}_\odot = R_2/\mathrm{R}_\odot$ for a secondary star near the lower main-sequence, then gives $P_{orb} \lesssim 13$ h. Another factor to keep in mind is the increasing observational difficulty involved in measuring periods above about 12 h. The few systems at greater P_{orb} contain evolved (giant or subgiant) secondaries and initially had $M_2 \gtrsim 1\,\mathrm{M}_\odot$. Rapid evolution of CVs through the phase spent at long P_{orb} is at least partially responsible for the decline in numbers towards longer periods starting just above the period gap.

2.5.2 The period gap

The conventional explanation for the period gap—disrupted magnetic braking—was first proposed by Robinson et al. (1981), who noticed that the masses of secondaries in the period gap fall roughly in the range where the internal structures of low-mass main-sequence stars change from deep convective envelopes to fully convective. When the secondary loses its radiative core, the magnetic braking mechanism is proposed to become less efficient, or to cease operating altogether, because of reduced magnetic activity, or a rearrangement of the magnetic field structure (Rappaport et al. 1983; Spruit & Ritter

[8]Observations indicate that mass transfer is stable in CVs. This implies $q \lesssim 1$, but the exact limit on q depends on the structure of the secondary (see e.g. Hjellming & Webbink 1987). The assumption $R_2 \propto M_2$ gives stable mass transfer for $q < 4/3$ (equation 2.17).

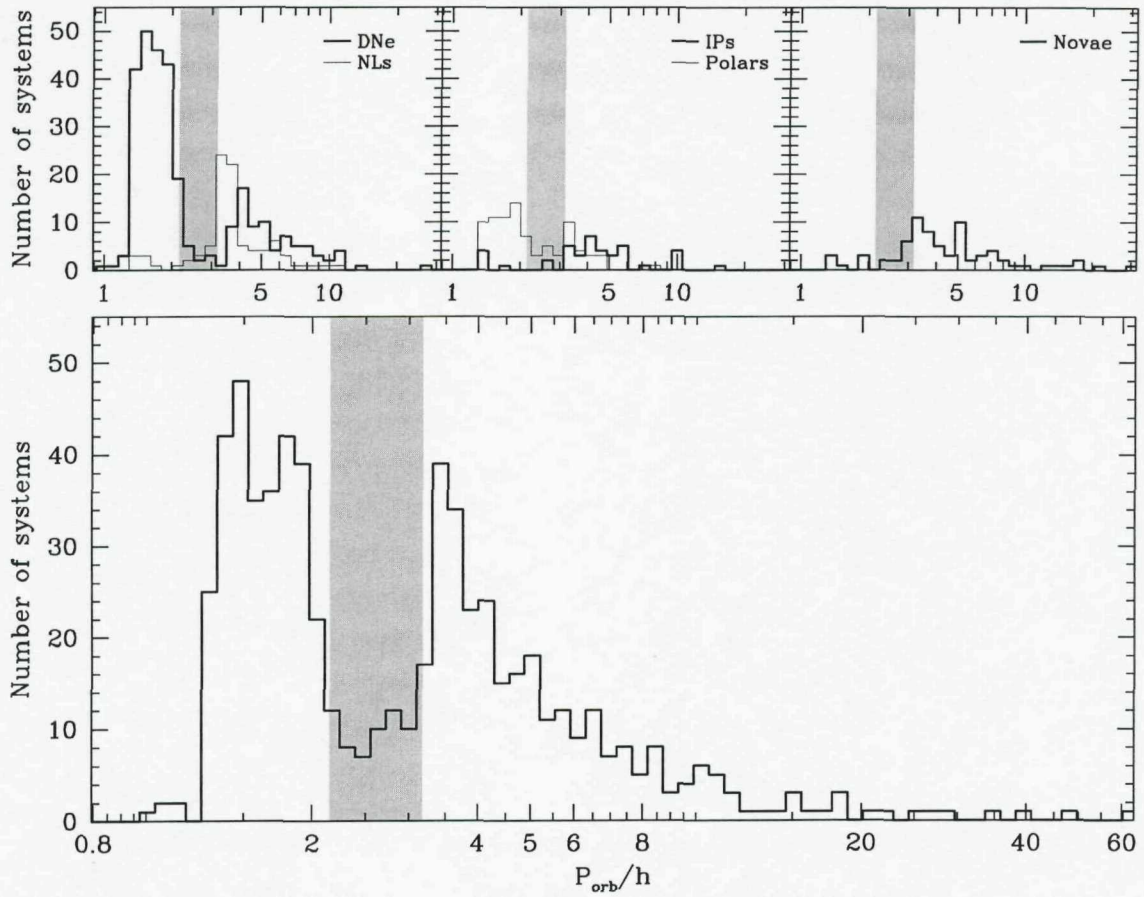

Figure 2.3: The orbital period distribution of known CVs with period measurements. The main panel shows all systems, while CVs are divided into subtypes in the upper three panels. Note that a CV can belong to more than one of these subtypes, e.g. novae also belong to one of the other classes (but the types DN and NL, as well as IP and polar are mutually exclusive; no magnetic system is counted as a NL, but IPs can be DNe). The period gap is indicated in all panels by shading of the range $2.15\,\mathrm{h} < P_{orb} < 3.18\,\mathrm{h}$ (Knigge 2006). The periods are from the Ritter & Kolb (2003) catalogue.

1983; Taam & Spruit 1989; see also Lanza et al. 2000). Angular momentum loss then proceeds at the much lower gravitational radiation rate. Because of its history of rapid mass loss, the secondary is at this point out of thermal equilibrium, which it now regains by shrinking in radius, thereby losing contact with its Roche lobe. The system is left as a detached binary, and it only regains contact with its Roche lobe, and reappears as a CV, when P_{orb} has decreased to approximately 2 h.

The evolutionary tracks of CVs starting mass transfer at different periods and with different M_2 quickly converge (e.g. Stehle et al. 1996). This explains the small scatter in the sequence of Knigge (2006), and, provided that $\dot{J}$ at $P_{orb} \gtrsim 3\,\mathrm{h}$ does not depend sensitively on M_1, it implies that almost all CVs enter the period gap with the same R_2 and M_2. The period gap for different CVs then correspond to the same P_{orb} range, so that there is a gap in the P_{orb} distribution of the overall population.

The disrupted magnetic braking model reproduces the position and width of the period

gap (e.g. Ritter 1985). The model is also broadly consistent with the relatively small number of short-period NLs and long-period DNe (see Fig. 2.3), the mass-radius relation of CV secondaries (e.g. Patterson et al. 2005), and with observational estimates of $\dot{M}$— these are on average much higher for long-period systems than for systems at $P_{orb} \lesssim 3$ h (e.g. Patterson 1984; Warner 1987). It is worth noting, though, that any mechanism that produces high $-\dot{J}$ in long-period CVs, and shuts off at $P_{orb} = 3$ h, would match these observations. That magnetic braking should be inefficient in a fully convective star has also been challenged both on theoretical (Tout & Pringle 1992a) and observational (Jones et al. 1996; Andronov et al. 2003) grounds. Nevertheless, disrupted magnetic braking remains the conventional explanation for the period gap, and a cornerstone of CV evolution theory.

2.5.3 The period minimum

There are essentially no hydrogen-rich CVs with $P_{orb} < P_{min} \simeq 76$ min, while many systems occur at periods just above this value. This sharp cut-off, the period minimum, is explained as a consequence of the response of a secondary of very small mass to continuing mass loss (e.g. Paczyński 1981; Paczyński & Sienkiewicz 1981; Rappaport et al. 1982).

By equation 2.9, $P_{orb}^2 \propto 1/\langle\rho_2\rangle$, i.e P_{orb} only decreases with mass loss from the secondary if $\langle\rho_2\rangle$ increases. Once M_2 has decreased to $\lesssim 0.08\,\mathrm{M}_\odot$, nuclear burning ceases; the star is then effectively a brown dwarf and expands in response to further mass loss. It is therefore inevitable that $\dot{P}_{orb}$ changes sign at some point. CVs in this final phase of evolution, where P_{orb} is increasing, are referred to as 'period bouncers'. This accounts for the period minimum, provided that CVs bounce at roughly the same period.

Period bounce does not necessarily happen exactly when M_2 is reduced to the hydrogen burning limit. The structure of the secondary does not change instantaneously, so that P_{orb} may continue to decrease for some time after M_2 reaches $\simeq 0.08\,\mathrm{M}_\odot$ (see e.g. Kolb & Baraffe 1999; Knigge 2006). It is also possible for period bounce to occur before M_2 reaches the hydrogen burning limit. The rate of angular momentum loss from the secondary is always at least as large as $-\dot{J}_{GR}$, therefore M_2 decreases on a time-scale that is at least as short as $\tau_{GR} = -J/\dot{J}_{GR}$. The secondary adjusts its radius in response to mass loss on the thermal time-scale, $\tau_{KH} \propto M_2^2/R_2 L$ (where L is the surface luminosity of the secondary). If τ_{KH} becomes longer than the mass loss time-scale (which is $\leq \tau_{GR}$) while the secondary is still burning hydrogen, the star will not be able to shrink rapidly enough to retain thermal equilibrium, and will become progressively oversized and overluminous for its mass. This will cause the direction of change in P_{orb} to reverse, since, while mass transfer will continue, $\langle\rho_2\rangle$ will no longer increase.

Because the evolutionary time-scale becomes very long for CVs that have evolved past the period minimum, the lifetime of a typical CV is expected to be long compared to a Hubble time. Therefore, in the standard evolutionary scenario, where gravitational radiation is the only angular momentum loss mechanism acting below the period gap, most CVs are never destroyed, but accumulate at periods near P_{min}, after evolving through period bounce (but see also Knigge et al. 2000).

2.6 The formation of CVs

A CV must form from a binary sufficiently close to become semi-detached inside the age of the Galaxy (this implies a ~ 1 to $\sim 100\,\mathrm{yr}$ orbit) that contains a low-mass star and a star massive enough to exhaust hydrogen in its core, but not so massive that it becomes a neutron star (between ~ 1 and $\sim 10\,\mathrm{M}_\odot$). The requirements in stellar masses and initial separation imply a 'common envelope' phase in the evolution of a binary that will become a CV—the radius of the white dwarf progenitor is at some point greater than the binary separation. Early work on common envelope evolution may be found in Paczynski (1976) and Meyer & Meyer-Hofmeister (1979), and Iben & Livio (1993) and Taam & Sandquist (2000) provide reviews.

When the more massive star evolves off the main-sequence, it fills its Roche lobe (either on the the red giant or asymptotic giant branch), and transfers material to the lower mass companion. Since $q > 1$ when this process starts, the Roche lobe of the mass losing star shrinks upon mass transfer (equation 2.13), and since the radius of a giant does not decrease in response to mass loss, this leads to a runaway feedback process (e.g. Tout & Hall 1991), during which mass is transferred on the dynamical time-scale, $\tau_{dyn} \sim \sqrt{R_2^3/GM_2}$, implying $\dot{M}_2 \sim M_2/\tau_{dyn} \sim M_2/\sqrt{R_2^3/GM_2} \sim 0.1\,\mathrm{M}_\odot/\mathrm{yr}$ (note M_2 and R_2 are again the mass and radius of the Roche lobe filling star, which is now the more massive component). It takes only years for the giant to lose its envelope. The rate at which the secondary accretes cannot exceed the Eddington limit (which will impose $\dot{M} \lesssim 2 \times 10^{-3}(R_1/R_\odot)\,\mathrm{M}_\odot/\mathrm{yr}$), but is limited also by the inability of the secondary to adjust its internal structure very rapidly ($\tau_{dyn} \ll \tau_{KH}$). Material therefore also overfills the Roche lobe of the secondary, first reaching the outer Lagrangian point (L_2 in Fig. 2.1), and then forming an extended common envelope around the binary.

Friction from the orbital motion of the stars inside the common envelope leads to angular momentum transfer from the binary into the common envelope, which shrinks the orbit and expels the envelope as a planetary nebula. The common envelope phase is very short (typically $\sim 10^3\,\mathrm{yr}$), and the companion star mass does not increase much during this phase (e.g. Hjellming & Taam 1991). The binary period is typically decreased by between 2 and 3 orders of magnitude (e.g. Taam & Bodenheimer 1989; Hjellming & Taam 1991). The large orbital decay during common envelope evolution is required to change the wide initial binary into a system that can become semi-detached within the age of the Galaxy.

The orbital period at the end of the common envelope phase (and thus whether the binary components coalesce before the common envelope can be expelled) is determined by the efficiency with which orbital binding energy is used to expel the common envelope. The ratio of the binding energy of the envelope to the change in orbital binding energy (from the beginning of the common envelope phase to the point when the envelope is expelled) is called the common envelope efficiency, α_{CE}. This parameter is not known with much certainty (see Section 2.8.5 for further discussion). Politano & Weiler (2007) explore the influence of α_{CE} on the properties of the zero-age CV population.

If the binary is detached once the common envelope is removed, but is expected to make Roche lobe contact in roughly less than a Hubble time, it is called a pre-CV. Some effort has been made to measure $\dot{P}_{orb}$ (and hence $\dot{J}$) in pre-CVs. Kilkenny et al. (1994) detect a P_{orb} change in HW Vir that is probably cyclical, rather than secular, since the implied $-\dot{J}$ is unreasonably large. In NN Ser, Brinkworth et al. (2006) find $\dot{P}_{orb}$ consistent with the high $-\dot{J}$ of e.g. Verbunt & Zwaan (1981), but larger than that implied by the more recent magnetic braking law of Ivanova & Taam (2003); this system has a low-mass, fully convective secondary. The period of the pre-CV V471 Tau also seems to be decreasing on a time-scale consistent with strong magnetic braking, but there are cyclical changes superimposed on the systematic decrease (Skillman & Patterson 1988).

If the initial a is small enough ($P_{orb} \lesssim 1\,\mathrm{yr}$) for the massive star to make contact on the giant branch, it loses its envelope before core He burning starts. This leads to a low-mass He white dwarf primary. If, on the other hand, the white dwarf progenitor starts core He burning before filling its Roche lobe, it contracts, and can only fill its Roche lobe on the asymptotic giant branch, by which time the core mass is larger, leading to a CO white dwarf primary. This leads to a bimodal distribution of primary masses in CVs, with CO primaries being more common (e.g. de Kool 1992; Politano 1996).

In the very dense environments of globular clusters, CVs are also expected to form dynamically through tidal capture and three-body collisions (e.g. Fabian et al. 1975; Hut & Verbunt 1983; Di Stefano & Rappaport 1994; Ivanova et al. 2006; Shara & Hurley 2006).

2.7 The standard theory of CV evolution versus observations

The theory outlined in Section 2.4 and 2.5 (disrupted magnetic braking, and period bounce caused by the structure of the secondary) successfully explains the period gap (as well as its position and width), the existence of the period minimum, and the fact that long-period CVs have higher $\dot{M}$ than short-period systems (which is clear from estimates of absolute magnitudes, as well as from the difference in period distributions of DNe and NLs). While reproducing these observational properties does not specifically require disrupted magnetic braking, but rather any fast angular momentum loss mechanism that stops acting at the top of the period gap, other theories that have been proposed are no more natural or successful than disrupted magnetic braking (e.g. King & Kolb 1995; Kolb et al. 1998).

However, CV evolution theory fails in other regards. Probably the most obvious problem is that models persistently place the period minimum about 10 min short of the observed cut-off (see e.g. Kolb 1993; Kolb & Baraffe 1999). Furthermore, although most DNe are short-period systems and most NLs are long-period systems, there are a few DNe (NLs) above (below) the period gap. The scatter in observationally inferred $\dot{M}$ at fixed period (Patterson 1984; Warner 1987) is also larger than expected, since the angular momentum loss mechanisms described above both produce $\dot{M}$ that depends almost exclusively on P_{orb} (either directly or via M_2).

Population synthesis methods combine the changing $\dot{J}$, $\dot{M}$ and P_{orb} with a model of the birthrate of CVs to predict the present-day distribution of CVs as a function of M_1, M_2, $\dot{M}$, and P_{orb}. Only one of these parameters, P_{orb}, has been measured for a large number of CVs. The orbital period distribution of known CVs is therefore one of the few observational characteristics of the CV population that can be used to constrain theory[9]. Population synthesis also predicts the overall size of the CV population, and this is a second prediction that can be tested observationally.

Commonly used CV birth rate models are presented by de Kool (1992) and Politano (1996), while population synthesis models are described by, e.g., Kolb (1993) and Howell et al. (1997, 2001).

These studies predict that $\simeq 99\%$ of the intrinsic present-day Galactic CV population should consist of systems with $P_{orb} \lesssim 3$ h, and that about 70% should be period bouncers (Kolb 1993; Howell et al. 1997). The first of these predictions is clearly not reflected in the known sample of CVs—long-period systems comprise significantly more than 1% of observed CVs (see Fig. 2.3). Furthermore, only a handful of known systems are likely period bouncers (e.g. Patterson et al. 2005; Littlefair et al. 2006, 2007). The explanation of the period minimum in terms of period bounce also predicts that a large number of CVs should have periods very close to P_{min} (since the number of CVs in a given period range is proportional to the time taken to evolve through that range, and $\dot{P}_{orb} = 0$ at P_{min}, so that P_{min} is a local maximum in the period distribution of CVs). This spike is, if at all present, not nearly as pronounced in the observed CV population as predicted. Clearly, if the standard theory of CV evolution is even approximately correct, the observed CV sample is not representative of the intrinsic population.

The important shortcoming of existing comparisons between predicted and observed period distributions is quantitative modelling of P_{orb}-dependent selection biases. Modelling these selection effects is the subject of Chapter 3.

The predicted size of the CV population depends on, amongst other things, the common envelope efficiency α_{CE}, the lifetime of a CV, and the formation rate of primordial binaries that will become CVs. Some theoretically predicted values of the CV space density are $(0.5-2)\times10^{-4}\,\mathrm{pc}^{-3}$ (de Kool 1992), $1.8\times10^{-4}\,\mathrm{pc}^{-3}$ (Kolb 1993), $2\times10^{-5}\,\mathrm{pc}^{-3}$ (Politano 1996), and $(1-2)\times10^{-4}\,\mathrm{pc}^{-3}$ (Ritter & Burkert 1986; Ritter & Özkan 1986; this value is not purely theoretical). Observational estimates are typically lower; some measurements are $\sim 10^{-5}\mathrm{pc}^{-3}$ (Patterson 1998), $\sim 3\times10^{-6}\mathrm{pc}^{-3}$ (Warner 2001), $\simeq (2-3)\times10^{-5}\mathrm{pc}^{-3}$ (Hertz et al. 1990), $\gtrsim 10^{-5}\mathrm{pc}^{-3}$ (Schreiber & Gänsicke 2003), $\gtrsim 4.4\times10^{-6}\mathrm{pc}^{-3}$ (Araujo-Betancor et al. 2005), and $0.9^{+1.5}_{-0.5}\times10^{-5}\,\mathrm{pc}^{-3}$ (Rogel et al. 2007)[10]. Where errors are quoted, or a range is given, the errors do not include all uncertainties.

Amongst the serious difficulties affecting observational ρ measurements is the incom-

[9]Component masses have been reliably measured for only a small number of CVs, but it is also possible to infer mass ratios in systems that display superhumps (e.g. Patterson 1998; see also Section 2.3.1.2). The observationally estimated values of $\dot{M}$ are too uncertain to provide tight constraints on theory.

[10]There are many more observational values in the literature, several of which are certainly incorrect. A few additional measurements will be discussed Chapter 5 to illustrate some of the errors that are commonly made in estimating ρ.

pleteness of almost all samples of known CVs. This is discussed further in Chapter 5.

Although it is not clear that the differences between predictions for the size and period distribution of the intrinsic CV population, and the size and period distribution of known CVs signal a real inconsistency, it has been argued that this is the case (e.g. Patterson 1984, 1989). On the other hand, it has also been argued that selection effects may hide the large predicted population of short-period CVs, and searches for this "missing" population have been conducted (e.g. Howell et al. 2001; Marsh et al. 2002; Gänsicke et al. 2005a; Witham et al. 2007).

2.8 Complications and additions to the standard theory

Because of the problems discussed in Section 2.7, as well as some further complications that will be mentioned below, many changes to the standard theory of CV evolution have been proposed. None of these different theories really amounts to an alternative to the standard theory (they all rely on some aspects of the model described above), and none is widely accepted.

Also included in this section are brief descriptions of how the evolution of CVs with nuclear evolved secondary stars, and that of magnetic CVs, is thought to differ from the standard evolutionary scenario.

2.8.1 Additional angular momentum loss below the period gap

Patterson (1998, 2001), and Patterson et al. (2003) propose that the problems with high predicted space density, the high predicted ratio of long- to short-period CVs, and the theoretical position of the period minimum can be solved by assuming $-\dot{J} > -\dot{J}_{GR}$ for short-period CVs (see also Section 4.6.3). This additional angular momentum loss may be provided by magnetic braking, which in that case does not shut off completely, or permanently (Patterson 2001; King et al. 2002). Kolb & Baraffe (1999) confirm that such an assumption moves the predicted period minimum roughly 10 min up (but does not remove the period spike from the predicted population).

King et al. (2002) suggest that $-\dot{J} > -\dot{J}_{GR}$ in a small fraction of CVs, with a range of values, will suppress the period spike, but Barker & Kolb (2003) perform a more realistic calculation, and find that this does not work as proposed.

Additional angular momentum loss mechanisms are also discussed in Section 2.8.3 and 2.8.4 below, and a completely different approach to solving the problems involving the position of the period minimum and the period spike is described in Section 2.8.5.

2.8.2 Mass transfer cycles

The magnetic braking $\dot{M}$ has a fairly sensitive dependence on P_{orb}, but is insensitive to other binary parameters (see equation 2.20). However, this is not reflected by observations—there is large scatter in observationally estimated $\dot{M}$ at fixed period and this cannot be explained purely by errors in these measurements, since different subtypes of CVs occur

in the same period intervals, as already mentioned in Section 2.7 (note that an assumption in this argument is that DNe and NLs have very different $\dot{M}$; I will return to the coexistence of DNe and NLs at the same P_{orb} in Section 6.4). In order for the period gap and the period minimum to be as sharply defined as they are, roughly constant $\dot{M}$ at a given P_{orb} is required, but only when averaged over evolutionary time-scales. Fluctuations in $\dot{M}$ around the secular mean on shorter time-scales will not affect the properties of the P_{orb} distribution, and it has been suggested that such fluctuations can be caused by irradiation of the secondary (e.g. Hameury et al. 1989; Wu et al. 1995; King et al. 1995, 1996; McCormick & Frank 1998; Ritter et al. 2000; Büning & Ritter 2004). Such mass transfer cycles will occur on the time-scale on which the Roche lobe moves through a stellar scaleheight; this time-scale is short compared to the evolutionary time-scale, but much longer than the observational baseline of about 100 yr.

The proposed origin of mass transfer cycles is variations in the radius of the secondary, caused by irradiation by the white dwarf or accretion flow. However, for M_2 in the range relevant to CVs, King et al. (1996), McCormick & Frank (1998), and Ritter et al. (2000) find that consequential angular momentum loss (see Section 2.8.4) is required for the proposed cyclical behaviour to occur. Büning & Ritter (2004) confirm that systems with M_2 and $\dot{M}$ in the ranges expected for CVs are stable to irradiation-driven mass transfer cycles.

It has also been suggested that increased irradiation of the secondary after a nova eruption may cause mass transfer cycles (Shara et al. 1986; Kovetz et al. 1988; Martin & Tout 2005).

2.8.3 Circumbinary discs

Material escaping from a CV through, e.g., nova eruptions or a disc wind, can settle into a disc in the orbital plane, outside the binary. Such a circumbinary disc interacts gravitationally with the stars, thereby extracting angular momentum from the binary orbit.

Spruit & Taam (2001) and Taam & Spruit (2001) investigate the influence of circumbinary discs on CV evolution and suggest that the presence of such discs might explain the observed range in $\dot{M}$ at fixed period (without requiring mass transfer cycles), reduce the predicted ρ (since the high $\dot{M}$ driven by circumbinary discs may destroy the secondary in less than a Hubble time), and increase the predicted minimum period. Because of the spread in $\dot{M}$ at fixed P_{orb}, model CVs with circumbinary discs follow several distinct evolutionary tracks. This smears out the edges of the period gap, which presents a serious problem for theories that rely on the influence of circumbinary discs (Spruit & Taam 2001); furthermore, the work of Knigge (2006) implies that most CVs follow a unique, standard evolutionary sequence. Spruit & Taam (2001) also point out that the discs may not survive nova eruptions.

Willems et al. (2005, 2007) have performed population synthesis studies that include angular momentum loss caused by circumbinary discs. Willems et al. (2005) confirm that

such additional angular momentum loss can increase the period minimum and suppress the period spike, and Willems et al. (2007) find that it may cause period bounce at around the position of the upper edge of the period gap.

Dubus et al. (2002) predict that circumbinary discs should dominate the SED of high-$\dot{M}$ CVs in the mid- and far-IR, and be detectable even in the near-IR.

Observations of excess mid-IR emission from several polars are best explained by circumbinary discs (Howell et al. 2006; Brinkworth et al. 2007; Hoard et al. 2007), but the masses implied for the discs are too small to impact the evolution of these systems (Brinkworth et al. 2007)[11]. Dubus et al. (2004, 2007) also find that their mid-IR observations of an IP and a non-magnetic CV hint that circumbinary discs may be present, but that the data provide no good evidence for the massive circumbinary discs needed to influence CV evolution.

2.8.4 Consequential angular momentum loss

An angular momentum loss mechanism that depends on $\dot{M}_2$, and acts only in the presence of systemic angular momentum loss (resulting from, e.g., magnetic braking or gravitational radiation), is called consequential angular momentum loss. King & Kolb (1995) show that consequential angular momentum loss caused by a magnetic wind from the disc (Livio & Pringle 1994) has difficulty in reproducing the observed period gap, and is not a viable alternative to disrupted magnetic braking. Furthermore, assuming that gravitational radiation is the only systemic angular momentum loss mechanism in short-period CVs, Barker & Kolb (2003) find that consequential angular momentum loss does not move the predicted period minimum the required 10 min up, and does not remove the predicted period spike.

Consequential angular momentum loss resulting from nova eruptions is similar to the angular momentum loss experienced during the common envelope phase (see e.g. Shara et al. 1986; Livio et al. 1991; Schenker et al. 1998). This mechanism does not significantly influence the evolution of CVs (Schenker et al. 1998)[12].

2.8.5 The binary age postulate

King & Schenker (2002) (see also Schenker & King 2002) propose that CVs take longer than the age of the Galaxy to evolve down to the period minimum, either because magnetic braking is very inefficient (as suggested by Andronov et al. 2003, but this has fallen out of favour, see e.g. Ivanova & Taam 2003, and was in any case incompatible with both the period gap and the luminosities of long-period CVs), or because very efficient common

[11]Note that the systems observed in these studies are low-$\dot{M}$ CVs, and that it would be surprising if they had massive circumbinary discs capable of driving high $-\dot{J}$.

[12]The reason that a nova shell (unlike a common envelope) does not cause large angular momentum loss is that it has much higher expansion velocity (and also lower mass). The friction between the stars and the nova shell is therefore lower, and the ejected material carries with it essentially only the specific angular momentum of the white dwarf.

envelope evolution leads to a wide binary at the end of the common envelope phase. No explanation is offered for α_{CE} to be larger than usually assumed.

However, accepting this 'binary age postulate' may solve several problems, namely the high predicted CV space density, the predicted spike at the period minimum, and the predicted position of the period minimum. It implies a higher space density for pre-CVs, but this is not inconsistent with observations, since the space density of pre-CVs is not observationally well constrained (e.g. Schreiber & Gänsicke 2003). The binary age postulate predicts that period bouncers should not exist, and two CVs with substellar secondaries are now known (Littlefair et al. 2006, 2007). However, it is possible for a CV to form with a substellar secondary (and this is suggested to be the case for one of these systems; see Littlefair et al. 2007). It is therefore not clear that there really is any observational evidence to rule out the binary age postulate.

2.8.6 CVs with evolved secondaries

Since the evolution of a CV depends on the structure of its secondary, systems with nuclear evolved secondaries (i.e., systems that formed with $M_2 \gtrsim 1\,\mathrm{M}_\odot$) follow different evolutionary sequences (e.g. Baraffe & Kolb 2000). Some of these evolved sequences have no period gap (since the secondaries become fully convective at smaller M_2), and CVs following some of these sequences experience period bounce near the top of the period gap (e.g. Baraffe & Kolb 2000).

Although most CVs fall on a unique, unevolved sequence (this is theoretically expected as well as observed; e.g. Stehle et al. 1996; Knigge 2006), CVs with evolved secondaries probably dominate the population at $P_{orb} \gtrsim 5\,\mathrm{h}$ (Beuermann et al. 1998; Baraffe & Kolb 2000; Podsiadlowski et al. 2003).

The very long-period ($P_{orb} \gtrsim 12\,\mathrm{h}$) CVs must have secondaries with radii that are much larger than that of main-sequence stars of the same mass (see Section 2.5.1). An example is GK Per, which has an orbital period near 2 d, and probably a subgiant secondary (e.g. Crampton et al. 1986; Morales-Rueda et al. 2002). There are also a few known CVs with evolved secondaries at short periods, e.g. V485 Cen, EI Psc, and QZ Ser (Augusteijn et al. 1996; Thorstensen et al. 2002a,b). The unusually short periods of V485 Cen and EI Psc (well below P_{min}) can be understood if these systems have M_2–R_2 relationships that differ significantly from those of most CV secondaries (e.g. Thorstensen et al. 2002a).

2.8.7 Magnetic systems

The stellar wind from the secondary in a polar is expected to be trapped in the magnetosphere of the white dwarf. Therefore, magnetic braking should not operate in polars, and this is consistent with the absence of a period gap in their P_{orb} distribution[13] (e.g. Wu &

[13]The period distribution of all known magnetic CVs shows a hint of a period gap (see Fig. 2.3), but this is not significant. The probability that this P_{orb} distribution is drawn from a distribution that is constant in the range $0.10 < \log(P_{orb}/h) < 0.85$, and zero elsewhere, is 0.1, according to a Kolmogorov–Smirnov test.

Wickramasinghe 1993; Li et al. 1994; Wickramasinghe & Wu 1994; Li et al. 1995; Webbink & Wickramasinghe 2002). Observational evidence in favour of this comes from lower white dwarf T_{eff} in polars than in non-magnetic CVs at similar P_{orb} (Araujo-Betancor et al. 2005), and also from the low luminosities of polars (including long-period polars; see table 6.1 of Warner 1995).

IPs are thought to evolve into polars as their accretion rates drop and the binary separations decrease (e.g. Webbink & Wickramasinghe 2002; Norton et al 2004; cf. Wickramasinghe 1993). Accepting that polars do not experience magnetic braking, and that their progenitors are IPs, the period distribution of polars provides support for disrupted magnetic braking as the cause of the period gap in non-magnetic CVs (Webbink & Wickramasinghe 2002).

It is, however, also possible for a polar to form from a pre-CV that is already synchronized when it becomes semi-detached (e.g. Schmidt et al. 2005), and for a long-period IP to evolve into a short-period IP (e.g. Norton et al 2004; Southworth et al. 2007a).

Chapter 3

The influence of selection effects on the observed cataclysmic variable population

3.1 Introduction

The rudiments of the theory of CV evolution, outlined in Section 2.4 and 2.5, have long been accepted, yet there are still significant discrepancies between the predictions of theory and the properties of the observed CV sample (see Section 2.7). Population synthesis studies predict the relative sizes of the long-period, short-period, and period bouncer populations as roughly $1 : 30 : 70$ (e.g. Kolb 1993; Howell et al. 1997). A glance at Fig. 2.3 is enough to determine that short-period CVs do not comprise 99% of the observed population; furtermore, the majority of known short-period systems are not period bouncers.

However, since different types of CVs differ in intrinsic brightness, and all surveys are limited in depth (and the majority severely so) there is no reason to think that an observed sample should be representative of the intrinsic population. Apparent brightness and large amplitude variability are two factors that obviously affect the discovery probability of a CV. Since both intrinsic brightness and the frequency of large amplitude brightness variations decrease with $\dot{M}$, short-period, low-$\dot{M}$ systems are necessarily under-represented in the known sample. The question is only whether these and other selection effects can account for the size of the discrepancy between the period distributions of the predicted and observed populations.

Fig. 3.1 goes some way towards illustrating the potential importance of the apparent magnitude dependent election effect, by comparing the period distributions of bright ($V < 17$) and faint ($V > 17$) sub-samples of the known CVs. The difference between the two distributions is striking, with the ratio of the number of short- to long-period CVs being much larger when only apparently faint systems are considered.

Although detailed models of the intrinsic CV population exist, very little effort has been made to model even the simplest observational selection effects. A commonly used assumption is that the discovery probability of CVs is proportional to $\dot{M}^{\delta}$, with δ some positive constant (e.g. Howell et al. 2001; King et al. 2002). This is clearly a gross sim-

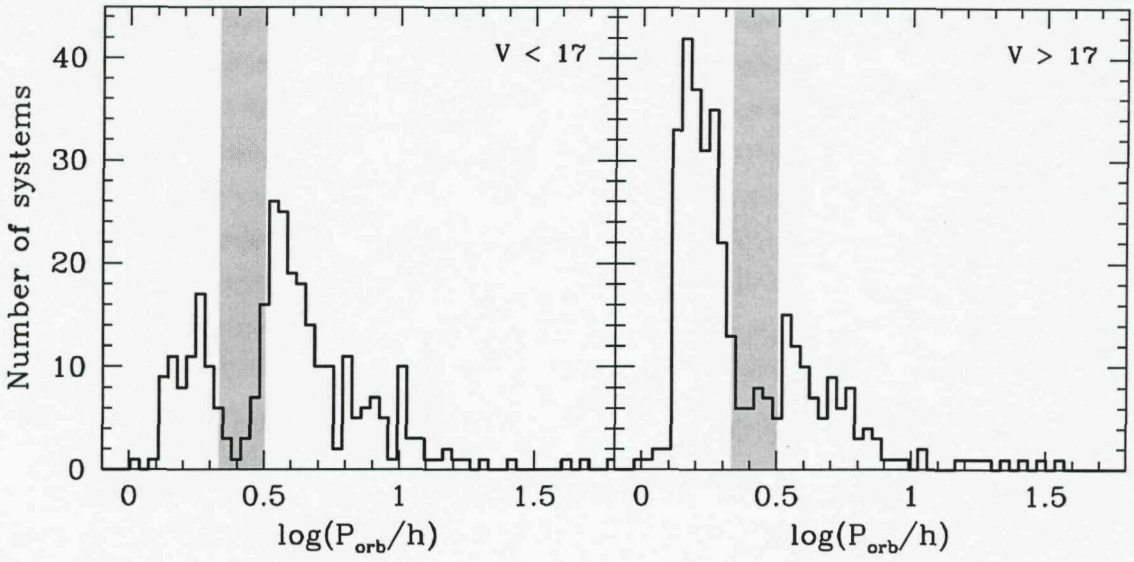

Figure 3.1: The orbital period distribution of CVs in two magnitude bins, $V < 17$ (left-hand panel) and $V > 17$ (right-hand panel). Periods are taken from Ritter & Kolb (2003). The magnitudes used are mag1 from Ritter & Kolb (2003), and systems for which V-band magnitudes were not available were discarded, unless it was possible to determine which V-bin it belongs in from a measurement in a different band-pass. An apparent magnitude of $V = 17$ was chosen as a divide because this is roughly the brightness where it becomes impractical to measure P_{orb} from radial velocity measurements with a 2-m class telescope. The period gap is indicated by light grey shading of the range $2.15\,\mathrm{h} < P_{orb} < 3.18\,\mathrm{h}$ in both panels.

plification, given that most known CVs were discovered because of variability or unusual optical colours, and that $L \propto \dot{M}^{\delta}$ is not a good description of the luminosities of CVs. It is therefore not clear to what extent theoretical predictions disagree with observations, or, indeed, whether there is a real inconsistency.

Here I present a Monte Carlo approach to modelling observational selection effects quantitatively, and use it to demonstrate how common selection effects influence the observed CV period distribution. I then apply this method to the well-defined observational CV sample detected in the Palomar–Green (PG) Survey, to determine definitively whether the intrinsic CV population predicted by the standard theory of CV evolution is inconsistent with observations, and, specifically, whether it predicts relatively too many short-period CVs.

3.2 The computational method

A Monte Carlo model is used to determine the effects of arbitrary selection criteria on observationally constructed CV samples. The key parameters that describe a CV are M_1, M_2, P_{orb} and $\dot{M}$. Given a description for the birthrate of CVs and a recipe for their subsequent evolution, population synthesis methods can be used to generate the predicted intrinsic CV population as a function of these parameters. A random sample of CVs, drawn from such a distribution, is generated and distributed within a model Galaxy.

By modelling the spectral energy distribution (SED) of each CV, a predicted sample, corresponding to an observational CV sample subject to given selection criteria, can be constructed.

Several aspects of the model are uncertain; specifically, the disc SEDs, DN outburst behaviour, and assumed vertical Galactic distributions of CVs can be questioned. Where possible, and where these uncertainties can be expected to have an important impact on the results, I will use a range of different assumptions (see Section 3.2.5 and 3.4), and I will return to the limitations of the modelling of selection effects in Chapter 6.

3.2.1 The predicted intrinsic CV population

The starting point of the modelling is the population of CVs resulting from model pm5 of Kolb (1993). This is the present-day population of CVs that results from the birth rate model of de Kool (1992) when systems are evolved using the magnetic braking prescription of Verbunt & Zwaan (1981) in the case of secondary stars with radiative cores, and gravitational radiation alone for fully convective secondaries[1]. The population synthesis model provides a probability distribution function (PDF) over the parameters P_{orb}, $\langle \dot{M} \rangle$ (the secular average $\dot{M}$), M_1, and M_2.

This model uses a bipolytropic treatment of the secondary, which becomes fully convective when $M_2 = 0.25\,\mathrm{M}_\odot$. The resulting period gap is between roughly 2.51 and 3.31 h, which is not where the observed gap is. This shortcoming can in principle be overcome; the recalibration needed to improve the match to the observed location of the period gap does not have very serious repercussions for the overall population synthesis results. The PDF is zero at $P_{orb} = 2.92\,\mathrm{h}$, and this is the value used to distinguish between short- and long-period systems in the theoretical distribution. M_1 is kept constant throughout the evolution; i.e., all the material transferred from the secondary to the primary is assumed to be ejected during nova eruptions (see Section 2.3.4). Period bounce occurs at $M_2 \simeq 0.07\,\mathrm{M}_\odot$[2], placing the period minimum at about 64 min. In this population, 99.7% of all systems are below the period gap, and 72% of all systems are period bouncers.

Magnetic systems are not accounted for separately, so if they evolve differently, as has been proposed at least for polars (e.g. Wu & Wickramasinghe 1993; Li et al. 1994; Webbink & Wickramasinghe 2002; see Section 2.8.7 for a more detailed discussion), they are not included in the population synthesis model. Furthermore, the largest secondary mass considered is $1\,\mathrm{M}_\odot$, and all secondaries are assumed to be completely unevolved at the onset of mass transfer.

[1] Kolb (1993) considered several combinations of birth rate models and magnetic braking prescriptions, and found similar resulting populations. The strength of magnetic braking is, however, not known with great certainty, and Ivanova & Taam (2003) have proposed a magnetic braking law that is significantly weaker than the Verbunt & Zwaan (1981) prescription (see also Section 2.4.2).

[2] I simply define period bouncers in this population as systems with $M_2 \leq 0.07\,\mathrm{M}_\odot$. This is close to correct, although systems actually bounce at a small range of M_2.

3.2.2 The model Galaxy

The model of the Galaxy consists solely of an axisymmetric disk, with no spiral structure, no additional thick disc, no halo, and no Galactic bulge. This is consistent with the Population I assumption made in the population synthesis model and is reasonable, since the bulk of the intrinsic CV population resides in the (thin) Galactic disk (e.g. Stehle et al. 1997).

Every system is assigned a position (r, z, ϕ) in space, where z is height above the Galactic plane, r is distance in the Galactic plane from the Galactic centre, and ϕ is azimuth. The positions are generated randomly in such a way that the overall distribution of CVs produces exponential density profiles:

$$\rho(z) \propto \exp(-|z|/h), \text{ and} \tag{3.1}$$

$$\rho(r) \propto \exp(-r/h_r), \tag{3.2}$$

where the radial scalelength is $h_r = 3\,000$ pc, and the vertical scaleheight is

$$h = \begin{cases} 120\,\text{pc} & \text{for long-}P_{orb}\text{ systems} \\ 260\,\text{pc} & \text{for normal short-}P_{orb}\text{ systems} \\ 450\,\text{pc} & \text{for period bouncers.} \end{cases} \tag{3.3}$$

Adopting different scaleheights for these three sub-populations is motivated by the fact that the long-period, short-period (pre-period bounce), and period bounce regimes are successive stages in the evolution of a single CV. The age of a CV is the sum of the time spent as a detached binary (pre-CV) and the time since becoming semi-detached, and systems first make Roche lobe contact at a range of orbital periods. This means that there is a spread in the ages of CVs at fixed period (besides that caused by period bounce), and, in fact, some overlap between the ages of sub-populations (see e.g. Kolb & Stehle 1996). Nevertheless, sub-populations have different representative, average ages. Long period CVs are typically younger than $\sim 10^{8.4}$ yr, while short-period, pre-period bounce systems are typically older than $\sim 10^{8.8}$ yr, and it takes $\sim 10^{9.4}$ yr to reach the period minimum (e.g. Howell et al. 2001). The scaleheights of the 3 sub-populations given in equation 3.3 were chosen to be representative of stellar populations with ages of $\simeq 10^{8.4}$, $\simeq 10^{9.2}$, and $\simeq 10^{9.6}$ yr (Robin & Crézé 1986).

The model assumes a Galactic Centre distance of 7 620 pc (Eisenhauer et al. 2005), and ignores the small offset of the Sun from the Galactic plane; i.e., the Earth is placed at $(r, z, \phi) = (7\,620\,\text{pc}, 0, 0)$. For computational simplicity, the Galaxy is divided along the two planes of symmetry that include both the Sun and the Galactic Centre (the planes $z = 0$ and $\phi = 0$) and only one quadrant of the Galaxy is simulated; i.e. $z \geq 0$ and $0 \leq \phi < \pi$.

Interstellar extinction is computed by integrating the density of the interstellar medium

$$\rho_{ISM} \propto \exp\left(\frac{7\,620\,\text{pc} - r}{4\,500\,\text{pc}}\right) \times \exp\left(\frac{-|z|}{140\,\text{pc}}\right) \tag{3.4}$$

(Robin et al. 2003) along the line of sight to each system to obtain the neutral hydrogen column density, N_H. The proportionality constant in equation 3.4 is found by setting $A_V = 30$ for an object at the Galactic Centre (up to a distance of 2 000 pc in the Galactic Centre direction, the extinction in V then turns out to be 3.8 mag, i.e., 1.9 mag/kpc). Extinctions in the U and B-bands are taken as $A_U = 1.531 A_V$ and $A_B = 1.324 A_V$ (Rieke & Lebofsky 1985).

3.2.3 The spectral energy distribution of CVs

Four components, namely the accretion disc, bright spot, white dwarf, and secondary star, are included in the model of the overall SED of each CV in the simulations.

A slight modification of the code described in Tylenda (1981a) was used to compute a 4D grid of accretion disc models over the variables $\dot{M}_d$ (the rate at which mass flows through the disc), M_1, the orbital inclination (i), and the outer disc radius (r_d). The viscosity parameter, α, was set to 0.01 for $\dot{M}_d \leq 10^{13}$ g/s, and 0.8 otherwise[3]. The disc model assumes a steady state disc structure and produces a blackbody spectrum for optically thick regions, while for a vertical optical depth $\lesssim 1$, the same procedure as explained in Tylenda (1981a) is adopted, so that emission lines appear in these regions. As will be explained in the next section, $\dot{M}_d = \langle \dot{M} \rangle$ is assumed only for systems with stable discs (these are a small minority of the population).

CVs are assumed to be randomly inclined with respect to Earth, therefore $\cos i$ for each system is selected as a uniformly distributed random number between 0 and 1. The inner disc radius is set equal to the radius of the primary (R_1), which is calculated using the approximate white dwarf mass-radius relation of Nauenberg (1972). The calculation of r_d will be explained in the next section.

The bright spot is modelled as a blackbody extending over an azimuth of 10° on the outer disc rim (see e.g. Wood et al. 1986).

The flux contribution of the secondary is computed using the spectral type – P_{orb} relation of Smith & Dhillon (1998):

$$SpT(2) = \begin{cases} 26.5 - 0.7 P_{orb}/\mathrm{h} & \text{for } P_{orb} < 4\,\mathrm{h} \\ 33.2 - 2.5 P_{orb}/\mathrm{h} & \text{for } P_{orb} \geq 4\,\mathrm{h}, \end{cases} \tag{3.5}$$

where $SpT(2) = 0$ means a spectral type of G0, $SpT(2) = 10$ is K0, $SpT(2) = 20$ is M0, etc[4]. The secondary is assigned the absolute magnitudes that a main-sequence star of the same spectral type would have. This is not strictly correct, since CV secondaries are not in thermal equilibrium. In systems with $M_2 \leq 0.07\,\mathrm{M}_\odot$ (i.e. period bouncers), the flux contribution of the secondary is neglected. The treatment of secondary stars is improved on in Chapter 4 by using the semi-empirical sequence of Knigge (2006). However, none

[3]This choice was made mostly for computational convenience and is not very physical, but the influence of α is small in all regards except $U - B$ colours (Tylenda 1981a). This is discussed further in Section 3.4.

[4]Because the predicted period minimum is shorter than observed, equation 3.5 is applied beyond the P_{orb} range where it can be expected to be valid. Since these very low-mass secondaries are faint compared to other components of the binaries, this is not an important concern.

of the results presented in this chapter would be changed if this sequence was used here instead of the Smith & Dhillon (1998) relation. This is because unevolved secondaries are not expected ever to be large contributors to the optical flux; in fact, with the exception of some edge-on systems, the secondary star is not an important component in the SED model of any of the simulated CVs.

The effective temperature of the primary is estimated from

$$T_{eff} = 15\,600\,\mathrm{K}\left(\frac{\langle\dot{M}\rangle}{10^{16}\,\mathrm{g\,s^{-1}}}\right)^{1/4}\left(\frac{R_1}{10^9\,\mathrm{cm}}\right)^{-1/2} \tag{3.6}$$

(Townsley & Bildsten 2003). The absolute U, B, and V magnitudes of the primary are then found using the tabulation for pure H white dwarfs of Bergeron et al. (1995). In systems with $\dot{M}_d > 2.0 \times 10^{17}$ g/s and $i > 86°$, it is assumed that the white dwarf is completely shielded by the disc, and makes no contribution to the flux[5].

3.2.4 Dwarf nova outburst cycles

Most CVs have values of $\dot{M}_2$ that cause their discs to be subject to a thermal instability; these systems are the DNe (introduced in Chapter 2), and they spend most of their time with $\dot{M}_d \neq -\dot{M}_2$, so that it is incorrect to use $\langle\dot{M}\rangle$ in the disc luminosity calculation. DNe are characterized by outbursts during which their luminosity increases by typically 2 to 5 magnitudes. Outburst durations are days to tens of days, and the recurrence interval ranges from tens of days to decades (see Section 2.3.1 for a more complete discussion).

To determine whether a system is a DN, equations 38 and 39 of Hameury et al. (1998) are used—systems with

$$\langle\dot{M}\rangle > 9.5 \times 10^{15}\alpha^{0.01}\left(\frac{M_1}{\mathrm{M}_\odot}\right)^{-0.89}\left(\frac{r_d}{10^{10}\,\mathrm{cm}}\right)^{2.68}\,\mathrm{g/s}$$

or

$$\langle\dot{M}\rangle < 4.0 \times 10^{15}\alpha^{-0.004}\left(\frac{M_1}{\mathrm{M}_\odot}\right)^{-0.88}\left(\frac{R_1}{10^{10}\,\mathrm{cm}}\right)^{2.65}\,\mathrm{g/s}$$

have stable discs. None of the CVs in the theoretical intrinsic population satisfy the second inequality, so that the model includes no systems that are stable on the lower branch of the S-curve (see Fig. 2.2). All short-period systems in the model population are DNe, and less than 0.1% of CVs in this population are permanently bright, nova-like (NL) systems.

In order to calculate the disc spectrum correctly for the systems with unstable discs, the mass accretion rates through the disc in outburst ($\dot{M}_{dO}$) and quiescence ($\dot{M}_{dQ}$) need to be found. These are related to the average value by

$$\langle\dot{M}\rangle = C\dot{M}_{dO} + (1-C)\dot{M}_{dQ}, \tag{3.7}$$

where C is the outburst duty cycle (assuming that outbursts are simple top-hat functions).

[5]In detail, the issue of shielding by the disc is more complicated than allowed for here; see e.g. Smak (1992), Meyer & Meyer-Hofmeister (1982), and Knigge et al. (2000, 2004).

The absolute V magnitude at maximum (M_{Vmax}) is found from the M_{Vmax}–P_{orb} relation of Warner (1987), as recalibrated by Harrison et al. (2004)[6]. Since the candidate period bouncers reach brighter maxima than given by this relation (these systems show only superoutbursts), period bouncers are all assigned the same maximum absolute magnitude, M_{Vmax}. The prescription used here is then

$$M_{Vmax} = \begin{cases} 5.92 - 0.383 P_{orb}/\mathrm{h} & \text{for normal DNe} \\ 5 & \text{for period bouncers.} \end{cases} \tag{3.8}$$

To find the disc luminosity (L_d) and hence the mass accretion rate through the disc at maximum,

$$\dot{M}_{dO} = \frac{2R_1 L_d}{GM_1}, \tag{3.9}$$

it is assumed that all of the outburst light originates from the disc, and that the bolometric correction is -1.8 (following Patterson et al. 2002a). The rate at which mass flows through the disc in quiescence is then

$$\dot{M}_{dQ} = \frac{\langle \dot{M} \rangle - C\dot{M}_{dO}}{1 - C}.$$

No clear empirical relation exists between the duty cycle and other observables, but for normal pre-period bounce DNe a duty cycle of $\sim$10% is in accord with observations (e.g. Warner 1995; Ak et al. 2002)[7]. For period bouncers, a duty cycle of $\sim 5 \times 10^{-3}$ is indicated by observations of the best candidates[8].

As it turns out, however, equation 3.8 and the mass transfer rates given by evolution theory cannot be reconciled with $C = 0.1$ ($C = 5 \times 10^{-3}$) for the majority of normal DNe (period bouncers). Duty cycles as large as these would imply $\langle \dot{M} \rangle < C\dot{M}_{dO}$ and thus $\dot{M}_{dQ} < 0$ (see equation 3.7). This is because equation 3.9 gives values of $\dot{M}_{dO}$ between $\sim 2 \times 10^{16}$ g/s and $\sim 8 \times 10^{17}$ g/s, while $\langle \dot{M} \rangle$ extends as low as 5×10^{13} g/s. This problem is dealt with by assuming that typical DN duty cycles are lower than those suggested by known systems. This is plausible, since the known sample of DNe is likely to be biased towards systems with unusually frequent outbursts. The grid of accretion disc models in fact extends only to $\dot{M}_d = 3.2 \times 10^{12}$ g/s (by this point the disc is in any case always fainter than the white dwarf). This leads to the requirement

$$\dot{M}_{dQ} = \frac{\langle \dot{M} \rangle - C\dot{M}_{dO}}{1 - C} \geq 3.2 \times 10^{12} \text{ g/s}.$$

[6] As with equation 3.5, the M_{Vmax}–P_{orb} relation is extrapolated to periods below the range where it is known to apply.

[7] Most (possibly all) short-period DNe are SU UMa stars and have superoutbursts in addition to normal outbursts (see Section 2.3.1.2). However, since the latter are considerably more frequent in short-period CVs that are not suspected to be period bouncers, this complication is ignored.

[8] The duration and recurrence time of outbursts in these systems are uncertain. WZ Sge, EG Cnc, and AL Com are considered good period bouncer candidates (e.g. Patterson 1998; Patterson et al. 2005), and appear to have outburst duty cycles of about 0.5%, but the observational baseline is not long enough for this to be firmly established. The two confirmed period bouncers (Littlefair et al. 2006, 2007) have never been observed in outburst.

Table 3.1: The DN outburst duty cycles that were adopted. The final column lists the fraction of the total intrinsic population represented by DNe with each duty cycle.

	DN outburst duty duty cycle	Percentage of the population
Period bouncers	5×10^{-3}	8.2
	5×10^{-4}	44
	0	20
Normal DNe	0.1	1.1
	0.01	22
	5×10^{-3}	2.1
	5×10^{-4}	2.6

For normal DNe, if $C = 0.1$ does not satisfy the above inequality, the code is set to try successively $C = 0.01$, $C = 5 \times 10^{-3}$, and $C = 5 \times 10^{-4}$, and to adopt the first value that gives $\dot{M}_{dQ} \geq 3.2 \times 10^{12}$ g/s. For period bouncers, the starting value is $C = 5 \times 10^{-3}$, and $C = 5 \times 10^{-4}$ is adopted if necessary. If $C = 5 \times 10^{-4}$ also leads to $\dot{M}_d < 3.2 \times 10^{12}$ g/s, it is assumed that the system will never be observed in outburst, and that the disc luminosity is negligible in quiescence. Table 3.1 summarizes the outburst duty cycles used.

Note that the need for small outburst duty cycles is not just a numerical problem or a quirk of a small number of peculiar model CVs. If only $\dot{M}_{dQ} \geq 0$ is required, then DNe that must have $C < 5 \times 10^{-4}$ comprise 19% of all systems, and less than 1% of the total population consists of DNe that can have $C \geq 0.1$.

Of course the procedure described above is very contrived, but, given that it is not possible to reproduce the DN outburst properties expected on empirical grounds, this approach is at least reasonable. A simple check can be made to verify that the duty cycles are not ruled out by the existing sample of DNe. Most known DNe were discovered through their outbursts. Assuming that (i) the space density of CVs is $5 \times 10^{-5}\,\mathrm{pc}^{-3}$; (ii) all DNe reach $M_V = 5$ in outburst; (iii) $C = 5 \times 10^{-4}$ implies an outburst recurrence time of 300 yr (i.e. that 1/6 of these systems had an outburst during the last 50 yr); and (iv) every DN that reached $V = 11$ at maximum during the last 50 yr was discovered and recognized as a DN, the assignment of duty cycles implies that about 10 systems with $C = 5 \times 10^{-4}$ should be known. Given the uncertainty in space density and discovery probability for DNe over the past few decades, and the fact that there are DNe that have had only one observed outburst[9], the—admittedly surprising—duty cycles are not in themselves inconsistent with observations. Patterson (1998) points out that a large population of low-$\dot{M}$ CVs could remain undiscovered if these systems have very long outburst recurrence times, and that, while this is not impossible, there is no empirical evidence of such behaviour. The above analysis shows that (accepting the mass transfer rates that result from gravitational radiation alone, that DN outbursts are caused by an increase in $\dot{M}_d$, and that DNe reach $M_V \simeq 5$ at maximum) very long outburst recurrence times are not only possible, but, in fact, inevitable.

[9]GD 552 is a well-known example of a low-$\dot{M}$ CV that has never had an observed outburst; e.g. Hessman & Hopp 1990.

Note that equation 3.8 is only used to estimate $\dot{M}_{dO}$ and $\dot{M}_{dQ}$, which are then used to calculate absolute magnitudes from the 4D grid of accretion disc models.

The probability of catching a DN in outburst is set equal to the duty cycle (which is correct for a single-epoch survey), and this probability is used to simulate some systems in outburst and others in quiescence. The outer disc radius is set to $r_d = 0.7R_{L,1}$ for NLs and DNe in outburst, and $r_d = 0.5R_{L,1}$ for quiescent systems (Harrop-Allin & Warner 1996), where $R_{L,1}$ is the Roche lobe radius of the primary (approximated using equation 2.6 of Warner 1995).

It has been suggested that $\dot{M}$ also fluctuates around the secular mean on time-scales that are too long to be observed, but shorter than the binary evolution time-scale (e.g. Hameury et al. 1989; Wu et al. 1995; King et al. 1995; McCormick & Frank 1998; Büning & Ritter 2004; Ritter et al. 2000; see also Section 2.7 and 2.8.2). Such cycles are not included in the population synthesis model used here.

3.2.5 Allowance for the main uncertainties

Uncertain components of the model include the Galactic distribution of CVs, the outburst frequency and amplitude of DNe, and, most importantly, the SEDs of accretion discs. Until better disc models are developed, not much can be done to improve the disc SED calculation, but I will verify later that the specific result derived from the PG survey (Section 3.5) does not depend sensitively on the predictions of the accretion disc model (see Section 3.4).

In order to allow for uncertainties in assigning appropriate Galactic scaleheights and outburst duty cycles to model CVs, a variety of simulations, using different assumed scaleheights and outburst properties were run.

By equation 3.3, the Gaussian scaleheight of 190 pc found empirically by Patterson (1984) is compatible with the vertical distribution used for the youngest systems. This measurement of the scaleheight was based on a sample of CVs with distance estimates, which is strongly biased towards intrinsically bright systems (this bias was even more pronounced two decades ago than it would be now). It seems reasonable that it may reflect the Galactic distribution of only the brighter, younger CVs (the difficulty in measuring the vertical density profile of CVs is discussed further in Chapter 6). Although younger stellar populations are expected to be more concentrated towards Galactic mid-plane than older populations, the observational evidence in the case of CVs is slim or nonexistent (Szkody & Howell 1992; van Paradijs et al. 1996). As a check, simulations were therefore also performed using the same vertical density profile for all systems. In those simulations

$$\rho(z) \propto 0.80\,\mathrm{sech}^2(z/323\,\mathrm{pc}) + 0.20\exp(-|z|/656\,\mathrm{pc}), \tag{3.10}$$

which results from counts of M stars (Gould et al. 1996), or a Gaussian profile,

$$\rho(z) \propto \exp\left[-\left(|z|/h\right)^2\right], \tag{3.11}$$

Table 3.2: Summary of the models considered here. The density profile given by equation 3.10 is not Gaussian or exponential, and therefore is not described by a scaleheight in the normal sense.

Galactic structure	DN outburst properties	Model
3 scaleheights (equation 3.1 and 3.3)	C chosen as described in Section 3.2.4	A1
Single large 'scaleheight' (equation 3.10)	C chosen as described in Section 3.2.4	A2
Single small scaleheight (equation 3.11)	C chosen as described in Section 3.2.4	A3
3 scaleheights (equation 3.1 and 3.3)	$\dot{M}_d = \langle \dot{M} \rangle$	B1
Single large 'scaleheight' (equation 3.10)	$\dot{M}_d = \langle \dot{M} \rangle$	B2
Single small scaleheight (equation 3.11)	$\dot{M}_d = \langle \dot{M} \rangle$	B3
3 scaleheights (equation 3.1 and 3.3)	$\dot{M}_{dQ} = 0$	C1

with scaleheight $h = 190$ pc (Patterson 1984) were used.

In addition to the treatment of DN outburst cycles described in Section 3.2.4, two limiting cases, namely $\dot{M}_d = \langle \dot{M} \rangle$ (which implies maximizing $\dot{M}_{dQ}$ and setting $C = 0$), and $\dot{M}_{dQ} = 0$ (which is equivalent to adopting the highest allowed value of C) will be explored.

3.2.6 Summary of computational details

In almost all cases, the accretion disc is the brightest SED component in high-$\dot{M}$ CVs (i.e. DNe in outburst and NL systems; exceptions are systems viewed at very high i). The white dwarf dominates the optical flux in a significant fraction of DNe in quiescence, both normal systems and period bouncers. The secondary star does not dominate the optical flux of any model CV.

All the models considered here are listed in Table 3.2. I view model A1 to be the most realistic amongst these, and will focus on this model in the next section, but results from other combinations of model Galaxies and DN outburst properties are also shown for the sake of comparison (Section 3.4).

Recall that the population synthesis model does not include evolved systems, and does not explicitly include magnetic CVs. Furthermore, the SED modelling does not make allowance for discless systems such as polars. These restrictions should be kept in mind when interpreting the results presented in the next section.

3.3 Selection effects

The scope of this chapter is restricted to three of the most common selection effects present in observational CV samples, namely magnitude limits, selection for blue $U - B$, and restricted ranges in Galactic latitude. The model is in principle also capable of quantifying the impact of large amplitude variability (DN outbursts and nova eruptions), and X-ray emission on discovery probability; these biases will be discussed further in Chapter 6.

3.3.1 Optical flux limits

Bias towards finding apparently bright objects is the simplest selection effect, and a very important one. The properties of (bolometric) magnitude-limited samples have been studied before, with the assumptions that the observed radiation is the time-averaged accretion luminosity, and that CVs are distributed uniformly in space (Kolb 1993; Howell et al. 2001). These assumptions make a comparison with data almost meaningless (as was recognized by Kolb 1993). Magnitude limits together with Galactic structure were considered by Ritter & Burkert (1986), Ritter & Özkan (1986), and Ritter (1986). However, the intrinsic CV populations assumed in these studies were not based on full population synthesis models, only bright CVs (NLs and DNe in outburst) were taken into account, and DN outbursts were not treated satisfactorily (it was assumed that all DNe will be observed in outburst, and that $\dot{M}_1$ exceeds $\dot{M}_2$ by a constant factor for all systems in outburst).

Fig. 3.2 displays period histograms of samples produced by my standard model A1, with three different magnitude limits ($V < 20$, $V < 16$, and $V < 14$). In this figure (and, with the exception of Fig. 3.4, all other model period histograms shown in this chapter) the number of systems in each bin is scaled to produce a local space density of $5 \times 10^{-5}\,\mathrm{pc}^{-3}$ (where local space density means counting systems inside a radius of 100 pc)[10]. The shape of the period distribution depends strongly on the magnitude limit. As is expected from the fact that long-period CVs are intrinsically brighter, the fraction of the total sample made up by long-period systems increases for brighter magnitude limits; it is 4.7%, 19%, and 33% for $V < 20$, 16, and 14 respectively. Dark grey shaded histograms represent period bouncers in each panel of Fig. 3.2, while the contributions of DNe simulated in outburst are shown by the fine black histograms.

Of course the known CV sample is not complete to 20th or even 16th magnitude, which raises the question of whether there is a magnitude limit for which known CVs can be directly compared to the predicted magnitude-limited samples. Fig. 3.3 shows the apparent magnitude distribution of known non-magnetic, hydrogen-rich CVs from the Ritter & Kolb (2003) catalogue, with the distribution in V of the complete model sample over-plotted in grey. Systems with $P_{orb} \geq 5\,\mathrm{h}$ are omitted from both the observed and model populations, because CVs with evolved secondaries probably dominate the population at periods above $\simeq 5$ h (e.g., Beuermann et al. 1998; Baraffe & Kolb 2000; Podsiadlowski et al. 2003; see also Section 2.8.6). The known samples with $P_{orb} < 5\,\mathrm{h}$, and $V < 12$ and < 13 contain only 5 and 17 systems, respectively. A Kolmogorov–Smirnov (KS) test shows that the magnitude distribution of known CVs becomes marginally consistent with that of the model sample only at $V \lesssim 13$. The probability that the model and observed distributions are drawn

[10]The CV space density is not known even to within a factor of 10 (see e.g. Ritter & Burkert 1986; Shara et al. 1986; Politano 1996; Patterson 1998; Schwope et al. 2002; Thorstensen et al. 2006). The choice of $5 \times 10^{-5}\,\mathrm{pc}^{-3}$ lies within the range suggested by different studies. When the model population is normalized to the formation rate of single white dwarfs, the predicted mid-plane CV space density is $1.8 \times 10^{-4}\,\mathrm{pc}^{-3}$. Existing empirical and theoretical estimates of ρ are outlined in Section 2.7, and a new measurement is presented in Chapter 5.

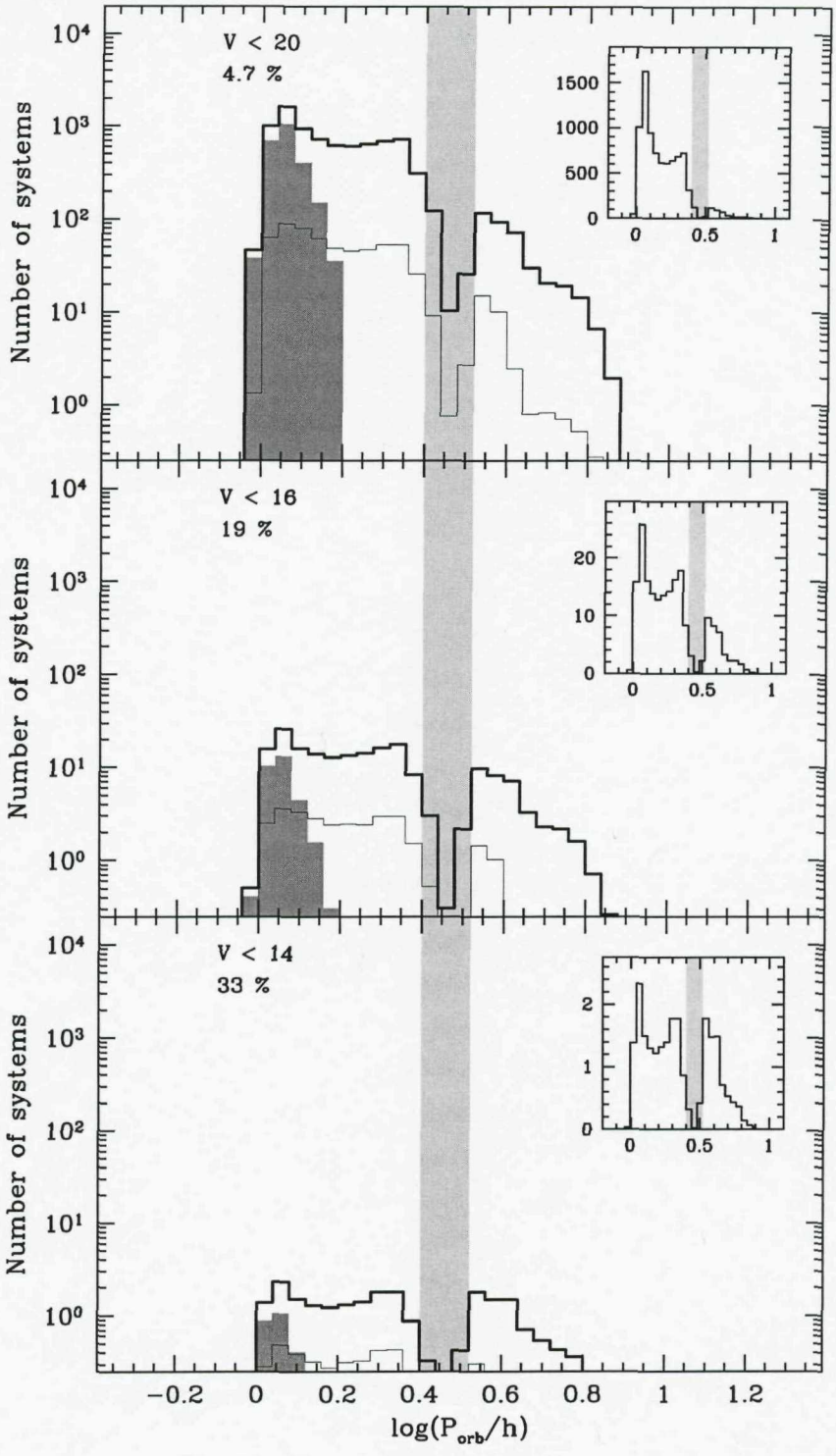

Figure 3.2: Magnitude-limited samples produced by model A1 (see Table 3.2). The magnitude limit is given in each panel, together with the fraction of the sample with periods above the period gap. Here, and in all other predicted period distributions in this chapter, light grey shading of the range 2.51 h $< P_{orb} <$ 3.31 h indicates the model period gap (see Section 3.2.1). Bold histograms are all systems detected; the contribution of period bouncers is shaded in dark grey; the fine black histograms show DNe that were simulated in outburst. The ratio of short- to long-period systems is 95:5, 81:19, and 67:33 at magnitude limits of $V < 20$, $V < 16$, and $V < 14$, respectively. Period distributions of all systems detected at each magnitude limit are plotted with linear vertical scales in the insets.

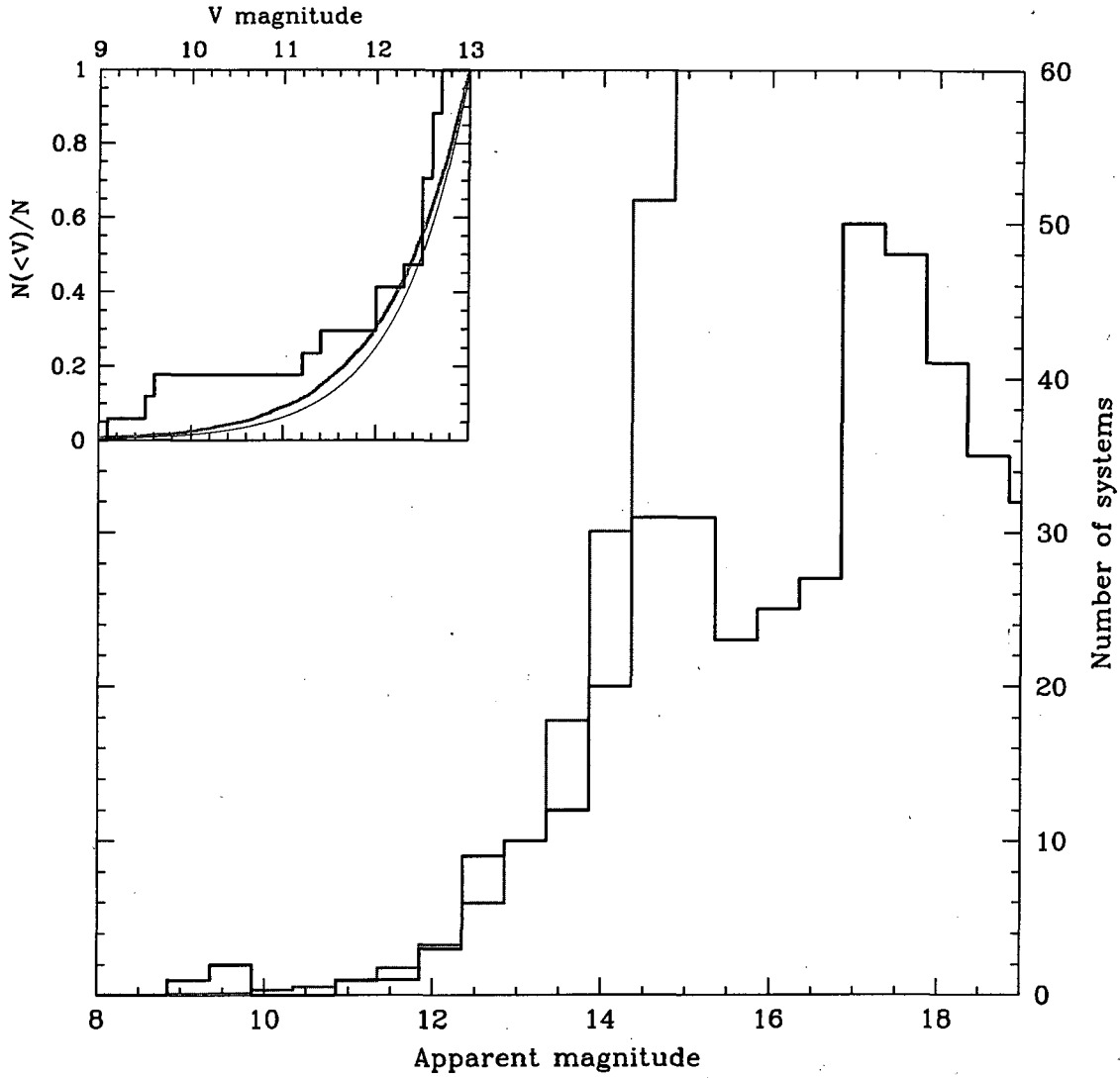

Figure 3.3: The distribution in apparent magnitude of known CVs (non-magnetic, hydrogen-rich systems in the Ritter & Kolb 2003 sample; black), and a complete sample produced by model A1 (grey; this histogram is arbitrarily scaled). Systems with $P_{orb} \geq 5\,\mathrm{h}$ were omitted from both samples (see text). The inset shows cumulative distributions for known CVs (black) and the model sample (grey), together with a sample of objects that are uniformly distributed in space and all have the same absolute magnitude (fine black curve). Magnitudes used for the histogram of the known sample are mag1 from Ritter & Kolb (2003), and are not in all cases V-band.

from the same parent population is 0.08, 0.004, and 6×10^{-16} for limiting magnitudes of $V < 13$, $V < 14$ and $V < 16$, respectively. This result is somewhat model-dependent. The inset in Fig. 3.3 shows cumulative distributions for the observed (bold black) and model (dark grey) samples. For comparison, the fine black curve represents objects with identical intrinsic brightness, that are uniformly distributed in space. Since the known CV sample is likely to be incomplete even for $V < 13$, it should not be compared to the predicted magnitude-limited samples presented here[11].

[11] Carefully chosen subsets of the known CV sample can be compared to predictions (see Section 3.5 and Chapter 4).

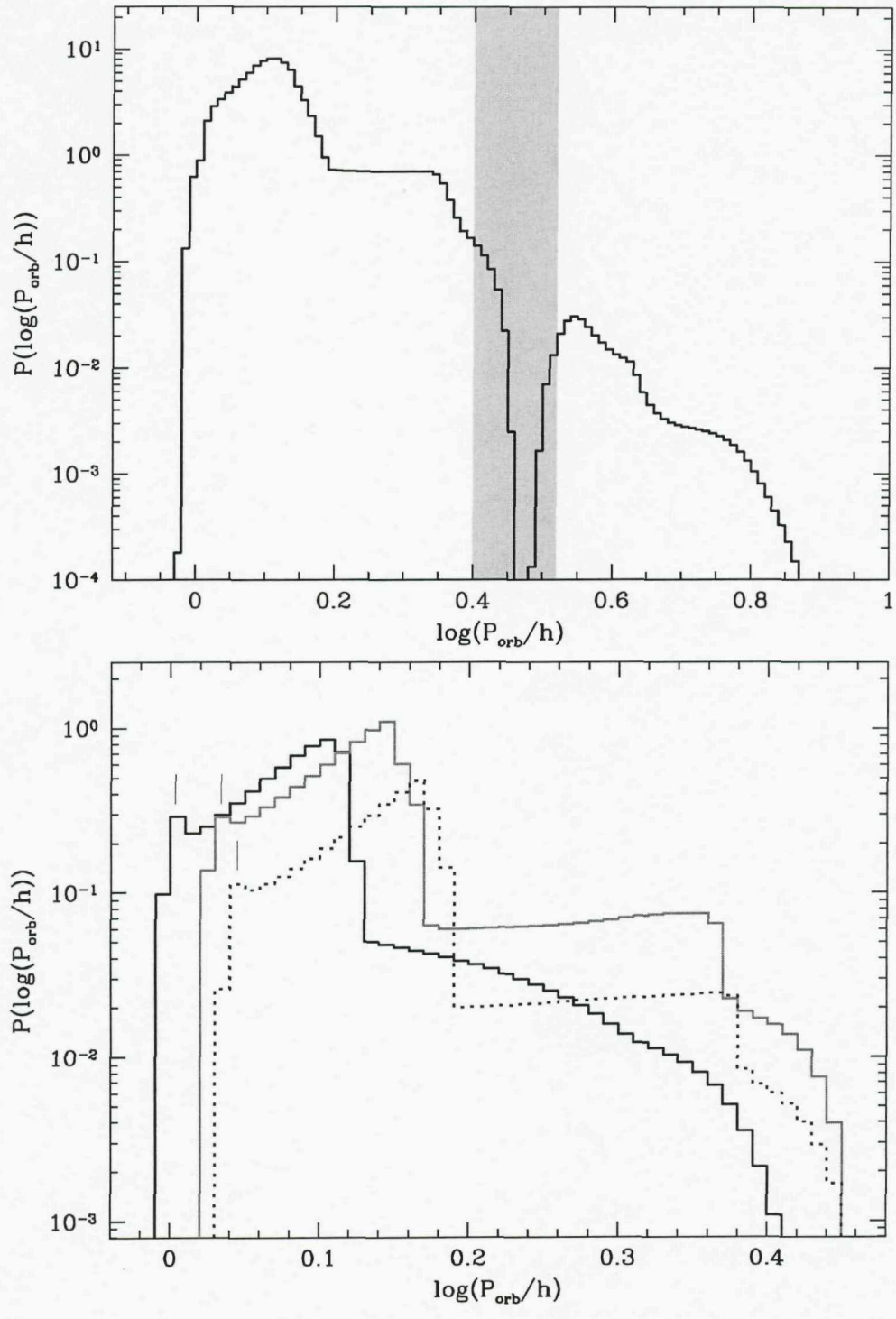

Figure 3.4: Upper panel: The orbital period distribution of the model intrinsic population. Lower panel: Orbital period distributions of model short-period systems with 3 different values of M_1. In order of increasing minimum period, $M_1 = 0.44$, 0.95, and $1.3\,\mathrm{M}_\odot$ for the sub-populations. The vertical bars mark the period spike of each distribution. Even in these single-M_1 distributions, the period spike is not very prominent, because the P_{orb} resolution is not sufficient to resolve it properly; it can be seen more clearly in fig. 2 and 3 of Kolb (1993).

The absence of a spike at the period minimum in the observed CV period distribution has been the subject of several theoretical papers. Barker & Kolb (2002) and King et al. (2002) attempt to explain this by removing the spike from the intrinsic distribution, whereas Kolb & Baraffe (1999) argue that it could possibly be a selection effect. The results presented here show that, relative to the whole population detected at a given magnitude limit, the spike at the period minimum indeed decreases in prominence at brighter magnitude limits, although it is present even in the sample with $V < 14$ (this can be most clearly seen in the insets in Fig. 3.2).

The upper panel of Fig. 3.4 illustrates that the spike cannot be discerned in the intrinsic period distribution. This is because CVs with different M_1 bounce at slightly different periods, and because the period spike is very narrow, and, in fact, very small, compared to the broad feature (between roughly $\log(P_{orb}/\mathrm{h}) = 0$ and 0.2) caused by period bounce and the increasing evolutionary time-scale of systems that have evolved through the period minimum. The period spike can be seen in the intrinsic distribution when systems with different M_1 are considered separately. The lower panel of Fig. 3.4 shows period distributions for model CVs with three values of M_1; the period spike is indicated by a vertical bar for each of these single-M_1 populations.

The magnitude limits considered here exclude relatively more systems beyond period bounce than right at the period minimum—this is the reason the period spike becomes visible in the magnitude-limited samples. The spike increases in prominence towards deeper magnitude limits, because the number of systems in the spike that satisfy the magnitude limit increases faster than the number of detected period bouncers, as the limiting magnitude is increased from $V = 14$ to 20. For even deeper magnitude limits, the spike will at some point start decreasing in prominence, until, in the limit of a sample deep enough to contain all CVs in the Galaxy, the spike will be invisible.

3.3.2 Blue optical colours

Most known CVs have $(U - B)_0 < -0.5$ (e.g. Bruch & Engel 1994). This is because high-$\dot{M}$ systems have high continuum colour temperatures, while known low-$\dot{M}$ systems have the Balmer lines and Balmer discontinuity in emission. However, in the systems with lowest $\dot{M}$, the (accretion heated) white dwarf is expected to dominate the optical flux, and this white dwarf may be quite cool ($T_{eff} \lesssim 10\,000$ K). Selection cuts in $U - B$ may therefore exclude the faintest CVs.

Two UV-excess surveys covering large areas at high Galactic latitude have produced reasonably large CV samples. These are the Palomar–Green (PG) Survey ($B < 16.2$; $U - B < -0.46$; Green et al. 1986), and the Edinburgh–Cape Blue Object (EC) Survey ($B < 16.5$; $U - B < -0.4$; Stobie et al. 1997; see also Chen et al. 2001). Follow-up of the EC Survey is still far from complete; the PG Survey will be considered in more detail in Section 3.5.

Fig. 3.5 shows the effect of a magnitude limit together with different $U - B$ selection criteria. In every panel the dotted histogram shows all systems with $V < 20$, and the solid

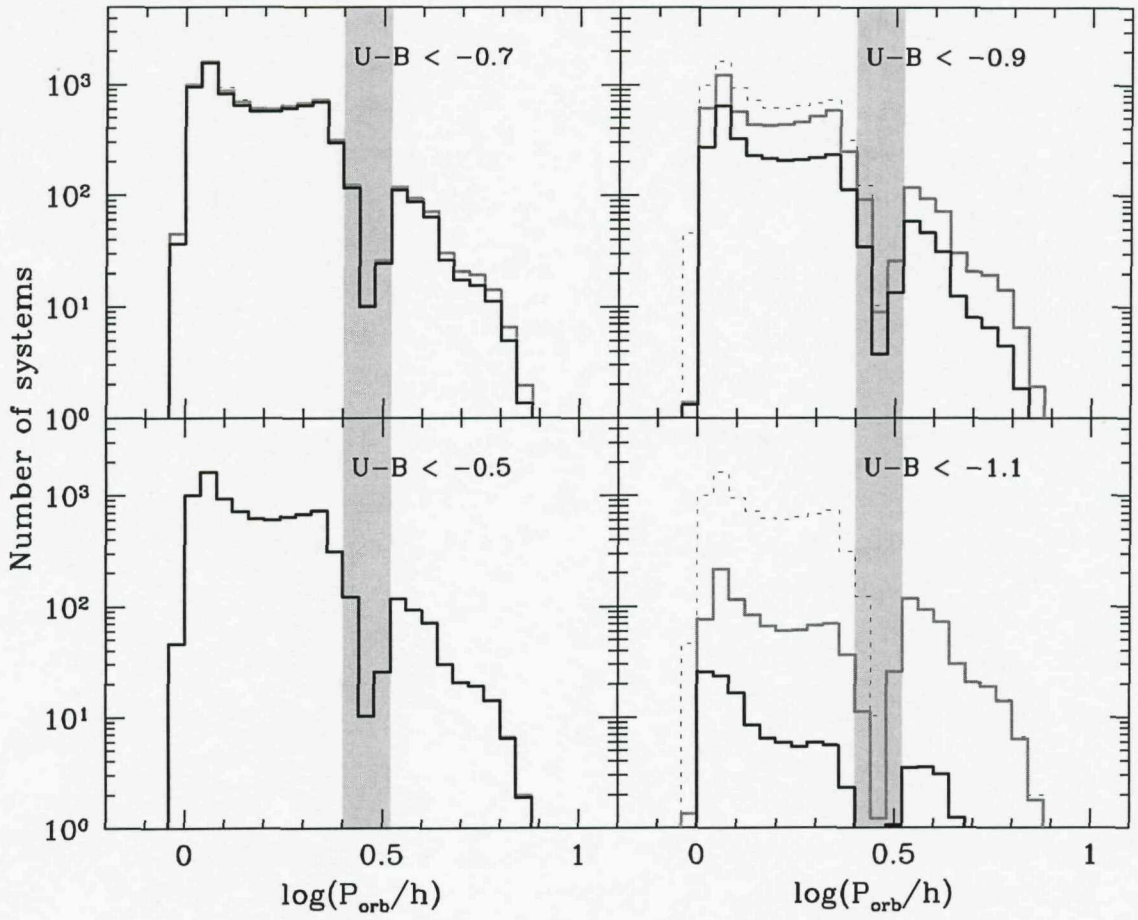

Figure 3.5: Period histograms of systems with $V < 20$ (dotted), and systems satisfying $V < 20$ and the $U - B$ requirement indicated in each panel (black). To illustrate the effect of reddening, dark grey histograms show the distributions obtained when the same blue cuts are applied to the intrinsic colours. Almost all systems with $V < 20$ also have both $(U - B)_0 < -0.7$ and $U - B < -0.7$, and virtually long-period CVs have $(U - B)_0 < -1.1$. These samples were produced by model A1.

black histogram shows systems that also satisfy the blue cut. It is only at $U - B < -0.9$ that the blue selection starts removing a large fraction of systems from the magnitude-limited sample.

In Fig. 3.6, P_{orb} distributions resulting from blue cuts imposed on a volume-limited sample are displayed. It is seen that even $U - B < -0.5$ excludes systems near the period minimum, while $U - B < -0.7$ introduces a severe bias against short-period systems. This shows that many CVs in the intrinsic population are not bluer than $U - B = -0.7$, but, in the samples shown in Fig. 3.5, these systems were already excluded by the magnitude limit. Thus, UV-excess surveys that select objects for $U - B \lesssim -0.7$ are expected to be seriously biased against short-period, low-$\dot{M}$ CVs, but such a blue cut introduces hardly any additional bias in a survey that is also severely flux-limited.

The grey histograms in Fig. 3.5 and 3.6 display samples with the same blue cuts as shown by solid black histograms, but here the blue cuts are applied to the intrinsic colours

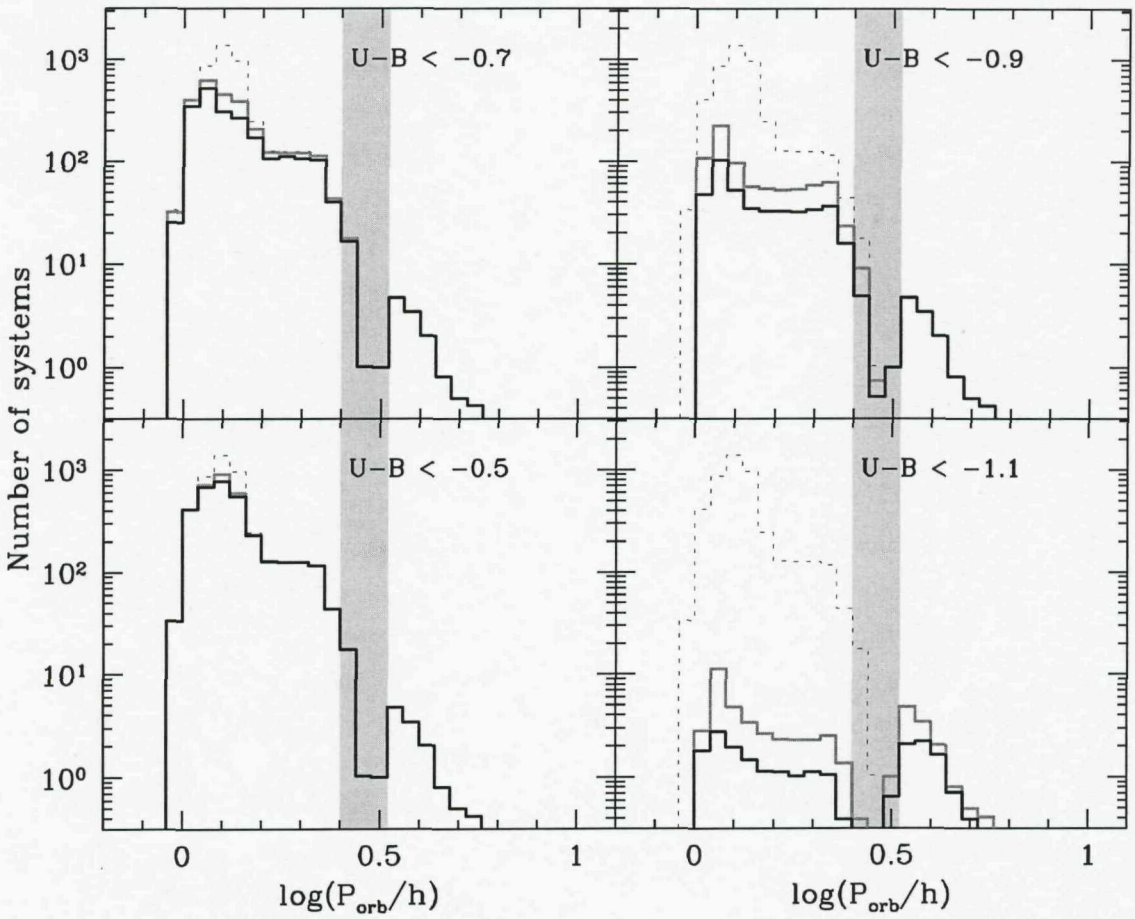

Figure 3.6: Period histograms of samples with the same $U-B$ and $(U-B)_0$ cuts as in Fig. 3.5, but here applied to a volume-limited sample. Dotted histograms show all systems at $d < 400\,\mathrm{pc}$; black are samples with observed colours satisfying the blue cut indicated in each panel, and grey shows systems with intrinsic colours blue enough to satisfy the selection cuts. These samples were produced by model A3; i.e., the volume-limited sample is representative of the intrinsic population.

to illustrate the influence of reddening. Notice that practically all long-period systems have $(U-B)_0 < -0.9$, but some get excluded from observed samples because, in a flux-limited sample, they are on average more distant than short-period systems, and thus more highly reddened. This is amplified by the fact that they are (in model A1) also more concentrated towards the Galactic plane.

3.3.3 Restrictions in Galactic latitude

Surveys at high Galactic latitude hold some promise of producing CV samples that are volume-limited. In a Galactic plane survey, on the other hand, intrinsically bright objects will be detected out to larger distances than fainter systems (for any practically achievable flux limit). The direction of this effect is obvious; I simply show its magnitude in Fig. 3.7, with period histograms of high (black) and low (dark grey) Galactic latitude samples with two magnitude limits. Since this is a case where the results can be expected to depend

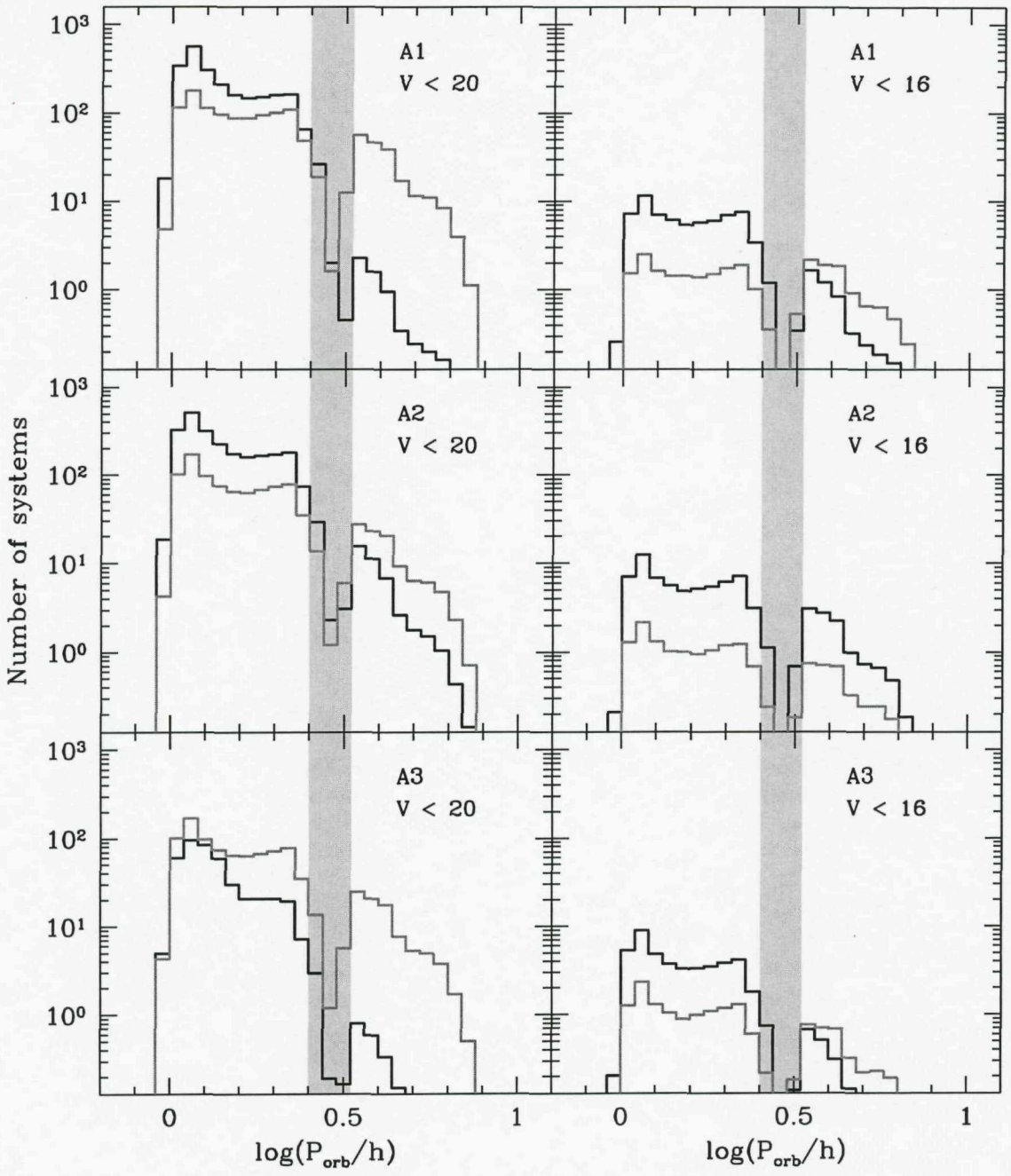

Figure 3.7: The orbital period distributions of high Galactic latitude ($|b| > 30°$; black) and Galactic plane ($|b| < 5°$; dark grey) samples with magnitude limits $V < 20$ (left) and $V < 16$ (right). The plots are repeated for all the models of Galactic structure. Surveys at different Galactic latitude include very different populations, and, as expected, the effect is larger for deeper samples.

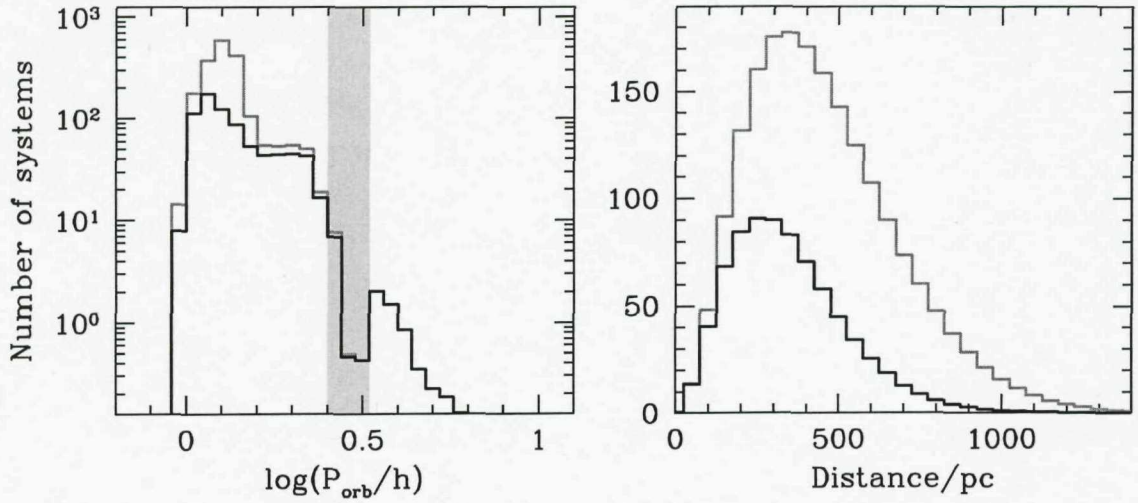

Figure 3.8: Period and distance distributions of all objects in the volume defined by $|b| > 20°$ (grey) and systems in that volume with $B < 20$ (black). Only 40% of CVs in the volume-limited sample are also in the magnitude-limited sample, and practically all systems excluded by the magnitude limit have periods below the period gap, implying a strong bias against short-period systems. Specifically, a $B < 20$ survey is incapable of finding most of the systems near the period minimum. This sample is from model A3, where the vertical density profile of stars is a Gaussian with a scaleheight of 190 pc.

sensitively on the assumptions concerning scaleheight, the corresponding histograms for model A2 and A3 (see Table 3.2) are included in Fig. 3.7. As expected, the ratio of long- to short-period systems is larger in the Galactic plane samples in all cases; the effect is the smallest in model A2 (middle panels of Fig. 3.7), because, with the largest assumed scaleheight, this is the model in which the Galaxy comes the closest to being an isotropic distribution of stars.

In a survey covering the area $|b| > 20°$, only 4.1% of CVs in the survey volume are detected above a magnitude limit of $B < 20$, in the case of model A1. For model A3, 40% of all systems in the survey volume have $B < 20$, and less than 0.5% of systems detected to this magnitude limit are long period systems; Fig. 3.8 illustrates this. The Sloan Digital Sky Survey (SDSS) reaches to $g \simeq 20$, and has sky coverage that can be very roughly approximated as $|b| > 20°$ (e.g. York et al. 2000). Because CVs found in the SDSS will in future comprise the largest uniformly selected sample, this survey is bound to be very important in the context of observational studies of CV populations (e.g. Szkody et al. 2002). However, the result illustrated in Fig. 3.8 implies that, even assuming a Galactic scaleheight that is probably unrealistically small, the SDSS CV sample will by no means be volume-limited (see Southworth et al. 2007b for further discussion). Clearly, even if no colour bias existed in the SDSS CV sample, modelling of selection effects is required to interpret it correctly.

More fundamentally, accepting that CV sub-populations with different typical ages do not share the same vertical Galactic distribution, a volume-limited, high-$|b|$ sample will in any case not reflect the intrinsic Galactic population. In fact, it is not practically possible

to construct a volume-limited observational sample in such a way that it does represent the intrinsic population. This is because the volume sampled by such a survey would have to be, e.g., a cylinder with its axis perpendicular to the Galactic plane (distances are needed to construct such a sample), or the whole Galaxy.

3.4 Sensitivity of the results to model assumptions

Since there are considerable uncertainties regarding the DN outburst properties of CVs and their distribution in the Galaxy, the effect of varying these assumptions is explored here, by comparing several combinations of assumed Galactic structure and outburst behaviour. In addition, the sensitivity of the results to the viscosity parameter used in the disc SED models is considered, since this is another potentially important source of error.

At fainter magnitude limits, all the predicted magnitude-limited samples (with the same $|b|$ coverage) become more similar to the intrinsic distribution, and hence more alike. Therefore, samples with bright limiting magnitudes are considered here. Fig. 3.9 displays period histograms of magnitude-limited samples produced by the first six models listed in Table 3.2. The grey histograms are samples with $V < 14$, while black shows $V < 16$; the fraction of the total made up by long-period systems is given in each panel for both magnitude limits. This fraction does not depend very sensitively on the assumptions about Galactic structure and DN outburst properties. As expected, it is more difficult to hide short-period systems if all CVs are assumed to accrete permanently at their long-term average rate, regardless of the adopted Galaxy model. The fraction of long-period systems increases towards brighter magnitude limits in all cases.

Model C1 produces the largest ratios of long- to short-period systems, and differs from, e.g., model A1 also in predicting fewer systems at a given magnitude limit, and in predicting that relatively more detected systems are DNe in outburst. Fig. 3.10 compares the period distributions of all-sky samples with $V < 16.5$ resulting from model A1 and C1.

Because of the Balmer discontinuity, the U band is the region of the optical spectrum where the SED modelling of the disc emission is the least reliable (there is also a large number of Balmer lines in the U band, and the model is not very successful in predicting the strength of these lines; see Chapter 4). Fig. 15 of Tylenda (1981a) shows that the $U-B$ colour of low-$\dot{M}$ discs is sensitive to the value of α (this sensitivity disappears at high $\dot{M}$). For fixed inclination, varying α from 1 to 0.1 can change $U-B$ by almost 0.35 mag for $\dot{M}_d = 10^{14}\,\mathrm{g/s}$ and $r_d = 10^{10}\,\mathrm{cm}$ (the effect is larger for larger r_d, but the low-$\dot{M}$ model discs have small outer radii). In the very low-$\dot{M}$ systems where $\alpha = 0.01$ was taken, the disc radiation has a negligible effect on the magnitudes and colours. Anticipating the application in Section 3.5, I am for the moment only concerned with the influence that incorrect $U-B$ colours may have when $U-B$ cuts are applied to samples with bright magnitude limits. To determine whether an error of $\simeq 0.35$ mag in the disc $U-B$ in systems with $10^{13}\,\mathrm{g/s} \lesssim \dot{M}_d \lesssim 10^{14}\,\mathrm{g/s}$ is important, the following test was performed.

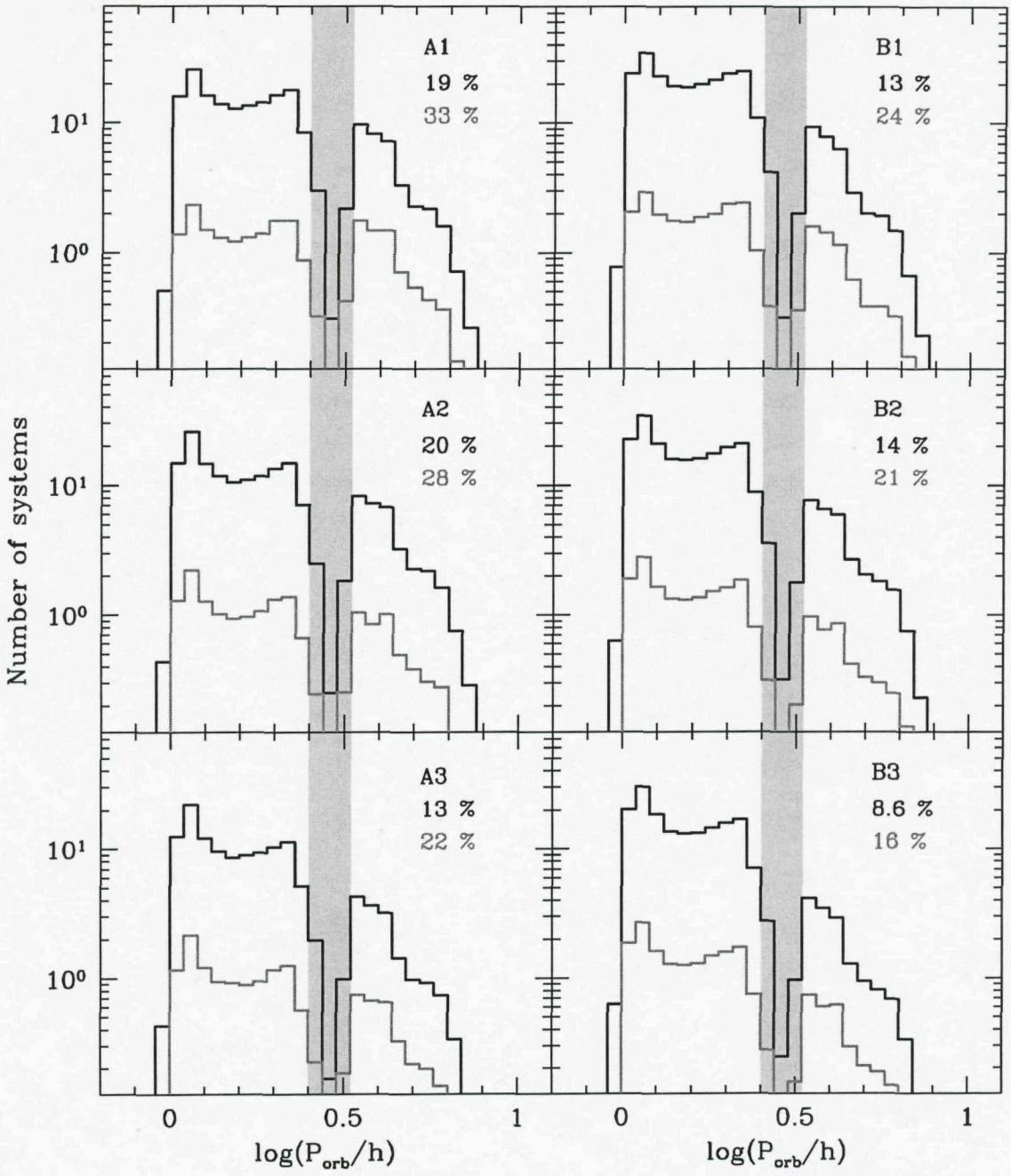

Figure 3.9: The orbital period distributions of magnitude-limited samples produced by the first 6 models listed in Table 3.2. These are in every case for all-sky samples. Black (dark grey) histograms are for a magnitude limit of $V = 16$ ($V = 14$). In each panel, the contribution of long-period systems is given as a percentage of the total for the fainter (black) and brighter (dark grey) magnitude limits.

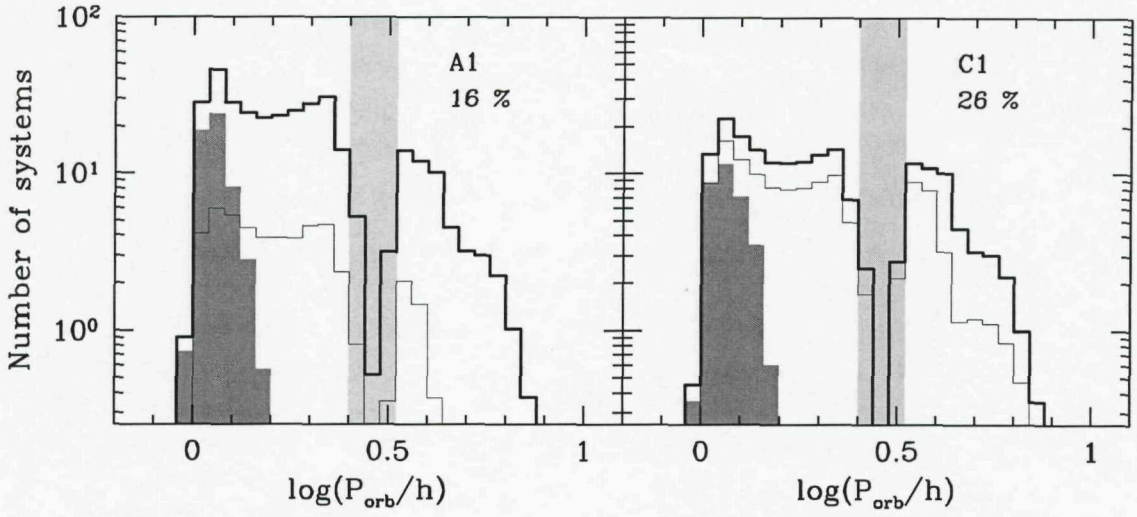

Figure 3.10: The orbital period distributions of samples produced by model A1 (left) and C1 (right). Both samples have a magnitude limit of $V < 16.5$. Dark grey shading and fine black histograms show the contributions of period bouncers and DNe in outburst, respectively. The contribution of long-period systems is given as a percentage of the total in each panel.

The $U-B$ colour of the disc is changed by adding 0.4 mag to the intrinsic disc U magnitude for all systems with $\dot{M}_d < 2 \times 10^{14}$ g/s. Taking the $B < 16.2$ sample produced by model A1, less than 0.5% of systems is lost from samples with blue cuts of $U - B < -0.7$ and $U - B < -0.9$ when their original colours are altered in this way. The reasons are that low-$\dot{M}$ systems are rare in the magnitude-limited sample, and that the flux contribution of the disc is increasingly unimportant compared to that of the white dwarf at lower accretion rates. Therefore, even quite large errors in the $U - B$ colours of low-$\dot{M}$ model CVs make no significant difference to blue-selected samples with bright flux limits.

3.5 Application to the Palomar–Green CV sample

The CVs collected in the Ritter & Kolb (2003) catalogue include systems that were discovered on the basis of very different characteristics, such as physically distinct types of large amplitude variability (nova eruptions, DN outbursts, VY Scl star low and high states), X-ray emission, blue colours, and emission lines. The resulting overall sample is too heterogeneous to permit a reliable evaluation of its selection biases. Note also that, in addition to the discovery bias, a second bias is introduced in the Ritter & Kolb (2003) sample by the restriction of the sample to CVs with known orbital periods. This is magnitude-dependent, but it is also, e.g., easier to measure shorter periods (although this is not very important at $P_{orb} \lesssim 8$ h) and observers are biased towards magnetic systems in deciding which CVs are worthy of follow-up observations to find P_{orb}. A quantitative comparison between theory and observations requires a reasonably large observed sample that has well-defined selection criteria and quantified completeness. At present, the observational sample that conforms to these requirements most closely is the sample of CVs

found in the PG Survey.

The PG Survey covered 10 700 deg^2 at $|b| > 30°$ and was intended to have a magnitude limit of $B < 16.16$ and a colour selection criterion of $U - B < -0.46$ (Green et al. 1986). The blue cut and magnitude limit were always known to vary from field to field; the error in $U - B$ and the completeness were thought to be 0.39 mag and between 66 and 86%, respectively. More recent analyses of the PG data have shown that the actual magnitude limit and blue cut used by the survey were $B < 16.16$ and $U - B < -0.71$, with errors of $\sigma_B = 0.34$ and $\sigma_{U-B} = 0.24$ (Jester et al. 2005; see also Liebert et al. 2005). The survey produced a sample of 36 CVs, of which 3 are magnetic systems, and 6 have $P_{orb} > 5\,\mathrm{h}$ (Ringwald 1993, 1994; Fred Ringwald, private communication). Depending on the nature of V378 Peg (the only PG CV that still does not have a period measurement) the remaining 27 systems should form a statistically complete sample of unevolved, non-magnetic CVs.

Following Jester et al. (2005), the probability of a system with $B = B'$ and $U - B = (U - B)'$ being detected in the PG Survey is taken as $P_1 P_2$, where

$$P_1 = 1 - \frac{1}{\sigma_B \sqrt{2\pi}} \int_{-\infty}^{B'} \exp\left[-\frac{1}{2}\left(\frac{B - 16.16}{\sigma_B}\right)^2\right] dB \tag{3.12}$$

and

$$P_2 = 1 - \frac{1}{\sigma_{U-B} \sqrt{2\pi}} \int_{-\infty}^{(U-B)'} \exp\left[-\frac{1}{2}\left(\frac{(U - B) + 0.71}{\sigma_{U-B}}\right)^2\right] d(U - B). \tag{3.13}$$

This detection efficiency was applied to systems at $|b| > 30°$ and $P_{orb} < 5$ h in the population produced by the standard model A1. A period histogram of the resulting predicted PG CV population is shown in Fig. 3.11, together with the distribution of the observed sample.

It is evident from Fig. 3.11 that the distribution produced by the simulation is inconsistent with the observed one, the most obvious discrepancy being that the ratio of long- to short-period CVs is much higher in the observed sample than is predicted. With the conservative assumption that V378 Peg is a short-period system, 14 out of 27 observed systems (52%) at $P_{orb} < 5$ h have periods above the gap. The prediction is only 6.7% (i.e. 2 systems). According to the binomial distribution, the probability that these numbers are consistent is about 3×10^{-10}. Also, none of the PG CVs is considered to be a candidate period bouncer, whereas the simulation predicts that 19% of the sample (i.e. 5 systems) should be period bouncers.

To verify that the PG CV sample is consistent with the assumed magnitude limit, the differential and cumulative B distributions of the model (bold black) and observed (grey) samples are shown in Fig. 3.12. The two distributions are quite clearly inconsistent, and this is confirmed by a KS test (the magnitude distribution of all 36 PG CVs does not differ significantly from that of the sample of 27 systems displayed in this figure). It might be that Jester et al. (2005) describe the magnitude limit and colour cut of objects selected for spectroscopic follow up in the PG survey correctly, but that the identification spectra of

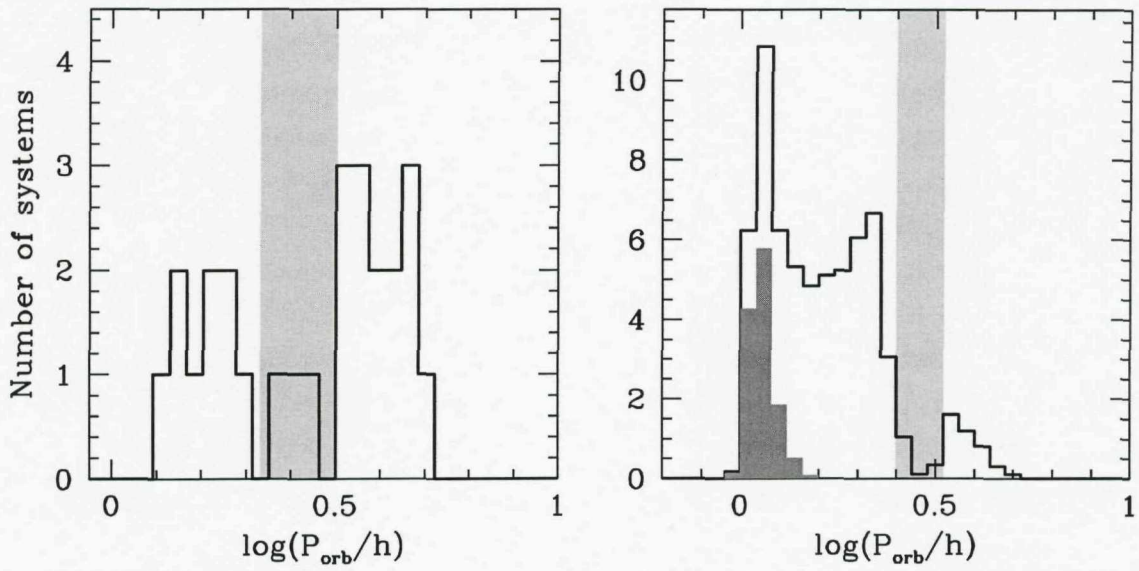

Figure 3.11: The orbital period distributions of the PG CV sample (including only non-magnetic system at $P_{orb} < 5$ h; left-hand panel), and the predicted sample (also with systems at $P_{orb} \geq 5$ h omitted; right-hand panel). Light grey shading of the range 2.15 h $< P_{orb} <$ 3.18 h in the left-hand panel, and 2.51 h $< P_{orb} <$ 3.31 h in the right-hand panel indicate the observed and model period gaps. Dark grey shading represents period bouncers in the predicted sample.

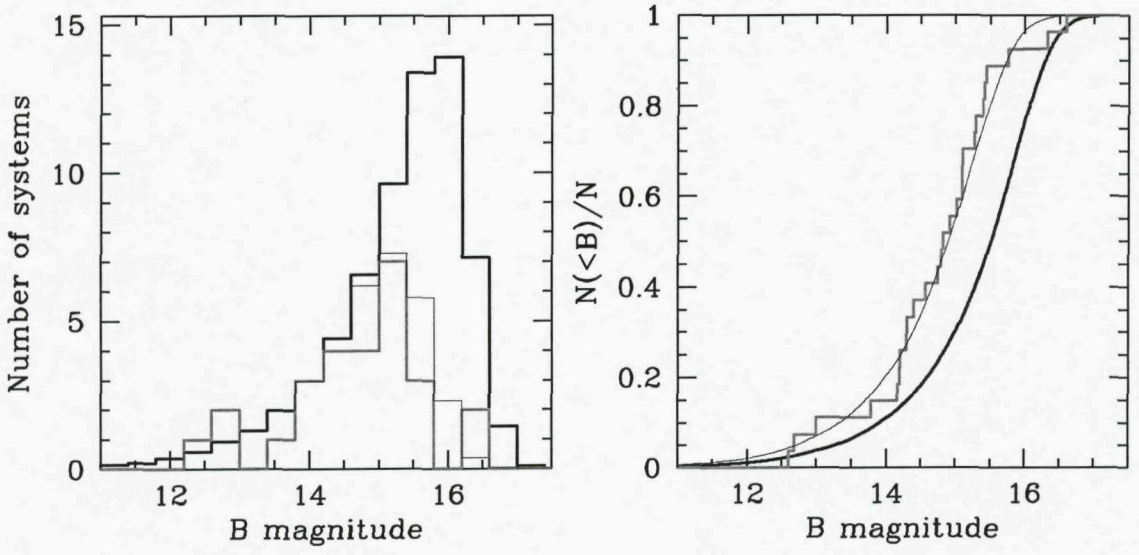

Figure 3.12: Differential and cumulative magnitude distributions of CVs detected in the PG survey. The B distributions of the observed sample is plotted as the grey histograms, while black histograms show the model distributions. The original model distributions (with B limit as given in equation 3.12) is plotted as the bold histograms, while the fine histograms show the distributions obtained if the magnitude limit is take as $B < 15.5$ and $\sigma_B = 0.4$.

CVs near the magnitude limit were too noisy to produce correct classifications. Without access to all of the PG identification spectra, it is not possible to determine what the reason for the apparent increasing incompleteness towards fainter magnitudes is, but it is clear that equation 3.12 does not reproduce the observed magnitude distribution. Replacing the magnitude limit in equation 3.12 with $B < 15.5$, and taking $\sigma_B = 0.4$ produces a predicted B distribution consistent with the observed sample (a KS tests gives a probability of 0.61 that the observed and new predicted distributions are drawn from the same population)[12]. This is plotted as the fine black histograms in Fig. 3.12.

With this adjustment, the predicted fraction of long-period CVs in the PG survey is 10%. Using the binomial distribution, the probability that this prediction is consistent with the observed fraction of 14 out of 27 systems is still only 1×10^{-7}; i.e., the conclusion based on the fainter assumed magnitude limit is unchanged. The new predicted sample contains 17% period bouncers. The new estimate of the magnitude limit is, of course, slightly model-dependent. It is, however, quite clear from the observed magnitude distribution, which peaks at about $B = 15.2$, that the flux limit is no brighter than $B = 15$. Even assuming this very conservative limit, the observed ratio of long- to short-period CVs is too large to be consistent with the model (the probability that the predicted and observed fraction of long-period CVs are consistent is then about 3×10^{-5}).

It was shown in Section 3.4 that the properties of the predicted detected sample are fairly insensitive to poorly constrained aspects of the modelling of disc SEDs, Galactic structure, and DN outburst properties. Of all the models considered here, model C1 allows for the largest population of short-period systems to remain undetected, because it combines a large Galactic scaleheight for these systems with an extreme assumption of DN outburst behaviour. Repeating this simulation using model C1 (with $B < 15.5$ and $\sigma_B = 0.4$) yields a prediction of 15% long-period systems in the PG sample, which is still inconsistent with the observed fraction. Based on this and also on the sheer size of the discrepancy between the predicted and observed PG samples, it can be said with confidence that the predicted intrinsic population that is the basis of the modelling is ruled out by observations. This is probably the strongest evidence yet that the standard disrupted magnetic braking model for CV evolution, with strong magnetic braking above the period gap and none below the gap, is incorrect. As has long been suspected, it predicts relatively too many short-period systems, and, more specifically, too many period-bouncers.

[12]Note that I have not proven that the magnitude limit really is $B = 15.5 \pm 0.4$, but only that this is consistent with the model, which assumes a scaleheight distribution and luminosity function. However, even for a single small scaleheight (120 pc), a luminosity function much flatter than the empirical magnitude distribution shown in fig. 2 of Patterson (1998) is required for a model magnitude distribution with a limiting magnitude of $B = 16.16$ to be consistent with the observed distribution. The CV luminosity function certainly rises more steeply towards faint magnitudes than the magnitude distribution of known CVs plotted by Patterson (1998). Thus the fainter magnitude limit usually quoted is incorrect, and assuming a limiting magnitude of $B = 15.5 \pm 0.4$ is an improvement.

3.6 Conclusions

I have presented a Monte Carlo technique that allows me to model selection effects in observed samples of CVs. Given any theoretical intrinsic population and any survey with well-defined selection criteria, this technique can be applied to predict the observed population. This method was used to explore the impact of flux limits, colour cuts, and observing restricted ranges of Galactic latitude, and finally applied to simulate the selection effects acting on the CV sample produced by the PG Survey.

Observational biases are not sufficient to reconcile the intrinsic population predicted by standard CV evolution theory (with strong magnetic braking above the period gap and only gravitational radiation below the gap) with the observed PG sample. The real intrinsic CV population cannot contain as large a fraction of short-period systems (or period bouncers) as is predicted by theory.

The model $U-B$ colours are not expected to be reliable, but this does not have any serious effect on the above result.

Although a blue selection cut of $U-B \lesssim -0.7$ is predicted to introduce a serious bias against detecting short-period systems in the absence of a flux limit, this bias is unimportant in a severely flux-limited sample. The effect of the survey flux limits is therefore the only important bias in existing UV-excess surveys (including the PG survey).

Flux limits are the most fundamental and important selection effects in observational CV samples. The properties of the period distribution of a magnitude-limited sample depend strongly on the magnitude limit. In particular, the size of the spike near the period minimum and the ratio of short- to long-period CVs detected decrease at brighter magnitude limits. For practically achievable flux limits, no flux-limited sample can be expected to reproduce the intrinsic CV population. It is therefore quite inappropriate to compare an observed sample with the predicted intrinsic population. Also, the apparent magnitude distribution of CVs suggests that the known CV sample is not approximately magnitude limited, even if a limiting magnitude as bright as $V = 13$ is adopted.

Magnitude-limited surveys at high Galactic latitude are expected to yield samples that are very different from those produced by Galactic plane surveys, because they detect a larger fraction of all systems inside the volume defined by the Galactic latitude range. However, a survey such as the SDSS is still not deep enough to be volume-limited for CVs. This means that, for some time to come, the effect of a magnitude limit will have to be considered when comparing an observed sample to theory.

An unexpected result of this work is that the mass transfer rates predicted by standard CV evolution theory are inconsistent with empirical estimates of the absolute magnitudes of DNe in outburst, unless typical outburst duty cycles are much lower than is generally assumed (i.e. $< 10\%$ for normal DNe and $< 0.5\%$ for period bouncers).

Chapter 4

An Hα-selected sample of cataclysmic variables

In this chapter, I compare a new, Hα-selected CV sample to the theoretical CV population, using similar modelling as in Chapter 3. The main purpose of constructing this sample is to provide independent confirmation of the PG survey result presented in Chapter 3. The choice of Hα emission as a selection criterion and the construction of the sample are explained in the next two sections. I then present observations of the newly discovered CVs, examine the completeness of the sample and the observational biases affecting it, and compare it to the predictions of theory. The results are used to constrain a very important ingredient of CV evolution theory, namely the angular momentum loss rates.

4.1 Introduction

Several complete, uniformly selected CV samples already exist, e.g., those that resulted from the PG Survey (discussed in Chapter 3), the *ROSAT* Bright Survey (Schwope et al. 2002), and the *ROSAT* North Ecliptic Pole Survey (Chapter 5). Ongoing surveys, e.g., the Hamburg Quasar Survey, and the SDSS (Gänsicke et al. 2002; Aungwerojwit et al. 2006; Szkody et al. 2002, 2003, 2004, 2005, 2006, 2007; Southworth et al. 2006, 2007) are in the process of producing similarly well-defined, but much deeper, samples. All CV samples are affected by a flux limit, which already implies a bias against intrinsically faint systems. But it is in fact very difficult to construct a sample that is reasonably large and deep, and purely flux-limited. Of the surveys mentioned above, only the very shallow *ROSAT* Bright Survey, and the very small *ROSAT* North Ecliptic Pole Survey do not contain a blue cut, in addition to a flux limit. The surveys that incorporate a blue- or variability-based selection cut include a second bias (besides that from the flux limit) against low-$\dot{M}$ CVs, since these systems are not only intrinsically faint, but also relatively red and have less frequent outbursts (note that a blue cut only becomes important at deep limiting magnitudes, and therefore made little impact on the PG sample, although it will be important in, e.g., the SDSS; see Chapter 3).

The presence of Balmer emission lines in the spectra of most CVs provides an alternative to the commonly used blue- and variability-based selection techniques. Selecting CVs for line emission discriminates only against the discovery of the intrinsically rare CVs with very bright, optically thick discs. In fact, there is a well known (and theoretically expected) anti-correlation between the equivalent widths of Balmer emission lines and the luminosity of CVs (Patterson 1984; Witham et al. 2006; I will take EWs of emission lines as positive throughout). The explanation for this anti-correlation is that intrinsically faint CVs are low-$\dot{M}$ systems with low-density discs, in which recombination line cooling is very efficient. Therefore, in contrast to other selection criteria (such as blue optical colours and variability), an emission line EW-based selection cut should favour the discovery of intrinsically faint, short-period systems.

A few surveys have already exploited the promise of discovering CVs via emission lines. CVs are selected from the Hamburg Quasar Survey based in part on Hβ emission; one of the selection criteria for CVs from the Calán–Tololo Survey is Balmer emission lines (Tappert et al. 2004). The INT/WFC photometric Hα survey of the northern galactic plane (IPHAS) is currently being used to find CVs (Witham et al. 2006, 2007), and Rogel et al. (2006) describe another Hα-based search for CVs. Hα emission has also been used to identify CV candidates in globular clusters (e.g. Bailyn et al. 1996; Cool et al. 1995).

The AAO/UKST SuperCOSMOS Hα Survey (SHS; Parker et al. 2005) can also be used in this way. It is currently the best available southern hemisphere resource for identifying Hα emission line point sources over a large area, and one CV has previously been discovered in this survey, partly on the basis of Hα emission (Howell et al. 2002).

I have used this survey to define a homogeneous sample of CVs, selected on the basis of Hα emission. As is the case with most existing CV samples, the new sample is also limited to apparently bright systems. However, it differs from other samples in that the only selection criterion (other than a flux limit) is based on line emission.

4.2 Identifying CVs in the AAO/UKST SuperCOSMOS Hα Survey

4.2.1 The survey data

The SHS is a photographic survey carried out with the UK Schmidt Telescope (Parker et al. 2005). Plates were scanned by the SuperCOSMOS digitizing machine, and the data are publicly available. The survey covered a total of $\sim 3\,700\,\mathrm{deg}^2$ (233 separate $4^\circ \times 4^\circ$ fields) at low Galactic latitude in the southern hemisphere ($|b| \lesssim +10^\circ$ and $\delta < +2^\circ$), in R and narrow-band Hα. The limiting magnitude is $\simeq 20.5$, and the angular resolution of the images is $\simeq 1''$.

The digitized plates are processed to extract sources and provide Image Analysis Mode (IAM) data for the detected objects. The analysis assigns, amongst other parameters, classification, quality, and blend flags to each source. This makes it possible to obtain catalogues containing only well-isolated point sources with relatively good photometry.

Older UKST broad-band surveys, including an I-band survey of the whole southern sky, have also been scanned by SuperCOSMOS (Hambly et al. 2001a,b,c). The photometric accuracy of these surveys is discussed in Hambly et al. (2001b). The SHS R and Hα data are expected to be of similar quality, since the survey was digitized and processed in the same way. The photometry is calibrated to remove systematic errors in colour as a function of magnitude and position on a given plate; this is described in Hambly et al. (2001b) and Parker et al. (2005). The result is that errors in colours are typically smaller than would be expected from the errors in magnitudes. By matching the UKST catalogues to CCD data from IPHAS (Drew et al. 2005) in regions near $\delta = 0°$ (where the two surveys overlap), a rough estimate of errors in the SHS colours was made. Typical errors for stars brighter than $R = 17$ are $\simeq 0.07$ in $R - \mathrm{H}\alpha$ and $\simeq 0.14$ in $R - I$, although these errors vary from field to field.

Given the limited quality of photographic photometry, no selection procedure is expected to identify emission line objects in this survey with complete reliability. Poor photometry is also not the only reason for the selection to fail. Because Hα and corresponding R-band plates were in many cases taken months or even years apart, and all I-band images were obtained decades earlier, variable stars can erroneously be included in the sample. Also, since M stars have strong molecular absorption bands in both the R and I passbands, they are another class of objects that can be selected, even if no emission lines appear in their spectra. Multi-object spectroscopy has been used for the follow-up of objects from this survey (e.g. Hopewell et al. 2005), and has yielded low hit-rates for identifying emission line objects. Quite conservative selection criteria, targeting only objects with large $R - \mathrm{H}\alpha$ excess, were therefore chosen.

4.2.2 The selection procedure

The selection is aimed at bright objects that are clear outliers in the $R - \mathrm{H}\alpha$ vs $R - I$ colour-colour plane. The selection procedure is similar to that of Witham et al. (2006), but simpler (the selection is done in only a single magnitude bin, and no attempt is made to isolate an unreddened main sequence, since this sequence is typically not separately discernible in the SHS photometry).

175 out of the 233 survey fields (i.e. 2 800 deg^2 in total) were considered. These fields were chosen to have relatively good photometry (colour-colour diagrams of $2° \times 2°$ sections of fields were inspected, and in cases where one or more of these sections had a very poorly defined stellar locus, the whole field was discarded); fields observed in the multi-object spectroscopy program of which some results are presented by Hopewell et al. (2005) were also avoided. Catalogues covering $4° \times 4°$ around every of the 175 field centres were extracted. These catalogues were then restricted to unblended point sources brighter than $R = 17.0$, and with good quality photometry in R-, Hα-, and I-bands[1].

[1]To be exact, objects that satisfied all of the following criteria were considered for selection (R and Hα magnitudes are here denoted SR and R_Ha, respectively). SR < 17, R_Ha < 99, I < 99, QUAL_SR < 128, QUAL_Ha < 128, QUAL_I < 128, BLEND_SR = 0, BLEND_Ha = 0, BLEND_I = 0, and CLASS = 2. The meaning of the quality flags (e.g. QUAL_SR) is described by Hambly et al. (2001b); the flag CLASS = 2 is

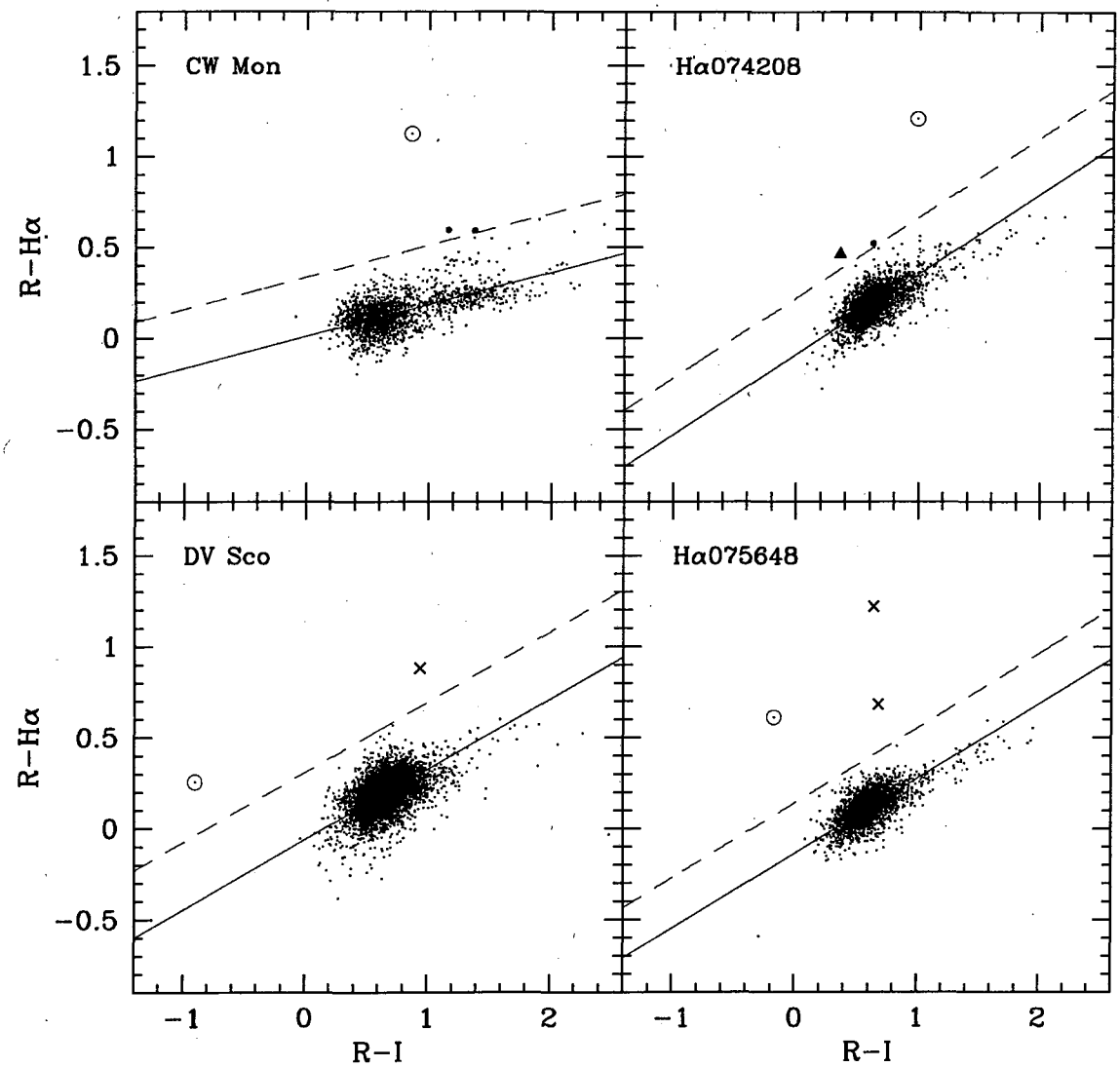

Figure 4.1: Colour-colour diagrams of 1° × 1° sections of four of the SHS fields in which CVs were identified. The solid lines are least-squares fits to all data points, while the dashed lines are displaced upwards by 4× the rms scatter in $R - \mathrm{H}\alpha$ around the best fits. Only sources above the dashed lines are considered for selection. Each panel is labeled with the name of the CV selected from the plot, and the colours of the CVs are plotted as circled points. The other points above the cut-off are plate defects (crosses), objects that were not included in the sample, despite satisfying the cut-off (filled circles), and an object that was observed but has no Hα emission (triangle).

Since the position of the stellar locus in the $R-\mathrm{H}\alpha$ vs $R-I$ plane changes, even across a single 4° × 4° field (mainly not because of reddening effects, but because the effective photometric calibration is not constant), each field was divided into 16 1° × 1° sub-fields, and these 1 deg^2 sub-fields were used individually in selecting Hα excess sources.

Fig. 4.1 shows the $R - \mathrm{H}\alpha$ excess as a function of $R - I$ colour of objects in four such sub-fields. The solid lines are linear fits to the colours of all objects; note that the stellar locus has a positive slope in all these plots. The necessary, but not sufficient, criterion for selection is that targets have $R - \mathrm{H}\alpha > 4\times$ the rms scatter in $R - \mathrm{H}\alpha$ around the best

assigned to objects classified as stellar.

linear fit to the stellar locus. The dashed lines are vertically displaced by this amount from the best fits, and are the cut-off criteria for inclusion in the sample.

In fields where not all objects above the cut-off are cleanly separated from the stellar locus, some objects satisfying the cut-off are not selected. Examples of such objects are plotted as large filled circles in Fig. 4.1. This amounts to subjectively excluding some potential targets, based on inspection of the colour-colour diagrams (or, equivalently, using a stricter $R - \mathrm{H}\alpha$ selection cut in some fields).

The colour-colour diagrams in Fig. 4.1 are for fields from which two new, and two previously known CV were selected. It illustrates that objects with fairly small $R - \mathrm{H}\alpha$ can be selected if they are blue in $R - I$ (e.g. DV Sco), and also that, because of the non-zero slope of the stellar locus, a selection algorithm based only on $R - \mathrm{H}\alpha$ will not successfully differentiate between true outliers and objects with red $R - I$.

A selection based on abnormal colours, not surprisingly, picks out a large number of objects with spurious photometry in one or more wave-band. Therefore, the Hα-, R-, and I-band images of all potential targets were inspected, and objects that are outliers because of, e.g., plate defects (some of the various kinds of plate defects that affect the data are illustrated in Hambly et al. 2001a and Parker et al. 2005) were discarded. Outliers that were excluded from the target list for this reason are plotted as crosses in Fig. 4.1. Next, I also excluded blends, objects from images that appear to have been taken in particularly poor seeing, and a few objects in areas with very high Hα background. Less than 30% of potential targets survive these quality cuts.

With the exception of objects that are known only as X-ray sources, the targets that could be matched to known objects in the SIMBAD Astronomical Database were also excluded. The known objects included planetary nebulae, T Tauri stars, CVs, and several other types of variable stars.

The selection produced 507 targets, and identification spectra were obtained for 460 of these sources (the observations are described in Section 4.3 below). 172 of the targets really are Hα emission line objects (a hit-rate of only 37%), and 14 (that is 3%) are CVs. Of the 288 targets with no Hα emission, 10 are M stars (the identification spectroscopy also turned up many M stars with Hα emission). Some combination of poor survey photometry and variability (probably in most cases continuum, rather than emission line variability) led to the selection of the remaining 278 targets found to have no Hα emission.

Fig. 4.2 shows $R - \mathrm{H}\alpha$ excess as a function of $R - I$ colour for all the objects observed during the spectroscopic follow-up. The colours of CVs are plotted as crosses; other emission line objects are shown as open square points, and objects without Hα emission are plotted as grey triangles. Note that some of the objects without Hα emission have very large $R - \mathrm{H}\alpha$, and that the CVs are systematically bluer in $R - I$ than the overall target sample.

Other optical colours, as well as near-IR colours of the targets were also investigated. While it is possible to separate the majority of late-type emission line stars from CVs using, e.g., Two Micron All Sky Survey (2MASS; Skrutskie et al. 2006) photometry, Be

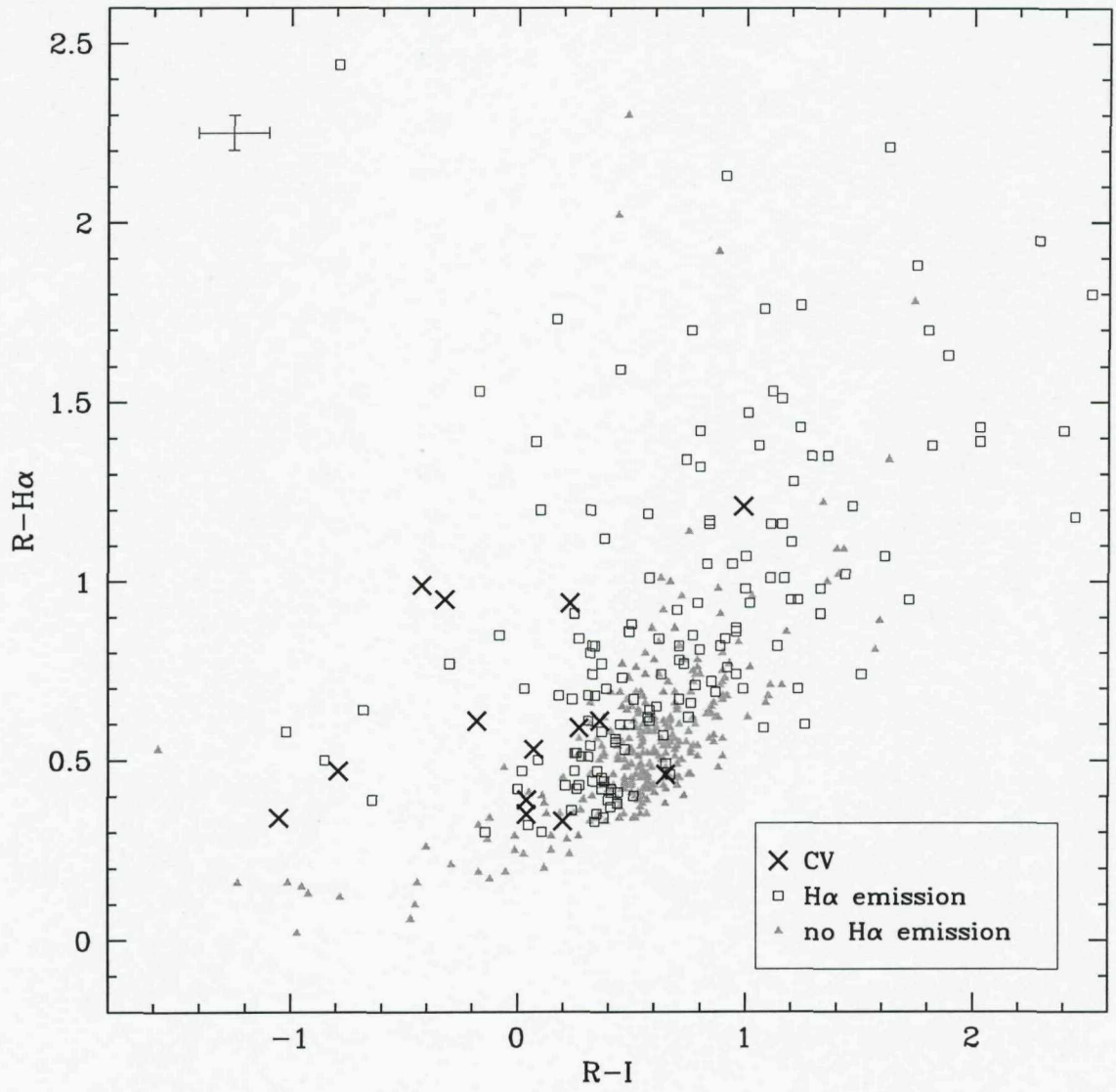

Figure 4.2: SHS colours of all objects for which identification spectra were obtained. Estimates of typical 1σ errors in these colours are shown in the top left-hand corner. Several objects lie outside the $R-I$ and $R-\mathrm{H}\alpha$ ranges plotted. Note that the relative positions of objects in this plot can be misleading, since the position and slope of the stellar locus vary with position on the sky.

stars and other early-type emission line stars, as well as the majority of objects without any line emission (the most important contaminant), occupy the same regions as most CVs in all the colour-colour and colour-magnitude planes. It will therefore not be easy to construct a much more efficient selection procedure to find CVs in this survey.

During one identification spectroscopy run, I experimented with selecting objects with $17.0 \leq R < 17.5$. Two CV candidates were discovered in the fainter magnitude bin. The observations of these two objects are discussed below, but they will not be included in the sample that will be compared to CV evolution theory.

4.3 Observations of the newly discovered CVs

Follow-up observations were obtained at the South African Astronomical Observatory (SAAO), the European Southern Observatory (ESO), and the Cerro Tololo Inter-American Observatory (CTIO). I initially took identification spectra of 460 of the targets, and later obtained time-resolved observations of the objects classified as CV candidates on the basis of the identification spectroscopy.

Fig. 4.3 gives finding charts for the new CVs and CV candidates turned up by the search, and Table 4.1 lists J2000 coordinates, broad-band magnitudes, Hα excesses and equivalent widths, orbital periods, and lower limits on distances. The objects will be named using their right ascension as 'Hαhhmmss'. Where two values of EW(Hα) are given, the first is obtained from the identification spectrum, and the second from the average of higher resolution spectra of that system. Errors in the equivalent widths were estimated using the method described by Howarth & Phillips (1986). Near-infrared magnitudes are from 2MASS[2]. The optical magnitudes listed in Table 4.1 are from SuperCOSMOS scans of the UKST Blue Southern and Equatorial Surveys (B), the UKST Red Southern and Equatorial Surveys (R_2), the ESO Schmidt Telescope Red Southern Survey ($\delta < -17.5°$) or (for $-17.5° < \delta < +2.5°$) the Palomar-I Oschin Schmidt Telescope (POSS-I) Red Southern Extension (R_1), and the UKST near Infrared Southern Survey (I). The orbital period measurements are discussed in Section 4.3.2 and 4.3.4, and lower limits on the distances to these sources (d_l) are derived in Section 4.4.2.

4.3.1 Identification spectroscopy

Medium-resolution identification spectra were taken with the Grating Spectrograph on the SAAO 1.9-m telescope. The no. 7 grating was used in combination with a slit width of 1.″8, yielding spectral resolution of $\simeq 5$ Å over the wavelength range 3 700 to 7 200 Å. Each object spectrum was bracketed with arc lamp exposures (taken with the telescope in the same position) to provide wavelength calibration. The flux calibration was achieved by observing spectrophotometric standard stars from Stone & Baldwin (1983) and Hamuy et al. (1994) on all except the nights of worst transparency. Note, however, that many of the identification spectra were obtained under non-photometric conditions; the absolute flux calibrations of some of the spectra shown below are therefore not reliable. The data were reduced using standard procedures in IRAF[3], including optimal extraction (Horne 1986).

Further details of the discovery observations are listed in Table 4.2, and spectra of the 16 objects identified as CV candidates are shown in Fig. 4.4. The classification of an object as a CV candidate relies mainly on the detection of broad Balmer emission lines in these spectra.

[2]Hα092751 was not detected in K_S by 2MASS; the 95% confidence lower limit on K_S is given as 16.65. This implies either very unusual near-IR colours for the source, or variability between the different IR images (which were taken on the same night). However, the number-magnitude count of sources detected in a 5 arc min radius around the position of Hα092751 indicates that the magnitude limit of the K_S-band image is about 15.7. I adopt this more conservative limit.

[3]IRAF is distributed by the National Optical Astronomy Observatories.

Table 4.1: Coordinates, broad-band magnitudes, $R-\mathrm{H}\alpha$ excess, Hα equivalent widths, orbital periods, and lower distance limits for the CVs and CV candidates.

Object/coordinates	B	R	R_2	R_1	I	J	H	K_S	$R-\mathrm{H}\alpha$	EW(Hα)/Å	P_{orb}/h	d_l/pc	Notes
073418.56−170626.5	17.8	16.7	—	18.3	17.4	16.23	15.93	>14.9	0.47	61(6)	3.18542(5)	320	1,2,3
074208.23−104932.4	16.5	15.3	15.4	16.0	14.3	14.26	13.59	13.36	1.21	63(3), 45(1)	5.706(3)	490	4,5
074655.48−093430.5	13.8	14.0	13.6	13.4	13.3	13.47	13.29	13.19	0.46	27(1), 23.6(3)	3.3984(4)	180	6
075648.83−124653.5	18.3	16.0	17.0	17.0	16.2	15.39	14.73	14.61	0.61	43(7), 47.1(6)	—	—	7
092134.12−593906.7	17.3	16.8	16.7	16.9	16.7	16.49	16.20	>15.8	0.53	56(6), 43.7(4)	3.041(9)	530	8
092751.93−391052.3	16.4	16.2	16.8	16.3	16.1	15.72	15.54	>15.7	0.35	15(2), 20.0(3)	4.1(3)	770	9
094409.36−561711.4	17.5	16.2	—	18.4	16.7	15.72	15.40	14.96	0.99	66(4), 67(1)	4.506(4)	520	1,2,3,8
102442.03−482642.5	17.1	16.4	17.6	16.4	16.2	15.83	15.57	15.41	0.94	125(2), 122(1)	3.673(6)	580	3
103135.00−462639.0	17.4	16.3	17.2	16.9	16.3	16.04	15.65	15.52	0.39	35(4), 19.4(3)	3.76(2)	630	9
103959.96−470126.1	17.0	16.4	16.9	16.7	16.8	15.87	15.69	15.63	0.95	31(3), 20.2(5)	3.785(5)	670	9
112921.67−535543.6	16.3	15.5	15.9	16.1	15.3	15.27	15.17	15.12	0.33	23(2), 17.4(5)	3.6851(4)	510	9
115927.06−541556.2	18.6	17.4	17.6	17.5	17.2	—	—	—	0.57	57(15)	—	—	10
122105.52−665048.8	17.8	17.3	17.5	16.9	17.4	16.43	>16.3	>16.4	0.58	22(3), 66.0(5)	—	—	7,9,11
130559.50−575459.9	17.2	16.5	16.4	—	16.2	15.99	15.55	>14.9	0.59	41(4), 58.3(5)	3.928(13)	500	8
163447.70−345423.1	16.8	16.7	16.7	17.0	16.3	15.88	15.42	>15.7	0.61	36(5), 34(3)	—	—	3,9
190039.83−173205.5	17.6	16.8	17.3	16.9	17.8	15.66	15.45	15.11	0.34	26(5)	—	—	9,10

Notes: (1) Eclipsing system. (2) Possibly an SW Sex star. (3) Large amplitude variability. (4) Secondary star spectral type M0 $\pm$ 1. (5) *ROSAT* source. (6) Bowen blend detected. (7) Highly variable Hα line profile. (8) Strong He II λ4686 emission. (9) Spectroscopic appearance of a nova-like variable. (10) Classification as a CV not certain. (11) Probable quasi-periodic oscillation (QPO) detected in one light curve.

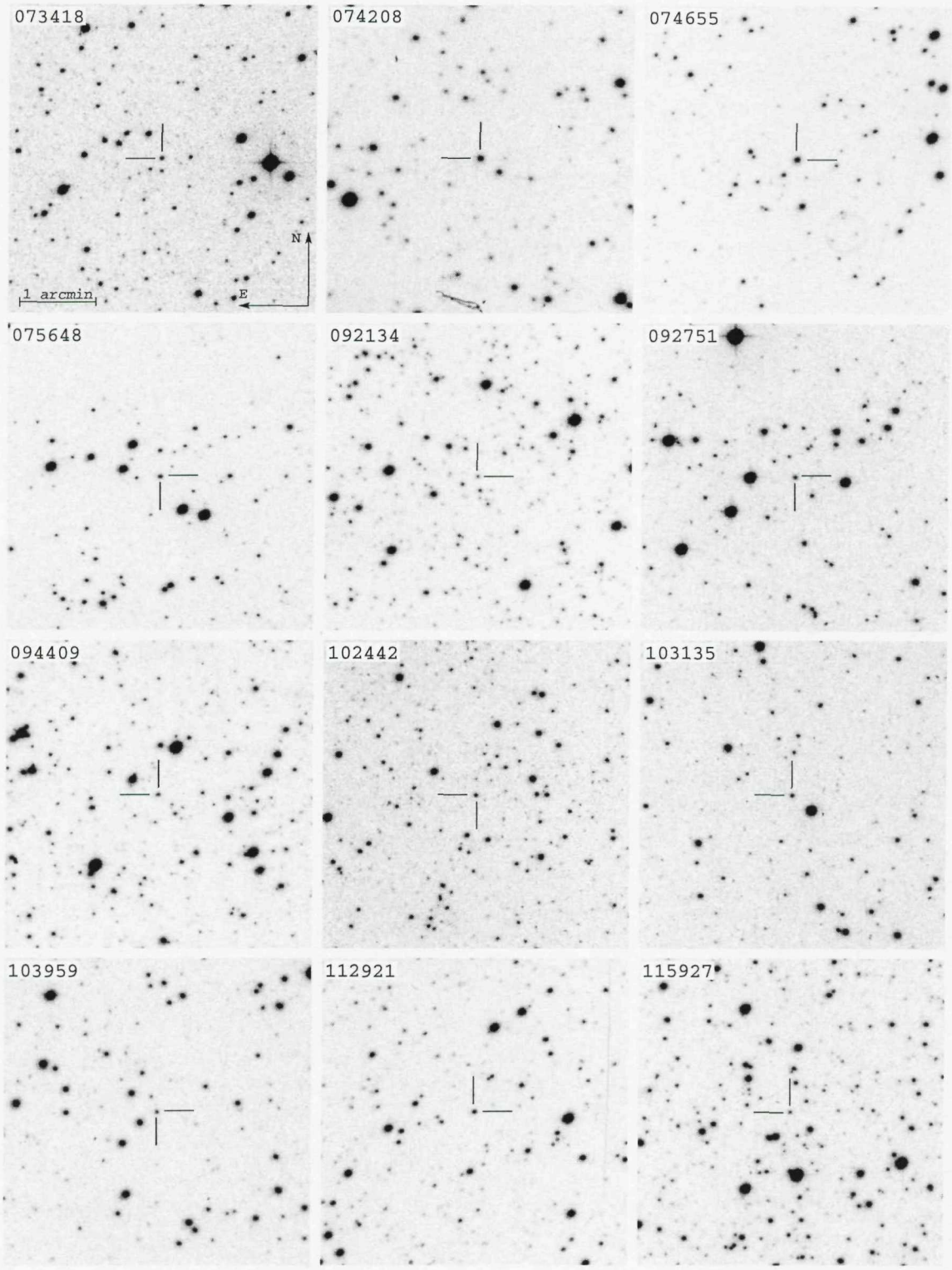

Figure 4.3: $4' \times 4'$ finding charts of the new CVs and CV candidates, made using UKST R-band plates digitized by SuperCOSMOS. The charts are labelled with the right ascension of the sources. North is at the top and east to the left in all images.

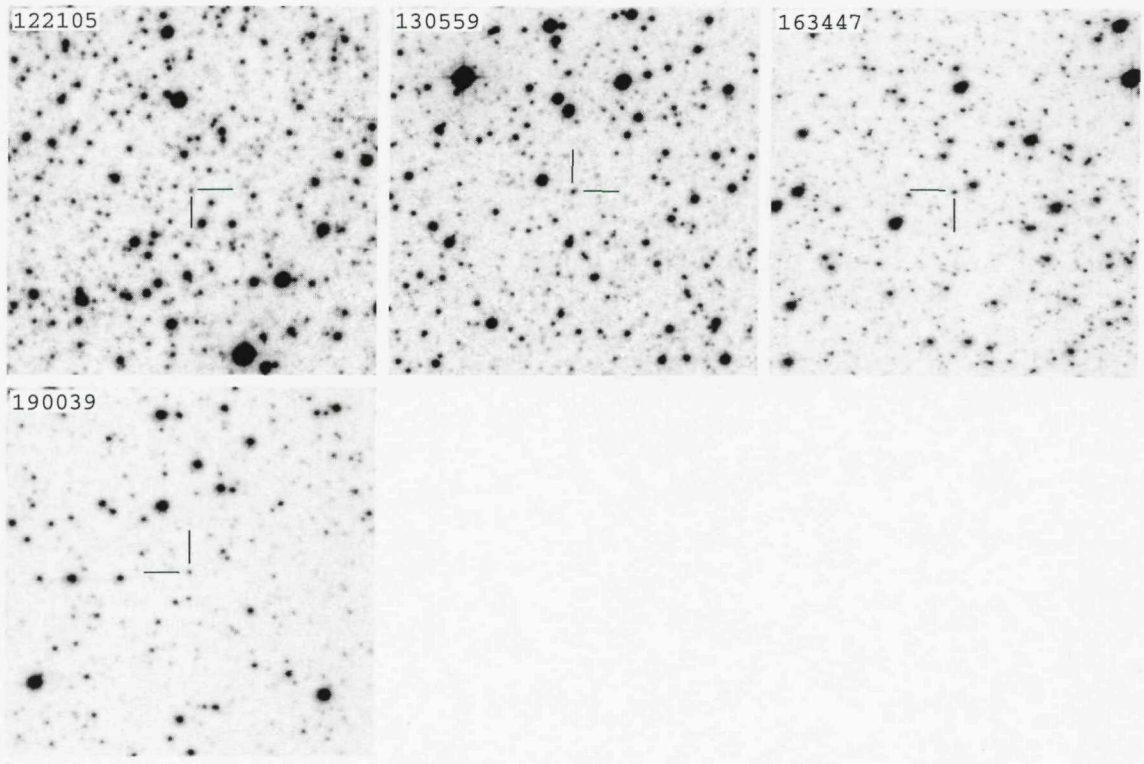

Figure 4.3: *Continued.* $4' \times 4'$ finding charts of the new CVs and CV candidates, made using UKST R-band plates digitized by SuperCOSMOS. The charts are labelled with the right ascension of the sources. North is at the top and east to the left in all images.

Table 4.2: Discovery observations. Dates are for the start of the night, and t_{int} is exposure time.

Object	Date	HJD 2453000.0+	t_{int}/s
Hα073418	2006 March 13	808.27607324	1200
Hα074208	2006 March 4	799.37595528	1100
Hα074655	2006 February 28	795.34335764	900
Hα075648	2006 April 5	831.26266972	1200
Hα092134	2006 March 4	799.40790090	1300
Hα092751	2006 March 4	799.42938229	1200
	2006 March 5	800.40408050	1200
Hα094409	2006 March 5	800.43760606	1200
Hα102442	2006 March 7	802.43638892	1000
Hα103135	2006 March 11	806.42886098	1300
Hα103959	2006 March 3	798.45787022	1200
Hα112921	2006 March 7	802.48228168	1100
Hα115927	2005 June 6	528.25724689	1300
Hα122105	2005 June 2	524.27931099	1300
	2006 March 5	800.52630675	1200
Hα130559	2006 March 3	798.54565116	1300
	2006 March 3	798.56223782	1300
Hα163447	2006 April 4	830.54425480	1200
Hα190039	2005 July 26	578.50057109	1800

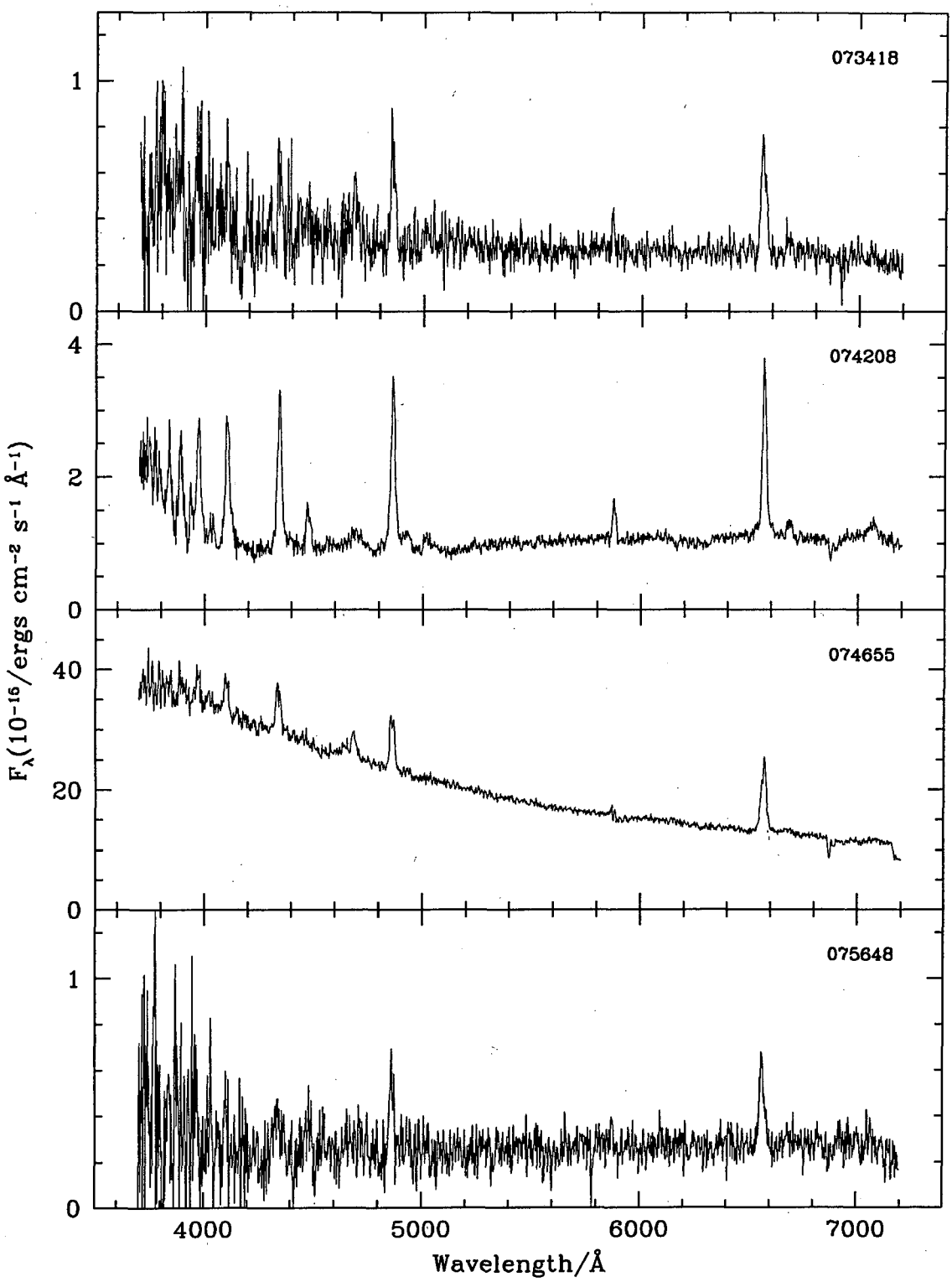

Figure 4.4: Identification spectra of the newly discovered CVs and CV candidates, obtained with the SAAO 1.9-m telescope. The panels are labelled with the right ascensions of the sources. All objects show the broad Balmer emission lines commonly seen in CVs. He I lines are detected in most, and He II λ4686 in some cases. For the systems where two observations are listed in Table 4.2 (Hα092751, Hα122105, and Hα130559) the spectrum shown here is the average of the two.

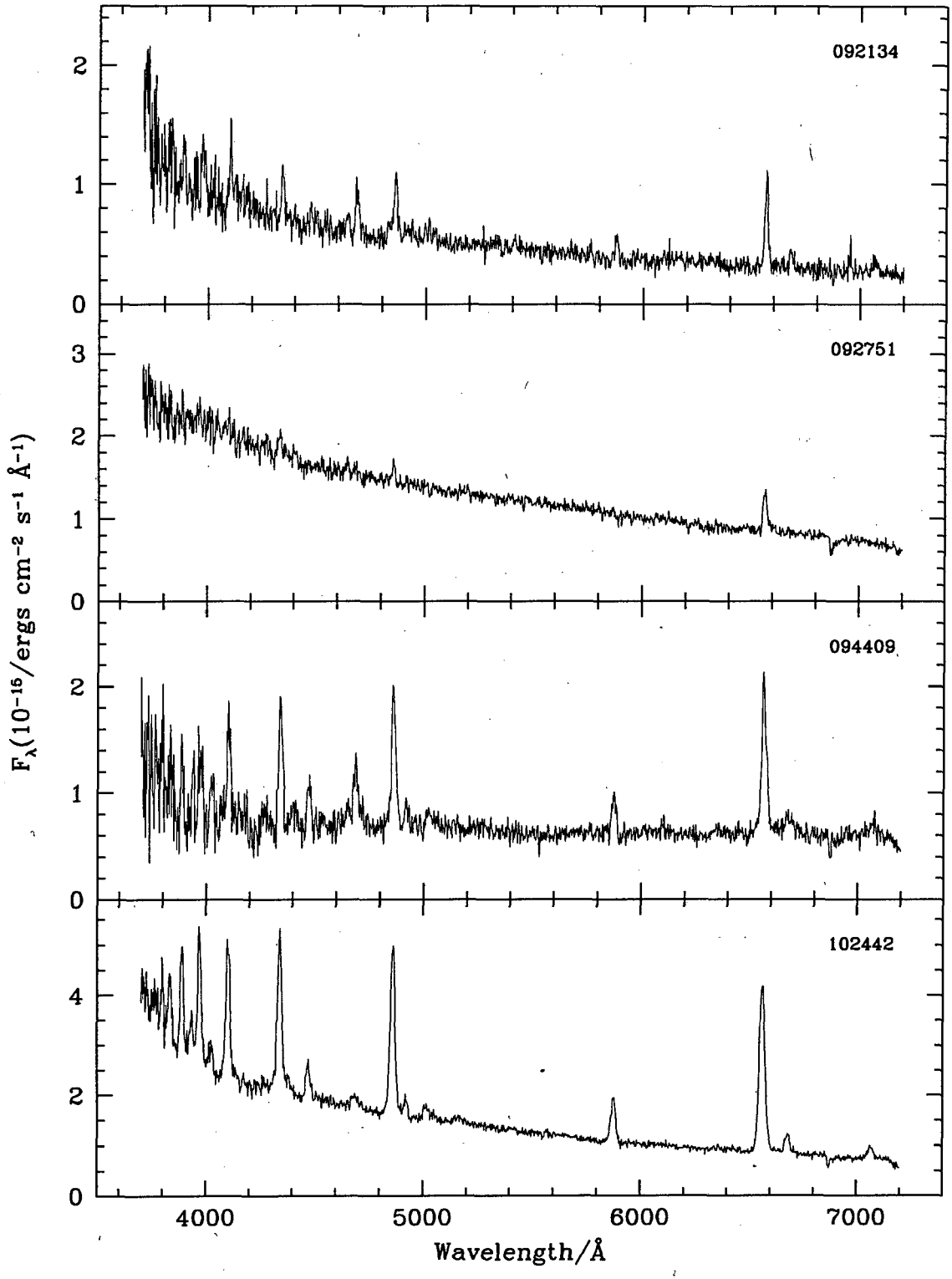

Figure 4.4: *Continued.* Identification spectra of the newly discovered CVs and CV candidates, obtained with the SAAO 1.9-m telescope. The panels are labelled with the right ascensions of the sources. All objects show the broad Balmer emission lines commonly seen in CVs. He I lines are detected in most, and He II λ4686 in some cases. For the systems where two observations are listed in Table 4.2 (Hα092751, Hα122105, and Hα130559) the spectrum shown here is the average of the two.

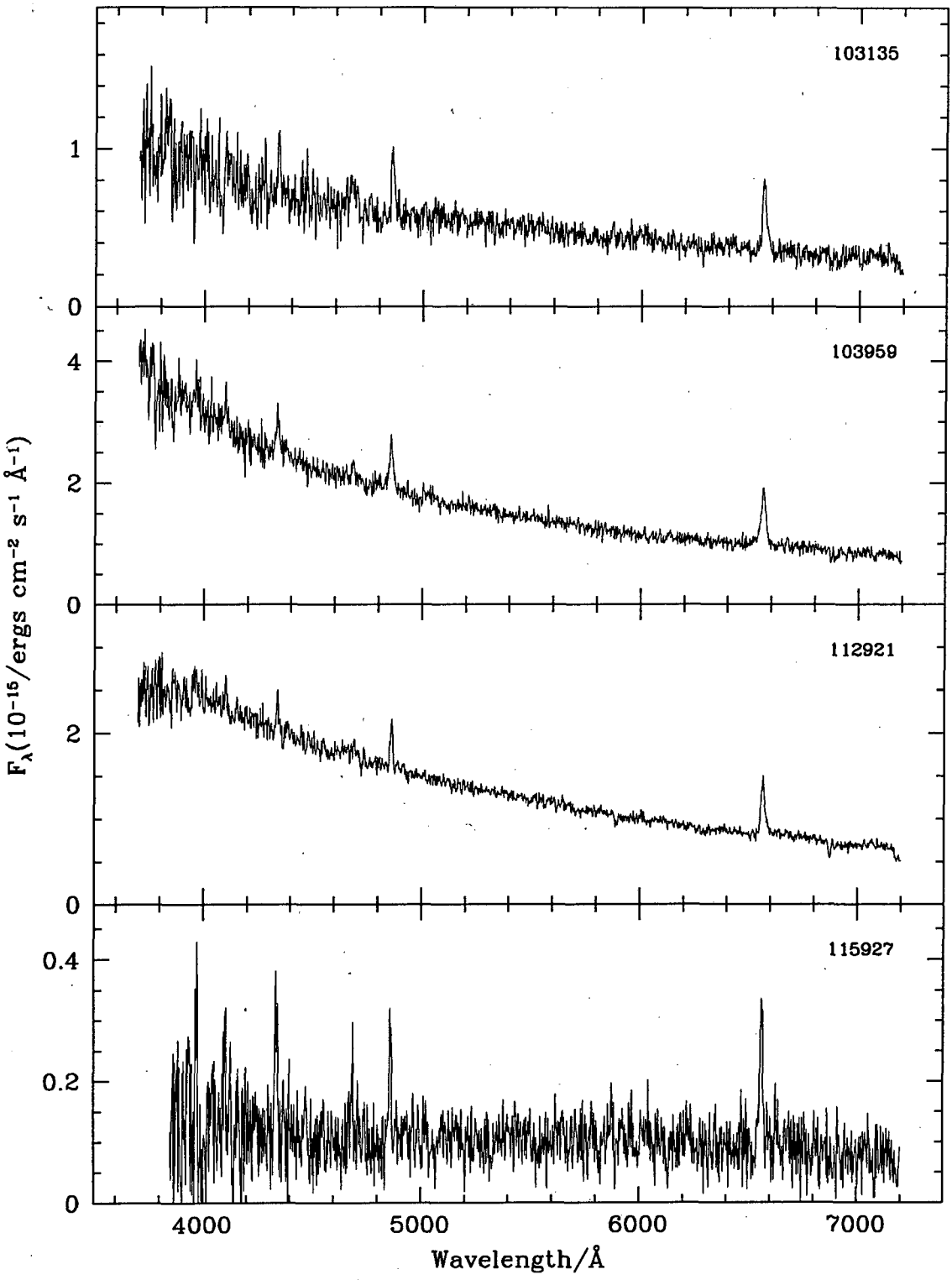

Figure 4.4: *Continued.* Identification spectra of the newly discovered CVs and CV candidates, obtained with the SAAO 1.9-m telescope. The panels are labelled with the right ascensions of the sources. All objects show the broad Balmer emission lines commonly seen in CVs. He I lines are detected in most, and He II λ4686 in some cases. For the systems where two observations are listed in Table 4.2 (Hα092751, Hα122105, and Hα130559) the spectrum shown here is the average of the two.

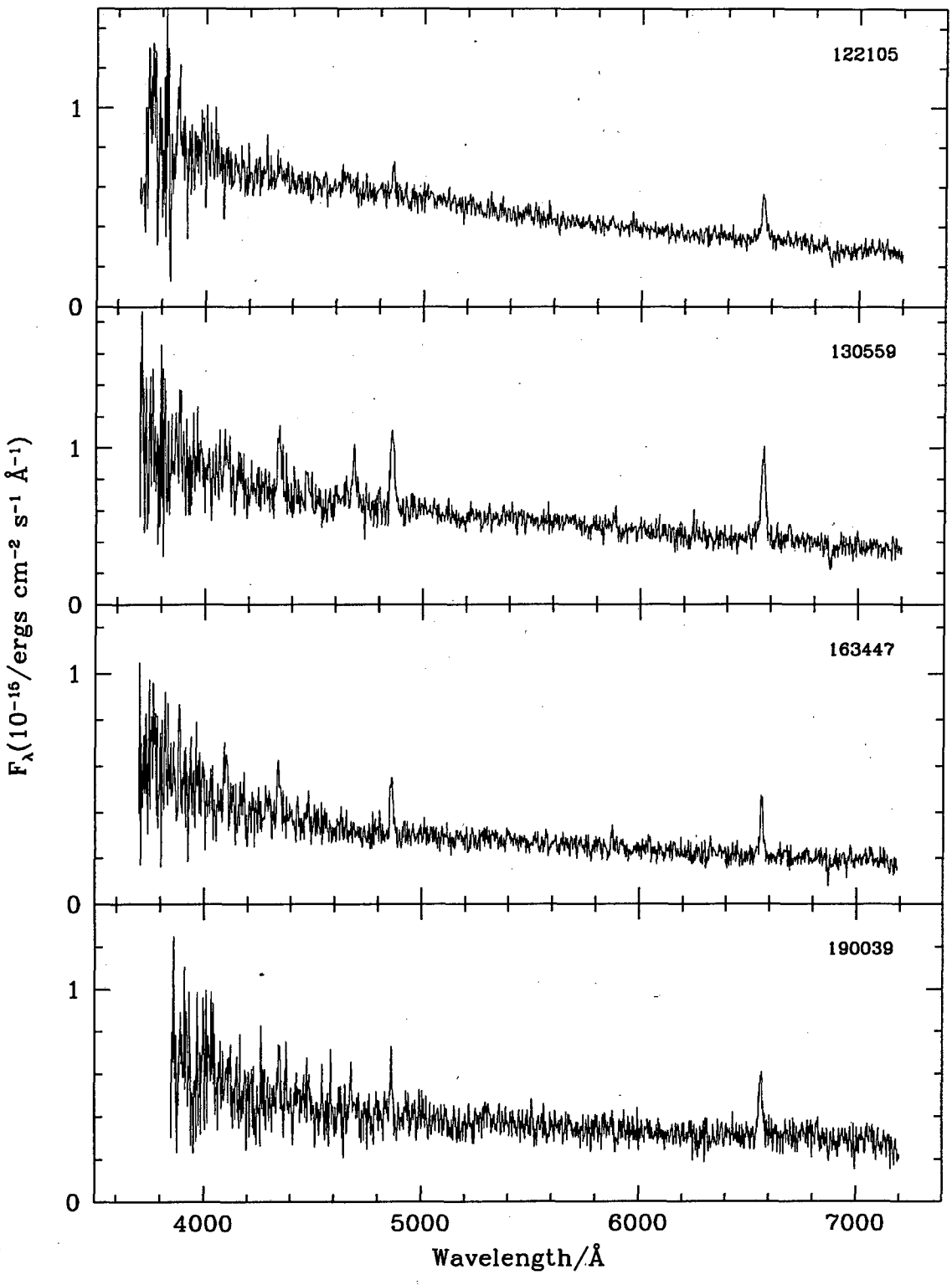

Figure 4.4: *Continued.* Identification spectra of the newly discovered CVs and CV candidates, obtained with the SAAO 1.9-m telescope. The panels are labelled with the right ascensions of the sources. All objects show the broad Balmer emission lines commonly seen in CVs. He I lines are detected in most, and He II λ4686 in some cases. For the systems where two observations are listed in Table 4.2 (Hα092751, Hα122105, and Hα130559) the spectrum shown here is the average of the two.

4.3.2 Time-resolved spectroscopy

In order to confirm the nature of the CV candidates and measure the orbital periods, I obtained medium-resolution, time-resolved spectroscopy of 13 systems. The brighter objects were observed with the SAAO 1.9-m telescope and the Grating Spectrograph, using grating no. 6 and a slit width of 1.″5. These spectra have $\simeq 2$ Å resolution over the wavelength range 5 220 to 6 960 Å. Additional data for 3 of the SAAO targets were obtained with the Cassegrain spectrograph on the CTIO 1.5-m telescope. The spectrograph was equipped with grating no. 47, which produced a spectral resolution of $\simeq 3.1$ Å, and covered wavelengths between roughly 5 740 and 6 850 Å. The fainter targets were observed with the ESO New Technology Telescope (NTT) and the ESO Multi-Mode Instrument (EMMI). The Red Medium-Dispersion (REMD) mode with grating no. 7 was used in combination with a 1″ slit. These spectra cover the wavelength range 5 550 to 7 035 Å at $\simeq 2.3$ Å resolution. The observing log for the time-resolved spectroscopy is given in Table 4.3.

Regular arc lamp exposures were taken to maintain an accurate wavelength calibration, and spectrophotometric standards were observed on each night to allow for flux calibration (as with the identification spectroscopy, many of these observations were obtained under conditions of poor transparency and seeing, but, since the purpose of the observations is to measure orbital periods, the flux calibration is not important). The time-resolved spectra were also extracted using IRAF. The wavelength calibration for each object spectrum was performed by interpolating the dispersion solutions (from fits to the positions of the arc lines) of the two arc lamp spectra taken before and after that object spectrum, and nearest to it in time.

Radial velocities were computed from the Hα lines, using the Fourier cross-correlation method described by Tonry & Davis (1979), as implemented in the FXCOR routine in IRAF. The radial velocities are found by correlating spectra with a template. The correlation was restricted to the wavelength range 6 450 to 6 650 Å. The template spectrum used for the measurements of radial velocities of a given CV is made, over a few iterations, by shifting all individual spectra of that system to 0 velocity (using the velocity measured in the previous iteration), and averaging them. In the cases where this method did not give satisfactory results (see e.g. Section 4.3.4.3 below), the double Gaussian technique of Schneider & Young (1980), as implemented in the program MOLLY, written by Tom Marsh, was used instead. Both methods give formal errors that appear to be too small in several cases (see Fig. 4.5) and, as expected, the errors are more badly underestimated in the systems where individual spectra have a higher signal-to-noise (S/N) ratio. This is not a serious concern, since the amplitudes of the orbital modulations are large compared to the uncertainty indicated by the scatter in radial velocity around these modulations.

Spectroscopic orbital periods were successfully measured for 10 systems. Fig. 4.5 shows Fourier transforms of the radial velocities of these CVs, together with phase-folded radial velocity curves. The largest amplitude signal in every Fourier transform was assumed to represent the orbital modulation of the system, although most of the data sets are actually aliased. These periods were used to phase-fold the data.

Table 4.3: Log of the time-resolved spectroscopy. Dates are for the start of the night, and t_{int} is the integration time.

Object	Date	HJD 2450000.0+	t_{int}/s	no. of spectra	telescope
Hα074208	2007 Jan 23	4124.57268179	600	36	CTIO 1.5-m
	2007 Jan 31	4134.29443787	900, 800	21	SAAO 1.9-m
	2007 Feb 2	4134.29443787	900	12	SAAO 1.9-m
	2007 Feb 3	4135.28935988	900	22	SAAO 1.9-m
Hα074655	2007 Feb 7	4139.34209354	900, 600	31	SAAO 1.9-m
	2007 Feb 8	4140.27308756	600	18	SAAO 1.9-m
	2007 Feb 9	4141.27007383	600	25	SAAO 1.9-m
	2007 Jan 25	4126.58152204	600	27	CTIO 1.5-m
Hα075648	2007 Mar 4	4164.65852881	800	9	ESO NTT
	2007 Mar 5	4165.54372639	800	21	ESO NTT
Hα092134	2007 Mar 7	4167.52424914	700	16	ESO NTT
	2007 Mar 8	4168.52563157	700	13	ESO NTT
Hα092751	2007 Mar 6	4166.52376369	600	24	ESO NTT
Hα094409	2007 Feb 6	4138.30240186	1000	22	SAAO 1.9-m
	2007 Feb 12	4144.29204597	1000	18	SAAO 1.9-m
	2007 Feb 13	4145.29538755	1000	20	SAAO 1.9-m
Hα102442	2006 Apr 9	3835.23557962	800	33	SAAO 1.9-m
	2006 Apr 10	3836.29186014	800	27	SAAO 1.9-m
Hα103135	2007 Mar 7	4167.70237491	700	20	ESO NTT
	2007 Mar 8	4168.65039829	700	14	ESO NTT
Hα103959	2007 Jan 31	4132.53336689	800, 1000	9	SAAO 1.9-m
	2007 Feb 2	4134.42759928	1000	17	SAAO 1.9-m
	2007 Feb 3	4135.53816631	1000	8	SAAO 1.9-m
	2007 Feb 4	4136.41314177	1000	5	SAAO 1.9-m
	2007 Feb 5	4137.40624764	1000	20	SAAO 1.9-m
Hα112921	2007 Feb 7	4139.57558033	1000	6	SAAO 1.9-m
	2007 Feb 8	4140.41105671	1000	19	SAAO 1.9-m
	2007 Feb 12	4144.51294292	1000	6	SAAO 1.9-m
	2007 Feb 13	4145.53923773	900, 1000	9	SAAO 1.9-m
	2007 Feb 20	4152.57276633	900	11	CTIO 1.5-m
	2007 Mar 31	4191.56402909	900	21	CTIO 1.5-m
Hα122105	2007 Mar 4	4164.76669129	800	14	ESO NTT
	2007 Mar 5	4165.78076644	800	7	ESO NTT
Hα130559	2007 Mar 6	4166.72655459	700	21	ESO NTT
	2007 Mar 8	4168.79295985	700	14	ESO NTT
Hα163447	2006 Apr 9	3835.56287275	1000, 1200	8	SAAO 1.9-m

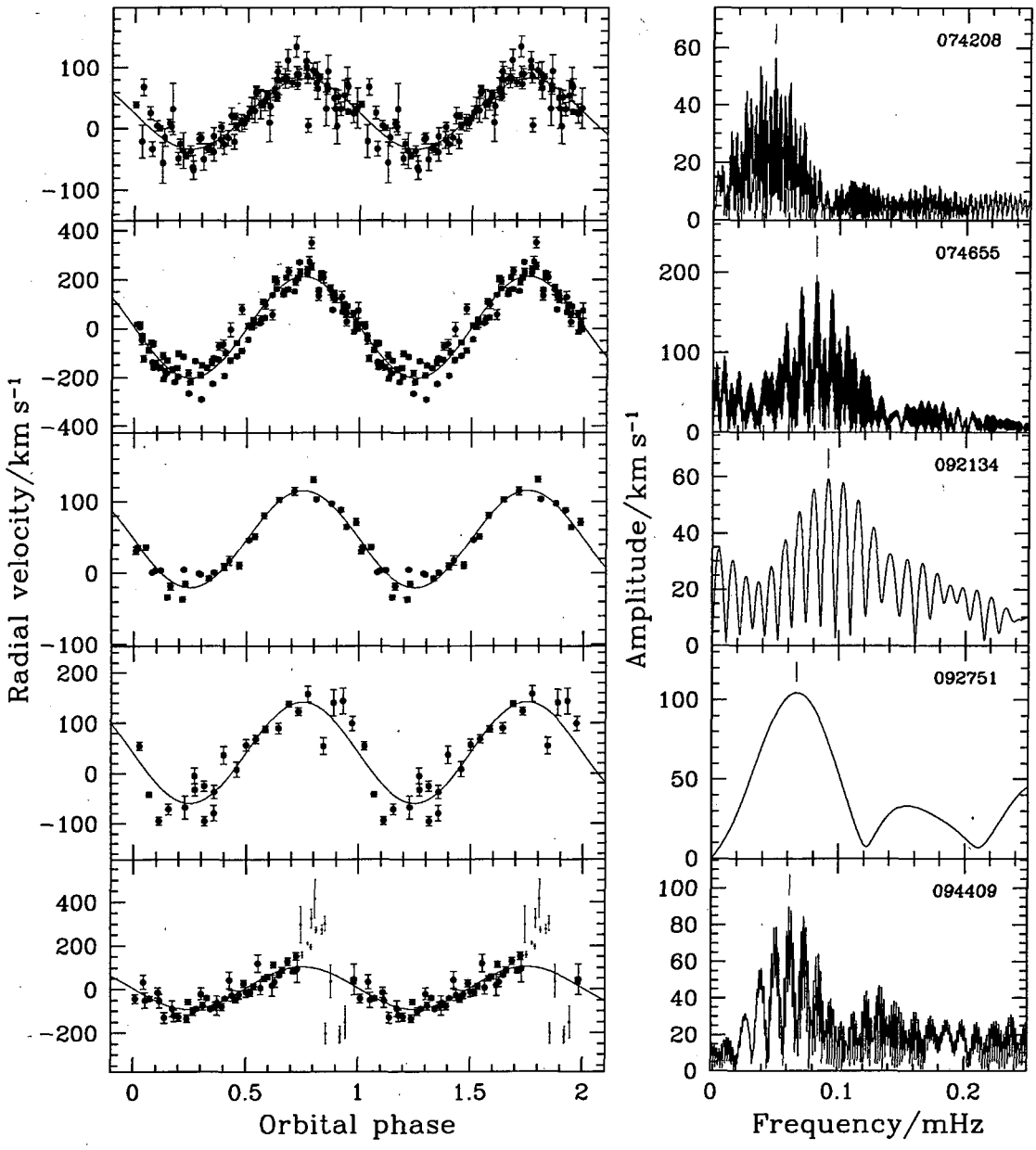

Figure 4.5: Fourier transforms and phase-folded radial velocity curves. Vertical bars in the Fourier transforms mark the periods used to fold the data. One cycle is repeated in the folded radial velocity curves, and the superimposed sine functions are least-squares fits to the (unfolded) radial velocities.

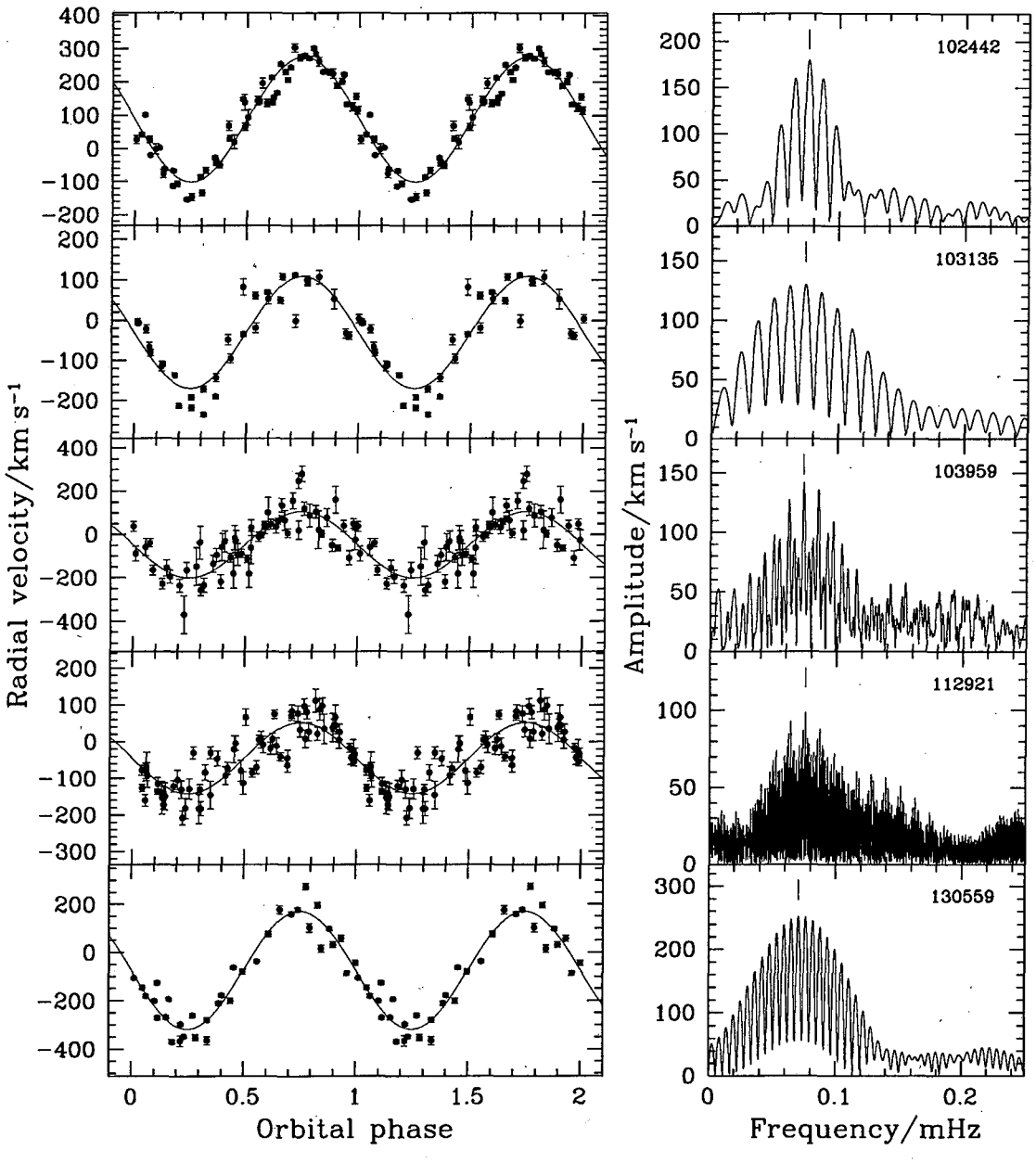

Figure 4.5: *Continued.* Fourier transforms and phase-folded radial velocity curves. Vertical bars in the Fourier transforms mark the periods used to fold the data. One cycle is repeated in the folded radial velocity curves, and the superimposed sine functions are least-squares fits to the (unfolded) radial velocities.

I use mostly qualitative criteria to decide, by inspection of the Fourier transforms and fits to radial velocity curves, whether it is impossible to determine the correct alias. A difficulty in making this more quantitative (through, e.g., the use of χ^2 statistics) is that the formal errors in radial velocities are often not very reliable (as noted above). This is a common problem (see e.g. fig. 6 of Southworth et al. 2007b, in which most points are more than 1-σ away from the best fit). In some of the cases below, where I state that a period cannot be measured unambiguously, it might in fact be possible to determine with reasonable confidence whether the alias choice is correct, using the analysis described by Thorstensen & Freed (1985). This additional information is of limited value in what I intend to do with the data (which is simply to determine whether systems are below or above the period gap), and, while qualitative, the method I use is sound and conservative.

A function of the form

$$v(t) = \gamma - K \sin\left[2\pi \left(t - T_0\right) / P_{orb}\right] \tag{4.1}$$

was fitted to the radial velocity curves by least-squares. T_0 is the epoch of red to blue crossing of the radial velocity (i.e. inferior conjunction of the secondary, if the emission lines trace the motion of the white dwarf). The fits are shown with the data in Fig. 4.5. The radial velocities of CV emission lines usually do not trace the dynamical motion of the white dwarf reliably, probably because of contamination from higher velocity components (e.g. Smak 1969; Stover 1981; Marsh et al. 1987; Hessman et al. 1989). However, since all velocity components are nevertheless modulated at the orbital period, and since this is the only binary parameter measured here, no serious attempt was made to find the true velocity of the primary.

The radial velocity curve of Hα094409 has a rotational disturbance near phase 0. The points that are plotted as smaller symbols in Fig. 4.5 were excluded from both the Fourier transform and the fit. For the other systems, all observations listed in Table 4.3 were used.

Phase-binned trailed spectra are shown in Fig. 4.6. Velocities are relative to the rest wavelength of Hα. For the systems where time-resolved spectra from both SAAO and CTIO are available, data from only one of the telescopes were used to make the trailed spectra (SAAO data for Hα074208 and Hα112921, and CTIO data for Hα074655). Individual spectra were continuum-normalized before being phase-binned.

Fig 4.7 displays higher quality spectra for some of the objects with low S/N identification observations. These spectra were made by averaging all the time-resolved spectra of a given system, after shifting each spectrum to the rest frame.

4.3.3 Time-resolved photometry

In addition to the time-resolved spectroscopy, I obtained high-speed photometry of several of the new CVs, using the University of Cape Town CCD photometer (UCT CCD; see O'Donoghue 1995) on the SAAO 1-m and 0.76-m telescopes. Table 4.4 gives a log of the photometry. These observations were made in white light. With the UCT CCD,

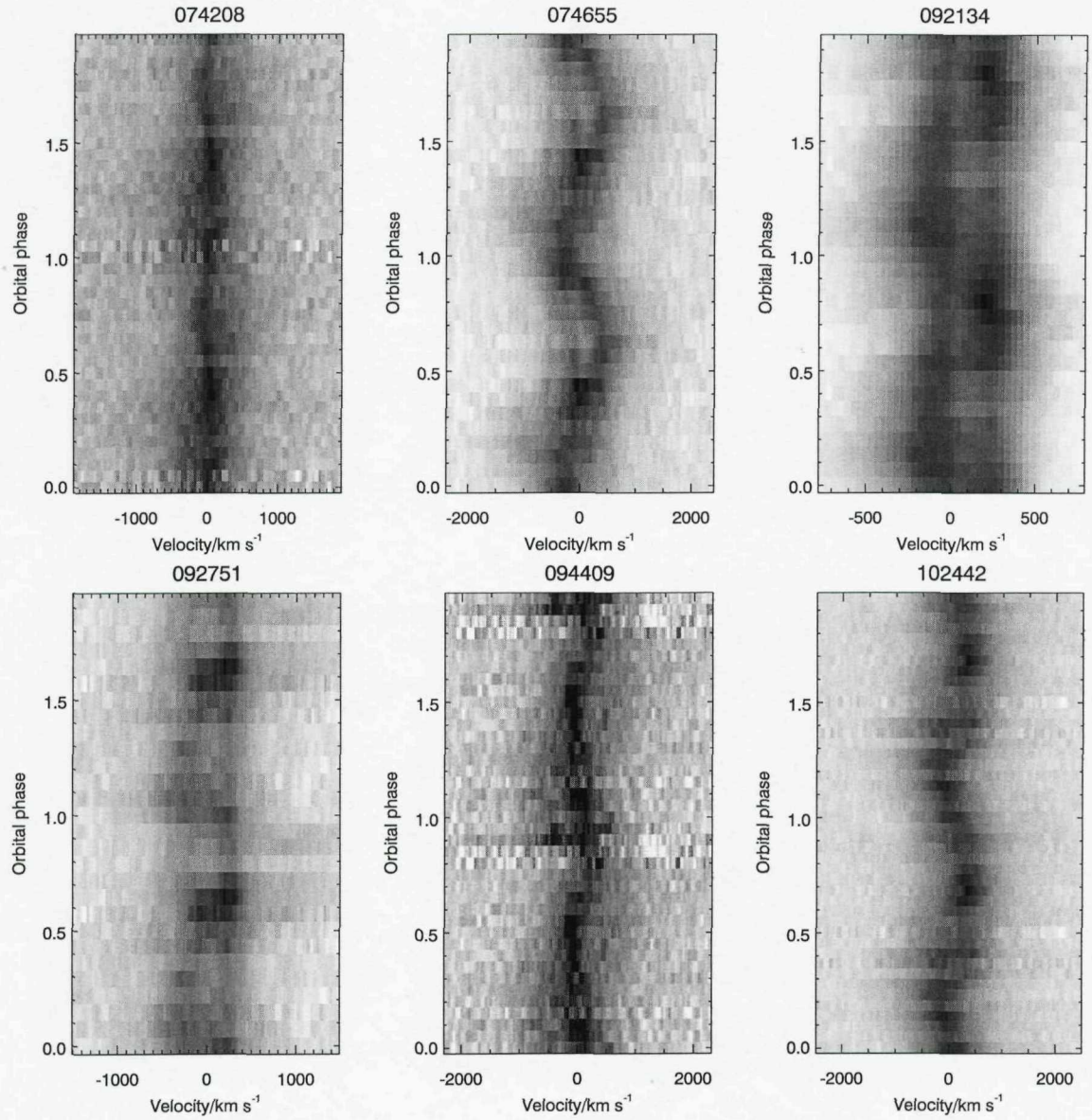

Figure 4.6: Phase-folded and -binned spectra. The individual spectra were normalized to the continuum before being binned. The grey-scale is linear, with higher flux being darker. Minimum and maximum threshold value were set for some of the images, to enhance the contrast.

unfiltered observations give photometry with an effective wavelength similar to Johnson V, but with a very broad bandpass. The non-standard flux distribution of CVs and the use of white light means that the observations cannot be precisely placed on a standard photometric system. Observations of standard stars allow for a magnitude calibration that approximates Johnson V to within $\simeq 0.1$ mag. I performed differential photometry, implying that colour differences between the targets and comparison stars were ignored in correcting the photometry for atmospheric extinction.

The light curves are shown in Fig. 4.8. The objects all display rapid flickering (the observational signature of mass transfer), and both Hα073418 and Hα094409 are found to

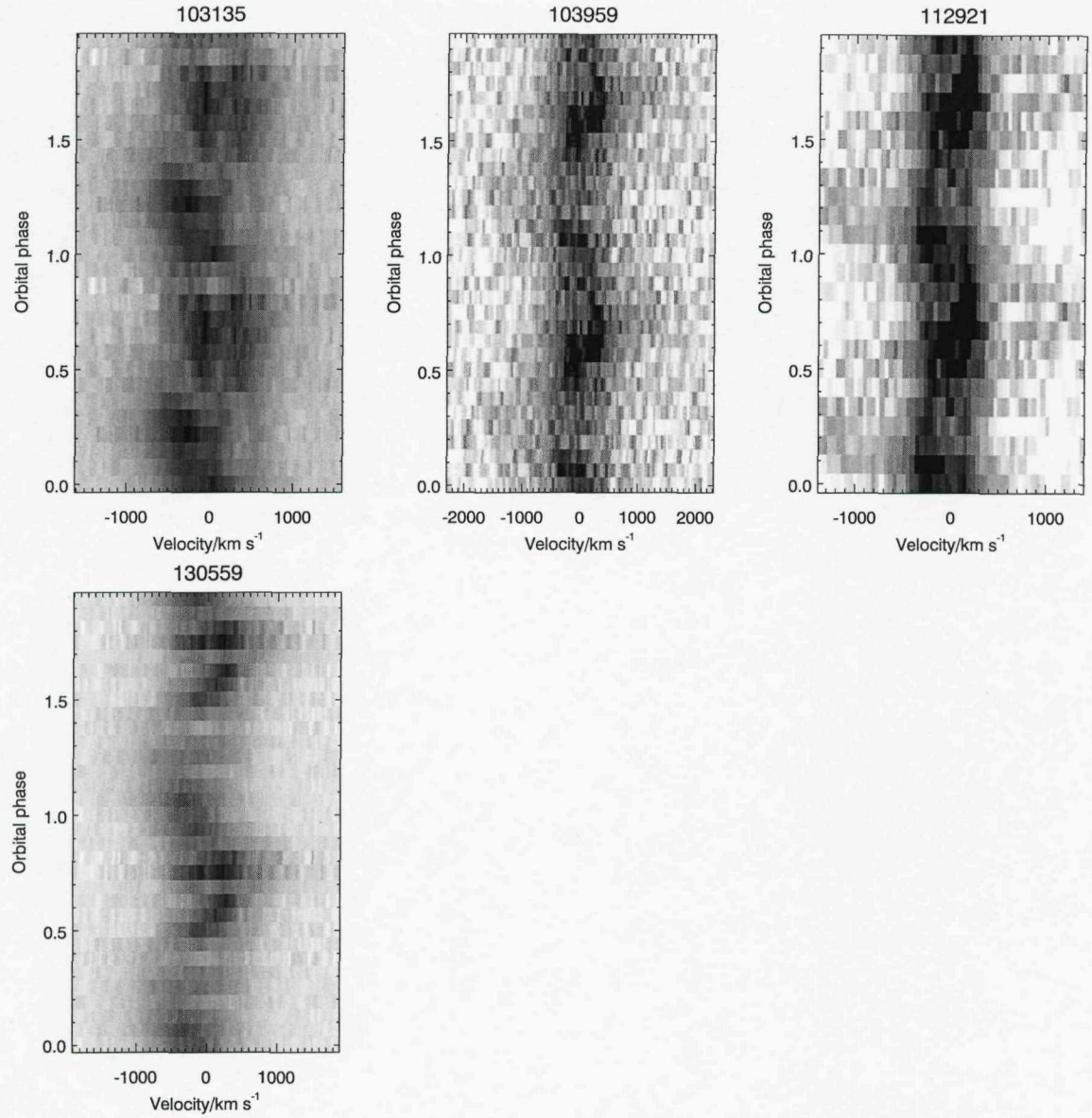

Figure 4.6: *Continued.* Phase-folded and -binned spectra. The individual spectra were normalized to the continuum before being binned. The grey-scale is linear, with higher flux being darker. Minimum and maximum threshold value were set for some of the images, to enhance the contrast.

be eclipsing systems. All light curves were searched for rapid oscillations, in part because there was reason to suspect that a few of the objects might be intermediate polars. No compelling evidence for coherent modulations on short time-scales was found in any of the photometry, but there is some indication of a $\simeq 15$ min quasi-periodic oscillation (QPO; e.g. Patterson et al. 1977; Warner 2004) in one of the light curves of Hα122105 (see Section 4.3.4.12).

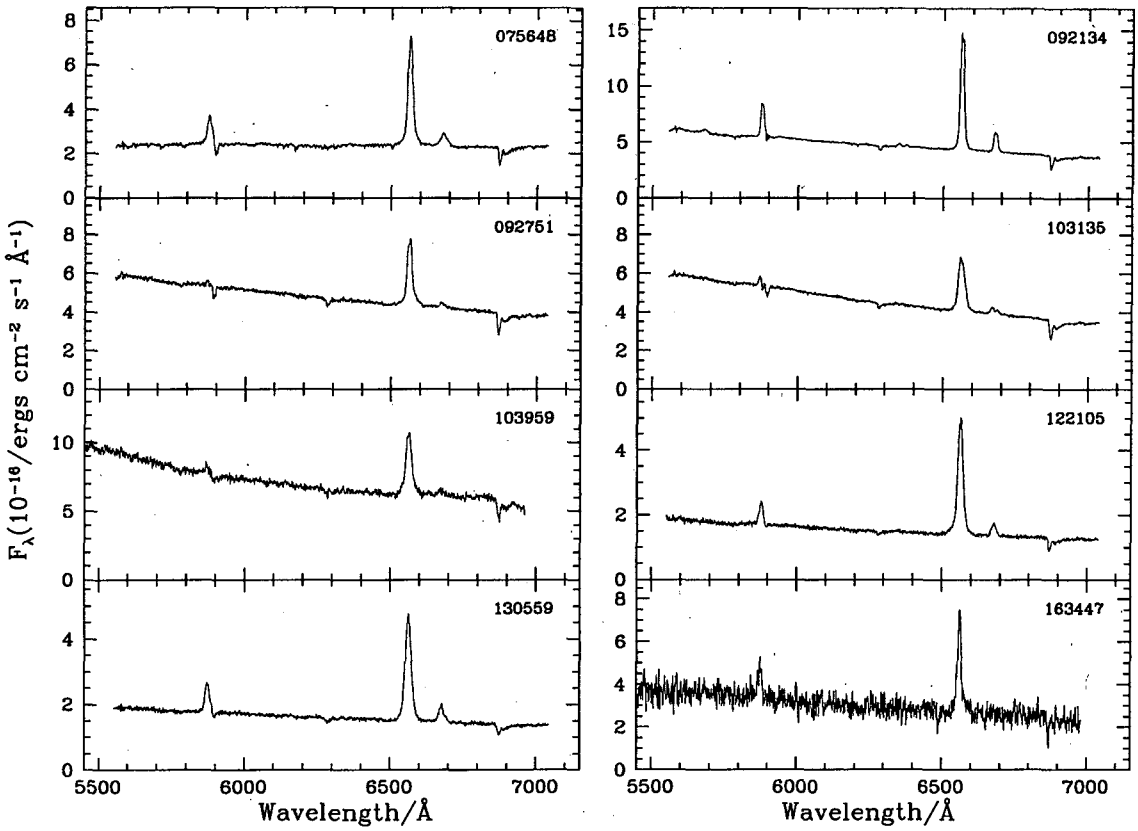

Figure 4.7: The averages of time-resolved spectra for the systems with the lowest S/N discovery observations, and for which additional observations were obtained. Individual spectra were shifted to the rest frame using the measured radial velocities before being averaged.

Table 4.4: Log of the high-speed photometry. Dates are for the start of the night, and t_{int} is the integration time (the photometer is a frame transfer CCD, so that there is no dead time between exposures).

Object	Run #	Date	HJD 2450000+	Run length/h	t_{int}/s	telescope	V
Hα073418	RP46	2007 Jan 26	4127.2845375	3.67	30	1-m	18.0[a]
	RP47	2007 Jan 27	4128.2790181	6.65	30	1-m	17.9[a]
Hα074655	RP53	2007 Jan 30	4131.2769557	2.07	8	1-m	14.0
Hα075648	RP49	2007 Jan 28	4129.2811127	1.90	10	1-m	16.6
Hα092134	RP50	2007 Jan 28	4129.3580250	2.11	10	1-m	17.0
Hα092751	RP51	2007 Jan 28	4129.4516001	1.85	10	1-m	17.8
Hα094409	RP54	2007 Jan 30	4131.3676657	1.52	10	1-m	16.7:[a]
Hα102442	RP41	2006 Apr 8	3834.3277709	3.58	10	0.76-m	16.2
	RP42	2006 Apr 9	3835.2742616	5.33	10	0.76-m	16.0
	RP44	2006 Apr 10	3836.2993854	3.40	10	0.76-m	16.0
Hα103135	RP52	2007 Jan 28	4129.5336457	2.30	10	1-m	17.2:
Hα103959	RP45	2007 Jan 24	4125.5677782	1.18	10	1-m	16.3:
	RP48	2007 Jan 27	4128.5618716	1.67	10	1-m	16.2
Hα122105	RP31	2005 Jun 10	3532.2414425	4.42	30	1-m	17.5
	RP34	2005 Jun 11	3533.2653467	2.48	20,30	1-m	17.5
Hα163447	RP43	2006 Apr 9	3835.5055942	4.12	10,14	0.76-m	18.3

Notes: [a]average magnitude outside of eclipse; ':' denotes an uncertain value.

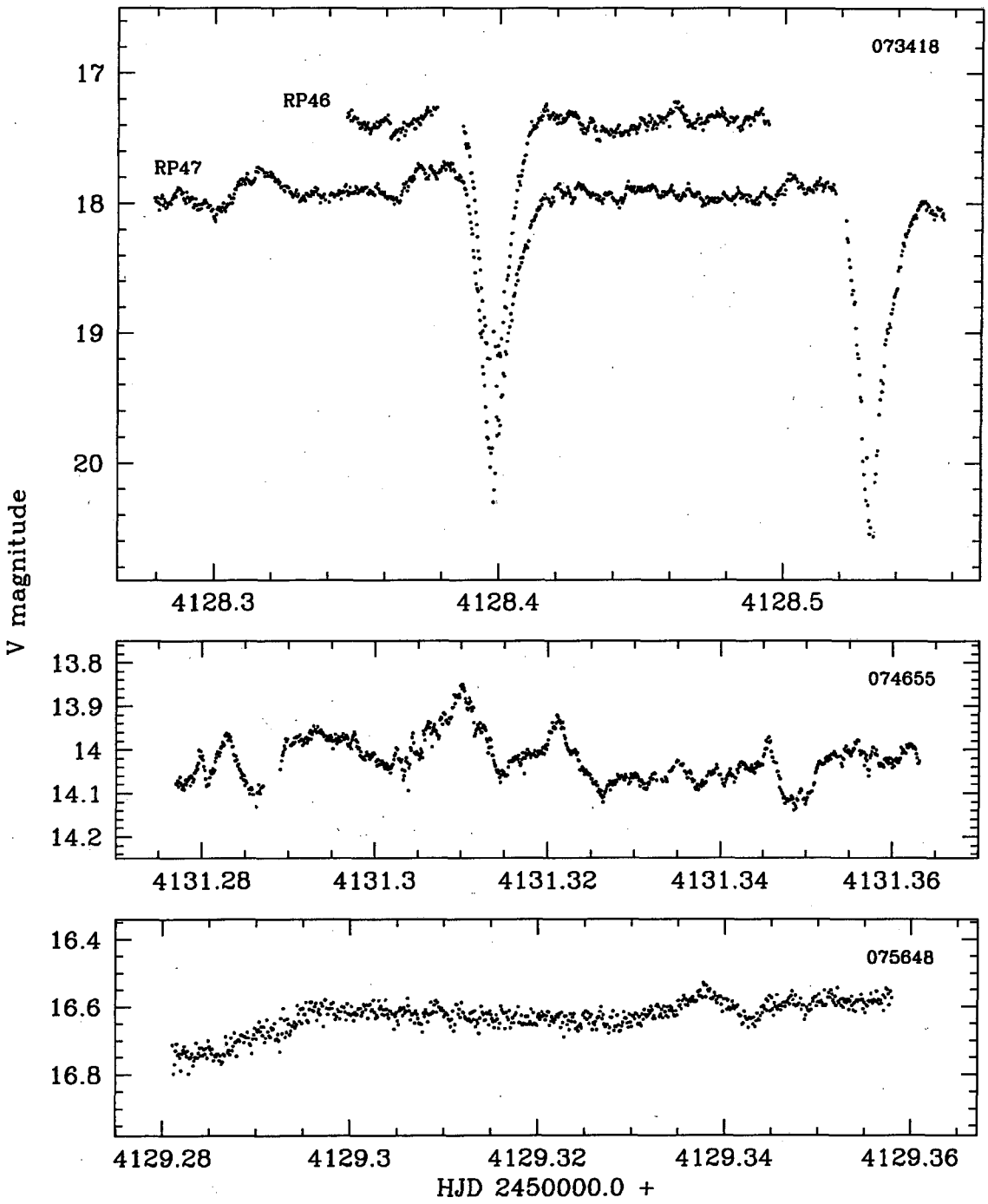

Figure 4.8: Light curves for some of the new CVs. Details of the observations are given in Table 4.4. For the systems with observations on more than one night (Hα073448, Hα102442, Hα103959, and Hα122105), arbitrary shifts were applied to one or two of the light curves, for display purposes, as specified in the text.

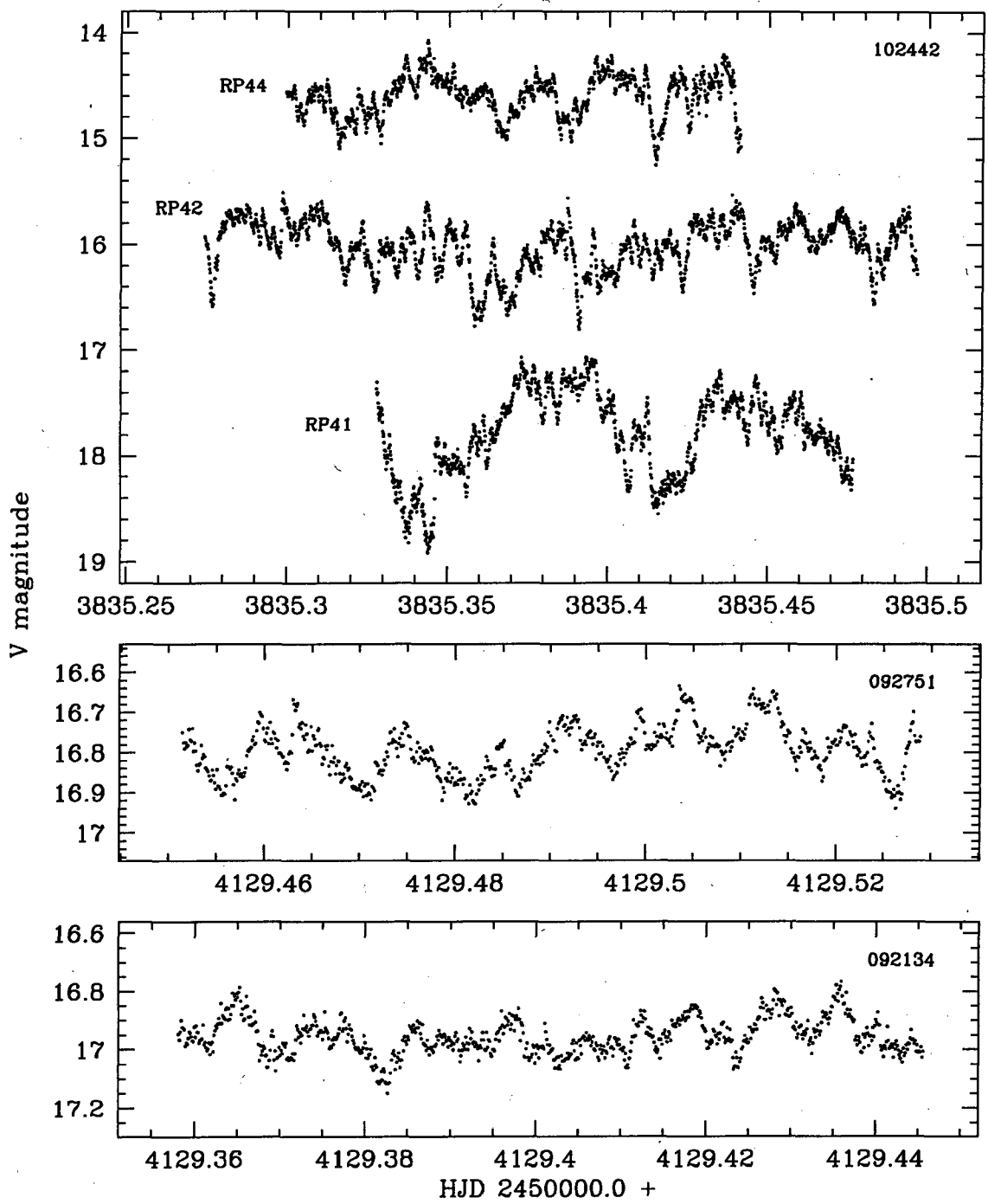

Figure 4.8: *Continued.* Light curves for some of the new CVs. Details of the observations are given in Table 4.4. For the systems with observations on more than one night (Hα073448, Hα102442, Hα103959, and Hα122105), arbitrary shifts were applied to one or two of the light curves, for display purposes, as specified in the text.

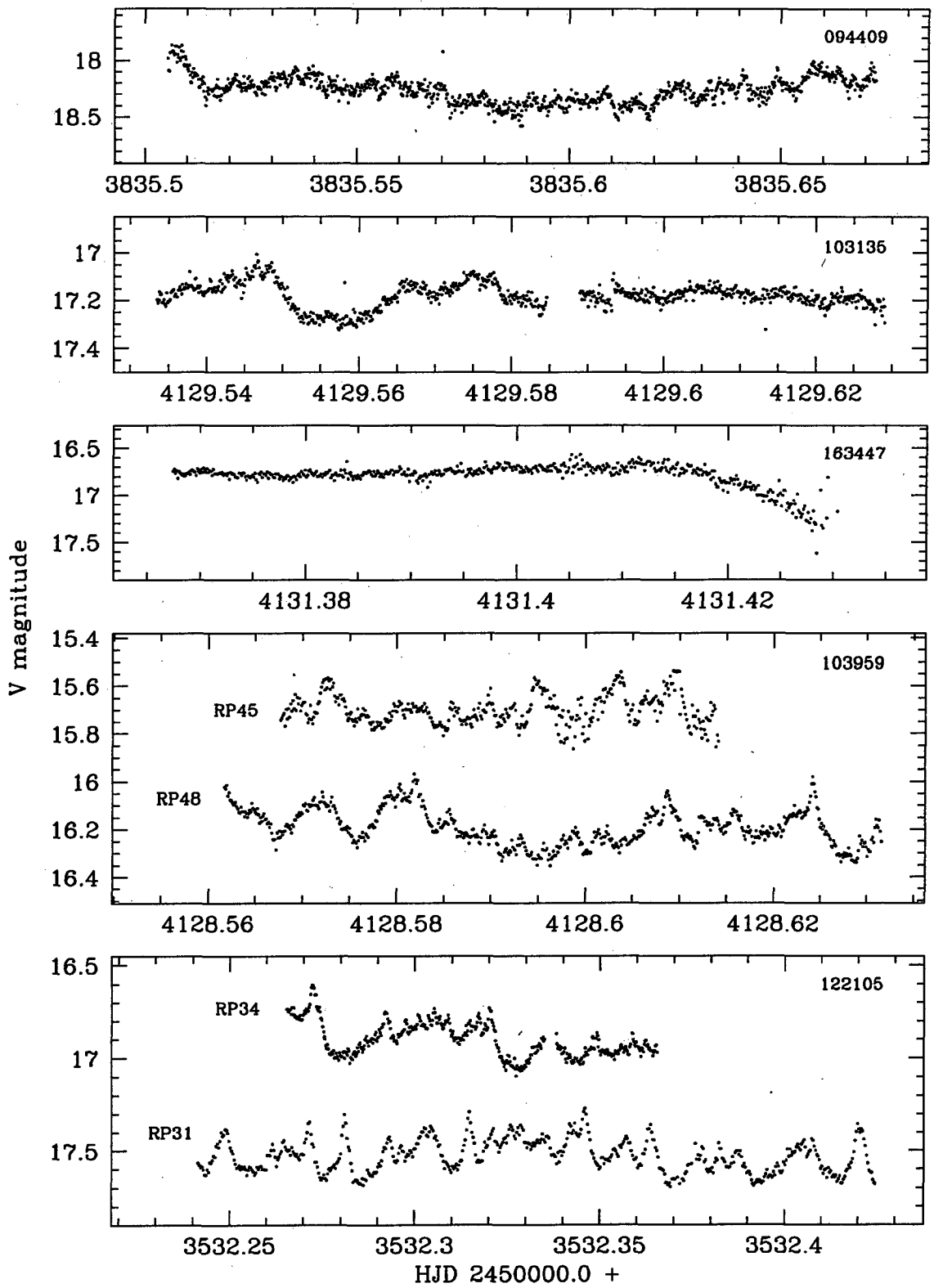

Figure 4.8: *Continued.* Light curves for some of the new CVs. Details of the observations are given in Table 4.4. For the systems with observations on more than one night (Hα073448, Hα102442, Hα103959, and Hα122105), arbitrary shifts were applied to one or two of the light curves, for display purposes, as specified in the text.

4.3.4 Results for individual systems

4.3.4.1 Hα073418

The identification spectrum of Hα073418 shows single-peaked Balmer, as well as He I and He II λ4686, emission lines on a reasonably flat continuum.

I obtained high-speed photometry on two consecutive nights, and found that Hα073418 is a deeply eclipsing system. The light curves are displayed in Fig. 4.8; the run RP46 data are shifted vertically by −0.6, and horizontally by 8 orbital cycles. The eclipse timings allowed for an unambiguous determination of the cycle count over the two nights. To derive an ephemeris, a line was fitted to the times of minimum by least-squares. The ephemeris of mid-eclipse is

$$\mathrm{HJD_{min}} = 2\,454\,127.33644(2) + 0.132726(2)\mathrm{E}. \qquad (4.2)$$

The absence of an orbital hump implies that this system has a high-$\dot{M}$ disc, and the single-peaked spectral lines and V-shaped eclipse profile suggest that it might be an SW Sex star (e.g. Thorstensen et al. 1991; Rutten et al. 1992; Horne 1999; Knigge et al. 2000; see also Section 2.3.2). The orbital period also fits in with this classification, since SW Sex stars are concentrated in the narrow period range 3–4 h (Thorstensen et al. 1991 already noted that SW Sex stars occupy a narrow range in P_{orb}; Rodríguez-Gil et al. 2007 recently argued that they are the dominant CV population in this period range). However, without time-resolved spectroscopy it is not possible to classify a CV as an SW Sex star with any certainty.

4.3.4.2 Hα074208

Hα074208 is probably the optical counterpart of the X-ray source 1RXS J074206.4−104929. Its spectrum has H I, He I, and He II emission lines, and a continuum that is red at wavelengths above $\simeq 5\,000$ Å, and blue below $\simeq 4\,200$ Å. Absorption bands from a late-type secondary star are also clearly detected.

No high-speed photometry was obtained for Hα074208. Time-resolved spectra were taken at both CTIO and SAAO. The Fourier transform of the radial velocity curve of the Hα line is shown, together with the phase-folded radial velocities, in Fig. 4.5. These data yield a measurement of $P_{orb} = 5.706 \pm 0.003$ h; the cycle count is unlikely to be wrong. It was not possible to measure the radial velocity of the secondary star.

The red end of the spectrum can be used to measure the spectral type of the secondary. A rough estimate of M0 ± 1 is found by visually comparing the spectra to templates from Jacoby et al. (1984) and Valdes et al. (2004)[4]. Fig. 4.9 shows the observed spectra, together with three templates.

Making the (very simplistic) assumption that the fractional flux contribution of other components is constant with wavelength over the continuum bands indicated by horizon-

[4]Note that the spectral classes M1 and M0 appear to have been inverted in Jacoby et al. (1984). The spectrum classified as M0V is clearly later than the one labelled M1V in their fig. 2g.

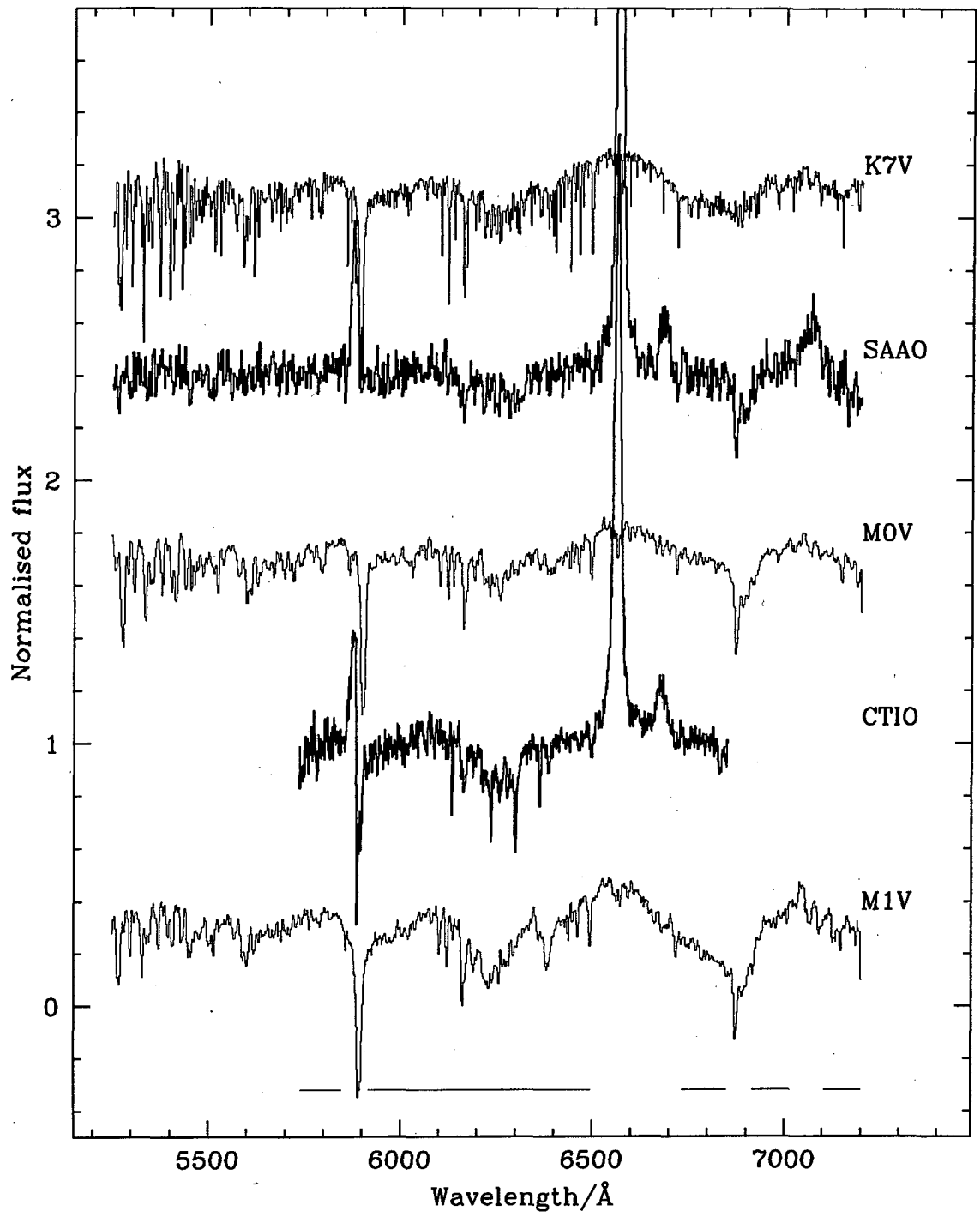

Figure 4.9: A comparison of the observed spectra of Hα074208 with late-type dwarf templates. All the spectra are normalized, and arbitrarily offset along the vertical axis. The bold spectra are the SAAO discovery spectrum and the average of all spectra obtained at CTIO.

tal bars along the bottom of Fig. 4.9, it is found that the secondary contributes between roughly 40 and 80% of the total flux at those wavelengths. The larger secondary contributions are found using the CTIO data. Available spectra of Hα074208 are not well suited to measuring broad-band magnitudes, since the wavelength coverage is not wide enough,

and the absolute flux calibration is not very reliable. However, rough R-band magnitudes of 15.8 ± 0.2 and 16.1 ± 0.3 can be estimated from the SAAO and CTIO data, respectively. Taking this at face value, the system was fainter when it was observed at CTIO, so that it is understandable that the secondary makes a larger relative flux contribution in those data. Knigge (2006) predicts $M_R = 7.3 \pm 0.4$ for a typical unevolved CV secondary with spectral type between K7 and M1. Using the extinction models of Drimmel et al. (2003) and Amôres & Lépine (2005), $A_R = 0.3 \pm 0.1$ is estimated for distances up to between 500 and 1 000 pc along this line of sight. This leads to a distance estimate of 580^{+160}_{-110} pc for Hα074208. There is no direct evidence that the system has an evolved secondary (unevolved CVs at 5.7 h have secondary spectral types of about M0.7; Knigge 2006). However, as noted before, CVs with evolved secondaries probably dominate the population at periods above $\simeq 5$ h (see Section 2.8.6). If Hα074208 is an evolved system, the distance estimate is invalid, since it assumes the luminosity predicted for an unevolved secondary.

4.3.4.3 Hα074655

At $V = 14.0$, Hα074655 is the brightest system in the sample of newly discovered CVs. The identification spectrum shows the double-peaked emission lines indicative of a high-inclination accretion disc, and a very blue continuum. In addition to H I and He I, He II λ4686 and the C III/N III λλ4640–4650 Bowen blend are detected in emission.

Probably because of variation in line profile shape as a function of orbital phase (see Fig 4.6), a cross-correlation with a single template spectrum produces a non-sinusoidal radial velocity curve (there is no reason to suspect that the orbit is eccentric). Radial velocities of this system were therefore measured with the double Gaussian technique. A Gaussian FWHM of 300 km/s and separation of 1 600 km/s were used to obtain the radial velocity curve shown in Fig. 4.5. The best-fitting sinusoid gives a rather high radial velocity amplitude of 208 km/s, which supports the suggestion that Hα074655 is view at high inclination. For this object, other aliases can be discarded as very unlikely to be the correct frequencies. The orbital period of Hα074655 is 3.3984 ± 0.0004 h. The only light curve of Hα074655 is shorter than the orbital period, and does not show any obvious orbital modulation.

4.3.4.4 Hα092134

The identification spectrum of Hα092134 has Balmer and He I emission lines, superimposed on a blue continuum. The data also show strong He II λ4686 emission. A higher quality spectrum is displayed in Fig. 4.7. The light curve of Hα092134 shows no modulation other than flickering.

Time-resolved spectroscopic observations were obtained on two consecutive nights. The Fourier transform and phase-folded radial velocity curve are shown in Fig. 4.5; note the small radial velocity amplitude (the best fit gives $K = 68.0$ km/s in equation 4.1). The strongest power in the Fourier transform of the radial velocity curve is at 9.134×10^{-2} mHz,

corresponding to 3.041 h. There is some possibility that the period is the next strongest alias (3.479 h). None of the other aliases provides acceptable fits to the data. Assuming that the largest amplitude signal represents the orbital modulation, the orbital period is 3.041 ± 0.009 h.

4.3.4.5 Hα092751

The spectrum of Hα092751 has quite weak emission lines (EW(Hα) is only ~ 20 Å, and He I is barely detected; see Fig. 4.4 and 4.7), and a blue continuum. One short light curve of this system is plotted in Fig. 4.8; it shows the usual short time-scale photometric behaviour of a CV.

Since time-resolved spectroscopy from only one night is available, only an imprecise period of 4.1 ± 0.3 h can be measured. The radial velocity data fortunately sample all orbital phases reasonably well (see Fig. 4.5). The amplitude of the best fit to the radial velocities is 100.9 km/s. The trailed spectrum of Hα092751, displayed in Fig 4.6, shows the double-peaked Hα profile typical of an accretion disc, and possibly also an S-wave component.

4.3.4.6 Hα094409

H I, He I, and strong He II λ4686 emission lines are detected in the spectrum of Hα094409. The lines are single-peaked in the identification spectrum, and the continuum is flat. Although the only light curve of Hα094409 was obtained under poor conditions, it shows that this is an eclipsing system. The eclipses are also seen in the time-resolved spectroscopy, both from the spectrophotometry and from the large rotational disturbance in the radial velocity curve (see Fig. 4.5).

If the largest amplitude signal in the Fourier transform of the radial velocity curve corresponds to the orbital modulation, then the orbital period of Hα094409 is 4.506 ± 0.004 h. The orbital frequency might, however, be identified with several other aliases (the shortest acceptable period is still above 3 h).

With phase 0 photometrically determined, the red to blue crossing of the radial velocities is at about phase 0.15. One of the defining characteristics of SW Sex stars is a phase shift between Balmer emission line velocities and the expected velocity of the white dwarf (Thorstensen et al. 1991). Two other factors, taken at face value, suggest that Hα094409 might be an SW Sex star. The first is that lines are single-peaked in the average spectrum, despite the high binary inclination. Secondly, the Hα line profiles seem to change as a function of orbital phase, possibly displaying central absorption at some phases (another phenomenon observed in SW Sex stars). However, the phase shift in the radial velocity curve of Hα094409 is only marginally significant, since no concerted attempt was made to trace the motion of the white dwarf, and since the low quality eclipse photometry does not allow for an accurate determination of phase 0. Thus, while there are some hints that Hα094409 might be an SW Sex star, the data presented here are not good enough to allow for a firm classification.

4.3.4.7 Hα102442

The member of this sample with the strongest Balmer emission is Hα102442, which has EW(Hα) $\simeq$ 120 Å. He I and He II λ4686 are also detected in emission. Time resolved spectra were taken over two nights, and the sampling and data quality were sufficient to establish an unambiguous cycle count between the two radial velocity curves (see the Fourier transform in Fig. 4.5). The orbital period of Hα102442 is 3.673 ± 0.006 h. A quite large radial velocity amplitude is measured for this system (the best-fitting amplitude is 188.3 km/s). The trailed spectrum given in Fig. 4.6 shows a pure S-wave modulation.

I obtained three light curves of Hα102442 on consecutive nights, the last two simultaneously with the time-resolved spectroscopy. These observations are displayed in Fig. 4.8. The run RP41 and RP44 data are shifted vertically by +1.6 and −1.4, respectively, and horizontally by +1 d and −1 d, respectively. The photometry shows large amplitude flickering, but nothing that can be recognized as an orbital modulation.

4.3.4.8 Hα103135

The identification spectrum of Hα103135, plotted in Fig. 4.4, has a blue continuum with Balmer and He II λ4686 emission. He I λ6678 is double-peaked in the average spectrum (Fig. 4.7). I obtained one light curve of fairly low quality of this system; it is shown in Fig. 4.8. The short gap in the light curve was caused by poor conditions.

A total of 34 spectra of Hα103135 were taken over two nights at ESO. The Fourier transform of the radial velocities measured from these spectra has maximum power at 7.40×10^{-2} mHz (3.76 h). It is also possible that the correct period corresponds to the second strongest aliases, at 3.22 h. Assuming that the highest amplitude alias represents the orbital modulation, the period is 3.76 ± 0.02 h. The trailed spectrum shows that the Hα line profile is double-peaked at some orbital phases (Fig. 4.6).

4.3.4.9 Hα103959

Hα103959 has a spectrum displaying Balmer, He II, and very weak He I emission lines, superimposed on a blue continuum (see Fig. 4.4 and 4.7). Two short light curves of this system are shown in Fig. 4.8; run RP45 was shifted vertically by −0.6, and horizontally by +3 d.

The orbital period is most likely 3.785 ± 0.005 h, but aliases at 3.266 h and 4.498 h cannot be ruled out (see the Fourier transform in Fig. 4.5). The trailed spectrum in Fig. 4.6 shows what is probably a double-peaked disc component, as well as a fainter, higher velocity component.

4.3.4.10 Hα112921

Weak Balmer emission lines are detected in the spectrum of Hα112921, superimposed on a blue continuum. The Hα line profile is double-peaked in some of the higher resolution spectra, and He I is weakly detected. No high-speed photometry is available for this system.

The sampling of the time-resolved spectroscopy, taken at both SAAO and CTIO, is unfortunately far from optimal, with long gaps between different observations; for this reason there is some uncertainty in cycle count. The strongest signal in the Fourier transform is at 7.538×10^{-2} mHz (corresponding to 3.685 h). The next largest amplitude aliases are at 3.196 h and 4.352 h (see Fig. 4.5). Assuming that the correct alias has been identified, the orbital period is 3.6851 ± 0.0004 h. The radial velocity amplitude is quite low (the fit gives 96.9 km/s), but there is also a fainter, much higher velocity modulation visible in the trailed spectrum (Fig. 4.6).

4.3.4.11 Hα130559

The spectrum of Hα130559 shows strong He II λ4686, and broad Balmer and He I lines (see Fig. 4.4 and 4.7). No photometry was obtained for this system.

Time-resolved spectra of Hα130559 were taken on 6 and 8 March 2007. The largest amplitude signal in the radial velocity curve of this system is at 7.072×10^{-2} mHz (3.928 h). However, there is clearly a serious aliasing problem (see the Fourier transform in Fig. 4.5). The two nearest aliases are at 4.273 h and 3.635 h. Assuming that the peak marked in the Fourier transform represents the orbital modulation, the orbital period is 3.928 ± 0.013 h. The radial velocity amplitude is large (the best fit gives 244.4 km/s). The trailed spectrum in Fig. 4.6 shows only an S-wave.

4.3.4.12 Hα075648 and Hα122105

I obtained time-resolved spectroscopy of Hα075648 and Hα122105, but was not able to measure orbital periods from the data. The spectra of both objects contain Balmer and He I lines in emission (Fig. 4.4 and Fig. 4.7). Only a single light curve is available for Hα075648. The observation was short and taken under poor conditions, but it does show the flickering expected in a mass-transferring system. The photometric variations in Hα122105 are faster and of slightly larger amplitude. Neither system shows a photometric modulation that is readily recognizable as orbital. A Fourier transform of the run RP31 light curve of Hα122105 shows that it contains a modulation with a period of roughly 920 s (this time-scale can be picked out in the light curve by eye). The signal was not present on the next night, and was probably a QPO (CVs in which QPOs have been detected usually do not persistently display them, even when at the same brightness; e.g. Warner 2004; Pretorius et al. 2006). Horizontal and vertical shifts of -1 d and -0.6 mag were applied to the shorter light curve of Hα122105 (run RP34) displayed in Fig. 4.8. The photometric and spectroscopic appearance of these two objects leave little doubt that they are both CVs.

Hα075648 and Hα122105 were observed for 7.3 h and 5.1 h, respectively, over 2 nights with EMMI, but these data failed to yield plausible radial velocity curves. The dispersion solutions were checked by measuring the wavelengths of the 6300.30 and 5889.95 Å night sky lines (Osterbrock et al. 1996) in all of the spectra. The rms errors obtained from the two lines are only 0.05 Å and 0.1 Å, respectively; there is therefore no concern regarding

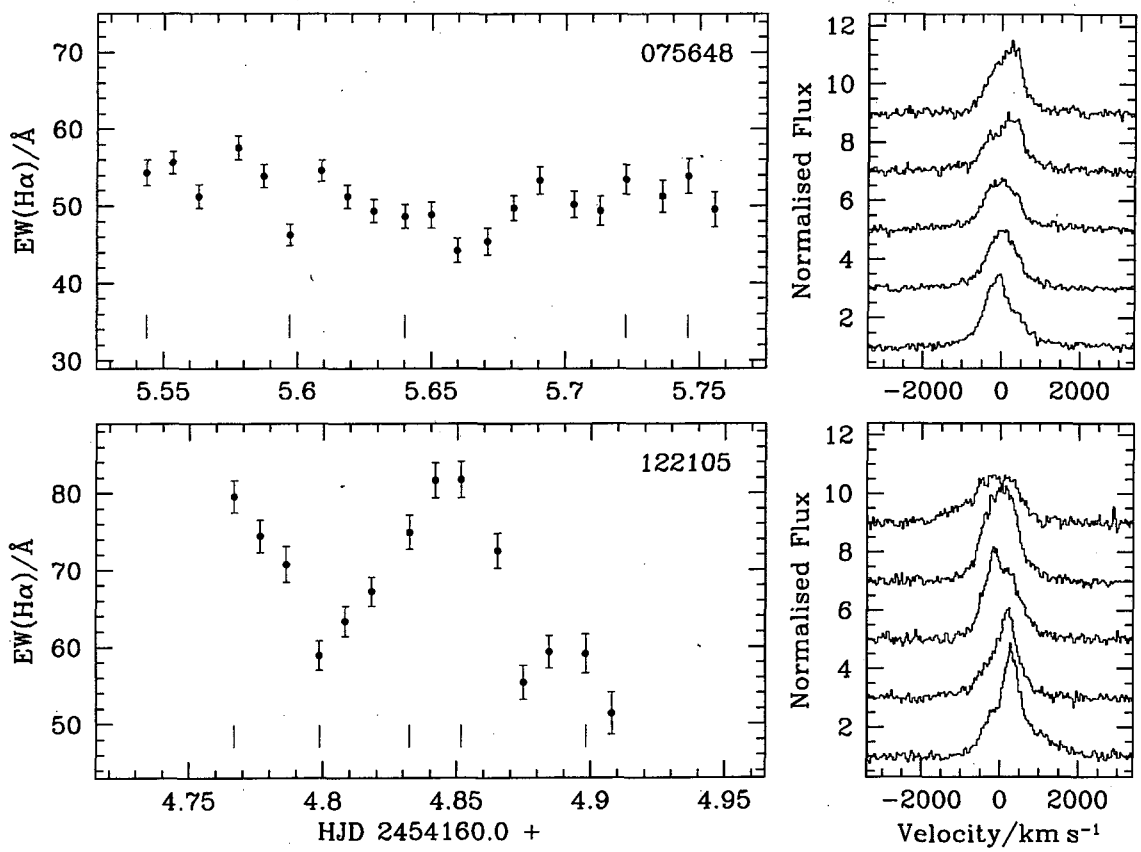

Figure 4.10: Left-hand panels show the equivalent widths of the Hα lines of Hα075648 and Hα122105 as a function of time for the longest spectroscopic runs on each of the systems. The Hα profiles of some spectra of Hα075648 (top) and Hα122105 (bottom) are shown on the right. These spectra are normalized to the continuum and vertically offset. Tick marks along the bottom of the EW curves indicate the spectra displayed in the right-hand panels; time increases upwards. Velocity is relative to the rest wavelength of Hα.

the wavelength calibration. Radial velocities were measured using a cross-correlation with template spectra, and also both a single Gaussian and a double Gaussian with a range of separations, for both the Hα and He I λ5876 lines. None of these techniques produced sinusoidal radial velocity curves. The results obtained are reminiscent of the radial velocity curve of the SW Sex star V380 Oph, displayed in fig. 13 of Rodríguez-Gil et al. (2007), which shows a shorter time-scale variation superimposed on the sinusoidal orbital modulation. If the same behaviour is displayed by Hα075648 and Hα122105, then less than one orbital cycle was observed on any one night.

The reason for the difficulty in finding radial velocities appears to be that the line profiles change dramatically on quite short time-scales, so that different velocity components are measured in different spectra. Hα122105 also displays large variability in EW(Hα). This is illustrated in Fig. 4.10. All standard techniques of measuring radial velocities assume that (at least) the line wings are constant in shape. The failure of these techniques here is therefore not surprising.

EW flaring is observed in intermediate polars and SW Sex stars (e.g. Morales-Rueda

et al. 1996; Smith et al. 1998; Rodríguez-Gil & Martínez-Pais 2002). Strong He II λ4686 emission would support an interpretation of these two systems as magnetic CVs; however, it is not detected in either system, and, if this line is present, it is significantly weaker than Hβ. The very structured and variable line profiles, as well as the EW variations in Hα122105, may indicate SW Sex star behaviour, but additional observations, perhaps of higher time and/or spectral resolution, are required to determine the CV sub-types of these two systems, and to measure their periods.

4.3.4.13 Hα163447

In addition to the noisy discovery observation, I obtained a few higher resolution spectra, as well as a light curve, of Hα163447. Spectra of the system display broad Balmer emission lines, and also He I λ5876 emission (see the average spectrum in Fig. 4.7). The light curve plotted in Fig. 4.8 also shows the flickering typical of CVs. The classification of Hα163447 as a CV is secure, but neither the time resolved spectroscopy nor photometry allows for an orbital period measurement.

4.3.4.14 Hα115927 and Hα190039

I obtained only identification spectra for Hα115927 and Hα190039, and both these spectra have low S/N. The objects are classified as CV candidates, since their spectra show resolved Balmer emission lines, flat Balmer decrements, and possibly He II λ4686 emission. However, better observations are needed to confirm the nature of these two objects.

4.4 The overall Hα-selected CV sample

In this section, I return to the selection of targets from the SHS, and discuss not only the newly discovered CVs, but also previously known CVs recovered by the selection of Hα emission line objects.

4.4.1 Recovery of previously known CVs

The fraction of known CVs recovered by the selection procedure gives an indication of the completeness of the CV sample. There are 42 previously known CVs with $R < 17$ in the survey area covered by the follow-up described above, and only 7 of these were selected as targets. The majority of the CVs that were not selected (30 systems) were excluded by the cuts in the class, quality, and blend IAM parameters. Of the other 5 that were missed, one was excluded because it is blended (despite being classified as a single point source in the SHS), and two did not satisfy the $R - \mathrm{H}\alpha$ vs $R - I$ cut-off criterion. The remaining two CVs that were not recovered had colours above, but very close to the selection cut.

With 7 recovered systems and 14 new CVs, the sample completeness can be no better than $(14 + 7)/(14 + 42)$, or 38%. Since 460 out of the 507 targets were observed, the efficiency of selecting previously known CVs is $(7/42)(460/507)$. That is, the selection is

expected to identify roughly 15% of all CVs at $R < 17$, if known CVs occupy the same general part of the $R - \mathrm{H}\alpha$ vs $R - I$ plane as the intrinsic CV population. Fig. 4.11 shows the R, $R - I$, and P_{orb} distributions of CVs with $R < 17$ in the survey area considered, highlighting the previously known CVs chosen as targets by the selection.

Although the CV recovery rate is low, a more important concern is magnitude- or period-dependent bias in the recovery rate (as that would almost certainly imply the same bias for the overall CV sample). It is important in this regard that a large fraction of CVs known to have been missed by the selection (30 out of 35) were excluded by the restrictions on IAM parameters, which are expected to be mostly insensitive to colour and apparent magnitude.

The magnitude distributions of both the selected CV sample and the recovered CVs appear to indicate that, up to $R = 17$, the CV sample is not affected by an apparent magnitude bias. This is illustrated both by the steep rise towards fainter magnitudes in the R distribution (top panel of Fig. 4.11)[5], and by the fact that the selection does not recover relatively more bright CVs (the same fraction of previously known CVs are recovered in the magnitude bins $R < 14$, $14 \leq R < 16$, and $16 \leq R < 17$). The bottom panel of Fig. 4.11 also shows clearly that a larger fraction of known CVs are recovered at short periods than at long periods. It is therefore tempting to conclude that, as expected (since short-period CVs have stronger emission lines), any period bias in the selection favours the inclusion of short-period CVs.

The central panel of Fig. 4.11 shows the distribution of CVs in $R-I$. The distribution of the sample of previously known CVs has a standard deviation of 1.0. This large spread in $R - I$ is not physical—it results from poor photometry and variability between the R and I epochs. The CVs included in the sample are on average bluer than the previously known CVs. This bias in $R-I$ is not as strong as it appears at first sight. As in Chapter 3, CVs at very long periods will not be considered, because they are likely to contain evolved secondary stars. Seven systems in the sample of previously known CVs have periods greater than 8 h, and 5 of these have $R - I$ colours between 0.36 and 0.70, i.e. in the two maximum bins of the $R - I$ distribution. With these 7 objects excluded, the probability that the $R-I$ distributions of the selected and previously known CVs are drawn from the same population is 0.54, according to a KS test. Therefore, there is no good evidence for a blue bias in $R-I$ from this comparison. However, the samples used for the comparison are both quite small, and the positive slope of the stellar locus in the $R - \mathrm{H}\alpha$ vs $R - I$ plane, which causes the selection to be more sensitive to objects with relatively small EW(Hα) at bluer $R - I$, implies that such a bias may be expected. The implications that this may have for P_{orb}- or R-dependent biases will be further discussed in Section 4.5.2.

[5]Note that the magnitude distribution of the sample of previously known CVs indicate that it is not approximately complete to $R = 17$. This is not surprising; see Section 3.3.1.

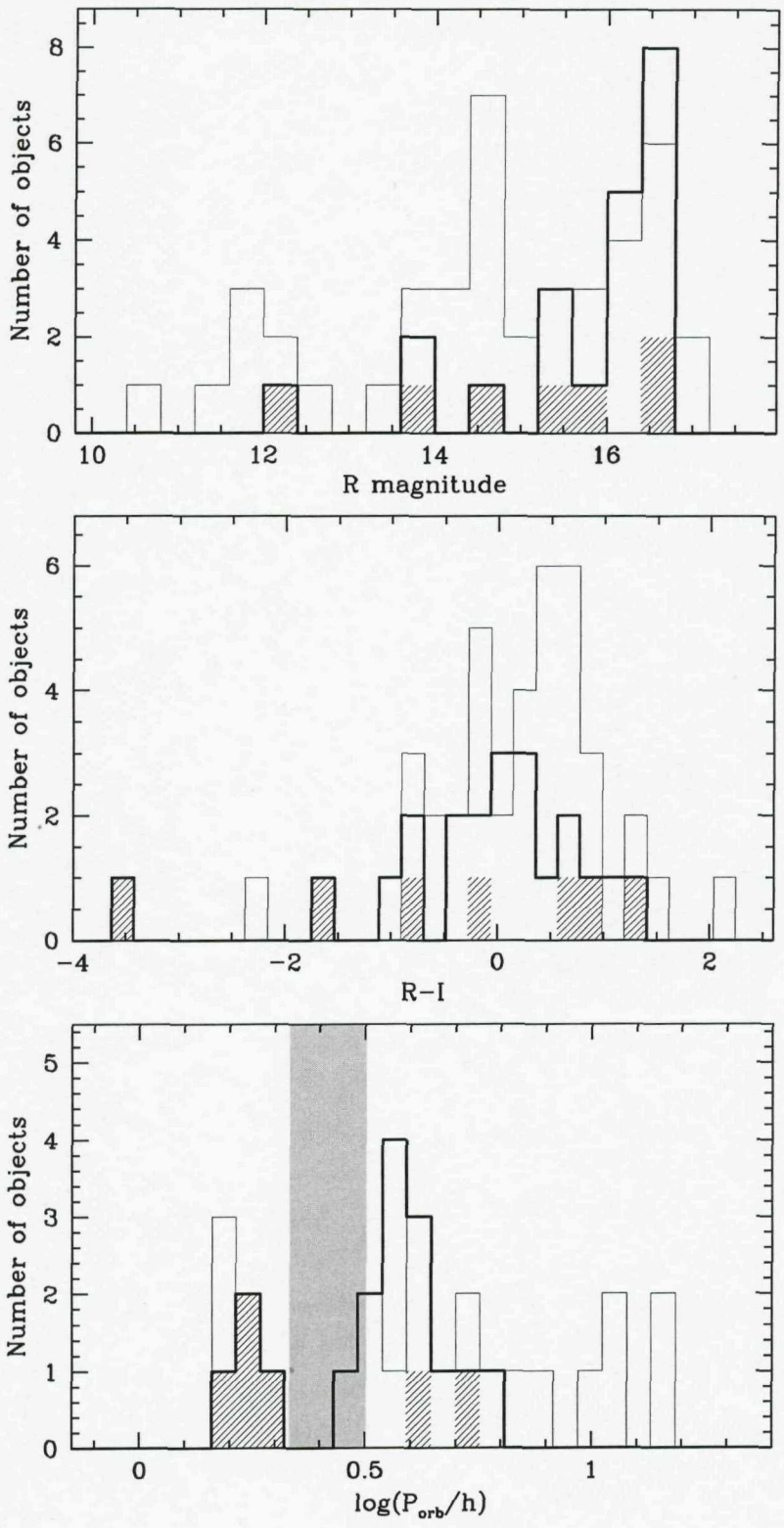

Figure 4.11: The R, $R-I$, and P_{orb} distributions of CVs with $R < 17$ in the area covered by the follow-up. The bold histograms show all systems in the selected sample. Previously known systems are plotted as fine histograms, and previously known systems recovered by the selection are shown as cross hatched histograms. The period gap is indicated in the middle panel by light grey shading of the period range 2.15 to 3.18 h. One known CV in the survey area covered in the follow-up, the nova V1017 Sgr, with $P_{orb} = 5.714$ d, is not shown on the scale of the P_{orb} histograms.

4.4.2 Distance limits, classification, and other properties

The selection identified a total of 21 CVs; two thirds of this sample consists of newly discovered systems. Some properties of the CVs comprising the sample are given in Table 4.5. Lower limits on the distances (d_l) are based on near-IR photometry, as described below. The last column of Table 4.5 lists references for the sub-types and orbital periods, where available.

The semi-empirical donor sequence of Knigge (2006) predicts absolute magnitudes of CV secondaries as a function of orbital period, and provides a useful technique for constraining the distances of CVs. The observed K_S magnitudes (or lower limits on K_S), and the predicted absolute K_S magnitudes of the secondaries in the systems for which period measurements are available, were used to find lower limits on their distances. The CIT magnitudes of Knigge (2006) were transformed to the 2MASS system using the prescription of Carpenter (2001), updated to reflect the final 2MASS data release[6]. Since these CVs are at low Galactic latitudes, it is not really appropriate to neglect extinction. Therefore the total Galactic N_H along the line of sight to each of the objects, taken from the Galactic H I map of Kalberla et al. (2005), was used to estimate upper limits on A_{K_S}. Values of extinction were obtained from the column densities with the aid of relations between N_H and A_V and between A_V and A_{K_S} from Predehl & Schmitt (1995) and Cambrésy et al. (2002). The resulting lower limits on distances for new as well as previously known CVs are listed in Table 4.5.

Hα092134 is in the period gap (the upper edge of the period gap is not very clearly defined, but Knigge 2006 places it at at 3.18 h), although it is clearly accreting (see the light curve and spectra). The predicted M_{K_S} of a typical CV secondary at 3.18 h was used for the upper limit on its distance. If the secondary in Hα092134 differs from a typical secondary in a CV at 3.18 h only in being of slightly lower mass, it would be fainter than assumed, and the distance limit would be too high. On the other hand, the fact that 2MASS provides only a lower limit on K_S takes the limit in the opposite direction. 2MASS photometry also gives only limits on K_S for Hα073418, Hα092751, and Hα130559, implying that the lower limits on the distances of these three systems are conservative. The distance limits assume that the predicted luminosities of the secondaries are appropriate for our systems (i.e. that the secondaries are unevolved). This assumption is more likely to be valid for CVs at $P_{orb} \lesssim 5$h.

The lower distance limits do not rule out the absolute magnitudes of quiescent DNe for any of the newly discovered CVs, and therefore do not lead to firm classifications. A blue continuum and weak emission lines characterize the spectra of many NLs. The spectroscopic appearance of several of the new CVs indicate that they are very likely NLs, with Hα092751 and Hα112921 being the clearest examples (see Fig. 4.4). The different photographic R-band epochs, as well as the new observations presented here, provide good evidence of large amplitude variability for the following systems: Hα073418, Hα094409,

[6]The updated colour transformations are available at http://www.astro.caltech.edu/~jmc/2mass/v3/transformations/.

Table 4.5: Sub-types, orbital periods, R-band magnitudes, and lower limits on distances of the CVs included in the survey. Entries for the systems that will not be included in the comparison to theory are in italics.

Object	Type	P_{orb}/h	R	d_l/pc	References
V1040 Cen	SU	1.45	13.9	40	1
DV Sco	SU	1.65:	16.7	270	2,3
VV Pup	*polar*	*1.67392*	*14.6*	*140*	*4,5*
CU Vel	SU	1.88:	15.8	120	6
Hα092134		3.043	16.8	530	7
Hα073418	SW:	3.18542	16.7	320	7
Hα074655		3.3984	14.0	180	7
Hα102442		3.673	16.4	580	7
Hα112921	NL:	3.6851:	15.5	510	7
Hα103135	NL:	3.76:	16.3	630	7
Hα103959	NL:	3.785:	16.4	670	7
Hα130559		3.93:	16.5	500	7
Hα092751	NL:	4.1	16.2	770	7
CW Mon	*DN, IP:*	*4.238*	*15.4*	*210*	*8*
Hα094409	SW:	4.506:	16.2	520	7
HZ Pup	*CN, IP*	*5.11*	*16.5*	*1010*	*9*
Hα074208		*5.706*	*15.3*	*490*	*7*
Hα075648	SW:	—	16.0	—	7
Hα163447	NL:	—	16.7	—	7
Hα190039	NL:	—	16.8	—	7
V383 Vel	DN	—	12.3	—	10

References: (1) Patterson et al. (2003); (2) vsnet-alert 8325; (3) Daisaku Nogami, private communication; (4) Herbig (1960); (5) Schneider & Young (1980); (6) Mennickent & Diaz (1996); (7) Paper I; (8) Kato et al. (2003); (9) Abbott & Shafter (1997); (10) Williams (2000).
Notes: The types are dwarf nova (DN); nova-like variable (NL); SU UMa star (SU); SW Sex star (SW); intermediate polar (IP); classical nova (CN). Uncertain values or classifications are denoted by ':'. Hα190039 is classified as a CV based only on a single, low quality spectrum.

Hα102442, and Hα163447. These data are, however, clearly not sufficient to distinguish between, e.g., DN and VY Scl star behaviour. There is no clear indication that any of the new CVs are magnetic (but note that these systems have not yet been thoroughly studied).

V1040 Cen, CU Vel, and DV Sco are SU UMa stars. The orbital period listed for DV Sco is uncertain because it was estimated from the superhump period (the superhump period is 1.71 h, but even this is uncertain, because the superhump photometry available for this system is aliased; Daisaku Nogami, private communication). V1040 Cen and CU Vel both have normal ϵ (fractional superhump period excess; see Section 2.3.1.2), and therefore are not expected to be period bouncers (Patterson et al. 2003). V1040 Cen reaches $V = 12.5$ at maximum, and is likely to be very nearby. The second bright DN in the sample, V383 Vel, was in outburst during the SHS observations. It is a poorly studied

system; the orbital period is not known.

The sample includes two magnetic CVs, namely VV Pup and HZ Pup. HZ Pup is a classical nova (nova Pup 1963), as well as an IP. VV Pup is a polar.

Kato et al. (2003) report a 37-min modulation in outburst photometry of the DN CW Mon, and suggest that the system might be an IP. However, the high coherence associated with the spin cycle of a white dwarf has not yet been demonstrated for this signal, and it is detected only near maximum of outburst. Warner (2004) classifies the 37-min modulation as a QPO—a phenomenon commonly seen in high-$\dot{M}$, non-magnetic CVs. Furthermore, CW Mon does not have particularly strong He II λ4686 emission (Szkody 1987). Note, however, that the IP HT Cam has a spectral appearance very similar to CW Mon, and an increased white dwarf spin pulse amplitude during outburst (Kemp et al. 2002).

Magnetic systems are not specifically dealt with in the population model used in the next section (this is the same model used in Chapter 3), and may evolve differently from non-magnetic CVs, as has already been noted. The magnetic CVs HZ Pup and VV Pup are therefore excluded from the observed sample. CW Mon is also excluded from the sample, despite the evidence for its magnetic nature not being compelling, because (in view of it being a long-period system) excluding it is a conservative choice. The conclusion regarding the ratio of long- to short-period CVs that will be derived in Section 4.6 would be even stronger had it been included in the sample.

As in Chapter 3, systems with $P_{orb} > 5\,\mathrm{h}$ are also excluded from both the model (see Section 4.5) and observed populations, since CVs with evolved secondaries probably dominate the population at these periods (see Section 2.8.6).

Therefore VV Pup, HZ Pup, CW Mon, and Hα074208 are not considered further. The entries for these 4 systems are given in italics in Table 4.5. The rest of the sample (17 CVs, of which at least 10 are long-period systems) likely consists of non-magnetic, unevolved CVs. There is no indication that any of these CVs are period bouncers.

4.5 Modelling selection effects

The computational method described in Chapter 3, specifically, model A1, with only a minor change to the SED calculation, is used again here to model the effects of the most important selection biases acting on the Hα-selected sample. A random sample of CVs is drawn from a predicted intrinsic CV population, and distributed in a model Galaxy. By modelling the SED and outburst properties of each CV, the observational appearance of this intrinsic population in a survey with the particular selection criteria of the new sample is predicted.

This Monte Carlo method is briefly outlined again in Section 4.5.1 below. It does not account for all the selection biases present in the sample. In Section 4.5.2, the assumptions that were made to deal with the remaining biases are discussed.

4.5.1 The Monte Carlo code

The Monte Carlo calculation uses as input a probability distribution function (PDF) for the present-day population of CVs over the parameters P_{orb}, $\langle \dot{M} \rangle$, M_1, and M_2. This PDF is taken from Kolb (1993). More information on the model population may be found in Section 3.2.1.

The Galaxy is treated as an axisymmetric disc with a Galactic Centre distance of 7 620 pc (Eisenhauer et al. 2005), a radial scalelength of 3 000 pc, and vertical scaleheights of 120, 260, and 450 pc for long-period CVs, pre-period minimum short-period CVs, and period bouncers, respectively. The assumption of different scaleheights for these three sub-populations of CVs is motivated by their different typical ages (see Section 3.2.2).

Flux from the accretion disc, bright spot, white dwarf, and secondary star is considered in the model of the overall SED of each CV in the simulation, with all except the secondary treated in the same way as in Chapter 3 (a description of the SED model for the disc, bright spot, and white dwarf may be found in Section 3.2.3). The flux contribution of the secondary star is obtained from the semi-empirical donor sequence of Knigge (2006)[7]. I emphasize again that none of the results in either this or the previous chapter would change if the relation of Smith & Dhillon (1998) was used here, or if the Knigge (2006) donor sequence was used before. This is because the secondary flux contribution in the optical is not very important in the model SEDs.

The only type of variability included in the model is DN outbursts. The modelling of outbursts relies on the well known empirical relation between P_{orb} and the luminosity of DNe at maximum (Warner 1987; Section 3.2.4 gives a more complete discussion).

The R and I magnitudes produced by the SED model are on the Kron–Cousins RI system, and were transformed to the photographic system of the SHS survey using Morgan & Parker (2005) and Bessell (1986). The differences between the photometric systems are small, especially compared to uncertainties in the SED model and photometric errors in the SHS data.

Model CVs satisfying $R < 17$ and $|b| < 10°$ are then selected. Fig. 4.12 shows the differential and cumulative apparent magnitude distribution, as well as the P_{orb} distribution, of the CV population predicted to be observed in this survey, if other selection cuts are neglected. The grey histogram in the top panel is the R distribution of the 17 observed CVs. The inset shows the cumulative R histograms of the model (black) and real samples (grey). A KS test gives the probability of the model and observed R distributions being drawn from the same parent population as 0.35, implying that the magnitude distributions are consistent. In the bottom panel, the bold histogram is the model P_{orb} distribution of all systems detected; the contribution of period bouncers is shaded in dark grey, and the fine black histogram shows the distribution of outbursting DNe expected in a single-epoch survey. The model histograms are scaled as described in Section 4.6.2 below.

[7]The high-resolution version of the donor sequence was interpolated onto the period grid of the model CV population, where possible. The upper edge of the model period gap is slightly above the observed location. The model period gap is also narrower than observed, so that the empirical sequence had to be extrapolated at the lower edge of the gap.

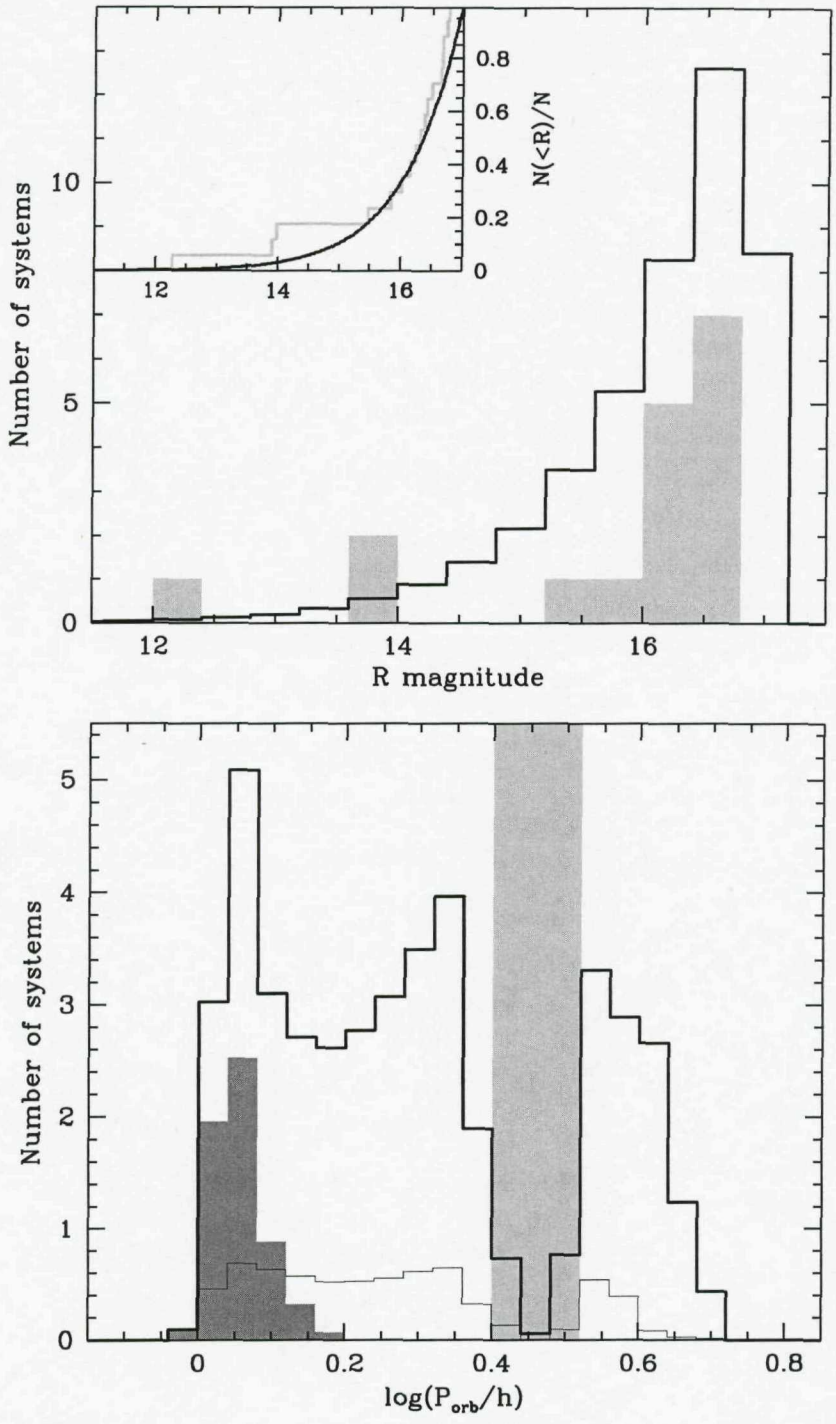

Figure 4.12: The differential and cumulative magnitude distributions, as well as the differential orbital period distribution, predicted by the simulation. The bold histograms in all three panels are the distributions of all systems predicted to be detected, with only the flux limit and $|b|$ constraint imposed. The R and cumulative R distributions of the 17 observed systems are also shown, in light grey, in the top panel and in the inset to the top panel. In the bottom panel, the contribution of period bouncers to the orbital period distribution is shaded in dark grey, and the fine histogram shows DNe that are found in outburst in a single epoch. The model R and P_{orb} distributions are scaled as described in Section 4.6.2.

4.5.2 Additional biases

The above modelling accounts for the effects of the magnitude limit, and the restriction of the survey to the Galactic plane. With only those selection effects included, the predicted period distribution is inconsistent with the observations (relatively too many short-period CVs are predicted). However, whether the remaining selection effects present in the sample could reconcile the predicted and observed distributions still needs to be determined. Therefore, conservative assumptions about the influence of these biases (i.e. assumptions that decrease the predicted ratio of short- to long-period CVs) are made.

4.5.2.1 The EW(Hα)-dependent selection cut

The dependence of selection probability on EW(Hα) is not included in the model. This is because the disc models predict EWs that are clearly too small (as demonstrated for Hβ by Patterson 1984; this is also true for Hα). The alternative of using an empirical relation is not available, because the dependence of EW(Hα) on, e.g., M_V is not known. One may expect that including this selection cut in the model would increase the predicted ratio of short- to long-period CVs, and therefore that not accounting for it is a conservative assumption.

Whether an object is selected as a target depends on its $R - \mathrm{H}\alpha$ and $R - I$ colours. The $R - I$ dependence arises from the non-zero slope of the stellar locus in the $R - \mathrm{H}\alpha$ vs $R - I$ plane. It is also likely that the selection probability depends on R magnitude, since the photometric uncertainty increases at fainter magnitudes. While the CV sample does not at first sight appear to be increasingly incomplete at fainter R, the sample of all emission line objects from the spectroscopic follow-up certainly is magnitude biased, with an R distribution that flattens off at around $R = 16$. The reason that the CV sample is not affected by the same magnitude bias as the overall emission line sample is not because CVs have systematically stronger Hα lines than other types of emission line objects selected for follow-up, but because the CVs are on average bluer in $R - I$. The selection technique used here is sensitive to faint objects with small EWs only if those objects are sufficiently blue in $R - I$. Redder faint objects must have stronger lines in order to be selected. The upper panel of Fig. 4.13 shows R as a function of $R - I$ for all the emission line objects targeted by the follow-up observations, while the lower panel shows EW(Hα) as a function of $R - I$ only for targets with $16 < R < 17$. The data for CVs are plotted as larger symbols. These plots illustrate that CVs are amongst the bluest faint emission line objects. Most of the faint objects with red $R - I$ and small EW(Hα) are M stars with strong molecular absorption bands.

To the extent that data can provide a guide, the resulting blue bias does not matter—intrinsically fainter, redder CVs have stronger emission lines. This is well established for normal short-period CVs, but observational information on period bouncers is scarce. There are now two confirmed period bouncers, namely SDSS J103533.03+055158.4, and SDSS J150722.30+523039.8 (Littlefair et al. 2006, 2007; Patterson et al., in preparation)

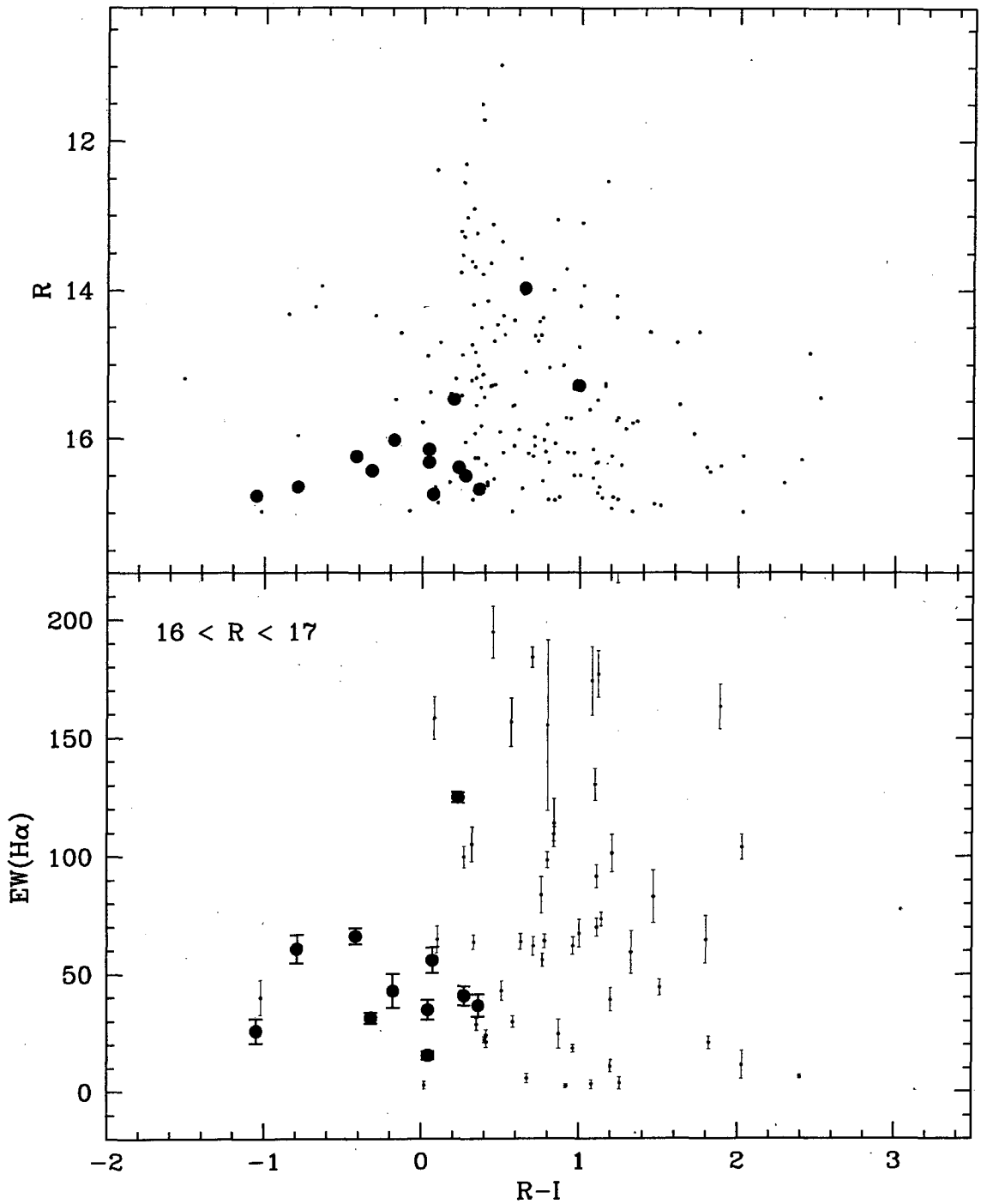

Figure 4.13: Upper panel: a colour–magnitude diagram for all the emission line targets found in the spectroscopic follow-up. Lower panel: EW(Hα) as a function of $R-I$ for emission line objects fainter than $R = 16$. CVs are plotted as larger symbols in both panels. CVs are systematically bluer than the complete emission line sample, but do not have systematically large EW(Hα). The majority of objects with EW(Hα) < 20 Å and $R - I > 1$ were selected because they have strong molecular absorption features and thus large $R -$ Hα.

and they have $EW(\mathrm{H}\alpha) = 44$ Å and 78 Å, and $R-I$ of 0.03 and 0.04, respectively (Szkody et al. 2005; Szkody et al. 2006; colour transformations from Jester et al. 2005). The selection technique is easily capable of identifying objects with these EWs and colours near $R = 17$.

In the absence of an undetected population of faint, red CVs with weak emission lines, the EW cut thus preferentially excludes intrinsically bright (i.e. long-period) CVs.

4.5.2.2 Variability

DNe in outburst probably have smaller EW(Hα) as a rule. This is certainly true for Hβ (Patterson 1984), and likely also for all Balmer lines (see, e.g., Hassall et al. 1983, and also the spectra in Fig. 5.5 in the next Chapter, which show that the EWs of Hα, Hβ, and Hγ are reduced during a DN outburst). This means that an outbursting DN is less likely to be identified in an Hα survey than a quiescent system. The problem here is slightly more complicated than whether a system has sufficiently large EW(Hα) at a single epoch, since observations in the three wavebands used in the selection were not taken simultaneously. Variability between the epochs of the R, I, and Hα observations can lead both to an object with Hα emission not being selected, and to an object without Hα emission being targeted. The most common large amplitude variability displayed by CVs is DN outbursts, and only this type of variability will be considered. Out of the 175 fields used in the selection, only 72 were observed in R and Hα on the same night; all I-band data were taken roughly 20 years earlier.

A system that is bright in both R and Hα but faint in I will probably be selected, because it will be very blue in $R-I$ (V383 Vel is an example—it was observed in outburst in R and Hα on the same night, but was faint during the I epoch). CVs are likely to be missed by the selection because of variability if they are bright in R and faint in Hα, or bright only in I. It is assumed here that the probability of a long-period system being excluded for reasons of variability is 0 (despite the fact that many long-period systems are DNe), and that the probability of a short-period system being excluded for being bright in R, is equal to C (the outburst duty cycle). Then, to allow for the possibility of a DN being bright in I, this is repeated with the remaining short-period DNe (i.e. a fraction of systems equal to the particular outburst duty cycle is excluded from the population predicted to be detected in the survey).

4.6 Comparison to theory

4.6.1 Relative numbers of short- and long-period CVs

After applying the cuts involving R, $|b|$, and variability described above, the sample is predicted to contain 13% period bouncers (i.e. about 2 systems in the sample of 17), whereas none are detected. This is not a serious discrepancy. The predicted fraction of long-period CVs is 30%. Assuming that the combined EW and $R-I$ cut makes it impossible to detect period bouncers, 34% of the sample is predicted to be long-period

systems. Using the binomial distribution, the probability that the observed ratio of at least 10/17 is consistent with this prediction is 0.031. The model is therefore inconsistent with observations at more than 2-σ.

The inconsistency would be a 3-σ result if two more systems in the sample had periods above the period gap. It is likely that this will prove to be the case. The spectrum of Hα190039 is characteristic of an intrinsically bright CV, and there is reason to suspect that Hα075648 is an SW Sex star.

4.6.2 Space density

This sample is not suitable for measuring the CV space density (ρ), but it can be compared to a specific prediction to verify whether the predicted and observed numbers of CVs are in reasonable agreement. de Kool (1992) and Kolb (1993) theoretically predict $\rho \sim 10^{-4}$ (see Section 2.7 for other theoretical values), with 1% of all CVs above the period gap. The space density of long-period CVs (ρ_l) is then predicted to be $\sim 10^{-6}\,\mathrm{pc}^{-3}$.

Setting $\rho_l = 10^{-6}\,\mathrm{pc}^{-3}$ in the simulation, about 22 long-period CVs should be detected if the sample really is 15% complete (with the area coverage and flux limit of the survey). This assumes that the only selection cut affecting long-period CVs is the magnitude limit and $|b|$ restriction. The sample contains at least 10 long-period CVs, perhaps as many as 14. The total number of observed long-period CVs is then consistent with the prediction if the true completeness for long-period systems is $\simeq 8\%$. This is entirely reasonable, especially since a bias against long-period CVs is expected, but given the uncertain completeness, it is not a very secure result[8].

The predicted R and P_{orb} histograms in Fig. 4.12 were scaled to reflect the number of CVs that should have been detected in this survey ($2\,800\,\mathrm{deg}^2$, $|b| < 10°$, and $R < 17$) if $\rho_l = 10^{-6}\,\mathrm{pc}^{-3}$, and if the survey is 8% complete, with no dependence of completeness on P_{orb}.

4.6.3 Evolutionary time-scales

It is usually assumed that the theoretical ratio of the number of short- to long-period CVs is larger than observed because theory predicts too large a population of short-period CVs. Several solutions to this problem have been proposed (see Section 2.8). The suggestion that there is an angular momentum loss mechanism that increases the absolute value of $\dot{J}$ in short-period CVs above that of the rate resulting from gravitational radiation ($\dot{J}_{GR}$) is considered here (see e.g. Patterson 1998, 2001; King et al. 2002; Patterson et al. 2003; Barker & Kolb 2003; more information may be found in Section 2.8.1). Higher $-\dot{J}$ below the period gap decreases the evolutionary time-scale of short-period CVs and therefore reduces the total number of CVs in this evolutionary phase[9].

[8]The available observational estimates of ρ_l are $\sim 2.5\times10^{-6}$ (Patterson 1998) and $\simeq 8\times10^{-6}$ (Chapter 5; note, however, that this value is expected to be high, since it is almost entirely based on a single system with unusually low L_X).

[9]Patterson (1998) also points out that a population synthesis model using such a higher $-\dot{J}$ could predict the position of the period minimum correctly, and would fit the observed relation between ϵ and

The evolutionary time-scale of a CV is

$$\tau \simeq \left\langle \frac{J}{-\dot{J}} \right\rangle \simeq \left\langle \frac{M_2}{\dot{M}} \right\rangle$$

where the angle brackets denote the secular average. Assuming that all CVs form at periods above $\simeq 5$ h, and only evolve through the period ranges considered, the number of CVs that exist in some particular period interval is proportional to the time CVs spend in that interval. The ratio of the numbers of long- and short-period CVs is therefore proportional to the ratio of their evolutionary time-scales (τ_l and τ_s for long- and short-period CVs, respectively).

The ratio of long- to short-period CVs observed in a survey for which the most important bias is a flux limit, can be written as

$$\left(\frac{n_l}{n_s}\right)_{obs} = f(\tau_l/\tau_s)\left(\frac{\tau_l}{\tau_s}\right). \tag{4.3}$$

Here, $f > 1$ is a monotonically decreasing function of τ_l/τ_s, since apparent brightness depends on accretion luminosity, which in turn scales inversely with τ. The form of f means that, by comparing the observed and predicted number ratios, a limit can be set on the true ratio of evolutionary time-scales of CVs above and below the period gap. Using equation 4.3, this ratio can be written as

$$\frac{\tau_l}{\tau_s} = \left(\frac{\tau_l}{\tau_s}\right)_{pred}\left[\frac{f((\tau_l/\tau_s)_{pred})}{f(\tau_l/\tau_s)}\right]\left[\frac{(n_l/n_s)_{obs}}{(n_l/n_s)_{pred}}\right], \tag{4.4}$$

where $(\tau_l/\tau_s)_{pred}$ is the predicted ratio of the evolutionary time-scale of long-period CVs to the evolutionary time-scale short-period CVs. I assume that the reason for finding $(n_l/n_s)_{obs} > (n_l/n_s)_{pred}$ is that $\tau_l/\tau_s > (\tau_l/\tau_s)_{pred}$. The monotonic nature of f then implies that $f((\tau_l/\tau_s)_{pred}) > f(\tau_l/\tau_s)$, so that

$$\frac{\tau_l}{\tau_s} > \left(\frac{\tau_l}{\tau_s}\right)_{pred}\left[\frac{(n_l/n_s)_{obs}}{(n_l/n_s)_{pred}}\right]. \tag{4.5}$$

Physically, this inequality holds because any adjustment to the predicted evolutionary time-scales that causes the short-period phase to be shorter relative to the long-period phase will also make short-period CVs brighter relative to long-period systems (and therefore less under-represented in a flux-limited sample[10]). The impact of such a time-scale adjustment on the predicted number ratio in a flux-limited sample is therefore always smaller than on the intrinsic number ratio.

To be more specific, I assume $(\tau_l)_{pred} = \tau_l$. Then, for this survey, with $(n_l/n_s)_{pred} \simeq 3/7$ and $(n_l/n_s)_{obs} \geq 10/7$, the model evolutionary time-scale of short-period CVs must be decreased by $\gtrsim 3$ to match the observations. Or, equivalently, $-\dot{J} \gtrsim -3\dot{J}_{GR}$ for short-

P_{orb} (or between q and P_{orb}) better than models assuming only gravitational radiation.

[10]The EW cut will not select against short-period CVs, unless their luminosity becomes similar to that of long-period CVs—this means an increase by $\gtrsim 10$.

period CVs is required in order to bring theory and observations into agreement. This factor of at least 3 would be an underestimate if the EW-based selection cut discriminates strongly against long-period CVs.

4.7 Summary and discussion

The aim of this study was to construct a new CV sample with uniform selection criteria. I discovered 16 CV candidates amongst 460 objects selected from the AAO/UKST SuperCOSMOS Hα Survey for Hα emission, and obtained additional observations for 14 of these systems, confirming their CV nature. Orbital periods were measured for 11 of the new CVs. All of these are long-period systems, and most have orbital periods in the range 3 to 4 h. There are two eclipsing systems in the sample, and one in which a quasi-periodic modulation on a $\sim 1\,000$ s time-scale was observed. The orbital periods and other properties of the new CVs are summarized in Table 4.1. Note that 6 of these periods were determined from aliased radial velocity curves, and may therefore only be correct to within $\sim 10\%$ (the quoted errors are for the strongest alias only).

Given the orbital periods of the new CVs, it is likely that many of them are SW Sex stars. Specifically, there is reason to suspect that Hα073418, Hα094409, Hα075648, and Hα122105 are SW Sex stars, but confirmation is needed for all of them. Hα075648 and Hα122105 are unusual in displaying large variations in line profiles, which prevented the measurement of orbital periods. Hα073418, Hα094409, Hα102442, and Hα163447 have been observed to display large amplitude variability. The blue, weak-lined spectra of Hα092751 and Hα112921 imply that they are very likely both NLs. The secondary star is detected in the spectrum of Hα074208. A spectral type of M0 $\pm$ 1 is measured, and it is estimated that the secondary contributes between 40 and 80% of the flux in the wavelength range from $\simeq 5\,700$ to $\simeq 7\,200$ Å.

The new CVs were combined with previously known systems recovered in the survey to define a homogeneous sample of 17 non-magnetic, unevolved CVs. Although the bright flux limit implies that the sample is biased against intrinsically faint CVs, there is no explicit second selection cut that compounds this bias (but note that there may be an effective $R - I$ cut). It is also the largest Hα-selected CV sample constructed to date.

Despite the very conservative assumptions outlined in Section 4.5.2, the model CV population and the observed sample do not agree. The result regarding the CV period distribution of Chapter 3 is thus confirmed with an independent observational sample. Standard CV evolution theory predicts too large a ratio of short- to long-period CVs. This is true even with the assumption that period bouncers are undetectable.

The data presented here cannot determine whether $(\tau_l)_{pred}$ is too short or $(\tau_s)_{pred}$ is too long. However, the favoured explanation for the large predicted ratio of short- to long-period CVs is that short-period systems evolve faster than predicted by the disrupted magnetic braking model, so that the predicted population of short-period CVs is too large (the motivation for preferring this explanation include the position of the period minimum

and the shape of the ϵ–P_{orb} relation; e.g. Patterson 1998, 2001; Patterson et al. 2003; see also Section 2.8.1). Using the Hα sample, I find that the evolutionary time-scale of short-period CVs in the model should be decreased by a factor of at least 3 in order for the model to agree with observations (if the predicted evolutionary time-scale of long-period CVs is correct).

Before an Hα-selected CV sample can be used to place tighter constraints on CV evolution, EW(Hα) must be modelled in terms of the parameters describing CVs in a theoretical population. It is known that the EWs of disc emission lines increase with decreasing luminosity. However, CV discs are observed together with a white dwarf primary. Very faint systems are white dwarf dominated (i.e., the continuum emission from the disc is low relative to that from the white dwarf). Also, the disc emission lines are superimposed on the absorption lines of the white dwarf. Therefore, at faint luminosity, the relation between EW and M_V is expected to flatten off (Patterson 1984 plots EW(Hβ) vs the estimated absolute magnitude of the disc alone; his relation therefore does not show this effect). This is observationally clear from the spectra of the faintest known CVs, and has already been remarked on by Aungwerojwit et al. (2006). Although the decrease of EW(Hα) at very faint M_V is expected to be less severe than that of EW(Hβ), this might ultimately place a limit on what can be achieved by an emission line survey.

The comparison of this CV sample to theory is also complicated by the possibility of variability between non-simultaneous observations in the three wave-bands used for the selection. Surveys such as IPHAS will overcome this difficulty, and provide deeper, larger samples. IPHAS will also provide much better photometric accuracy than can be achieved photographically, so that the photometry will allow for the identification of objects with smaller EWs in all parts of the colour-colour plane; any blue bias will therefore be weaker (see Drew et al. 2005; Witham et al. 2006, 2007, 2008). Furthermore, the emission line samples constructed from IPHAS data will be much deeper. This is very important, since a selection technique capable of identifying intrinsically faint CVs is of limited value in a survey with a bright flux limit. The main challenge for IPHAS will be the amount of observational effort needed to finish the identification and follow-up of the CV sample. The same is true for other large, deep surveys—the completion of the resulting new CV samples is still some time in the future.

In the meantime, it is already possible to recognize the qualitative changes that are needed to reconcile theory with observations, using smaller CV samples, such as the one constructed here.

4.8 Conclusions

I have constructed a homogeneous sample of 17 non-magnetic CVs with unevolved secondary stars, selected for Hα emission. The sample has a bright flux limit, but contains no explicit blue- or variability-based selection cut.

This new sample was compared to a model CV population, based on standard CV

evolution theory. The magnitude limit and Galactic latitude range of the observed sample was modelled in some detail, while conservative assumptions were made to account for the effects of variability and the EW(Hα)-based selection cut. The model population is inconsistent with the observed sample. Specifically, the model predicts relatively too many short-period CVs. This confirms earlier results, based on independent observations.

The reason for the mismatch between the predicted and observed ratio of short- to long-period CVs is probably mainly that the theoretical evolutionary time-scale for CVs below the period gap is too long. A very simplistic consideration of the relative numbers of long- and short-period CVs included in the sample indicates that the disrupted magnetic braking model underestimates $-\dot{J}$ of short-period CVs by a factor of at least 3, assuming that the model is correct for long-period CVs.

It is clear that the standard magnetic braking model is in need of revision. Furthermore, it seems that the correct approach to take is to investigate angular momentum loss rates in excess of the gravitational radiation rate in CVs below the period gap.

Chapter 5

Constraints on the space density of cataclysmic variables

5.1 Introduction

Quantitative constraints on the key parameters predicted by CV formation and evolution scenarios are necessary for progress to be made in the theoretical understanding of the subject. The most fundamental of these parameters is the overall space density of CVs, ρ. Some existing observational estimates of ρ were listed in Section 2.7. These differ by more than an order of magnitude, and little effort has been made to quantify the uncertainties affecting these estimates. Such measurements are of very limited value in constraining theory.

In order to understand the uncertainties in estimates of ρ, it is useful to take a closer look at some of the more extreme values in the literature. Cieslinski et al. (2003) suggested a very low space density of $\rho \leq 5 \times 10^{-7}\mathrm{pc}^{-3}$ for dwarf DNe, the most common type of CV. This result was based on DN outbursts detected in the OGLE-II survey, and assumes that essentially all DNe in the OGLE-II fields within 1 kpc had been detected. However, the time coverage of the survey ($\simeq 4$ yr) was much shorter than the longest DN recurrence time-scales, and long inter-outburst intervals are known to be associated precisely with the intrinsically faintest CVs that probably dominate the overall population. At the other end of the spectrum, Shara et al. (1993) obtained a quite high estimate of $\rho \sim 10^{-4}\mathrm{pc}^{-3}$ from a photometric survey for faint CVs, but here the CV nature of the objects that were counted was never established. Finally, Schwope et al. (2002) obtained $\sim 3 \times 10^{-5}\,\mathrm{pc}^{-3}$ from a CV sample constructed from the *ROSAT* Bright Survey. However, this number was primarily based on two systems with estimated distances of ~ 30 pc, both of which were subsequently shown to be 5 to 10 times more distant (Thorstensen et al. 2006).

These examples illustrate that the statistical errors associated with observational space density estimates are usually dominated by uncertain distances and small number statistics, whereas the dominant systematic errors are caused by selection effects (or, equivalently, by a misunderstanding of the completeness of a given sample). It also seems likely

that the hard-to-quantify systematic uncertainties usually outweigh the statistical errors, which might explain why very few space density estimates in the literature have come with error estimates.

An attribute that should be shared by all CVs is X-ray emission generated in the accretion flow. This is useful, because it is much easier to construct a reasonably deep flux-limited CV sample in X-rays than it is in the optical. For an optical sample, it is usually necessary to cut down on the number of sources that will be followed up, by introducing additional selection criteria based on, e.g., colour, variability, or emission lines; any such selection makes it more difficult to model the completeness of the resulting sample. Another advantage of an X-ray flux-limited sample is that the ratio of X-ray to optical flux (F_X/F_{opt}) decreases with increasing P_{orb} (i.e. with increasing optical luminosity; e.g. Patterson & Raymond 1985a; van Teeseling & Verbunt 1994; van Teeseling et al. 1996). This means that CVs do not span as wide a range in X-ray as in optical luminosity.

The *ROSAT* North Ecliptic Pole (NEP) survey (e.g. Gioia et al. 2003; Henry et al. 2006) is constructed using *ROSAT* All Sky Survey (RASS; see Voges et al. 1999, 2000) data around the north ecliptic pole; the RASS reaches its greatest sensitivity in this $81\,\mathrm{deg}^2$ region, centred on $\alpha_{2000} = 18^{\mathrm{h}}00^{\mathrm{m}}$, $\delta_{2000} = +66°33'$. The NEP survey is thus the deepest ever X-ray observation over a wide-angle, contiguous region; it consists of a complete sample of 442 sources above a flux of about $10^{-14}\,\mathrm{erg\,cm^{-2}s^{-1}}$ in the 0.5 to 2.0 keV band. The flux limit varies from 1.2×10^{-14} to $9.5 \times 10^{-14}\,\mathrm{erg\,cm^{-2}s^{-1}}$ over the survey area (assuming a 10 keV thermal bremsstrahlung spectrum; this choice is justified in Section 5.3). The NEP survey flux limit map is shown in Fig. 5.1. The structure of this map is produced mainly by satellite scan restrictions. The 2° diameter field of view of the *ROSAT* Position Sensitive Proportional Counter (PSPC) corresponds roughly to the $\simeq 2\,\mathrm{deg}^2$ region of maximum depth surrounding the NEP.

The unique combination of depth and breadth of the NEP survey, together with moderate Galactic latitude and extinction, provides an excellent opportunity to investigate the space density of CVs. Very importantly, out of the 442 X-ray sources included in the survey, all but 2 (the number of spurious sources expected in a sample such as this; Gioia et al. 2003) have been optically identified and spectroscopically observed. Therefore, a complete, purely X-ray flux-limited CV sample can be constructed from the NEP survey.

Thanks to the very simple, well-defined selection criteria of this CV sample, it does not suffer from unquantifiable systematic errors. Therefore it is possible to provide meaningful errors on ρ that fully account for small number statistics and uncertain distances. Here I estimate ρ, using the observed sample of CVs in the NEP survey, and place upper limits on the size of a hypothetical population of CVs with X-ray luminosities low enough to evade the survey entirely. I also present radial velocity studies of the two new CVs discovered in this survey.

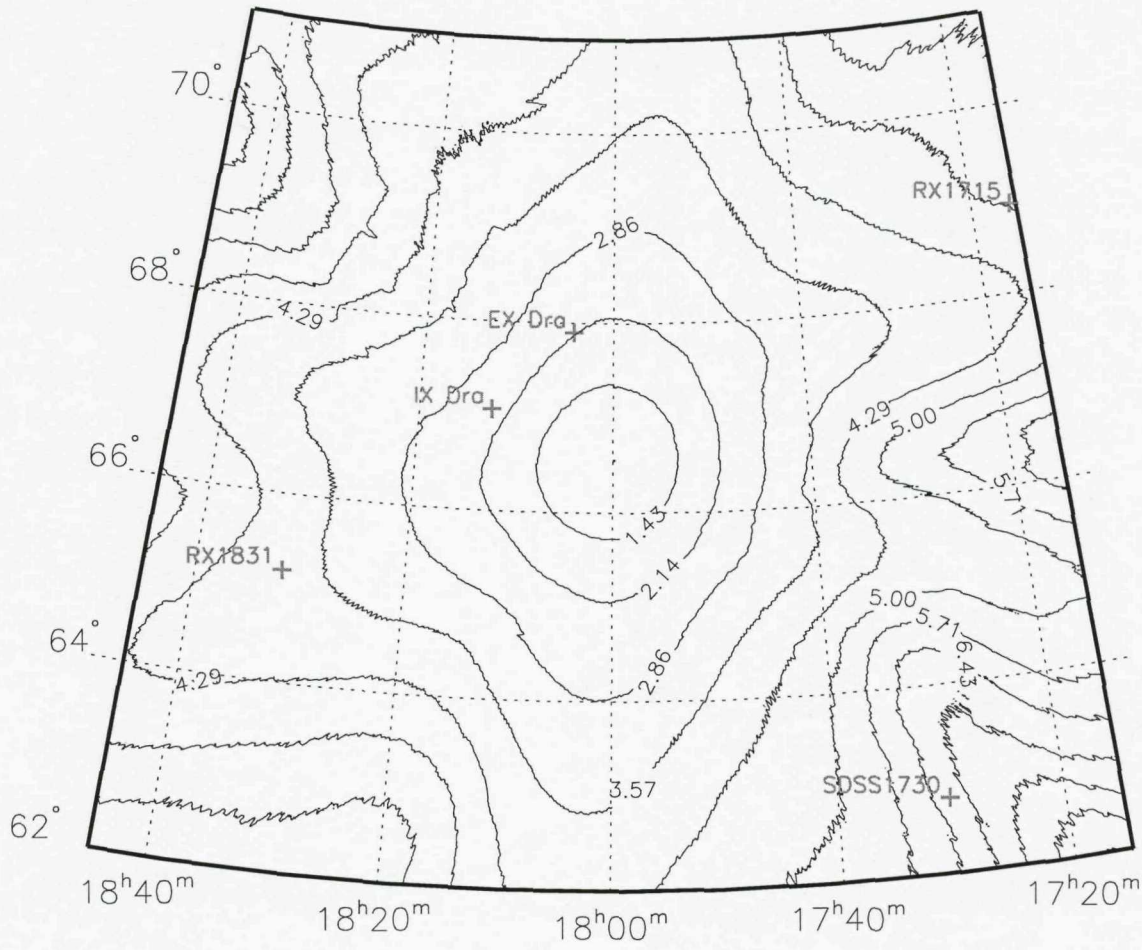

Figure 5.1: The NEP survey flux limit map. This is obtained from the two-dimensional survey selection function, which is based on count rate, by assuming a 10 keV thermal bremsstrahlung spectrum. The contour levels are labelled in units of $10^{-14}\,\mathrm{erg\,cm^{-2}s^{-1}}$. Further details on the construction of the selection function may be found in Henry et al. (2006). The positions of the five CVs in the NEP area are indicated. This figure was made using data provided by Isabella Gioia.

5.2 CVs in the *ROSAT* North Ecliptic Pole Survey

The NEP survey area includes three known CVs, namely IX Dra, EX Dra, and SDSS J173008.38+624754.7 (abbreviated here to SDSS J1730). All three were detected in the RASS, but IX Dra is slightly too faint to be formally included in the NEP sample.

Inspection of the optical spectra of all Galactic NEP sources led to the discovery of only two additional objects with the spectral appearance of interacting binaries. A more detailed study of stellar sources included in the survey has yielded accurate spectral classifications of all stellar NEP sources (Micela et al. 2007), and no additional CV candidates. Therefore, every CV in the NEP sample has been identified.

The two interacting binary candidates are RX J1715.6+6856 and RX J1831.7+6511, and were confirmed as CVs by the follow-up observations described below. Fig. 5.2 gives finding charts for the two newly discovered CVs; their coordinates are listed in Table 5.1.

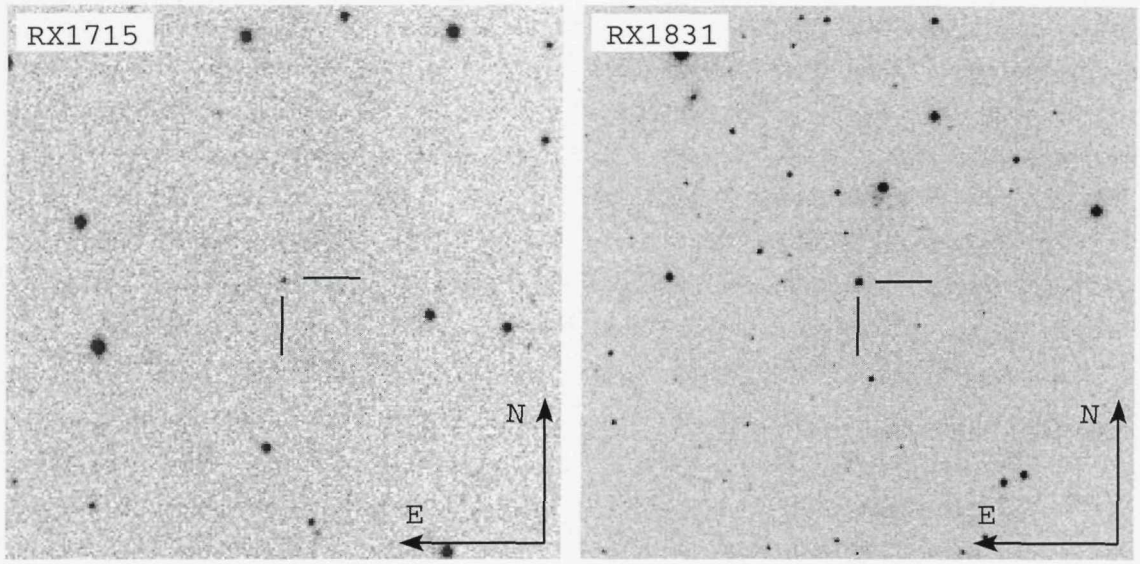

Figure 5.2: $4' \times 4'$ finding charts of the optical counterparts of RX J1715.6+6856 (left) and RX J1831.7+6511 (right), made using white light acquisition images taken with CAFOS. North is at the top and east to the left in both images.

Table 5.1: Log of the observations, and coordinates for the optical counterparts of the two X-ray sources. t_{int} is the integration time.

Object	α_{2000}	δ_{2000}	Date (start of night)	First integration HJD 2453900.0+	Grism	t_{int}/s	No. of spectra
RX J1715.6+6856	17:15:41.7	+68:56:43	2006 Jul 27	44.36780950	B-200	1 000	7
			2006 Jul 28	45.37354850	G-100	1 000	14
			2006 Jul 29	46.35562975	G-100	800	9
RX J1831.7+6511	18:31:44.4	+65:11:32	2006 Jul 27	44.51118822	G-100	600	16
				44.66093472	B-200	600	2
			2006 Jul 28	45.59054418	G-100	600	10
			2006 Jul 29	46.47792121	G-100	600	22

Gioia et al. (2003) report photographic magnitudes of $E = 18.6$ and $O = 18.3$ for RX J1715.6+6856, and $E = 14.8$ and $O = 15.2$ for RX J1831.7+6511 (the errors in these measurements are ± 0.5 mag; O and E are similar to Johnson B and Kron–Cousins R, respectively).

5.2.1 Observations of the newly discovered CVs

In order to confirm that RX J1715.6+6856 and RX J1831.7+6511 are CVs, and to measure their orbital periods, I obtained medium-resolution, time-resolved spectroscopy with the Calar Alto Faint Object Spectrograph (CAFOS) on the Calar Alto 2.2-m telescope. Table 5.1 gives a log of the observations. The G-100 grism was used in combination with a slit width of $1\farcs2$, yielding a spectral resolution of $\simeq 4.2$ Å over the wavelength range 4 300 to 8 000 Å. A few spectra of each object were also taken using the B-200 grism, and a slit width of $1\farcs5$. These spectra have lower resolution ($\simeq 9.4$ Å) and were not used for radial

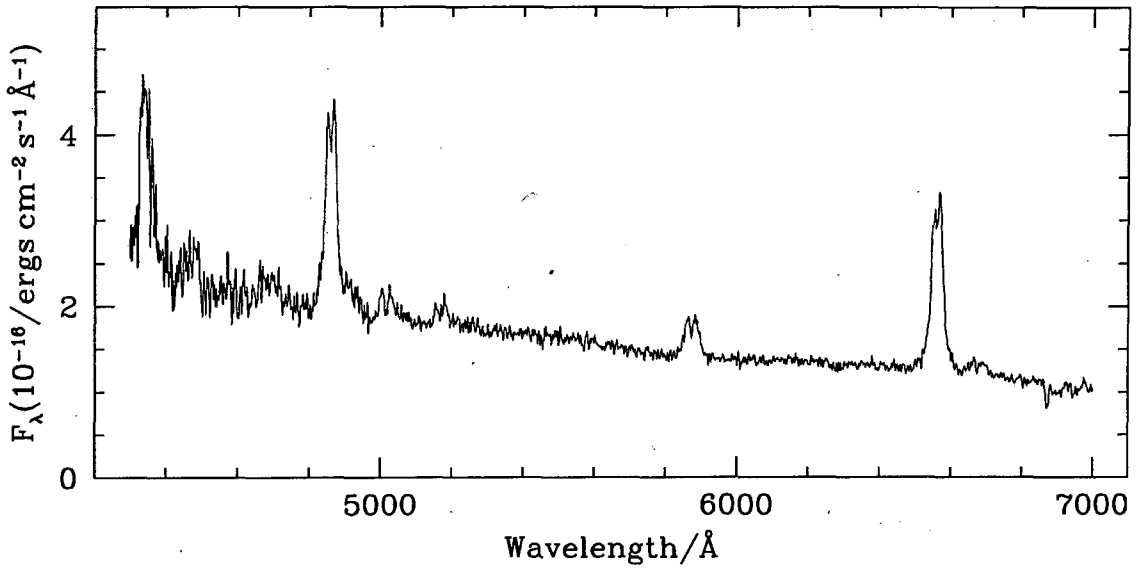

Figure 5.3: The average of all the spectra of RX J1715.6+6856 taken with the G-100 grating. Individual spectra were shifted to the rest frame using the radial velocities calculated from the Hα line before being averaged. The system is identified as a CV by its broad, double-peaked Balmer, He I, and He II emission lines. Also present is the Fe II λ5169 line.

velocity measurements. Regular arc lamp exposures were taken to maintain an accurate wavelength calibration. The spectrophotometric standard star BD+28°4211 (Oke 1990) was observed on all three nights to provide flux calibration. Except for the first hour of the first night, conditions were photometric during the observations.

The data were reduced using standard procedures in IRAF, as described in Chapter 4. Radial radial velocities of both the Hα and Hβ lines were measured by means of a cross-correlation with a template spectrum, using FXCOR. This method produced satisfactory results for all the data. In the case of the Hα line, the wavelength range 6 450 to 6 650 Å was correlated, while for the measurements of Hβ radial velocities, the correlation was restricted to the range from 4 700 to 5 020 Å. For both RX J1715.6+6856 and RX J1831.7+6511, the Hα line yielded higher S/N radial velocity curves; therefore, the radial velocities measured for this line are used in determining the orbital periods.

5.2.1.1 Observational results for RX J1715.6+6856

Radial velocity measurements for RX J1715.6+6856 were obtained on only two nights. The average spectrum, shown in Fig. 5.3, displays broad, double-peaked Balmer and He I emission lines superimposed on a blue continuum; He II λ4686 and Fe II λ5169 are also detected in emission. The system has the spectral appearance of a quiescent DN. No large amplitude brightness variations were evident in the data, and $V = 18.3 \pm 0.2$ is estimated from the spectroscopy (where the uncertainty is dominated by slit losses).

At $V = 18.3$, RX J1715.6+6856 is close to the magnitude limit of the telescope and instrument combination used, and the time resolution and base line of the data yield only

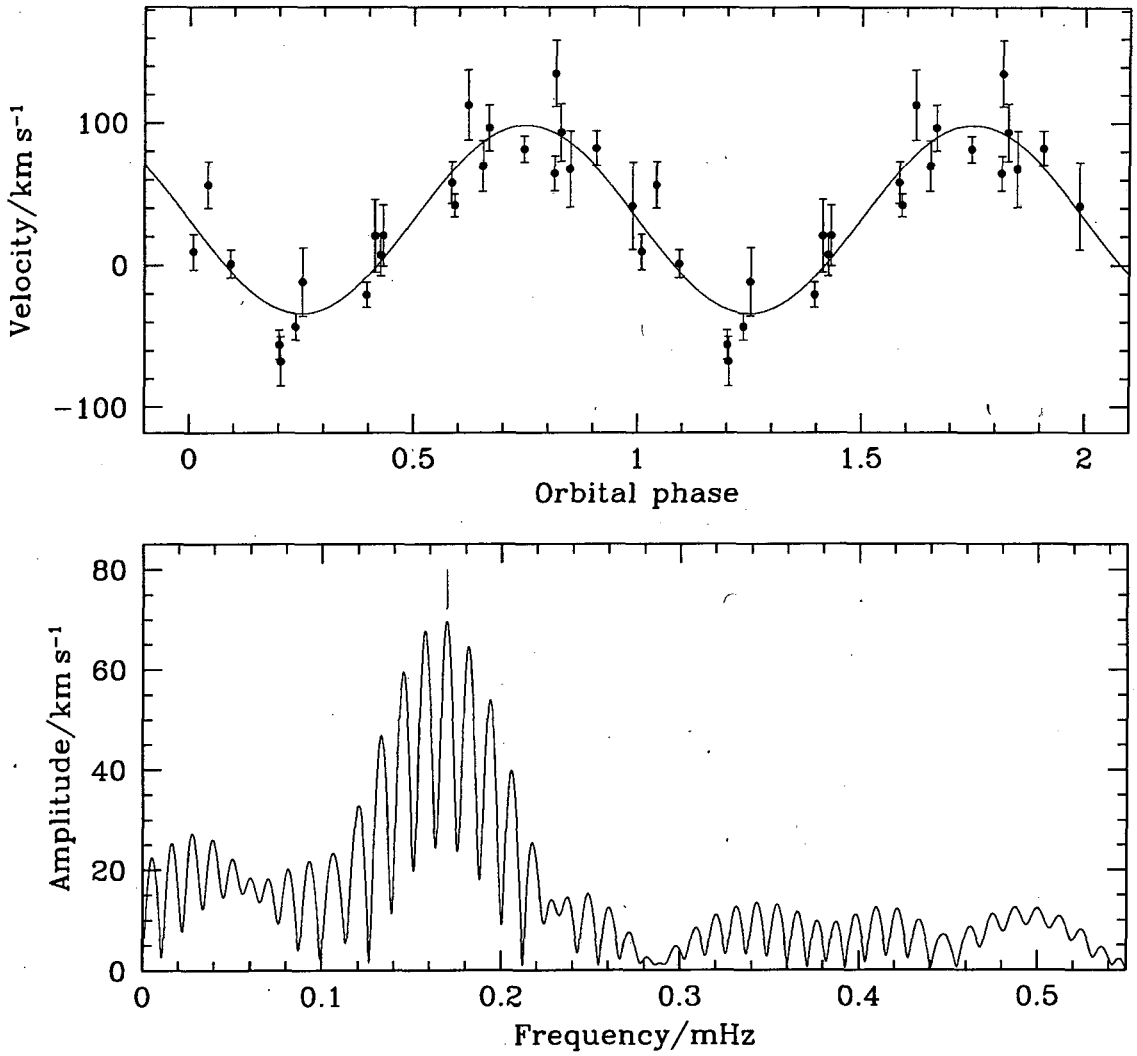

Figure 5.4: Lower panel: The Fourier transform of the Hα radial velocity curve of RX J1715.6+6856 obtained on 28 and 29 July 2006. A vertical bar at 0.1695 mHz (1.639 h) indicates the period that provides the best fit to the data. Upper panel: The radial velocity measurements, folded in the best-fitting period. One cycle is repeated in this plot; the superimposed sine function is a non-linear least-squares fit to the data.

a fairly uncertain period. The Fourier transform in Fig. 5.4 shows that the radial velocity curve is aliased; the largest amplitude signal is at 0.1695 mHz (corresponding to a period of 1.639 h), and is marked by a vertical bar in the lower panel of Fig. 5.4. The two nearest peaks are at 0.1575 and 0.1816 mHz. Sinusoids were fitted to the data by non-linear least-squares, using the periods and amplitudes of these three signals as starting values. The 1.639 h period provides a significantly better fit than the other aliases (the standard deviation of the residuals for a fit near this period is $\simeq$ 15 % lower than for either of the other choices). The 1.639 h period also yields the largest best-fit amplitude (66.1 km/s). Nevertheless, there is some uncertainty in the cycle count. Assuming that the correct alias has been identified, the orbital period is of RX J1715.6+6856 is 1.64 ± 0.02 h. The top

panel of Fig. 5.4 shows the radial velocities of Hα, phase-folded using this period, with the sine fit overplotted.

5.2.1.2 Observational results for RX J1831.7+6511

RX J1831.7+6511 was descending into a photometric low state over the three nights of observations, fading by roughly a magnitude in V. This was most likely the decline from a dwarf nova outburst. The spectra show fairly narrow Balmer and He I emission lines (the FWHM of the Hα line is $\simeq$ 800 km/s). The Hβ and Hγ line profiles change from broad absorption wings with emission cores in the bright state, to pure emission in the faint state. This transition is illustrated in Fig. 5.5, which displays nightly averages of the G-100 spectra after shifting to the rest frame using the radial velocities calculated from the Hα line. Fe II λ5169 is also detected in RX J1831.7+6511, increasing in strength as the system fades.

The lower panel of Fig. 5.6 shows a Fourier transform of the radial velocity curve of RX J1831.7+6511 (including all 3 nights of data). A vertical bar at 0.0693 mHz (4.01 h) indicates the highest amplitude signal, but there is also strong power present at the one-day aliases (0.0578 mHz and 0.0808 mHz). Non-linear least-squares fits of sine functions to the data produce the largest amplitude for the 4.01 h period; the standard deviation of the residuals is also roughly 45% larger for fits using the other two candidate periods. It is therefore very likely that the signal at 4.01 h represents the orbital modulation. The orbital period of RX J1831.7+6511 is then 4.01 ± 0.03 h. The top panel of Fig. 5.6 shows the Hα radial velocity curve, phase-folded using the orbital period, together with the best-fit sine function. The ampliude of the fit is 79.7 km/s.

5.2.2 Distance estimates

Several independent methods of estimating distances to CVs are discussed by Patterson (1984) and Warner (1987). Methods based on DN outburst maximum, the strength of emission lines, and the brightness of the secondary star will be used here.

The relation between orbital period and the absolute V magnitudes of DNe at maximum found by Warner (1987), as recalibrated by Harrison et al. (2004), is

$$M_{Vmax} = 5.92 - 0.383 P_{orb}/\mathrm{h}. \tag{5.1}$$

In this equation, M_{Vmax} is corrected for binary inclination (i) using

$$\Delta M_V(i) = -2.50 \log\left[(1 + 1.5\cos i)\cos i\right] \tag{5.2}$$

(Paczyński & Schwarzenberg-Czerny 1980). To apply this relation one thus needs knowledge of i, as well as a measurement of V at maximum. The scatter of data around the M_{Vmax}–P_{orb} relation is roughly $\pm$0.5 mag.

The equivalent widths (as before, the EWs of emission lines are taken as positive) of

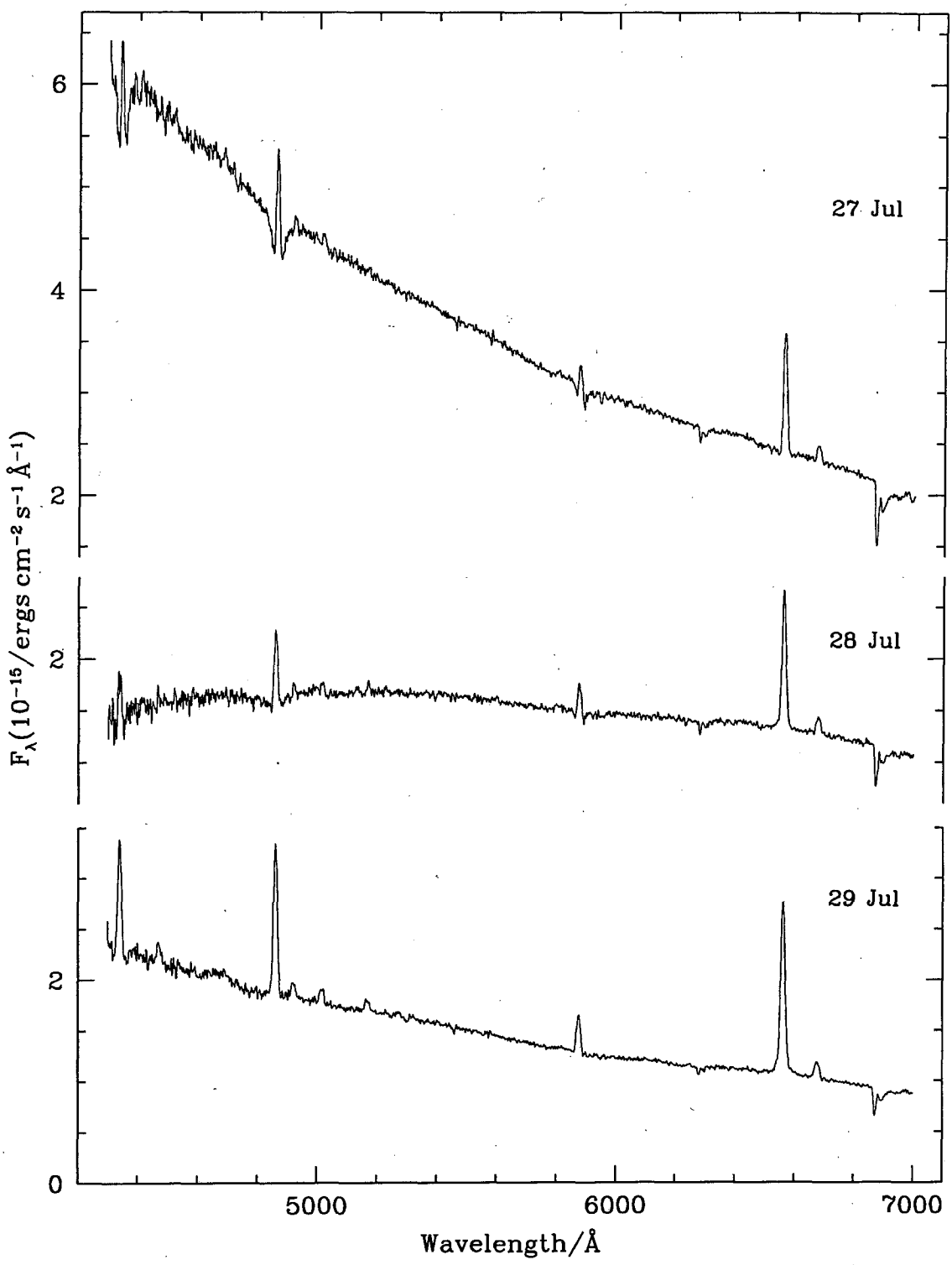

Figure 5.5: The average nightly spectrum of RX J1831.7+6511. The system faded from $V = 15.0$ to $V = 15.9$ over the three nights, with the strength of the emission lines increasing, as is commonly seen during the decline from dwarf nova outbursts (e.g. Hessman et al. 1984).

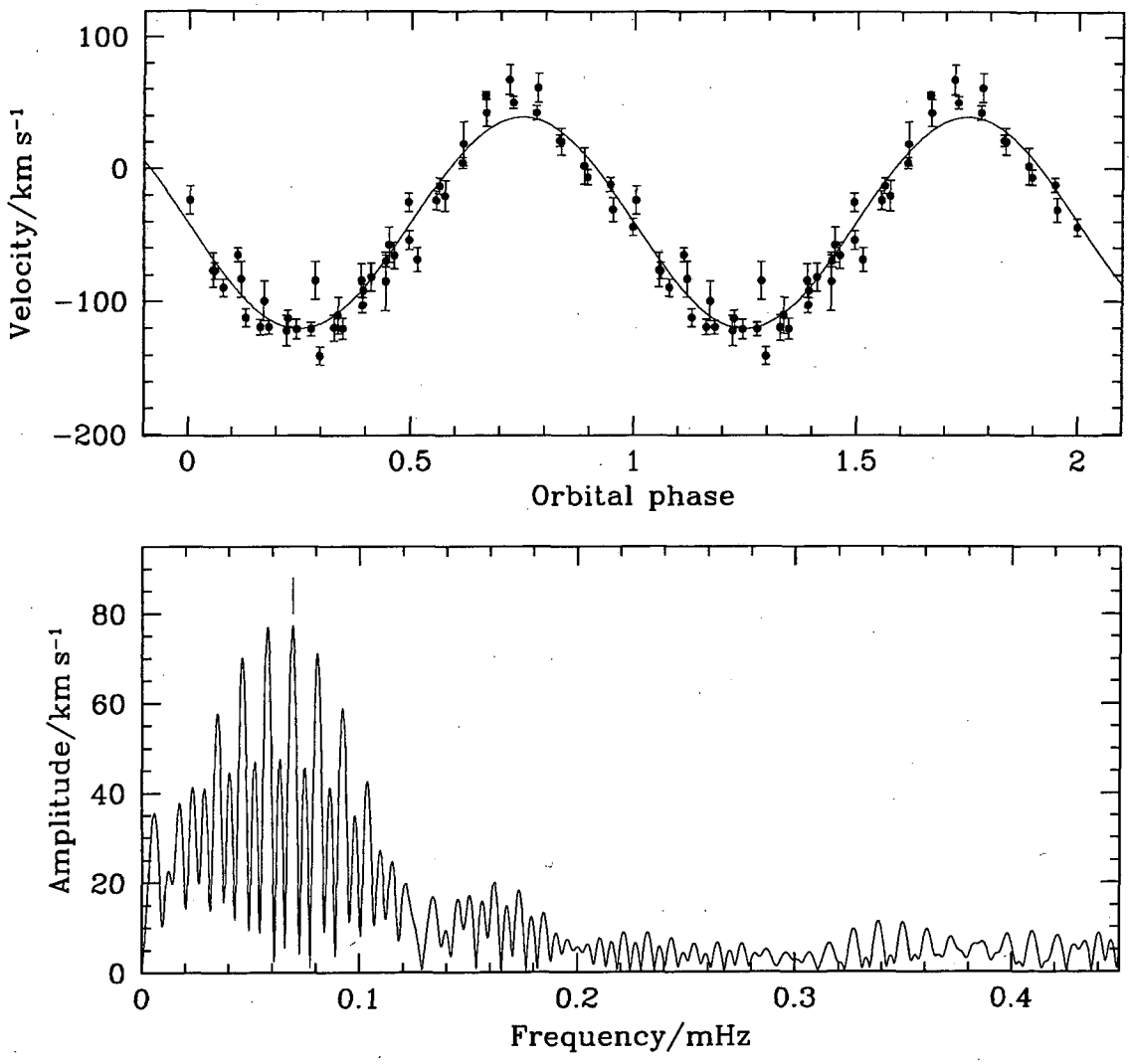

Figure 5.6: The low-frequency end of the Fourier transform of the Hα radial velocity curve of RX J1831.7+6511 (lower panel). A vertical bar at 0.0693 mHz (4.01 h) marks the signal that most likely corresponds to the orbital period. The upper panel shows the phase-folded radial velocity curve, with the best-fit sine function overplotted (all data are plotted twice).

disc emission lines are expected to increase with $\dot{M}$; Patterson (1984) gives an empirical relation

$$\mathrm{EW(H}\beta) = 0.3 M_{V,disc}^2 + \mathrm{e}^{0.55(M_V - 4)} \tag{5.3}$$

that predicts $M_{V,disc}$ (the absolute V magnitude of the disc) to within about 1.5 mag for CVs with EW(Hβ) $\gtrsim 15$ Å. For EW(Hβ) $\lesssim 15$ Å, the data imply only $M_{V,disc} \lesssim +6$.

Bailey (1981) describes a method of estimating distances to CVs that relies on finding the K-band surface brightness of the secondary star from the $V-K$ colour of the system. It has since been shown that this method is not as reliable as was first thought, and that the V and K magnitudes of a CV alone cannot provide a secure distance estimate (e.g. Beuermann 2000). Knigge (2006) provides an alternative, based on a semi-empirical donor sequence for CVs that gives absolute magnitudes for the secondaries as a function of P_{orb}.

This sequence has already been used, in Chapter 4, to find lower limits on the distances to CVs; the limits are simply found by neglecting the disc contribution to the flux in a near-IR band, but it is also possible to obtain distance estimates from the sequence. Knigge (2006) finds offsets of $\Delta J = 1.56$, $\Delta H = 1.34$, and $\Delta K = 1.21$ between his sequence and the absolute JHK magnitudes of a sample of CVs with parallax distances. The scatter of the sample magnitudes around the offset sequence are $\sigma_{\Delta J} = 1.25$, $\sigma_{\Delta H} = 1.12$, and $\sigma_{\Delta K} = 1.07$. These offsets and errors will be used to obtain distance estimates. The estimates assume that the disc contributions to the IR flux of the sample of CVs with known distances are similar to those of the CVs considered here, and also that the CVs for which I estimate distances have unevolved secondaries. The limitations of the method are discussed in more detail by Knigge (2006).

The near-IR observations used here are again from 2MASS. The high resolution version of the donor sequence is linearly interpolated to find predicted absolute magnitudes for the secondaries at the orbital periods of the observed CVs. The updated transformations of Carpenter (2001) were again used to transform the CIT magnitudes of Knigge (2006) to the 2MASS photometric system. Errors from the transformation are insignificant for the purposes of the distance calculations, and will not be quoted (although they were included).

Detailed models were investigated to estimate extinction. Amôres & Lépine (2005) presents two Galactic extinction models. The one that takes into account the spiral structure of the Galaxy was compared to the model of Drimmel et al. (2003) at several positions in the NEP region. An average difference of $\simeq$45 % was found between the A_V values predicted by the two. The Amôres & Lépine (2005) extinction predictions are used below, and errors of 50 % are assumed on these values. Extinction is of course a function of distance; a few iterations are therefore made to ensure that the value finally used in the distance calculation is that given by the model at the estimated distance to the object; the total Galactic extinction is used for lower limits on distances. The conversion from visual extinction to extinction in the 2MASS bands uses the relations $A_J = 0.282A_V$, $A_H = 0.175A_V$, and $A_{K_S} = 0.112A_V$ (Cambrésy et al. 2002).

In finding a probability distribution for the distance to each source, it is assumed that errors in absolute magnitude, apparent magnitude, and extinction are Gaussian. The distances quoted are in all cases the median, together with the symmetric 1-σ confidence interval around the median (this is the interval defined so that the integral of the distribution between its lower bound and the median, as well as between the median and its upper bound, is 34% of the integral over all distances).

Two of the three techniques used to estimate distances require the orbital period of the CV. For RX J1715.6+6856, RX J1831.7+6511, and SDSS J1730 there is some cycle count ambiguity in the P_{orb} measurements, and there is also some uncertainty in the orbital period of IX Dra (see below). However, the period uncertainty in all cases considered here makes a negligible contribution to the error in the distance estimates.

5.2.2.1 RX J1715.6+6856

RX J1715.6+6856 was not detected in 2MASS; $K_S > 15.6$ is estimated from the magnitude of the faintest stars detected in the field. At the period of RX J1715.6+6856 (1.64 h), the donor sequence predicts $M_{K_S} = 8.74$ for the secondary star (if this system is not a period bouncer), giving $d > 235$ pc.

The $M_{V,disc}$–EW(Hβ) relation, and EW(Hβ) = 62 Å (measured from the spectroscopy presented in Section 5.2.1.1) gives $M_V = 10.2 \pm 1.5$ (assuming that the disc dominates the flux in V). This, together with $A_V = 0.08 \pm 0.04$ leads to $d = 400^{+400}_{-200}$ pc.

5.2.2.2 SDSS J1730

The discovery of SDSS J1730 was announced by Szkody et al. (2002), who observed a DN outburst, and measured EW(Hβ) = 63 Å (in quiescence) and an orbital period of roughly 1.95 h; the refined value is $P_{orb} = 1.837 \pm 0.002$ h (John Thorstensen, private communication). As expected at this orbital period, SDSS J1730 is an SU UMa star (vsnet-alert 6798); the fractional superhump period excess, ϵ, indicates that it has not evolved to the period minimum (Patterson et al. 2005).

Knigge (2006) gives $M_{K_S} = 8.22$ for a typical secondary at the orbital period of SDSS J1730. From the observed $K_S = 15.22 \pm 0.18$ a lower limit of $d > 250$ pc, and an estimate of $d = 440^{+280}_{-170}$ pc is therefore obtained (using $A_V = 0.08 \pm 0.04$).

The observed EW(Hβ) gives $M_{V,disc} = 10.3 \pm 1.5$. Combined with $V = 16.1$ (obtained from the Sloan magnitudes given by Szkody et al. 2002, using the transformation of Jester et al. 2005) this implies $d = 140^{+140}_{-70}$ pc (again assuming that the V-band flux originates only from the disc). Since this distance is only barely consistent with the robust lower limit, and since any white dwarf contribution to the V-band flux will imply that it is too low, the donor-based distance estimate will be adopted for this system.

5.2.2.3 RX J1831.7+6511

RX J1831.7+6511 has $P_{orb} = 4.01$ h (implying $M_{K_S} = 6.20$ for the secondary), $K_S = 14.96 \pm 0.14$, and $A_V = 0.11 \pm 0.06$ (i.e. $A_{K_S} = 0.012 \pm 0.007$). This gives a lower limit of $d > 559$ pc, and an estimate of $d = 980^{+630}_{-380}$ pc.

For comparison, EW(Hβ) = 14 Å and $V = 15.9 \pm 0.2$ is measured from the 29 July 2006 spectra. Assuming the system was in quiescence, the $M_{V,disc}$–EW(Hβ) relation gives $M_V \lesssim +6$, and thus $d \gtrsim 900$ pc.

5.2.2.4 EX Dra

Being a deeply eclipsing system, EX Dra has been the subject of several detailed studies. It is a U Gem star with $P_{orb} = 5.0385$ h (Fiedler et al. 1997), a secondary spectral type between M1V and M2V (Baptista et al. 2000; Billington et al. 1996; cf. Harrison et al. 2005), and an orbital inclination of $i = 85^{+3}_{-2}$ deg (Baptista et al. 2000; Fiedler et al. 1997 obtained a similar value). The out-of eclipse quiescent V magnitude is 15.3, and the

system reaches $V = 12.3$ at maximum. At mid-eclipse in quiescence, $V = 16.66 \pm 0.07$, $I = 14.46 \pm 0.05$, and essentially all of the light originates from the secondary star (Baptista et al. 2000; Baptista & Catalán 2001; Shafter & Holland 2003). Mid-eclipse photometry has provided distance estimates based on the photometric parallax of the secondary of 240 ± 90 pc (Shafter & Holland 2003) and 290 ± 80 pc (Baptista et al. 2000).

The above distance estimates can be checked against the CV donor sequence of Knigge (2006). For this, it is assumed that, in quiescence, the secondary is the only source of mid-eclipse light. The sequence predicts $M_V = 8.80 \pm 0.37$ for secondaries with spectral types in the range M1 to M2. This gives a distance of 360^{+70}_{-60} pc. At $P_{orb} = 5.0385$ h, predicted magnitudes for the secondary star are $M_V = 9.56 \pm 0.96$ and $M_I = 7.51 \pm 0.77$ (the errors are derived from an error of ± 1 spectral type in the sequence, and are probably conservative). Using the measured period rather than spectral type, distance estimates of 260^{+140}_{-90} and 240^{+120}_{-80} pc result from the apparent mid-eclipse V and I magnitudes, respectively. The first of these estimates uses $A_V = 0.08 \pm 0.04$, while for the other two A_V was set to 0.06 ± 0.03. The reason these distances differ is that EX Dra is not exactly on the donor sequence (see fig. 9 of Knigge 2006).

The M_{Vmax}–P_{orb} relation gives $d = 140^{+60}_{-50}$ pc. A likely reason for this small value is that the dependence on i given by equation 5.2 is too sensitive at large i, because radiation from the disc rim becomes significant (Smak 1994).

The three donor-based distance estimates derived here and those of Shafter & Holland (2003) and Baptista et al. (2000) are, of course, not independent, but they are all formally consistent with each other. A distance of 260^{+140}_{-90} pc is adopted for this system.

5.2.2.5 IX Dra

Liu et al. (1999) confirmed IX Dra as a CV. It is a member of the group of SU UMa stars with unusually short outburst recurrence times, sometimes referred to as ER UMa stars (Ishioka et al. 2001). The quiescent brightness of IX Dra is $V = 17.5$, and maximum of normal outburst is roughly $V = 15.4$. Olech et al. (2004) measured a superhump period of 1.6072 h, and found a second photometric period of 1.595 h in superoutburst light curves. If the second period is interpreted as P_{orb}, the small resulting ϵ implies a very low mass ratio (Patterson 1998), and thus that IX Dra has a secondary of substellar mass (Olech et al. 2004). However, the period bouncer status of IX Dra is suspect for two reasons. The first is that the high outburst duty cycle (about 30%) implies a high $\dot{M}$ (however, note that DI UMa has very low ϵ, and similar outburst characteristics; Patterson 1998). More importantly, it relies on the 1.595 h signal being the orbital period; a large amplitude (in this case about 0.05 mag) photometric orbital modulation is not usually seen during superoutburst, and the superhump modulation makes it dificult to measure other signals reliably. Confirmation of the orbital period is needed to decide whether this system is likely to be a period bouncer.

The inclination of IX Dra is not known, but the absence of an eclipse (even at supermaximum) constrains it to $< 70°$. This gives a limit of $d \gtrsim 545$ pc from the M_{Vmax}–P_{orb}

relation.

2MASS provides only a lower limit on K_S and a marginal detection in H for IX Dra; the J-band magnitude of 16.47 ± 0.12 is therefore used in the donor-based distance estimate. The pre-period minimum branch of the donor sequence (predicting $M_J = 9.85$) is used, despite the possibility that IX Dra is a period bouncer. In the direction of IX Dra, $A_V \simeq 0.1$ for distances greater than $\simeq 400\,\mathrm{pc}$. With the J-band offset of 1.56, a distance of $430^{+340}_{-190}\,\mathrm{pc}$ is found.

The reasons for not using the period bouncer branch of the donor sequence for the distance estimate are that (i) the evidence for IX Dra being a period bouncer is questionable; (ii) the offsets are calibrated using only two candidate period bouncers, and therefore cannot be expected to produce robust distance estimates for period bouncers; (iii) even if IX Dra really is a period bouncer, its high outburst duty cycle indicates that the disc contribution to its IR flux is probably more typical of a normal short-period CV than a period bouncer; and (iv) a distance estimate that is inconsistent with the M_{Vmax}–P_{orb}-based lower limit is obtained if the period bouncer branch is used.

5.3 The space density of CVs

Here, an estimate of the space density of CVs based on the NEP sample is presented (Section 5.3.1), and the maximum size of a population of systems with given (low) L_X that could have escaped detection in the NEP survey is found (Section 5.3.2).

An exponential vertical density profile

$$\rho(z) = \rho_0 \mathrm{e}^{-|z|/h} \tag{5.4}$$

is assumed for CVs, with z the perpendicular distance from the Galactic plane (i.e. $z = d \sin b$, where b is Galactic latitude). The local space density is defined as $\rho_0 = \rho(0)$, the mid-plane value of ρ. Any radial dependence of ρ is ignored in Section 5.3.1 (it certainly has a negligible effect on the results presented there), but such a dependence is included in Section 5.3.2 (simply because it is not too computationally difficult).

Widely used empirical values of the Galactic scaleheight of CVs, h, may be found in Patterson (1984) and Duerbeck (1984). However, since all observational CV samples contain a serious z-dependent bias (I will return to this in Chapter 6), theoretical h values were used in this work instead. Also, rather than assuming a single scaleheight for all CVs, h is set to $h = 120$, 260, and 450 pc for long-period systems, short-period systems, and period bouncers, respectively, as in previous chapters.

DNe typically have softer X-ray spectra in outburst than in quiescence, although a wide range in X-ray behaviour has been observed in different systems (e.g. Warner 1995). The RASS was conducted over a period of about 6 months, and during this time the NEP area was observed many times. This means that, while the duration of the survey was short compared to the outburst recurrence time-scale of faint DNe, high duty cycle, frequently outbursting CVs, such as EX Dra, were probably observed both in outburst

and quiescence. No attempt will be made to account for this complication.

CVs are expected to have X-ray emission that can be described as thermal bremsstrahlung with kT roughly between 5 and 20 keV (Patterson & Raymond 1985a), although observations indicate a larger variety of X-ray spectral shapes (e.g. Naylor et al. 1988; Vrtilek et al. 1994; Richman 1996). Besides the large statistical errors in distances, uncertainty in spectral shape is not expected to be important. The range in F_X resulting from varying kT from 5 to 20 keV for a thermal bremsstrahlung spectrum is about as large as the error in F_X from observational error in count rate (which is an insignificant contribution to the uncertainty in ρ_0). It is therefore simply assumed that all CVs have a $kT = 10\,\mathrm{keV}$ thermal bremsstrahlung spectrum. Following Henry et al. (2006), the quoted X-ray fluxes and luminosities are in the 0.5–2.0 keV band, as calculated from *ROSAT* PSPC count rates in the 0.1–2.4 keV band.

5.3.1 The $1/V_{max}$ method

The space density is found by counting the CVs inside the volume observed, while accounting both for the fact that the sample is flux- rather than volume-limited, and for the variation of space density with z. The method involves essentially allowing the 'volume limit' to vary according to the luminosities of the systems in the sample, while the dependence on z is taken care of by defining a 'generalized' volume

$$V_{max,j} = \Omega \frac{h^3}{|\sin b|^3} \left[2 - \left(x_j^2 + 2x_j + 2\right) \mathrm{e}^{-x_j}\right] \tag{5.5}$$

(e.g. Schmidt 1968; Felten 1976; Stobie et al. 1989; Tinney et al. 1993), where Ω is the solid angle covered by the survey and $x_j = d_{max,j}|\sin b|/h$, with $d_{max,j}$ the maximum distance at which a CV included in the sample could have been detected (given its L_X and the survey flux limit). Equation 5.5 assumes that ρ is a function only of z, and that this dependence is given by equation 5.4. The index j represents the CVs in the sample. Because both b and the flux limit are variable over Ω, each $V_{max,j}$ is computed as a sum over solid angles $\delta\Omega$ small enough so that b and the flux limit (and thus $d_{max,j}$) can be assumed to be constant over each $\delta\Omega$. This is done by dividing the NEP area into a 36×36 pixel grid (this is fine enough to preserve most of the important structure in the flux limit map). ρ_0 is then the sum of the space densities represented by each CV, i.e.

$$\rho_0 = \sum_j 1/V_{max,j}.$$

The $1/V_{max}$ values for the 5 CVs, obtained by using the best distance and F_X estimates, are given in Table 5.2, together with other relevant parameters. These values are only intended to provide an indication of the relative contribution that individual CVs make to the total space density. All significant uncertainties are accounted for in the final calculation of ρ, as described below.

Extinction is neglected in finding the maximum distance at which a source could be

Table 5.2: Orbital periods, X-ray fluxes, distances, and luminosities of the five CVs in the NEP survey area, together with the contribution each systems makes (if errors are ignored) to the mid-plane space density. Note that, although IX Dra is in the area covered by the survey, it is not included in the NEP sample.

Object	P_{orb}/h	F_X/erg cm^{-2} s^{-1}	d/pc	L_X/erg s^{-1}	$(1/V_{max})$/pc^{-3}
EX Dra	5.0385	$(6.4 \pm 0.7)10^{-14}$	260^{+140}_{-90}	5×10^{29}	8.8×10^{-6}
RX J1831.7+6511	4.01	$(1.7 \pm 0.2)10^{-13}$	980^{+630}_{-380}	2×10^{31}	1.4×10^{-6}
SDSS J1730	1.837	$(3.4 \pm 0.3)10^{-13}$	440^{+280}_{-170}	8×10^{30}	3.1×10^{-7}
RX J1715.6+6856	1.64	$(8.5 \pm 1.7)10^{-14}$	400^{+400}_{-200}	2×10^{30}	1.3×10^{-6}
IX Dra	1.595	$(2.2 \pm 0.5)10^{-14}$	430^{+340}_{-190}	5×10^{29}	5.4×10^{-6}

detected from its estimated distance (for which extinction was included) and observed F_X. This is reasonable because extinction is low in the NEP area (the absorbed F_X is at least 0.78 times the unabsorbed flux for all positions in the survey volume), and because, for the distances of most of the sources, the column densities are already at close to the total Galactic values. In other words, at distances beyond the CVs, extinction is approximately constant, so that the maximum volumes are unaffected if extinction is ignored.

Both distance errors and the small sample size contribute significantly to the overall uncertainty in ρ_0, although the latter effect dominates. In order to account fully for all sources of error (including the uncertainty in distances, the error on F_X, and small number statistics), the probability distribution of ρ_0 is determined via a Monte Carlo simulation. For this simulation, a large number of mock CV samples with properties designed to fairly sample the full parameter space permitted by the data is created. Then an estimate of ρ_0 is computed for each mock sample, so that a probability distribution for ρ_0 is gradually generated.

The generation of appropriate mock samples is the key step in the simulation. This is achieved by treating each CV in the real sample as a representative of a larger population of similar CVs, and allowing each of these populations to contribute to each mock sample. In creating a particular mock sample, a mock counterpart to each CV in the real sample is generated by drawing the X-ray flux and distance from the appropriate probability distributions. This takes care of the observational uncertainties in F_X, as well as the uncertainties in distances. However, there is also Poisson uncertainty associated with the small sample size, which would be ignored if each mock sample contained exactly the same number of CVs as the real sample. This is accounted for by a weighting factor assigned to counterpart CVs in the mock samples. The weighting factor needs to be drawn independently for each counterpart CV in each mock sample from the probability distribution of the expected number of sources belonging to this population in a survey with the specifications of the NEP survey. This probability distribution can be constructed from Bayes' theorem. If the expected number of sources in a NEP-like survey is μ for a

particular population[1], the actual number observed in a particular survey will be N_{obs}, where this is drawn from the Poisson distribution $P(N_{obs}|\mu)$. Then Bayes' theorem gives

$$P(\mu|N_{obs}) \propto P(N_{obs}|\mu)P(\mu),$$

where $P(\mu)$ is the prior on μ. Note that, in practice, $N_{obs} \equiv 1$ by construction for each population represented in the real sample (since each CV is taken to represent a population of similar CVs). Also, since μ is a scale factor for the space density of each population, the appropriate uninformative prior to use is $P(\mu) = 1/\mu$ (e.g. Jeffreys 1961).

Several tests were carried out to check that this technique produces reliable error estimates. In the tests, a space density, luminosity function, and flux limit are taken as input, and used to simulate observed samples. The ρ_0 distribution implied by each sample is then calculated in the same way as described above. In $\simeq$68% of these ρ_0 distributions the true input ρ_0 is contained in any particular 1-σ interval. This holds when the expected number of detected sources is as small as 4, but also for much larger samples, when the distributions become narrower. I ignored Galactic structure in these tests (i.e. ρ was taken to be constant), but experimented with several different (simple) luminosity functions, as well as with including errors in luminosity. Simulations were also performed to verify that a uniform prior is not appropriate in this calculation. These numerical tests indicate that the method is reliable, and that the $1/\mu$ prior is suitable.

To summarize, the calculation of ρ_0 works as follows. The simulation draws a random distance and F_X from the appropriate probability distribution functions (assuming that the error in F_X is Gaussian) for each of the systems in the sample, computes $V_{max,j}$, generates μ_j, and obtains ρ_0 by summing $\mu_j/V_{max,j}$ over j. Repeating this a large number of times produces a probability distribution for ρ_0.

Fig. 5.7 shows the ρ_0 histogram obtained from this calculation. The mode, median, and mean of this distribution are 4.7×10^{-6}, 1.1×10^{-5}, and $2.4 \times 10^{-5}\,\mathrm{pc}^{-3}$, and are marked by solid lines. The dotted lines show the symmetric 1-σ confidence interval around the median, which is 4.4×10^{-6} to $3.5 \times 10^{-5}\,\mathrm{pc}^{-3}$.

A reason for some concern is that IX Dra was only just too faint to be included in the NEP sample (the possibility that it might be a period bouncer adds to this problem). More importantly, a single system, EX Dra, dominates the space density estimate. The choice of scaleheights is also non-standard[2]. To investigate the sensitivity of the result to these factors, Table 5.3 lists the space densities that would be obtained by (i) using a single scaleheight of 120 pc, (ii) including IX Dra, and (iii) excluded EX Dra. Note that as different as the best estimates are (I give the median of each distribution), they are all consistent with each other. Table 5.3 also gives the space densities for short- and long-period systems separately.

[1]Note that μ does not need to be an integer.

[2]Although it is certainly an improvement over assuming a single small scale height for the entire CV population.

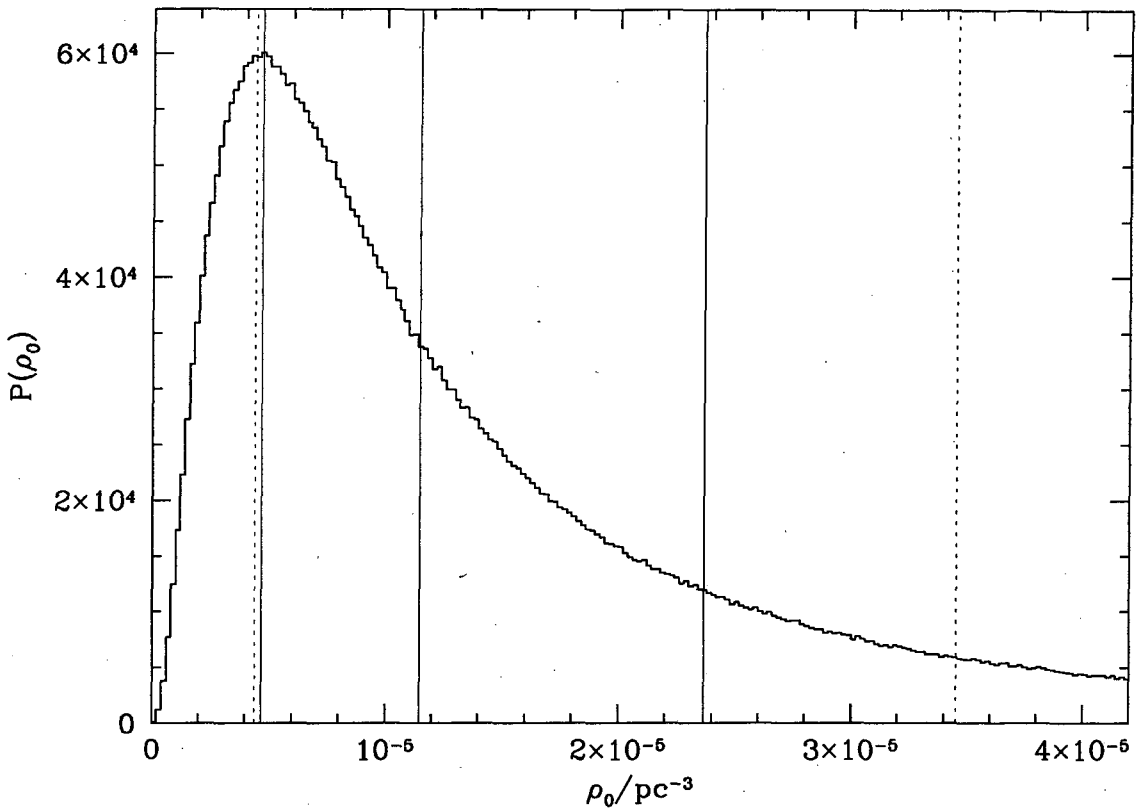

Figure 5.7: The ρ_0 distribution resulting from the simulation. This sample includes RX J1715.6+6856, SDSS J1730, RX J1831.7+6511, and EX Dra; scaleheights of 260 pc and 120 pc for short- and long-period systems, respectively, were used. Solid lines mark the mode, median, and mean at 4.7×10^{-6}, 1.1×10^{-5}, and $2.4 \times 10^{-5}\,\mathrm{pc}^{-3}$, and dotted lines show a 1-σ interval from 4.4×10^{-6} to $3.5 \times 10^{-5}\,\mathrm{pc}^{-3}$.

Table 5.3: ρ_0 from different simulations. h_{sp} and h_{lp} are the scaleheights, in parsecs, assumed for short- and long-period systems, respectively. The values given for ρ_0 are the medians of the ρ_0 distributions, and the errors represent symmetric 1-σ confidence intervals around the median.

Sample and scaleheight	ρ_0/pc^{-3}
EX Dra, RX J1831.7, SDSS J1730, RX J1715.6; $h_{sp} = 260$, $h_{lp} = 120$	$1.1^{+2.3}_{-0.7} \times 10^{-5}$
EX Dra, RX J1831.7, SDSS J1730, RX J1715.6; $h_{sp} = h_{lp} = 120$	$1.5^{+2.5}_{-0.8} \times 10^{-5}$
EX Dra, RX J1831.7, SDSS J1730, RX J1715.6, IX Dra; $h_{sp} = 260$, $h_{lp} = 120$	$2.1^{+4.2}_{-1.3} \times 10^{-5}$
RX J1831.7, SDSS J1730, RX J1715.6; $h_{sp} = 260$, $h_{lp} = 120$	$3.1^{+5.5}_{-1.9} \times 10^{-6}$
EX Dra, RX J1831.7; $h_{lp} = 120$ (long-period)	$7.7^{+18}_{-5.1} \times 10^{-6}$
SDSS J1730, RX J1715.6; $h_{sp} = 260$ (short-period)	$1.4^{+5.2}_{-1.0} \times 10^{-6}$

5.3.2 Upper limits on the space density of an undetected population

An unavoidable assumption of the $1/V_{max}$ method is that the detected objects are representative of the luminosity function of the true underlying CV population. No evidence of even a large population of CVs is expected to show up in a flux-limited survey, if such a population is sufficiently faint.

The faintest measured values of L_X for CVs are a few times $10^{29}\,\mathrm{erg\,s^{-1}s}$ (e.g. Verbunt et al. 1997; Wheatley et al. 2000; Schwope et al. 2007)[3]. However, it is not really known how faint CVs can be: the faintest expected secular luminosities can be estimated from the gravitational radiation $\dot{M}$, but, since faint CVs are DNe, they spend most of their time at fainter luminosities (the question of what L_X can reasonably be expected in low-$\dot{M}$ CVs is further discussed in Chapter 6).

Riaz et al. (2006) find $10^{27}\,\mathrm{erg\,s^{-1}} < L_X < 10^{33}\,\mathrm{erg\,s^{-1}}$ for a large sample of nearby dwarfs with spectral types between K5 and M6; brown dwarfs have $L_X < 10^{29}\,\mathrm{erg\,s^{-1}}$ (often several orders of magnitude less than $10^{29}\,\mathrm{erg\,s^{-1}}$; e.g. Stelzer et al. 2006). CV secondaries have shorter spin periods than expected for the objects in these studies, but, even so, one cannot be confident that the secondary star alone guarantees $L_X > 10^{29}\,\mathrm{erg\,s^{-1}}$. This is especially true in the case of period bouncers.

Another Monte Carlo simulation is used to find the upper limit on the space density of a hidden population, assuming that all members of this population have the same (low) L_X. As in Chapter 3 and 4, the Galaxy is modelled as an axisymmetric disc, with exponential vertical and radial (r) density profiles, the Galactic Centre distance is taken as 7 620 pc (Eisenhauer et al. 2005), and the small offset of the Sun from the Galactic plane is neglected. At least part of a hidden CV population may consist of pre-period bounce systems, but I conservatively assume a single scaleheight of 450 pc (appropriate to period bouncers). The radial scalelength is taken as 3 000 pc. The local space density is then ρ_0, where $\rho = \rho_0 \exp(-|z|/450\,\mathrm{pc})$, for r near 7 620 pc.

Because the upper limits will be systematically low if extinction is neglected, it is included here, using the model of Amôres & Lépine (2005) to estimate N_H for every simulated system.

This simulation finds the value of ρ_0 for which the predicted number of faint systems detected in the NEP survey is 3 (detecting 0 such systems is then a 2-σ result). Fig. 5.8 shows the maximum allowed ρ_0 as a function of L_X for CVs that make up the hidden population. Results from the simulation are plotted as a fine histogram, while the bold curve is a fit to the data. The fit is given by

$$\rho_{max} = 5.7 \times 10^{-4} (L_X/10^{29}\,\mathrm{erg\,s^{-1}})^{-1.39}\,\mathrm{pc^{-3}}.$$

Thus for $L_X = 2 \times 10^{29}\,\mathrm{erg\,s^{-1}}$, one obtains $\rho_0 < 2 \times 10^{-4}\,\mathrm{pc^{-3}}$. Note that here ρ_0 refers

[3]Verbunt et al. (1997) list $L_X = 3.16 \times 10^{28}\,\mathrm{erg\,s^{-1}}$ for AY Lyr, but this resulted from a very low distance estimate of 57 pc (Sproats et al. 1996). The distance is based on a measurement of $K = 13.08$, taken during outburst. 2MASS photometry indicates $K_S > 15.6$ in quiescence; combined with the Knigge (2006) sequence this gives $d > 277$ pc, implying that the system is not particularly faint in X-rays.

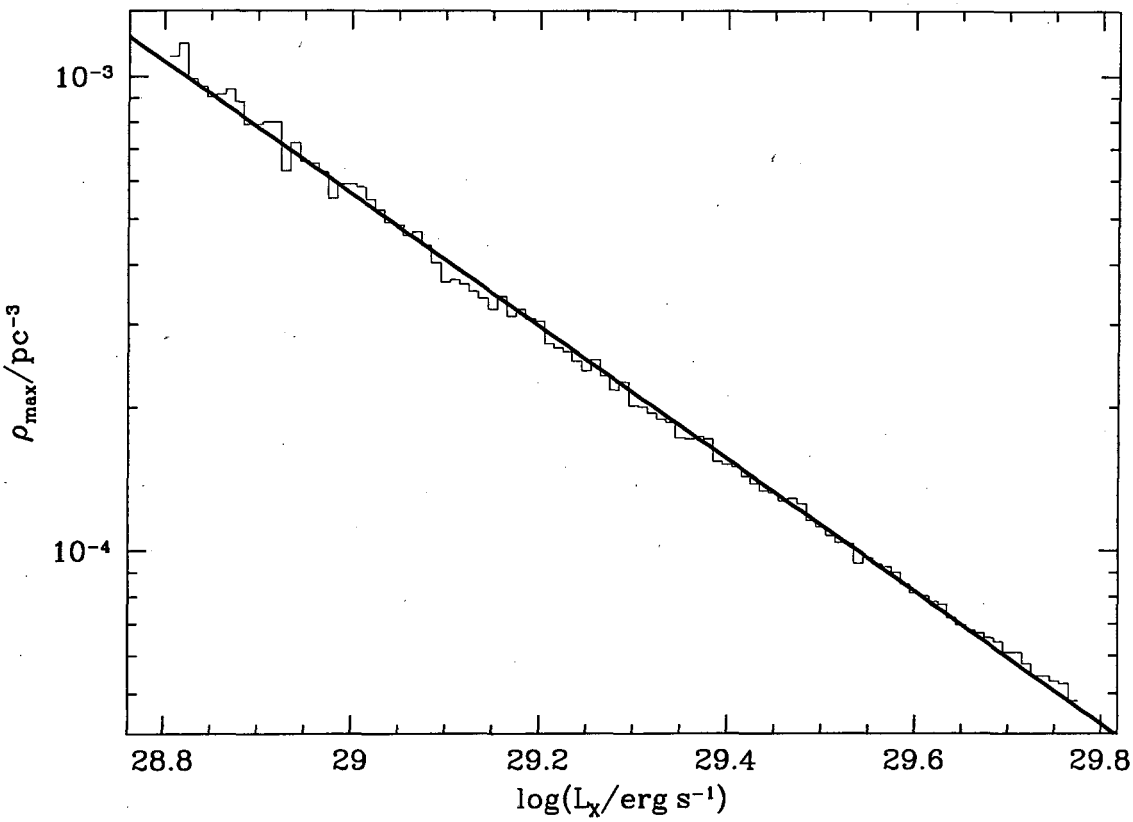

Figure 5.8: The upper limit on the mid-plane space density as a function of X-ray luminosity for an undetected population of CVs. The data from the simulation are shown as a fine histogram, and a fit to the data is overplotted as a bold curve.

only to the hypothesized undetected population, and does not include the contribution from the brighter, detected systems.

5.4 Discussion

The ρ_0 measurement from the NEP survey is consistent with several previous observational estimates, e.g., $\sim 10^{-5}\mathrm{pc}^{-3}$ (Patterson 1998) and $\sim 3 \times 10^{-6}\mathrm{pc}^{-3}$ (Warner 2001). A particularly relevant study to compare to is Hertz et al. (1990), since it was also based on a sample of 4 X-ray selected CVs. Hertz et al. find $\rho_0 \simeq (2-3) \times 10^{-5}\mathrm{pc}^{-3}$ (where the uncertainty includes only the possible incompleteness of the sample), again consistent with the estimate presented here. The Chandra Multiwavelength Plane (ChaMPlane) survey (Grindlay et al. 2005; Rogel et al. 2006, 2007) has produced a second recent ρ_0 estimate based on a small CV sample (perhaps surprisingly, this sample is not X-ray selected). Rogel et al. (2007) uses 5 CVs [4] to derive $\rho_0 = 0.9^{+1.5}_{-0.5} \times 10^{-5}\,\mathrm{pc}^{-3}$, in close agreement with the measurement presented here. Note, however, that, while the ChaMPlane estimate includes

[4] I suspect that one member of this sample is misidentified—see fig. 4 of Rogel et al. 2006. The very steep Balmer decrement and the narrowness of the Hα line argue against the classification of ChOPS J182723.91-040715.9 as a CV. This would imply a significant systematic error in the ρ estimate.

Poisson statistics, it assumes a completeness of 50%, as well as a luminosity function (based on data presented by Patterson 1998) for CVs. For the NEP measurement the data were in effect used to estimate the luminosity function. The NEP data are better suited to estimating the CV luminosity function than those of Patterson (1998), because the NEP sample is complete.

The most important concern with the measurement presented here is that the NEP CV sample is so small that it almost certainly does not fairly represent the underlying CV population. This is apparent from the higher space density found for long- than for short-period systems. The reason is that the estimate is dominated by the long-period system EX Dra, which has an unusually low L_X for its orbital period, probably because of its very high inclination (see e.g. van Teeseling et al. 1996). Note, however, that if the X-ray luminosity of EX Dra had been higher, that would only reduce the ρ_0 estimate given here.

Theoretical predictions of the CV space density are typically higher than most observational values. A space density of $(0.5-2)\times10^{-4}\,\mathrm{pc}^{-3}$ results from the CV birth rate of de Kool (1992), together with the assumptions that the age of the Galaxy is 10 Gyr, and that the lifetime of a CV is longer than that (Warner 1995). When the model population of Kolb (1993) is normalized to the formation rate of single white dwarfs, the predicted mid-plane CV space density is $1.8\times10^{-4}\,\mathrm{pc}^{-3}$ (see Section 2.7 for a more complete discussion). These values are not ruled out, but the data do show that if ρ_0 is really as high as $2\times10^{-4}\,\mathrm{pc}^{-3}$, then the dominant CV population must have $L_X \lesssim 2\times10^{29}\,\mathrm{erg\,s}^{-1}$. It is suspected that the mass transfer rates of CVs fluctuate around the secular mean on time-scales much longer than the total observational baseline (see the discussion in Section 2.8.2). Because the time-scale of such mass transfer cycles is not accessible to observations, it can only be noted that surveys useful for finding CVs typically have no sensitivity to objects that are not currently accreting.

The fact that stellar populations of different ages do not have the same Galactic distribution has to be kept in mind when interpreting (and, indeed, measuring) space densities. While the situation is clearly not really as simple as three distinct subpopulations with three scaleheights, long-period CVs make up a significantly younger population than, say, period bouncers. One should therefore clearly not expect the ratio of the mid-plane space densities of these subpopulations to be the same as the ratio of their total Galactic numbers. This may be a trivial point, but it has been completely ignored in the literature. If, e.g., one assumes that 70% of all CVs in the Galaxy are period bouncers, and only 1% are long-period systems, and if the space densities of these two subpopulations are given by

$$\rho_{pb}(z) = \rho_{pb}(0)\exp(-|z|/450\,\mathrm{pc})$$

and

$$\rho_{lp}(z) = \rho_{lp}(0)\exp(-|z|/120\,\mathrm{pc}),$$

respectively, then (from integrating the vertical density profiles and assuming the radial

and azimuthal dependences are the same in both cases)

$$\rho_{pb}(0) = 70(120/450)\rho_{lp}(0) \simeq 20\rho_{lp}(0).$$

This argument can also be used to place a tentative limit on the ratio of the total numbers of period bouncers and long-period CVs in the intrinsic CV population. Assuming $\rho_{pb}(0) < 2 \times 10^{-4}\,\mathrm{pc}^{-3}$ and $\rho_{lp}(0) > 2.0 \times 10^{-6}\,\mathrm{pc}^{-3}$, this ratio must be less than about 400 (this is, of course, not a very constraining result; note also that $\rho_{pb}(0) < 2 \times 10^{-4}\,\mathrm{pc}^{-3}$ may not be a very good assumption, since the typical X-ray luminosities of period bouncers are not known).

There are several ongoing surveys that will produce large new samples of CVs. Examples are the Hamburg Quasar Survey, the Sloan Digital Sky Survey, and the INT Photometric Hα Survey of the Northern Galactic Plane (e.g. Gänsicke et al. 2002; Szkody et al. 2002; Witham et al. 2006). Although these samples will all be subject to more complicated selection effects than the NEP sample, they will be much larger, which will remove the main shortcoming of the present study (although it should be kept in mind that space density estimates based on larger samples can still be dominated by 1 or 2 systems; e.g. Schwope et al. 2002).

5.5 Conclusions

Using the complete X-ray flux-limited CV sample detected in the *ROSAT* NEP survey, I have estimated the space density of CVs bright enough to be represented in the survey, and placed limits on the size of a fainter population that may have remained undetected.

I have presented observations of two newly discovered CVs, namely RX J1715.6+6856 and RX J1831.7+6511, and measured orbital periods of 1.64 h and 4.01 h respectively for these systems. RX J1715.6+6856 and RX J1831.7+6511 are probably both DNe. This completes the identification of CVs in the *ROSAT* NEP survey.

Distances were estimated for the 4 systems in the NEP sample, as well as for IX Dra, which is in the area covered by the survey, but below the survey flux limit.

With the assumption that the 4 CVs included in the NEP survey are representative of the intrinsic CV population, the space density of CVs is $1.1^{+2.3}_{-0.7} \times 10^{-5}\,\mathrm{pc}^{-3}$. Space densities as high as the theoretically predicted $\simeq 2 \times 10^{-4}\,\mathrm{pc}^{-3}$ are excluded by the data, unless the dominant CV population is fainter than $\simeq 2 \times 10^{29}\,\mathrm{erg\,s}^{-1}$ in X-rays.

Finally, it is worth emphasizing again that long-period CVs, short-period CVs, and period bouncers have different Galactic scaleheights. This needs to be accounted for when mid-plane space densities are translated to total Galactic number of systems.

Chapter 6

Discussion

One of the most active areas of research on CVs involves the evolution of these systems. The consequences of CV evolution can be observed in the period distribution of CVs, and several other predictions of evolution theory can be tested empirically (e.g. ρ and $\dot{M}$). It is therefore possible to study this subject observationally. Many such studies have been made, and intensive observational effort is going into producing CV samples suitable for constraining evolution theory.

As soon as populations synthesis studies became available, it was recognized that the period distribution of the known population of CVs has properties that are at odds with those predicted for the intrinsic CV population by the standard CV evolution scenario. However, given the form of the correlations of intrinsic brightness, outburst frequency, optical colours, and age with orbital period, it does not take much thought to realize that the selection effects that must be present in all CV samples go in the direction of making theory and observations consistent. A direct comparison between an observed CV sample and the predicted intrinsic population is therefore almost meaningless. To determine whether selection effects are strong enough to reconcile theory and observations, quantitative modelling of these effects is needed.

A second long-standing problem concerns the space density of CVs. Almost all observational estimates are lower than theoretical predictions. However, the incompleteness of observational samples means that most existing empirical estimates are really lower limits, so that no obvious inconsistency between theory and observations is implied. Besides the fact that the completeness of samples is very often misunderstood or overestimated, no previous observational estimate has been accompanied by a realistic and full estimate of its associated uncertainty.

By using carefully constructed observational samples, together with numerical modelling, it is possible to constrain both the period distribution and the size of the intrinsic CV population quantitatively.

I discuss below the methods that I have used, the overall implications of the separate studies presented in the three preceding chapters, and some possibilities for future observational studies of CV evolution.

6.1 Modelling selection effects

Quantitative allowance for selection effects requires models of the spatial distribution of CVs in the Galaxy, and of their SEDs and outburst properties. I have developed and implemented a Monte Carlo technique that allows me to model the effects of almost arbitrary selection biases on observationally constructed CV samples.

I have used this technique to examine the effects of selection cuts based on apparent magnitude, optical colours, and Galactic latitude. Although the directions of the effects of these biases on the observed CV period distribution are obvious, the magnitudes are in some cases surprising. The most important and inescapable result of the investigation of various biases is that the selection effects commonly present in observational CV samples are strong and cannot be ignored.

Earlier work on selection effects in the observed CV population is presented by Ritter & Burkert (1986), Ritter & Özkan (1986), and Ritter (1986). In these studies, flux limits were considered together with Galactic structure, but low-$\dot{M}$ CVs were not included, little effort was made to account for DN outburst cycles, and the analytical approach of Ritter (1986) restricted him to unphysical limiting cases in his treatment of Galactic structure. It is not possible to compare, e.g., predicted and observed period distributions using the results of these three papers. Subsequent studies of selection effects were either unrealistic (Howell et al. 2001) or more qualitative in nature (e.g. Patterson 1998; Gänsicke et al. 2002; Aungwerojwit et al. 2006).

The modelling of selection effects presented in Chapter 3 is the first practical and quantitative treatment of the problem. Although details of the model will no doubt be improved on in future, the underlying method is likely to be used for any successful interpretation of the results of existing and ongoing surveys.

6.1.1 Possible future applications

Several uniformly selected, independent samples of interacting binaries are currently being constructed. Surveys such as IPHAS (Drew et al. 2005), and its extension to the European Galactic Plane Surveys (which is imaging the Galactic plane in u, g, r, i, Hα, and He I λ5876, down to 21st magnitude; see Groot et al. 2006) are expected to produce large, well-defined samples of CVs. Also, roughly 300 CVs have already been discovered in the SDSS (Szkody et al. 2002, 2003, 2004, 2005, 2006, 2007). All of these samples will be affected by complicated observational biases, and their potential for understanding CV evolution will only be realized if it is possible to deal with these biases.

The code that I have developed is quite versatile, and although I only presented results for selection cuts based on optical observations, it is trivial to simulate X-ray flux-limited samples, given a prescription for L_X. For example, equation 16 of Patterson & Raymond (1985a) estimates L_X as a function of $\dot{M}$ and M_1:

$$L_X = f \times 8.7 \times 10^{31} \left(\frac{M_1}{0.7\,\mathrm{M}_\odot}\right)^{1.8} \left(\frac{\dot{M}}{10^{16}\,\mathrm{g\,s^{-1}}}\right) \mathrm{erg/s} \qquad (6.1)$$

where

$$f = \begin{cases} 1 & \text{for } \dot{M}/10^{16}\,\mathrm{g\,s^{-1}} < 0.62 \\ \mathrm{erfc}(k^{-1/2}) & \text{for } \dot{M}/10^{16}\,\mathrm{g\,s^{-1}} \geq 0.62 \end{cases}$$

and

$$k = -\ln\left[0.68\left(\dot{M}/10^{16}\,\mathrm{g\,s^{-1}}\right)^{-0.82}(M_1/0.7\,\mathrm{M_\odot})^{-1.28}\right].$$

The motivation for this L_X–$\dot{M}$ relation is that, in the case of low-$\dot{M}$ CVs, the boundary layer is optically thin and cools inefficiently, so that about half of the accretion luminosity is radiated in hard X-rays (with a correction factor of 0.25 for the instrument passband). At high $\dot{M}$, however, observationally inferred values of L_X are lower than would be calculated under this assumption. The reason is believed to be that most of the boundary layer luminosity emerges at lower energies (soft X-ray or UV), because the boundary layer is optically thick and hence cooler. A small, hot region above the orbital plane is thought to still emit some hard X-rays, so that $L_X \sim const$ at high $\dot{M}$. The L_X–$\dot{M}$ relation is thus semi-empirical, and fits observations reasonably well (see Patterson & Raymond 1985a). Because this relation flattens off at large L_X, long-period CVs are less over-represented in X-ray than in optical flux-limited samples.

Fig. 6.1 displays predicted P_{orb} distributions for X-ray flux-limited samples with two flux limits. The fraction of the sample that consists of long-periods CVs, and the imposed flux limit, is given in each panel. These histograms should be compared to the period distributions shown in Fig. 3.2. Note that even for the very bright flux limit of $F_X > 2 \times 10^{-12}\,\mathrm{erg\,cm^{-2}s^{-1}}$, the predicted fraction of long-period CVs in the detected sample is small. Predictions such as these could be quantitatively compared to, e.g., the period distribution of the CVs detected in the *ROSAT* Bright Survey (Schwope et al. 2002) or the *ROSAT* NEP Survey.

Another possibility is variability-based selection criteria. It is impractical to quantify the selection biases affecting the presently known sample of CVs that were discovered because of variability, but it could be done for a systematic survey, where the depth, and area and time coverage is known. Many CVs (mainly DNe) will be detected as large amplitude variables by, e.g., the Large Synoptic Survey Telescope (Walker 2003), and many must already be recorded in the SDSS-II Supernova survey (Frieman et al. 2008) and in the survey described by Kraus et al. (2007). Constructing a large, well-defined CV sample out of such surveys will require a serious observational effort; it might be worth while to use X-ray emission as a second selection criterion to decrease the number of CV candidates (see Pretorius & Knigge 2007 for an application of a combination of variability- and X-ray emission-based selection cuts), although this will entail a sacrifice in depth and an increase in the complexity of selection effects.

The short-baseline variability surveys mentioned above are useful mainly for detecting DNe. A second type of large amplitude variability, which has much lower duty cycle, is nova eruptions. The observed population of classical novae may be a particularly useful sample to compare to predictions, since (i) known novae were all discovered in exactly the same way, namely through their nova eruptions, (ii) all CVs are expected to undergo

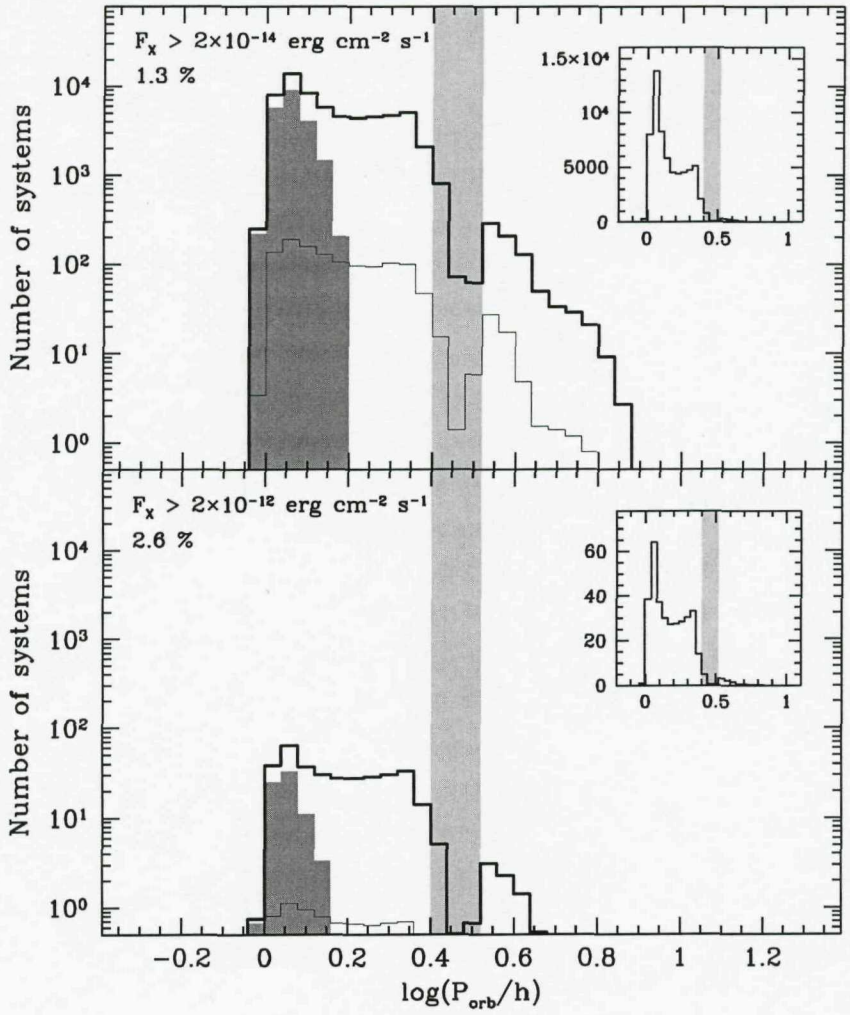

Figure 6.1: Predicted X-ray flux-limited all-sky CV samples, produced by model A1 (see Table 3.2). The flux limit is $F_X > 2 \times 10^{-14}\,\mathrm{erg\,cm^{-2}s^{-1}}$ in the upper panel and $F_X > 2 \times 10^{-12}\,\mathrm{erg\,cm^{-2}s^{-1}}$ in the lower panel. The period distributions of all systems detected are plotted as bold histograms, the contribution of period bouncers is shaded in dark grey, and the fine black histograms show DNe that were simulated in outburst. Light grey shading indicates the period gap. The ratio of short- to long-period systems is 98.7 : 1.3 and 97.4 : 2.6 for the faint and bright flux limits, respectively. The histograms are scaled in the same way as those in Fig. 3.2.

nova eruptions, (iii) novae at maximum are approximately standard candles, and (iv) the frequency of nova eruptions depends on $\dot{M}$ averaged over evolutionary time-scales. The recurrence time of nova eruptions can be predicted from M_1 and $\dot{M}$ (and, therefore, as a function of P_{orb}; Townsley & Bildsten 2004).

There are 48 known novae with periods below 5 h. This is of course a very incomplete subset of all CVs that had nova eruptions over the past few centuries. This sample can be restricted by a cut in peak apparent brightness, but even then, it will contain period-dependent biases if the brightness of a nova remnant (which affects the probability of recovering a system and measuring P_{orb}) or the peak brightness (which is related to the discovery probability) is correlated with P_{orb}. Townsley & Bildsten (2005) neglect selection

biases and conclude that the observed period distribution of classical novae is consistent with standard CV evolution theory; however, it is really not clear that selection effects are insignificant. Selection effects impacting on the P_{orb} distribution can in principle be modelled, but thus far only M_1-dependent biases have been studied in detail (Ritter et al. 1991).

All my simulations have used the same model for the intrinsic population as input. The populations resulting from the other models of Kolb (1993), as well as the model of Howell et al. (1997) are similar to this predicted population. However, it would be useful to repeat the comparisons to observed samples with different population synthesis models. It is already clear that the majority of alternative theories does not represent an improvement over the standard theory (see Section 2.8), but scenarios that would be worth testing in this way include the weaker magnetic braking law of Ivanova & Taam (2003). It is also possible to compute an empirical evolutionary sequence, using mass loss rates derived from observations of donor stars (Knigge 2006).

6.1.2 Limitations of the model

Many details of the modelling can be questioned. Probably the most serious potential flaw is in the SED model, and particularly the emission from the disc. Very good models for optically thin discs simply do not exist, and not much progress has been made since the work by Tylenda (1981a), who assumes a a stationary disc structure, with emission line formation in optically thin outer annuli. The stationary disc assumption is clearly incorrect for the majority of CVs, and it is likely that the disc chromosphere is more important for emission line formation in CVs. The most unreliable predictions of the SED model are probably emission line strengths and $U-B$ colours—both of these are important in the surveys discussed in Chapter 3 and 4.

To assume that discs radiate as blackbodies at all $\dot{M}$ is clearly not an improvement, but this assumption can be made the sake of an instructive comparison. I have therefore made the simple check of using equation A6 of Webbink et al. (1987) to calculate the absolute V magnitude of the disc from $\dot{M}_d$, M_1 and i, and compared the results to those obtained using the Tylenda (1981a) disc model. All other SED components were treated in the same way. With a blackbody disc spectrum, the difference in brightness between low- and high-$\dot{M}$ discs is slightly smaller than predicted by Tylenda (1981a). This means that, in a flux-limited survey, the predicted ratio of long- to short-period CVs is smaller with the blackbody disc assumption. As an example, the ratio of long- to short-period CVs is predicted to be 13 : 87, using model A1, and a magnitude limit of $V < 16$; this ratio is 19 : 81, using the Tylenda (1981a) disc model (see Section 3.3.1). Therefore, the PG and SHS CV samples would be even more inconsistent with predictions if, instead of a more sophisticated disc model, I had simply assumed a blackbody disc spectrum.

DN outbursts are a second disputable aspect of the model. Although the outburst treatment is based mainly on empirical estimates of absolute magnitudes at maximum, it also includes several less secure assumptions.

In all cases where poorly constrained parts of the model can be expected to be important, I have shown that the results do not depend very sensitively on these assumptions. The conclusions regarding the ratio of short- to long-period CVs derived from the PG and SHS CV samples are quite robust.

An improvement to the treatment of Galactic structure would be to use the age of every CV in the simulation, as given by the population synthesis model, to assign systems to a larger number of populations, with a much finer division in scaleheights. Some surveys might also warrant more detailed Galactic structure models than the smooth, axisymmetric Galactic discs I assumed. IPHAS might be an example of a survey where spiral structure has a significant impact (evidence of spiral structure, and also of the warp of the Galactic disc, in IPHAS data is presented by Witham et al. 2008). Inhomogeneities may also be important in surveys that cover only small areas (since such a survey may, e.g., happen to cover an over- or under-density of stars, or an area of unusual extinction). I used a more detailed extinction model in the work on the NEP survey for this reason, but still relied on the simple assumption of a smooth distribution of stars. Detailed models of Galactic structure already exist, and Rogel et al. (2007) present an application to CVs.

Although modelling observational bias is not a simple problem, it has to be faced. The unavoidable fact is that selection effects must somehow be accounted for in observational work on CV evolution.

6.2 The orbital period distribution of CVs

The Monte Carlo code was used to model the selection effects acting on two CV samples—one selected for blue $U-B$ colours from the PG Survey, and the other selected on the basis of Hα emission from the SHS.

I showed that selection effects cannot reconcile the predictions of standard CV evolution theory with the properties of the PG survey CV sample. In particular, the standard model predicts a much higher fraction of short-period systems and period bouncers than is observed. This result was confirmed using the new SHS CV sample. Because the Galactic plane Hα-selected sample and the high Galactic latitude blue-selected PG sample are subject to different selection biases, concerns regarding details of the SED and Galactic structure models are alleviated by the consistent results from these two independent samples.

As the largest uniform and supposedly complete (e.g. Ringwald 1994) CV sample, the PG sample has had fairly large impact in observational studies of CV evolution. It has been used to estimate the CV space density (Ringwald 1993; Patterson 1998), the fraction of eclipsing CVs (Ringwald 1994), and the size of the period bouncer population (Patterson 1998). However, the magnitude distribution of CVs from the PG survey shows that the depth of the sample was significantly overestimated. This does not imply very large errors in an estimate of the space density of long-period CVs, since their luminosity function does not rise steeply towards faint magnitudes, but it certainly matters for placing

limits on the size of the intrinsically faint period bouncer population. Considerable care needs to be taken in understanding the completeness of a CV sample before it is used in a quantitative study of CV evolution.

I showed that any P_{orb}-dependent incompleteness in the Hα-selected CV sample presented in Chapter 4 goes in the direction of making the sample biased against long-period CVs, and therefore cannot invalidate my result regarding the relative sizes of the long- and short-period CV populations. However, the low and uncertain completeness would be a serious concern if this sample is used, e.g., to constrain the CV space density. Furthermore, the sample is quite small and not very deep. These problems are related to the poor photometric accuracy of the photographic survey. Even with very conservative selection cuts, which certainly exclude a large fraction of CVs (see Section 4.4.1), the low hit rate for identifying emission line objects places a quite severe limit on the number of CVs that can practically be found using data from the SHS. With the use of large CCDs, it is now possible to perform surveys with similarly wide area coverage, but much better photometric quality. It is likely that the Hα-selected CV sample I constructed will soon be superseded by a much larger sample from IPHAS (the discovery of the first IPHAS CVs is presented by Witham et al. 2007).

Despite the shortcomings of the PG and SHS CV samples, there are currently no better observational samples available, and the PG and SHS data are sufficient for deriving some important results. However, these two samples are not deep enough to have much sensitivity to period bouncers. Constraints on the relative sizes of the period bouncer and normal short-period CV populations will require the results of surveys such as IPHAS or the SDSS.

6.3 The space density of CVs

The *ROSAT* NEP survey produced a sample of 4 CVs that is complete and purely X-ray flux-limited, and therefore does not suffer from any complicated systematic bias. I used this survey to estimate the space density of CVs, including, for the first time, all sources of uncertainty. The resulting estimate is imprecise, but is the first realistic attempt at a measurement better than an order of magnitude estimate.

The *ROSAT* NEP sample is small, and what makes this worse is that it includes a system with very unusual L_X for its P_{orb} (the long-period system, EX Dra). Nevertheless, there is probably no better CV sample for this particular purpose (although the *ROSAT* Bright Survey is a possibility; see below).

It is not simple to compare the results of the Hα-selected or PG samples to the new ρ measurement, since the samples both have rather uncertain completeness. I found (see Section 4.6.2) that the Hα-selected sample is consistent with a space density of $10^{-6}\,\mathrm{pc}^{-3}$ for long-period CVs, although it requires a quite low completeness (8%, compared to the 15% estimated from recovery of previously known CVs). The same comparison can be made for CVs from the PG Survey. Again setting $\rho_l = 10^{-6}\,\mathrm{pc}^{-3}$, and assuming that

the model mass transfer rates of long-period CVs, as well as the Galaxy and SED models described in Chapter 3, are correct, $\simeq 18$ long-period CVs should have been detected in the PG survey if the completeness of the survey is 100% (here a limiting magnitude of $B = 15.5 \pm 0.4$ is assumed; see Section 3.5). There are 14 or 15 non-magnetic CVs with periods between the top of the period gap and 5 h in the observed sample. This means that the long-period PG CV sample is consistent with the prediction—a completeness of about 78% is required for the predicted and observed numbers to agree[1].

Both the PG and Hα long-period CV samples then seem to be consistent with the model, provided that $\rho_l \sim 10^{-6}\,\mathrm{pc}^{-3}$. The available observational estimates of ρ_l are $\sim 2.5 \times 10^{-6}$ and $\simeq 8 \times 10^{-6}$ (Patterson 1998; Chapter 5). These are both higher than, but consistent with $\rho_l \sim 10^{-6}\,\mathrm{pc}^{-3}$ (especially considering that the ρ_l measurement of Chapter 5 is expected to be high, because of the unusually low L_X of EX Dra). However, the uncertainties are so large that this is not a very constraining result.

Theoretical predictions of ρ are very uncertain, since they depend on knowledge of the space density of single white dwarfs, the evolutionary time-scales of CVs and pre-CVs, the efficiency of common envelope evolution, and the formation rate and distribution of primordial binaries in P_{orb} and q. The dependence of ρ on the more uncertain aspects of CV formation and evolution theory has not been fully explored. However, an observational constraint on ρ clearly has potential value in guiding theory. I have found that the space density of CVs with $L_X \gtrsim 5 \times 10^{29}\,\mathrm{erg\,s}^{-1}$ is $1.1^{+2.3}_{-0.7} \times 10^{-5}\,\mathrm{pc}^{-3}$. The predicted $\simeq 2 \times 10^{-4}\,\mathrm{pc}^{-3}$ requires $L_X \lesssim 2 \times 10^{29}\,\mathrm{erg\,s}^{-1}$ for the majority of CVs in the intrinsic population.

It is possible to give an indication of whether this limit on L_X is consistent with the other properties of the predicted CV population. I again use the relation of Patterson & Raymond (1985a), repeated as equation 6.1 above, to find the L_X distribution of the model intrinsic CV population, for both the assumptions $\dot{M} = \langle \dot{M} \rangle$ and $\dot{M} = \dot{M}_d$. In the calculation using $\dot{M} = \dot{M}_d$, $\dot{M}_d$ was obtained as described in Section 3.2.4, and it is assumed that the probability of a DN being in outburst equals the outburst duty cycle. This gives the PDF of L_X at a single epoch. For about 20% of CVs in the model population, $\dot{M}_d = 0$ is assumed (see Table 3.1); for these I set $L_X = 0$.

The *ROSAT* passband (0.1 to 2.4 keV) is narrower and softer than the 0.2 to 4.0 keV passband used by Patterson & Raymond (1985a). I have not accounted for this difference, but, for a thermal bremsstrahlung spectrum with kT between 5 and 20 keV, the resulting error in L_X is only a factor of $\simeq 2$.

Fig. 6.2 shows the PDF of L_X for both $\dot{M} = \langle \dot{M} \rangle$ (fine histogram) and $\dot{M} = \dot{M}_d$ (bold histogram). The majority of CVs in the intrinsic population is predicted to be much brighter than $2 \times 10^{29}\,\mathrm{erg\,s}^{-1}$ in X-rays. Errors introduced by the X-ray spectral shape and the mismatch of band-passes cannot reduce L_X by the 1 or 2 orders of magnitude required to make a large fraction of the model population fainter than $L_X \lesssim 2 \times 10^{29}\,\mathrm{erg\,s}^{-1}$.

[1] Green et al. (1986) estimated that the PG survey completeness to $B = 16.16$ is between 66 and 86%, but I showed in Section 3.5 that this cannot be true for the CV sample.

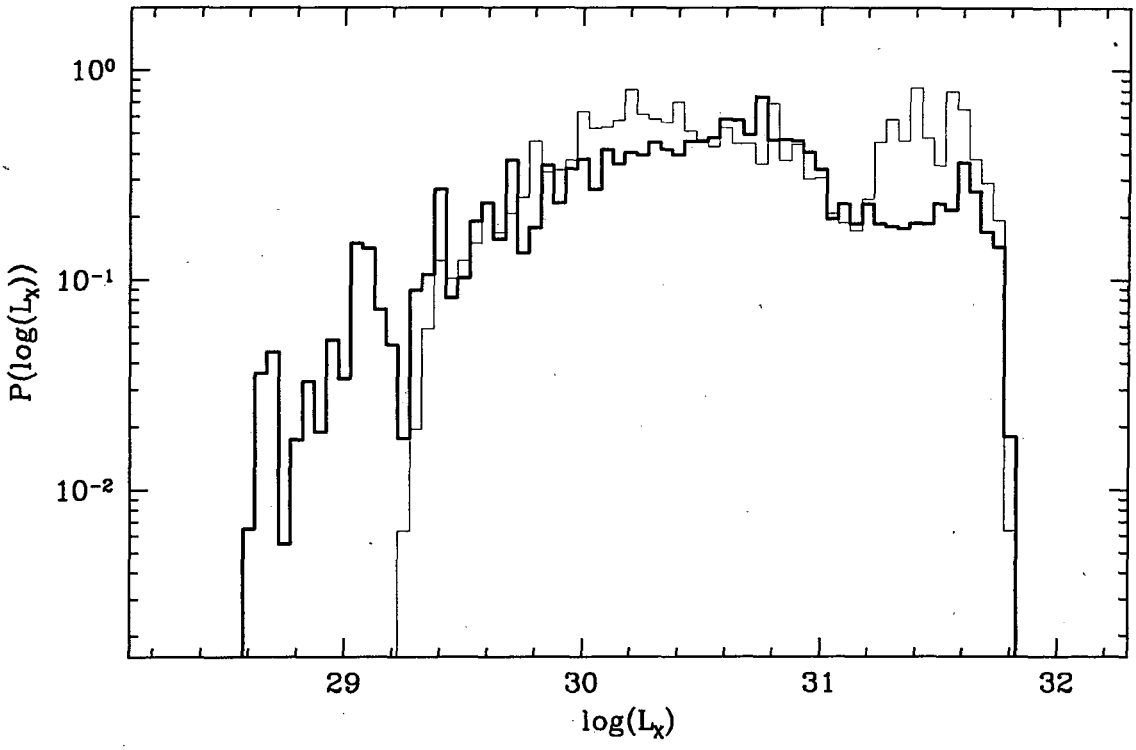

Figure 6.2: The PDF of the intrinsic CV population in L_X. The fine histogram uses $\dot{M} = \langle \dot{M} \rangle$ in the Patterson & Raymond (1985a) relation, whereas $\dot{M} = \dot{M}_d$ is assumed for the bold histogram. For the bold histogram, roughly 20% of the distribution is not shown on the scale given, because $\dot{M}_d = 0$ for these systems in the model (see Section 3.2.4).

It could be that, during quiescence of low-$\dot{M}$ systems, no material reaches the white dwarf surface, perhaps because the inner accretion disc is truncated[2]. While the scatter of data around the L_X–$\dot{M}$ relation is large (see fig. 7 of Patterson & Raymond 1985a), there is no observational evidence that it predicts X-ray luminosities that are systematically high for low-$\dot{M}$ CVs. However, very few of the low-$\dot{M}$ CVs in the sample of Patterson & Raymond (1985a) can be expected to be period bouncers, so that the relation certainly is not proven to be valid for period bouncers. Neither of the confirmed period bouncers has been detected in X-rays, so that perhaps the most useful specific example to look at is WZ Sge. It is not clear whether WZ Sge is a period bouncer (Steeghs et al. 2007), but it is considered a good candidate (e.g. Patterson 1998; Howell et al. 2004). It has $L_X \simeq 4 \times 10^{29}\,\mathrm{erg\,s^{-1}}$ (Wheatley et al. 2000) and $\dot{M}_2 \sim 10^{15}\,\mathrm{g\,s^{-1}}$ (estimated from the quiescent bright spot luminosity; Patterson et al. 2002b). It is expected to be brighter than most period bouncers, because it has either not reached the period minimum yet, or has not evolved very far away from it (it has $P_{orb} = 81.63$ min.; Krzemiński & Smak 1971), but its X-ray luminosity is about an order of magnitude below what the relation of

[2]It has been suggested that truncation of the disc might explain some of the phenomenology of low-$\dot{M}$ systems, e.g., the size of the UV delay (see Section 2.3.1.1) and the absence of DN outbursts in VY Scl stars in the low state (e.g. Livio & Pringle 1992; Hameury et al. 1999; Hameury et al. 2000; Hameury & Lasota 2002).

Patterson & Raymond (1985a) gives for this $\dot{M}$ (note, however, that the measured $\dot{M}$ is not $\dot{M}_1$ in quiescence, and is not very precise). Therefore, if WZ Sge is a period bouncer, and if its L_X and $\dot{M}$ are representative of the values for period bouncers, it is possible that many CVs do not obey the Patterson & Raymond (1985a) L_X–$\dot{M}$ relation (although it is not clear why period bouncers should generally be fainter in X-rays than normal short-period CVs with similar $\dot{M}$).

Unless the L_X–$\dot{M}$ relation does overestimate L_X by a factor of 10 or more for a large fraction of CVs, most CVs in the predicted intrinsic population have $L_X > 2 \times 10^{29}\,\mathrm{erg\,s^{-1}}$. This cannot be decreased by lowering $\dot{M}$, because it already assumes that angular momentum loss in short-period CVs is driven by gravitational radiation alone. Then a space density as high as $\simeq 2 \times 10^{-4}\,\mathrm{pc^{-3}}$ is inconsistent with the NEP survey data.

6.3.1 Possible future measurements of ρ

As mentioned in Chapter 4 and 5, and Section 6.1.1, there are several ongoing surveys that will produce large new samples of CVs; these include the Hamburg Quasar Survey, the SDSS, and IPHAS. The PG survey CV sample is already available, but since the completeness of this sample is somewhat questionable, it is perhaps not ideal for a rigorous measurement of ρ.

At present only one other CV sample is really well suited to another measurement of ρ. This is the sample of non-magnetic CVs detected in the *ROSAT* Bright Survey. The measurement of Schwope et al. (2002) can be repeated with a full accounting for uncertainties and better distance estimates. This would complement the NEP survey measurement, since, while the *ROSAT* Bright Survey CV sample is not as deep, it is significantly larger than the NEP sample.

The *XMM-Newton* Large Scale Structure Survey will cover $64\,\mathrm{deg^2}$ of sky to a flux limit of $3 \times 10^{-15}\,\mathrm{erg\,cm^{-2}s^{-1}}$ (e.g. Valtchanov & Pierre 2003). Of all large present surveys, this will probably provide the best CV sample for the problem of placing tight constraints on the space density of CVs. The main difficulty in obtaining this measurement will be the follow-up required to identify all CVs in the survey.

It would be of some value to have a new estimate of the Galactic scaleheight (or, more correctly, scaleheight distribution) of CVs, but it is not often acknowledged how challenging such a measurement really is. Existing observational estimates of the CV scaleheight probably all reflect the increasing incompleteness of samples with distance, rather than the Galactic distribution of CVs. An illustrative example is the recent measurement by Ak et al. (2008), using a sample of CVs with uncertain distance estimates, and unknown completeness. In the bottom panel of Fig. 6.3, I have plotted the z histogram from which Ak et al. (2008) measured a scaleheight of $179 \pm 13\,\mathrm{pc}$. CVs in this sample are not distant enough to probe the radial density distribution of the Galaxy. Therefore, in the absence of serious biases, the same vertical density profile should be obtained if the sample is divided into sub-samples consisting of systems inside concentric cylindrical shells with axis perpendicular to the Galactic plane. However, when the sample is divided into

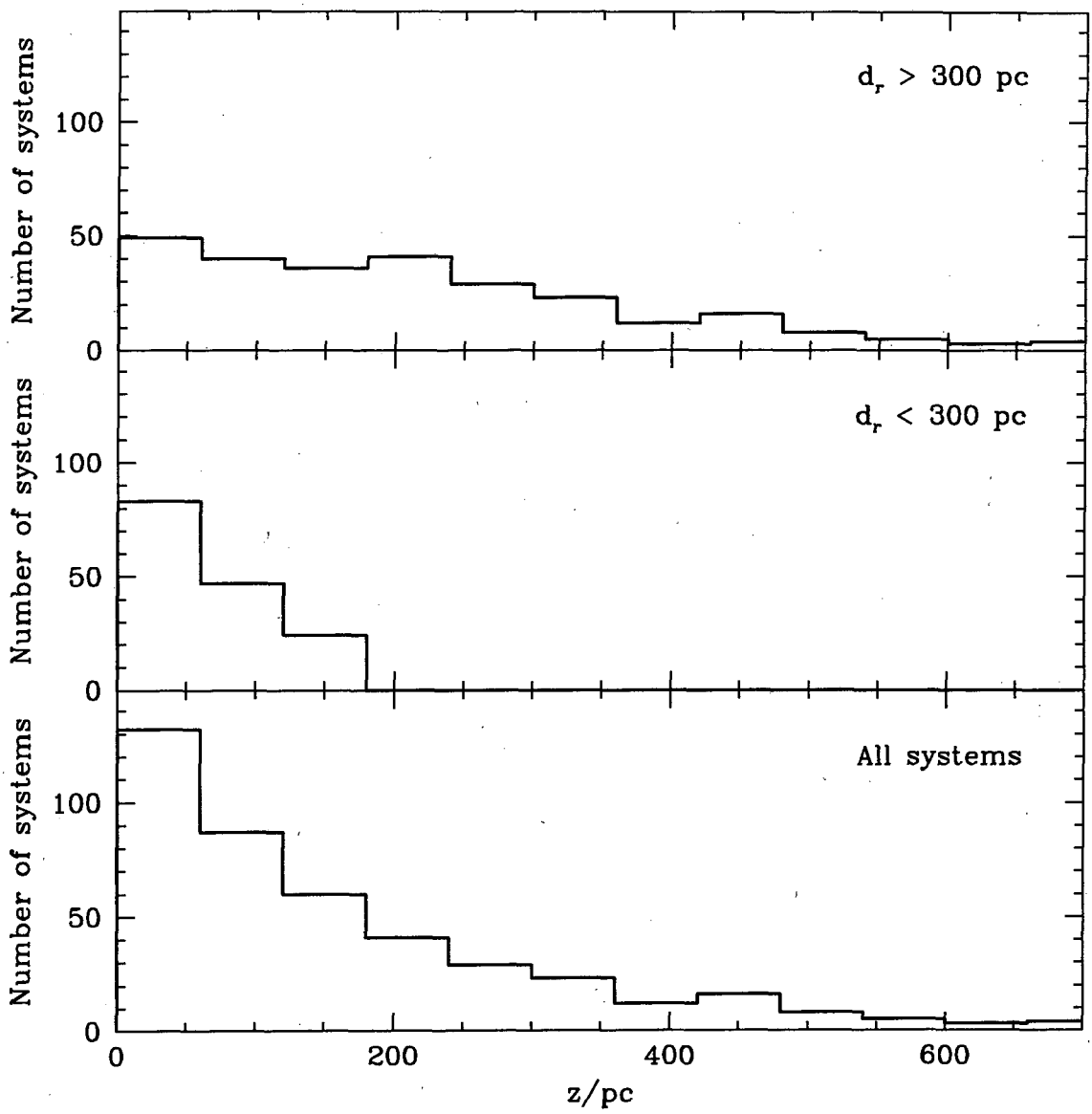

Figure 6.3: The distribution in z of CVs in the sample of Ak et al. (2008). The bottom panel shows the z-distribution of all systems in the sample used to measure $h = 179 \pm 13$ pc (these are CVs with estimated $J_0 \leq 16.5$). In the two upper panels, the sample is divided, using the distance component perpendicular to z, into systems at distances in the Galactic plane greater than or less than 300 pc. The three distributions clearly have very different scaleheights, although the radial scalelength of the Galaxy is too large for the vertical density profile to vary measurably in the area within several 100 pc of the Sun.

systems with cylindrical radial distances greater or less than 300 pc, the z-distributions of the sub-samples are markedly different (see the upper panels of Fig. 6.3). It is clear that a scaleheight measurement based on this sample is suspect, and that the quoted error of ± 13 pc is incorrect. The same problem probably affects the CV samples used for scaleheight measurements by Patterson (1984) and Duerbeck (1984).

6.4 Implications for CV evolution theory

With the small CV samples available at the moment, it is already possible to recognize the qualitative changes that are needed to reconcile theory with observations.

If the formation of CVs inside some period interval is unimportant compared to the number of systems entering the period interval by evolving down from longer periods, then the number of CVs in that interval is proportional to the time taken to evolve through it. It is then possible to constrain the ratio of time-scales of distinct phases of evolution, using the ratio of the numbers of systems detected in those phases. This is because the function that accounts for the relative severity of the selection effects acting on CVs in distinct period intervals is monotonic (at least for the simple case of a sample in which the most important bias is due to a flux limit). Together with the assumption that the model is correct for long-period CVs, this allowed me to find the constraint $\dot{J} \gtrsim 3\dot{J}_{GR}$ for short-period CVs from the Hα-selected sample (see Section 4.6.3).

For the PG CV sample, I found $(n_l/n_s)_{pred} \simeq 10/90$, compared to an observed ratio of $(n_l/n_s)_{obs} \geq 14/13$, in Section 3.5. With the same reasoning as in Section 4.6.3, this implies that the evolutionary time-scale of short-period CVs in the model is too long by more than a factor of 9. This is surprisingly large, especially when compared to the result of Patterson (2001), who finds that $-\dot{J} = -3\dot{J}_{GR}$ for short-period CVs provides a satisfactory fit to his data. This hints that the assumption $(\tau_l)_{pred} = \tau_l$ may be wrong. The observational constraints on the size of the long-period CV population and $\dot{M}$ above the period gap are not sufficiently precise to answer this question definitively, but it certainly has been suggested that the Verbunt & Zwaan (1981) magnetic braking law used in the model is too strong (e.g. Ivanova & Taam 2003). The model may therefore not only predict too many short-period CVs, but also too few long-period CVs.

In this regard, it is also worth noting that recent estimates of $\dot{M}$ in a small sample of short-period CVs are consistent with the values expected from angular momentum loss through gravitational radiation (Littlefair et al. 2006; Littlefair et al., in preparation)[3]. However, Townsley & Bildsten (2003) found $\dot{M}$ higher than predicted for short-period CVs and lower than predicted for long-period CVs, using measurements of white dwarf T_{eff} tabulated by Winter & Sion (2003). It is not clear how to reconcile these results, but a possible resolution is that many white dwarf T_{eff} measurements in non-eclipsing CVs are unreliable, because contamination from light originating from the disc or boundary layer is not correctly accounted for.

$-\dot{J} > -3\dot{J}_{GR}$ for short-period CVs from the SHS sample is obviously in itself consistent with $-\dot{J} > -9\dot{J}_{GR}$ from the PG survey. It is also to be expected that the SHS sample has produced a weaker constraint. The reasons for this are the very conservative assumptions about variability and EW-dependent biases made in the case of the Hα sample, and also the larger number of CVs in the Hα-selected sample without period mea-

[3]Littlefair et al. (2007) have also estimated $\dot{M}$ for SDSS J150722.30+523039.8, but they find that this system probably has an unusual evolutionary history (it is argued that SDSS J150722.30+523039.8 did not evolve through the period minimum, but rather formed with a secondary of substellar mass).

surements. Basically, the factor of > 3 is an underestimate unless (i) all the CVs without periods are short-period systems, (ii) the EW-based bias does not preferentially exclude long-period CVs, and (iii) it really is the case that variability has excluded a significant number of short-period systems but no long-period systems. Clearly these assumptions are conservative, rather than reasonable.

Although it is not possible to distinguish between too short $(\tau_l)_{pred}$ and too long $(\tau_s)_{pred}$ using the PG and SHS CV samples, $\tau_s < (\tau_s)_{pred}$ is favoured as the dominant effect explaining the large predicted ratio of short- to long-period CVs. Amongst the reasons are that $-\dot{J} > -\dot{J}_{GR}$ for short-period CVs may in addition solve the problem of the theoretical position of the period minimum (see also the discussion in Section 2.8.1 and 4.6.3).

Higher angular momentum loss rates in short-period CVs may also be important to the problem of mass transfer cycles. Large scatter is seen in estimates of $\dot{M}$ and absolute magnitudes of CVs at fixed P_{orb} (see Warner 1987 and especially fig. 7 of Patterson 1984). However, since these measurements are subject to large uncertainties, the fact that DNe and NLs are observed in the same ranges of P_{orb} is often taken as the most compelling evidence for mass transfer cycles (e.g. King et al. 1995, 1996). The explanation of DN outbursts in terms of the thermal instability (see Section 2.3.1.1), and the faint absolute magnitudes of DNe relative to NLs (see e.g. fig. 9.8 of Warner 1995) leave little doubt that DNe typically have lower average $\dot{M}$ than NLs.

The implicit assumption that a large difference in $\dot{M}$ is required for NLs and DNe to exist at the same P_{orb} is, however, incorrect. The P_{orb} histograms displayed in, e.g., Fig. 3.2 show that the standard model does allow for long-period DNe. The model population in fact contains similar numbers of DNe and NLs at long periods, but no short-period NLs. Fig. 2.3 shows that short-period NLs are rare in the observed CV sample, while the non-magnetic, long-period CV sample is almost evenly split between DNe and NLs[4].

The model population would contain short-period NLs if $-\dot{J}$ is increased below the period gap. Again using equations 38 and 39 of Hameury et al. (1998) to distinguish between stable and unstable discs (see Section 3.2.4), short-period NLs appear in the model population when $\langle\dot{M}\rangle$ in short-period systems is increased by a factor of 4. Fig. 6.4 shows the distribution of the predicted intrinsic population over $\langle\dot{M}\rangle$ and P_{orb}, after the predicted $\langle\dot{M}\rangle$ of short-period CVs is increased by a factor of 6; for secondaries near the main sequence, this is equivalent to $\dot{J} = 6\dot{J}_{GR}$ (see e.g. equation 2.17)[5]. In the lower panels of Fig. 6.4, DNe and NLs are shown separately; a small population of short-period NLs is predicted.

Therefore, accepting that gravitational radiation is not the only angular momentum loss mechanism in short-period CVs, and if the observationally inferred values of $\dot{M}$ that

[4]There are 387 known DNe and NLs. Roughly the same numbers of the two subtypes occur above the period gap (82 DNe and 75 NLs), while only about 7% of short-period, non-magnetic CVs are NLs, and the majority of short-period NLs are in the period gap.

[5]Note that, realistically, the position of the evolutionary track cannot only be shifted upward in the $\langle\dot{M}\rangle$–P_{orb} plane—an increase in $\langle\dot{M}\rangle$ below the period gap also shifts the position of the period minimum.

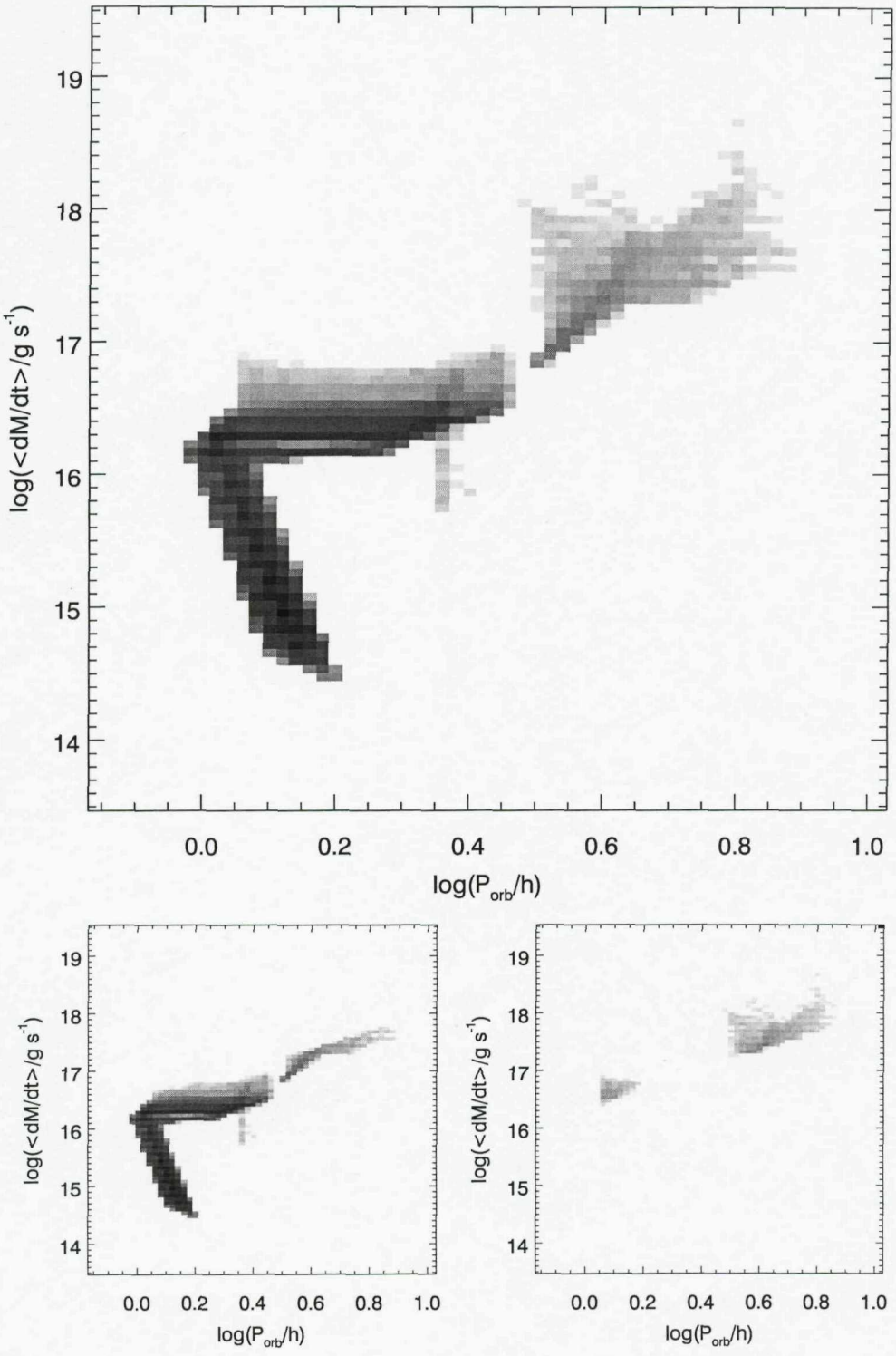

Figure 6.4: The distribution of the predicted intrinsic CV population in the $\langle \dot{M} \rangle$ vs P_{orb} plane, after $\langle \dot{M} \rangle$ of short-period CVs is scaled by 6. The grey-scale is logarithmic, and represents the number of systems in each ($\langle \dot{M} \rangle$,P_{orb}) bin. The upper panel shows all model CVs. In the lower panels, the population is divided into DNe (left) and NLs (right). Short-period NLs exist in the predicted population if $\langle \dot{M} \rangle$ is increased for short-period CVs.

do not rely simply on CV subtype (those of e.g. Warner 1987 and Patterson 1984) are not considered compelling evidence for mass transfer cycles, then such cycles are not required by observations.

Another motivation for assuming $-\dot{J} > -\dot{J}_{GR}$ for short-period CVs is that it would mean that the lifetime of a CV may be shorter than the age of the Galaxy, thereby reducing the predicted space density of CVs. In Section 6.3 above I have shown that the high theoretical values of ρ can only be consistent with the NEP survey result if a quite extreme assumption is made about the relation between L_X and $\dot{M}$. It has of course long been argued that the predicted values of ρ are too high, but this was based on incomplete samples that, in a realistic calculation, could not decide the issue.

All of the alternative scenarios for CV evolution discussed in Section 2.8 rely on some aspects of the standard model (and none of them has yet been shown to be very successful). A few more radically different theories have also been proposed, but these seem to be seriously flawed. Clemens et al. (1998) suggest that the period gap is caused by a change in the slope of the secondary mass–radius relation, but this has been discredited by Kolb et al. (1998). Motivated by the proposal that magnetic braking is much weaker than usually assumed (Andronov et al. 2003), Andronov & Pinsonneault (2004) discuss the the possibility that the period gap is produced by two bursts of star formation, together with the finite age of the Galaxy (in this model, the present-day long-period CVs do not have time to evolve into short-period CVs, while the short-period CVs were formed in the earlier star formation burst). However, it is of course essentially impossible to reproduce the sharp edges of the observed period gap in this way.

It is worth pointing out that available population synthesis models generally assume a Galactic age of 10 Gyr or more. There is evidence that the Galactic thin disc is only 7 to 8 Gyr old, while the thick disc is no older than 10 Gyr, and has a scaleheight of $\sim$750 pc and a density more than a factor of 10 lower than that of the thin disc (e.g. Reylé & Robin 2001; Siegel et al. 2002; Reid 2005). If this is correct, the oldest CVs in the predicted populations should be removed, which would reduce the predicted number of period bouncers.

A successful model of CV evolution has to predict a smaller ratio of short- to long-period CVs, and very likely also a smaller space density, than the standard theory. It may be that both these requirements can be met without any fundamental change to the standard evolution model, but simply by assuming a smaller Galactic age, and a weaker magnetic braking law. However, this will not change the predicted position of the period minimum. It seems that the only promising way of adjusting the predicted minimum period is an increase in the angular momentum loss rate below the period gap (e.g. Kolb & Baraffe 1999), and that this would also be a solution to other discrepancies between theory and observations. If the additional angular momentum loss is supplied by magnetic braking (which would be in accord with the indications that magnetic braking does act in fully convective stars; e.g. Tout & Pringle 1992a; Jones et al. 1996; Andronov et al. 2003) then this needs to be done in a way that still leads to a period gap. King et al. (2002)

point out that the conventional explanation of the period gap requires only that magnetic braking is at least temporarily interrupted; the period gap would be preserved if magnetic braking resumes at periods below $\simeq 2\,\mathrm{h}$.

Although surveys now in progress will in future be capable of providing much better observational constraints on CV evolution than can be derived at the moment, it is already clear that the standard magnetic braking model is in need of revision. Furthermore, it seems that the correct approach to take is to investigate primarily angular momentum loss rates in excess of the gravitational radiation rate in CVs below the period gap.

Chapter 7

Conclusions

I have presented empirical constraints on the space density and composition of the intrinsic CV population. Some of these constraints were obtained by applying more rigorous modelling to the existing PG survey CV sample, but I also constructed two new samples with specific goals in mind. One of these is a complete X-ray flux-limited sample of CVs detected in the *ROSAT* NEP survey. The second is a Galactic plane CV sample, selected on the basis of Hα emission from the SHS. This the largest Hα-selected CV sample constructed to date.

The new observations obtained for the definition of the Hα-selected and *ROSAT* NEP CV samples represent a significant fraction of the work presented here. I discovered 18 CVs in total, and measured the orbital periods of 13 of these systems.

The constraints these data, together with the simulations described in Chapter 3, 4 and 5, place on both the size and period distribution of the intrinsic CV population are the most quantitative available. Beyond these results, the work may be of lasting value, since the method for modelling observational biases developed here is likely to be the only practical approach to confronting a theoretical evolutionary scenario for CVs with observations.

The most important conclusions from the three different studies presented in this thesis are repeated below.

1. A simulation of the selection effects present in the PG survey shows that observational biases are not sufficient to reconcile the intrinsic population predicted by standard CV evolution theory (with strong magnetic braking above the period gap and only gravitational radiation below the gap) with the observed PG CV sample. The intrinsic CV population cannot contain as large a fraction of short-period systems as is predicted by theory.

2. I confirmed the result based on the PG survey by comparing a homogeneous new CV sample, selected for Hα emission, to the same model population. Standard CV evolution theory predicts relatively too many short-period CVs; this is true even with the assumption that period bouncers are undetectable.

3. The high Galactic latitude, blue-selected PG CV sample and the Galactic plane, Hα-selected SHS CV sample are independent, and subject to very different selection biases. The consistent result from these two surveys relieves concerns regarding uncertainties in the modelling of Galactic structure and the SEDs of CVs.

4. The favoured explanation for the mismatch between the predicted and observed ratio of short- and long-period CVs is that short-period systems evolve faster than predicted by the disrupted magnetic braking model, so that the predicted population of short-period CVs is too large. The relative numbers of long- and short-period CVs included in the Hα-selected sample, together with the modelling of selection effects, indicates that the disrupted magnetic braking model underestimates $-\dot{J}$ of short-period CVs by a factor of at least 3 (assuming that the predicted evolutionary time-scale of long-period CVs is correct).

5. The same argument, applied to the PG CV sample, indicates that the model $-\dot{J}$ of short-period CVs is at least a factor of 9 too low. This is surprisingly large and suggests that the model may predict not only too many short-period CVs, but also too few long-period CVs.

6. It is clear from these observations (as well as from the position of the period minimum) that the standard magnetic braking model of CV evolution is in need of revision. Furthermore, it seems that the change required is a mechanism of angular momentum loss, besides gravitational radiation, acting on CVs below the period gap.

7. In the standard model, both DNe and NLs occur at all periods above the period gap, and if predicted angular momentum loss rates for short-period CVs are increased to $-\dot{J} \gtrsim -4\dot{J}_{GR}$, then the predicted population also contains short-period NLs. With such higher angular momentum loss rates below the period gap, mass transfer cycles are thus no longer required to explain the existence of DNe and NLs in the same P_{orb} intervals.

8. With the assumption that the 4 CVs included in the *ROSAT* NEP survey are representative of the intrinsic CV population, the space density of CVs is $1.1^{+2.3}_{-0.7} \times 10^{-5}\,\mathrm{pc}^{-3}$.

9. Space densities as high as the theoretically predicted $\simeq 2 \times 10^{-4}\,\mathrm{pc}^{-3}$ are ruled out by the NEP survey data, unless the dominant CV population is fainter than $\simeq 2 \times 10^{29}\,\mathrm{erg\,s}^{-1}$ in X-rays.

10. Assuming that the L_X–$\dot{M}$ relation of Patterson & Raymond (1985a) does not underestimate L_X for low-$\dot{M}$ CVs by about an order of magnitude, only a small fraction of the predicted intrinsic CV population consists of systems with $L_x \lesssim 2 \times 10^{29}\,\mathrm{erg\,s}^{-1}$. Since $-\dot{J} \geq -\dot{J}_{GR}$, short-period CVs cannot have lower $\dot{M}$ than predicted by this model. The CV space density then cannot be as high as $\simeq 2 \times 10^{-4}\,\mathrm{pc}^{-3}$.

11. Stellar populations of different typical ages have different Galactic scale heights. Significant errors result if this fact is neglected when deriving the total Galactic numbers of long-period CVs, short-period CVs, and period bouncers from the mid-plane space densities of these three populations.

12. The apparent magnitude distribution of the sample of all known non-magnetic, hydrogen-rich CVs with period measurements suggests this sample is not approximately complete, even to $V = 13$.

13. For practically achievable optical flux limits, no flux-limited CV sample can be expected to be representative of the intrinsic CV population. It is therefore quite inappropriate to compare an observed sample with the predicted intrinsic population.

14. The properties of the period distribution of a magnitude-limited sample depend strongly on the magnitude limit. The ratio of short- to long-period systems and the prominence of the spike near the period minimum decrease at brighter magnitude limits.

15. A blue selection cut of $U - B \lesssim -0.7$ introduces a serious bias against detecting short-period CVs. However, for existing UV-excess surveys, the systems that would fail to be detected because of this bias are already excluded by the survey flux limits.

16. Magnitude-limited surveys at high Galactic latitude are expected to yield CV samples that are very different from those produced by Galactic plane surveys, because they detect a larger fraction of all systems inside the volume defined by the galactic latitude range. However, even a deep, high-$|b|$ survey such as the SDSS is not volume limited for CVs.

17. The mass-transfer rates predicted by standard CV evolution theory are inconsistent with empirical estimates of the absolute magnitudes of DNe in outburst, unless the outburst duty cycles of most CVs are much lower than is generally assumed (specifically, $< 10\%$ for normal DN and $< 0.5\%$ for period bouncers).

References

Abbott T.M.C., Shafter A.W., 1997, in Wickramasinghe D.T., Bicknell G.V., Ferrario L., eds, ASP Conf. Ser. Vol. 121, Accretion Phenomena and Related Outflows. Astron. Soc. Pac., San Francisco, p. 679

Abt H.A., Boonyarak C., 2004, ApJ, 616, 562

Ak T., Özkan M.T., Mattei J.A., 2002, A&A, 389, 478

Ak T., Bilir S., Ak S., Eker Z., 2008, NewAR, 13, 133

Allan A., Hellier C., Ramseyer T.F., 1996, MNRAS, 282, 699

Amari S., Anders A., Virag A., Zinner E., 1990, Nature, 345, 238

Amôres E.B., Lépine J.R.D., 2005, AJ, 130, 659

Andronov N., Pinsonneault M., Sills A., 2003, ApJ, 582, 358

Andronov N., Pinsonneault M.H., 2004, ApJ, 614, 326

Araujo-Betancor S., Gänsicke B.T., Long K.S., Beuermann K., de Martino D., Sion E.M., Szkody P., 2005, ApJ, 622, 589

Augusteijn T., van der Hooft F., de Jong J.A., van Paradijs J., 1996, A&A, 311, 889

Aungwerojwit A., et al., 2006, A&A, 455, 659

Bailey J., 1980, MNRAS, 190, 119

Bailey J., 1981, MNRAS, 197, 31

Bailey J., Cropper M., 1991, MNRAS, 253, 27

Bailey J., Ferrario L., Wickramasinghe D.T., 1991, MNRAS, 251, 37P

Bailey J., Wickramasinghe D.T., Ferrario L., Hough J.H., Cropper M., 1993, MNRAS, 261, L31

Bailyn C.D., Rubenstein E.P., Slavin S.D., Cohn H., Lugger P., Cool A.M., Grindlay J.E., 1996, ApJ, 473, L31

Balbus S.A., Hawley J.F., 1991, ApJ, 376, 214

Baptista R., Catalán M.S., 2001, MNRAS, 324, 599

Baptista R., Catalán M.S., Costa L., 2000, MNRAS, 316, 529

Baraffe I., Kolb U., 2000, MNRAS, 318, 354

Barker J., Kolb U., 2002, in Gänsicke B.T., Beuermann K., Reinsch K., eds, ASP Conf. Ser. Vol. 261, The Physics of Cataclysmic Variables and Related Objects. Astron. Soc. Pac., San Francisco, p. 271

Barker J., Kolb U., 2003, MNRAS, 340, 623

Barlow E.J., Knigge C., Bird A.J., J Dean A., Clark D.J., Hill A.B., Molina M., Sguera V., 2006, MNRAS, 372, 224

Bath G.T., Evans W.D., Pringle J.E., 1974, MNRAS, 166, 113

Bergeron P., Wesemael F., Beauchamp A., 1995, PASP, 107, 1047

Bessell M.S., 1986, PASP, 98, 1303

Beuermann K., 2000, NewAR, 44, 93

Beuermann K., Thomas H.-C., 1990, A&A, 230, 326

Beuermann K., Baraffe I., Kolb U., Weichhold M., 1998, A&A, 339, 518

Billington I., Marsh T.R., Dhillon V.S., 1996, MNRAS, 278, 673

Brinkworth C.S., Marsh T.R., Dhillon V.S., Knigge C., 2006, MNRAS, 365, 287

Brinkworth C.S., et al., 2007, ApJ, 659, 1541

Bruch A., Engel A., 1994, A&AS, 104, 79

Buckley D.A.H., Sekiguchi K., Motch C., O'Donoghue D., Chen A.-L., Schwarzenberg-Czerney A., Pietsch W., Harrop-Allin M.K., 1995, MNRAS, 275, 1028

Buckley D.A.H., Haberl F., Motch C., Pollard K., Schwarzenberg-Czerney A., Sekiguchi K., 1997, MNRAS, 287, 117

Büning A., Ritter H., 2004, A&A, 423, 281

Cambrésy L., Beichman C.A., Jarrett T.H., Cutri R.M., 2002, AJ, 123, 2559

Campbell C.G., 1989, MNRAS, 236, 475

Campbell C.G., Schwope A.D., 1999, A&A, 343, 132

Cannizzo J.K., 1993, ApJ, 419, 318

Cannizzo J.K., Pudritz R.E., 1988, ApJ, 327, 840

Cannizzo J.K., Gosh P., Wheeler J.C., 1982, ApJ, 260, L83

Carpenter J.M., 2001, AJ, 121, 2851

Chanan G.A., Nelson J.E., Margon B., 1978, ApJ, 226, 963

Chen A., O'Donoghue D., Stobie R.S., Kilkenny D., Warner B., 2001, MNRAS, 325, 89

Chester T.J., 1979, ApJ, 230, 167

Cieslinski D., Diaz M.P., Mennickent R.E., Pietrzyński G., 2003, PASP, 115, 193

Clemens J.C., Reid I.N., Gizis J.E., O'Brien M.S., 1998, ApJ, 496, 352

Cool A.M., Grindlay J.E., Cohn H.N., Lugger P.M., Slavin S.D., 1995, ApJ, 439, 695

Crampton D., Fisher W.A., Cowley A.P., 1986, ApJ, 300, 788

Cropper M., et al., 1989, MNRAS, 236, 29P

Cropper M., 1990, SSRv, 54, 195

de Kool M., 1992, A&A, 261, 188

della Valle M., 1991, A&A, 252, L9

Dhillon V.S., Marsh T.R., 1995, MNRAS, 275, 89

Dhillon V.S., Jones D.H.P., Marsh T.R., 1994, MNRAS, 266, 859

Dhillon V.S., Jones D.H.P., Marsh T.R., Smith R.C., 1992, MNRAS, 258, 225

Dhillon V.S., Littlefair S.P., Howell S.B., Ciardi D.R., Harrop-Allin M.K., Marsh T.R., 2000, MNRAS, 314, 826

Di Stefano R., Rappaport S., 1994, ApJ, 423, 274

Dreizler S., Werner K., 1996, A&A, 314, 217

Drew J.E., 1987, MNRAS, 224, 595

Drew J.E., et al., 2005, MNRAS, 362, 753

Drimmel R., Cabrera-Lavers A., López-Corredoira M., 2003, A&A, 409, 205

Dubus G., Taam R.E., Spruit H.C., 2002, ApJ, 569, 395

Dubus G., Campbell R., Kern B., Taam R.E., Spruit H.C., 2004, MNRAS, 349, 869

Dubus G., Taam R.E., Hull C., Watson D.M., Mauerhan J.C., 2007, ApJ, 663, 516

Duerbeck H.W., 1984, Ap&SS, 99, 363

Duerbeck H.W., 1987, SSRv, 45, 1

Eisenhauer F., et al., 2005, ApJ, 628, 246

Elitzur M., Clarke J.T., Kallman T.R., 1988, ApJ, 324, 405

Elsner R.F., Lamb F.K., 1977, ApJ, 215, 897

Eracleous M., Halpern J., Patterson J., 1991, ApJ, 382, 290

Fabian A.C., Pringle J.E., Rees M.J., 1975, MNRAS, 172, 15P

Faulkner J., 1971, ApJ, 170, L99

Feline W.J., Dhillon V.S., Marsh T.R., Stevenson M.J., Watson C.A., Brinkworth C.S., 2004a, MNRAS, 347, 1173

Feline W.J., Dhillon V.S., Marsh T.R., Brinkworth C.S., 2004b, MNRAS, 355, 1

Feline W.J., Dhillon V.S., Marsh T.R., Watson C.A., Littlefair S.P., 2005, MNRAS, 364, 1158

Felten J.E., 1976, ApJ, 207, 700

Fiedler H., Barwig H., Mantel K.H., 1997, A&A, 327, 173

Flannery B.P., 1975, MNRAS, 170, 325

Frank J., King A.R., Raine D.J., 1985, Accretion Power in Astrophysics. Cambridge Univ. Press, Cambridge

Frank J., King A.R., Sherrington M.R., Jameson R.F., Axon D.J., 1981, MNRAS, 195, 505

Frieman J.A., et al., 2008, AJ, 135, 338

Fujimoto M.Y., 1982, ApJ, 257, 767

Gänsicke B.T., Hagen H.-J., Engels D., 2002, in Gänsicke B.T., Beuermann K., Reinsch K., eds, ASP Conf. Ser. Vol. 261, The Physics of Cataclysmic Variables and Related Objects. Astron. Soc. Pac., San Francisco, p. 190

Gänsicke B.T., et al., 2005a, MNRAS, 361, 141

Gänsicke B.T., Szkody P., Howell S.B., Sion E.M., 2005b, ApJ, 629, 451

Gehrz R.D., Truran J.W., Williams R.E., Starrfield S., 1998, PASP, 110, 3

Ghosh P., Lamb F.K., 1978, ApJ, 223, L83

Ghosh P., Lamb F.K., 1979a, ApJ, 232, 259

Ghosh P., Lamb F.K., 1979b, ApJ, 234, 296

Gioia I.M., Henry J.P., Mullis C.R., Böhringer H., Briel U.G., Voges W., Huchra J.P., 2003, ApJS, 149, 29

Gould A., Bahcall J.N., Flynn C., 1996, ApJ, 465, 759

Green R.F., Schmidt M., Liebert J., 1986, ApJS, 61, 305

Greenstein J.L., 1957, ApJ, 126, 23

Grindlay J.E., et al., 2005, ApJ, 635, 920

Groot P. J., et al., 2006, IAU Joint Discussion 13, Exploiting Large Surveys for Galactic Astronomy. p. 54

Hambly N.C., et al., 2001a, MNRAS, 326, 1279

Hambly N.C., Irwin M.J., MacGillivray H.T., 2001b, MNRAS, 326, 1295

Hambly N.C., Davenhall A.C., Irwin M.J., MacGillivray H.T., 2001c, MNRAS, 326, 1315

Hameury J.-M., Lasota J.-P., 2002, A&A, 394, 231

Hameury J.-M., King A.R., Lasota J.-P., 1986, MNRAS, 218, 695

Hameury J.M., King A.R., Lasota J.P., 1989, MNRAS, 237, 39

Hameury J.-M., Lasota J.-P., Dubus G., 1999, MNRAS, 303, 39

Hameury J.-M., Lasota J.-P., Warner B., 2000, A&A, 353, 244

Hameury J.-M., Menou K., Dubus G., Lasota J.-P., Hure J.-M., 1998, MNRAS, 298, 1048

Hamuy M., Suntzeff N.B., Heathcote S.R., Walker A.R., Gigoux P., Phillips M.M., 1994, PASP, 106, 566

Han Z., Podsiadlowski P., Lynas-Gray A.E., 2007, MNRAS, 380, 1098

Harlaftis E.T., Marsh T.R., 1996, A&A, 308, 97

Harrison T.E., Osborne H.L., Howell S.B., 2005, AJ, 129, 2400

Harrison T.E., Johnson J.J., McArthur B.E., Benedict G.F., Szkody P., Howell S.B., Gelino D.M., 2004, AJ, 127, 460

Harrop-Allin M.K., Warner B., 1996, MNRAS, 279, 219

Hartley L.E., Murray J.R., Drew J.E., Long K.S., 2005, MNRAS, 363, 285

Hassall B.J.M., Pringle J.E., Schwarzenberg-Czerny A., Wade R.A., Whelan J.A.J., Hill P.W., 1983, MNRAS, 203, 865

Haug K., 1988, MNRAS, 235, 1385

Heinke C.O., Ruiter A.J., Muno M.P., Belczynski K., 2008, in Bandyopadhyay R.M., Wachter, S., Gelino D., Gelino C.R., eds, A Population Explosion: The Nature and Evolution of X-ray Binaries in Diverse Environments. in press (arXiv:0801.1279)

Hellier C., 1991, MNRAS, 251, 693

Hellier C., 2000, NewAR, 44, 131

Hellier C., 2001, Cataclysmic Variable Stars: How and why they vary. Springer-Praxis, Chichester

Henry J.P., Mullis C.R., Voges W., Böhringer H., Briel U.G., Gioia I.M., Huchra J.P., 2006, ApJS, 162, 304

Herbig G.H., 1960, ApJ, 132, 76

Hertz P., Bailyn C.D., Grindlay J.E., Garcia M.R., Cohn H., Lugger P.M., 1990, ApJ, 364, 251

Hessman F.V., Hopp U., 1990, A&A, 228, 387

Hessman F.V., Koester D., Schoembs R., Barwig H., 1989, A&A, 213, 167

Hessman F.V., Robinson E.L., Nather R.E., Zhang E.-H., 1984, ApJ, 286, 747

Hirose M., Osaki Y., 1990, PASJ, 42, 135

Hjellming M.S., Taam R.E., 1991, ApJ, 370, 709

Hjellming M.S., Webbink R.F., 1987, ApJ, 318, 794

Hoard D.W., Thorstensen J.R., Szkody P., 2000, ApJ, 539, 936

Hoard D.W., Howell S.B., Brinkworth C.S., Ciardi D.R., Wachter S., 2007, ApJ, 671, 734

Hoare M.G., 1994, MNRAS, 267, 153

Honeycutt R.K., Schlegel E.M., Kaitchuck R.H., 1986, ApJ, 302, 388

Hopewell E.C., et al., 2005, MNRAS, 363, 857

Horne K., 1986, PASP, 98, 609

Horne K., 1999, in Hellier C., Mukai K., eds, ASP Conf. Ser. Vol. 157, Annapolis Workshop on Magnetic Cataclysmic Variables. Astron. Soc. Pac., San Francisco, p. 349

Horne K., Saar S.H., 1991, ApJ, 374, L55

Hoshi R., 1979, Progress of Theoretical Physics, 61, 1307

Howarth I.D., Phillips A.P., 1986, MNRAS, 222, 809

Howell S.B., Rappaport S., Politano M., 1997, MNRAS, 287, 929

Howell S.B., Nelson L.A., Rappaport S., 2001, ApJ, 550, 897

Howell S.B., Harrison T.E., Szkody P., 2004, ApJ, 602, L49

Howell S.B., Gänsicke B.T., Szkody P., Sion E.M., 2002, ApJ, 575, 419

Howell S.B., Mason E., Huber M., Clowes R., 2002, A&A, 395, L47

Howell S.B., et al., 2006, ApJ, 646, L65

Hut P., Verbunt F., 1983, Nature, 301, 587

Iben I.J., Livio M., 1993, PASP, 105, 1373

Idan I., Lasota J.-P., Hameury J.-M., Shaviv G., 2008, in Abramowicz, M., ed, NewAR, X-ray binaries, accretion disks and compact stars. in press (arXiv:0801.1051)

Ishioka R., Kato T., Uemura M., Iwamatsu H., Matsumoto K., Martin B.E., Billings G.W., Novak R., 2001, PASJ, 53, L51

Ivanova N., Taam R.E., 2003, ApJ, 599, 516

Ivanova N., Heinke C.O., Rasio F.A., Taam R.E., Belczynski K., Fregeau J., 2006, MN-

RAS, 372, 1043

Jacoby G.H., Hunter D.A., Christian C.A., 1984, ApJS, 56, 257

Jameson R.F., King A.R., Sherrington M.R., 1980, MNRAS, 191, 559

Jeffreys H., 1961, Theory of probability, 3rd edn. Oxford Univ. Press, Oxford

Jester S., et al., 2005, AJ, 130, 873

Jones M.H., Watson M.G., 1992, MNRAS, 257, 633

Jones B.F., Fischer D.A., Stauffer J.R., 1996, AJ, 112, 1562

Joy A.H., 1954, AJ, 59, 326

Kafka S., Honeycutt R.K., 2004, AJ, 128, 2420

Kahabka P., van den Heuvel E.P.J., 1997, ARA&A, 35, 69

Kalberla P.M.W., Burton W.B., Hartmann D., Arnal E.M., Bajaja E., Morras R., Pöppel W.G.L., 2005, A&A, 440, 775

Kaluzny J., Chlebowski T., 1988, ApJ, 332, 287

Kato T., et al., 2003, PASJ, 55, 491

Katz J.I., 1975, ApJ, 200, 298

Kemp J., Patterson J., Thorstensen J.R., Fried R.E., Skillman D.R., Billings G., 2002, PASP, 114, 623

Kiel P.D., Hurley J.R., 2006, MNRAS, 369, 1152

Kilkenny D., Marang F., Menzies J.W., 1994, MNRAS, 267, 535

King A.R., 1988, QJRAS, 29, 1

King A.R., 1993, MNRAS, 261, 144

King A.R., Cannizzo J.K., 1998, ApJ, 499, 348

King A.R., Kolb U., 1995, ApJ, 439, 330

King A.R., Schenker K., 2002, in Gänsicke B.T., Beuermann K., Reinsch K., eds, ASP Conf. Ser. Vol. 261, The Physics of Cataclysmic Variables and Related Objects. Astron. Soc. Pac., San Francisco, p. 233

King A.R., Rolfe D.J., Schenker K., 2003, MNRAS, 341, L35

King A.R., Schenker K., Hameury J.M., 2002, MNRAS, 335, 513

King A.R., Frank J., Kolb U., Ritter H., 1995, ApJ, 444, L37

King A.R., Frank J., Kolb U., Ritter H., 1996, ApJ, 467, 761

Kiplinger A.L., 1979, ApJ, 234, 997

Kiplinger A.L., 1980, ApJ, 236, 839

Kley W., 1991, A&A, 247, 95

Knigge C., 2006, MNRAS, 373, 484

Knigge C., King A.R., Patterson J., 2000, A&A, 364, L75

Knigge C., Woods J.A., Drew J.E., 1995, MNRAS, 273, 225

Knigge C., Long K.S., Hoard D.W., Szkody P., Dhillon V.S., 2000, ApJ, 539, L49

Knigge C., Araujo-Betancor S., Gänsicke B.T., Long K.S., Szkody P., Hoard D.W., Hynes R.I., Dhillon V.S., 2004, ApJ, 615, L129

Ko Y.-K., Lee Y.P., Schlegel E.M., Kallman T.R., 1996, ApJ, 457, 363

Kolb U., 1993, A&A, 271, 149

Kolb U., Baraffe I., 1999, MNRAS, 309, 1034

Kolb U., Politano M., 1997, A&A, 319, 909

Kolb U., Stehle R., 1996, MNRAS, 282, 1454

Kolb U., King A.R., Baraffe I., 2001, MNRAS, 321, 544

Kolb U., King A.R., Ritter H., 1998, MNRAS, 298, L29

Kovetz A., Prialnik D., Shara M.M., 1988, ApJ, 325, 828

Kraft R.P., 1964, ASPL, 9, 137

Kraft R.P., Mathews J., Greenstein J.L., 1962, ApJ, 136, 312

Kraus A.L., Craine E.R., Giampapa M.S., Scharlach W.W.G., Tucker R.A., 2007, AJ, 134, 1488

Krzemiński W., 1965, ApJ, 142, 1051

Krzemiński W., Smak J., 1971, AcA, 21, 133

Lada C.J., 2006, ApJ, 640, L63

La Dous C., 1989, A&A, 211, 131

Landau L.D., Lifschitz E.M., 1958, The Classical Theory of Fields. Pergamon, Oxford

Lamb D.Q., 1974, ApJ, 192, L129

Lamb F.K., Aly J.-J., Cook M.C., Lamb D.Q., 1983, ApJ, 274, L71

Lanza A.F., Rodonò M., Rosner R., 2000, MNRAS, 314, 398

Li J., Wickramasinghe D.T., Wu K., 1995, MNRAS, 276, 255

Li J.K., Wu K.W., Wickramasinghe D.T., 1994, MNRAS, 268, 61

Liebert J., Bergeron P., Holberg J.B., 2005, ApJS, 156, 47

Liller W., Shao C.Y., Mayer B., Garnavich P., Harbrecht R.P., Wallentine D., Simmons K., Maley P., 1975, IAUC, 2848, 4

Littlefair S.P., Dhillon V.S., Marsh T.R., Gänsicke B.T., Southworth J., Watson C.A., 2006, Science, 314, 1578

Littlefair S.P., Dhillon V.S., Marsh T.R., Gänsicke B.T., Baraffe I., Watson C.A., 2007, MNRAS, 381, 827

Liu W., Hu J.Y., Zhu X.H., Li Z.Y., 1999, ApJS, 122, 243

Livio M., 1993, in Wheeler J.C., ed, Accretion Discs in Compact Stellar Systems. Advanced Series in Astophysics and Cosmology, Vol. 9, World Sci. Publ., Singapore p. 243

Livio M., Pringle J.E., 1992, MNRAS, 259, 23P

Livio M., Pringle J.E., 1994, ApJ, 427, 956

Livio M., Truran J.W., 1992, ApJ, 389, 695

Livio M., Govarie A., Ritter H., 1991, A&A, 246, 84

Lubow S.H., Shu F.H., 1975, ApJ, 198, 383

Lynden-Bell D., 1969, Nature, 223, 690

Lynden-Bell D., Pringle J.E., 1974, MNRAS, 163, 603

Marsh T.R., 1987, MNRAS, 228, 779

Marsh T.R., Horne K., Shipman H.L., 1987, MNRAS, 225, 551

Marsh T.R., et al., 2002, in Gänsicke B.T., Beuermann K., Reinsch K., eds, ASP Conf. Ser. Vol. 261, The Physics of Cataclysmic Variables and Related Objects. Astron. Soc. Pac., San Francisco, p. 200

Martin R.G., Tout C.A., 2005, MNRAS, 358, 1036

McClintock J.E., Petro L.D., Remillard R.A., Ricker G.R., 1983, ApJ, 266, L27

McCormick P., Frank J., 1998, ApJ, 500, 923

McDermott P.N., Taam R.E., 1989, ApJ, 342, 1019

Mclaughlin D.B., 1945, PASP, 57, 69

Mennickent R.E., Diaz M., 1996, A&A, 309, 147

Mestel L., Spruit H.C., 1987, MNRAS, 226, 57

Meyer F., Meyer-Hofmeister E., 1979, A&A, 78, 167

Meyer F., Meyer-Hofmeister E., 1981, A&A, 104, L10

Meyer F., Meyer-Hofmeister E., 1982, A&A, 106, 34

Micela G., Affer L., Favata F., Henry J.P., Gioia I., Mullis C.R., Sanz Forcada J., Sciortino

S., 2007, A&A, 461, 977

Mineshige S., Osaki Y., 1985, PASJ, 37, 1

Morales-Rueda L., Still M.D., Roche P., 1996, MNRAS, 283, L58

Morales-Rueda L., Still M.D., Roche P., Wood J.H., Lockley J.J., 2002, MNRAS, 329, 597

Morgan D.H., Parker Q.A., 2005, MNRAS, 360, 360

Muno M.P., et al., 2003, ApJ, 589, 225

Nauenberg M., 1972, ApJ, 175, 417

Naylor T., Bath G.T., Charles P.A., Hassal B.J.M., Sonneborn G., van der Woerd H., van Paradijs J., 1988, MNRAS, 231, 237

Norton A.J., Watson M.G., 1989, MNRAS, 237, 715

Norton A. J., Wynn G. A., Somerscales R. V., 2004, ApJ, 614, 349

O'Donoghue D., 1995, BaltA, 4, 519

Oke J.B., 1990, AJ, 99, 1621

Olech A., Zloczewski K., Mularczyk K., Kedzierski P., Wisniewski M., Stachowski G., 2004, AcA, 54, 57

Osaki Y., 1974, PASJ, 26, 429

Osaki Y., 1985, A&A, 144, 369

Osaki Y., 1996, PASP, 108, 39

Osaki Y., Hirose M., Ichikawa S., 1993, in Wheeler J.C., ed, Accretion Discs in Compact Stellar Systems. Advanced Series in Astophysics and Cosmology, Vol. 9, World Sci. Publ. Singapore p. 272

Osterbrock D.E., Fulbright J.P., Martel A.R., Keane M.J., Trager S.C., Basri G., 1996, PASP, 108, 277

Paczyński B., 1967, AcA, 17, 287

Paczyński B., 1971, ARA&A, 9, 183

Paczynski B., 1976, in Eggleton P., Mitton S., Whelan J., eds, IAU Symp. 73, Structure and Evolution of Close Binary Systems. Reidel, Dordrecht, p. 75

Paczyński B., 1977, ApJ, 216, 822

Paczyński B., 1981, AcA, 31, 1

Paczyński B., Sienkiewicz R., 1981, ApJ, 248, L27

Paczyński B., Schwarzenberg-Czerny A., 1980, AcA, 30, 127

Panek R.J., Holm A.V., 1984, ApJ, 277, 700

Parker E.N., 1970, in Habing H.J., ed, IAU Symp. 39, Interstellar Gas Dynamics. Reidel, Dordrecht, p. 168

Parker Q.A., et al., 2005, MNRAS, 362, 689

Patterson J., 1984, ApJS, 54, 443

Patterson J., 1994, PASP, 106, 209

Patterson J., 1998, PASP, 110, 1132

Patterson J., 2001, PASP, 113, 736

Patterson J., Raymond J.C., 1985a, ApJ, 292, 535

Patterson J., Raymond J.C., 1985b, ApJ, 292, 550

Patterson J., Robinson E.L., Nather R.E., 1977, ApJ, 214, 144

Patterson J., Robinson E.L., Nather R.E., 1978, ApJ, 224, 570

Patterson J., Thorstensen J.R., Kemp J., 2005, PASP, 117, 427

Patterson J., et al., 2002a, PASP, 114, 721

Patterson J., et al., 2002b, PASP, 114, 1364

Patterson J., et al., 2003, PASP, 115, 1308

Patterson J., et al., 2005, PASP, 117, 1204

Penning W.R., Schmidt G.D., Liebert J.E., 1986, ApJ, 301, 885

Petterson J.A., 1979, in Van Horn H.M., Weidemann V., eds., Proc. IAU Coll. 53, White Dwarfs and Variable Degenerate Stars. University of Rochester, Rochester, p. 412

Petterson J.A., 1980, ApJ, 241, 247

Pfahl E., Rappaport S., Podsiadlowski P., 2003, ApJ, 597, 1036

Podsiadlowski Ph., Han Z., Rappaport S., 2003, MNRAS, 340, 1214

Pojmanski G., 1986, AcA, 36, 69

Politano M., 1996, ApJ, 465, 338

Politano M., Weiler K.P., 2007, ApJ, 665, 663

Potter S.B., Romero-Colmenero E., Watson C.A., Buckley D.A.H., Phillips A., 2004, MNRAS, 348, 316

Predehl P., Schmitt J.H.M.M., 1995, A&A, 293, 889

Pretorius M.L., Knigge C., 2007, A&A, 461, 1103

Pretorius M.L., Warner B., Woudt P.A., 2006, MNRAS, 368, 361

Prialnik D., 1986, ApJ, 310, 222

Pringle J.E., 1977, MNRAS, 178, 195

Pringle J.E., 1981, ARA&A, 19, 137

Pringle J.E., Savonije G.J., 1979, MNRAS, 187, 777P

Proga D., 2003, ApJ, 592, L9

Rappaport S., Joss P.C., Webbink R.F., 1982, ApJ, 254, 616

Rappaport S., Verbunt F., Joss P.C., 1983, ApJ, 275, 713

Regev O., Shara M.M., 1989, ApJ, 340, 1006

Reid I.N., 2005, ARA&A, 43, 247

Retter A., Leibowitz E.M., Naylor T., 1999, MNRAS, 308, 140

Reylé C., Robin A.C., 2001, A&A, 373, 886

Riaz B., Gizis J.E., Harvin J., 2006, AJ, 132, 866

Richman H.R., 1996, ApJ, 462, 404

Rieke G.H., Lebofsky M.J., 1985, ApJ, 288, 618

Ringwald F.A., 1993, PhD thesis, Dartmouth Coll.

Ringwald F.A., 1994, in Shafter A.W, ed, ASP Conf. Ser. Vol. 56, Interacting binary stars. Astron. Soc. Pac., San Francisco, p. 294

Ritter H., 1985, A&A, 145, 227

Ritter H., 1986, A&A, 168, 105

Ritter H., Burkert A., 1986, A&A, 158, 161

Ritter H., Kolb U., 2003, A&A, 404, 301 (update RKcat7.6)

Ritter H., Özkan M.T., 1986, A&A, 167, 260

Ritter H., Zhang Z.-Y., Kolb U., 2000, A&A, 360, 969

Ritter H., Politano M., Livio M., Webbink R.F., 1991, ApJ, 376, 177

Robin A., Crézée M., 1986, A&A, 157, 71

Robin A.C., Reylé C., Derrière S., Picaud S., 2003, A&A, 409, 523

Robinson E.L., Barker E.S., Cochran A.L., Cochran W.D., Nather R.E., 1981, ApJ, 251, 611

Robinson E.L., 1973, ApJ, 186, 347

Robinson E.L., 1976, ARA&A, 14, 119

Rodríguez-Gil P., Martínez-Pais I.G., 2002, MNRAS, 337, 209

Rodríguez-Gil P., Potter S.B., 2003, MNRAS, 342, L1

Rodríguez-Gil P., Schmidtobreick L., Gänsicke B.T., 2007, MNRAS, 374, 1359

Rodríguez-Gil P., Casares J., Martínez-Pais I.G., Hakala P., Steeghs D., 2001, ApJ, 548, L49

Rodríguez-Gil P., et al., 2007, MNRAS, 377, 1747

Rogel A.B., Lugger P.M., Cohn H.N., Slavin S.D., Grindlay J.E., Zhao P., Hong J., 2006, ApJS, 163, 160

Rogel A.B., Cohn H.N., Lugger P.M., 2007, in press (arXiv:0711.1813)

Romanova M.M., Ustyugova G.V., Koldoba A.V., Wick J.V., Lovelace R.V.E., 2003, ApJ, 595, 1009

Romanova M.M., Ustyugova G.V., Koldoba A.V., Lovelace R.V.E., 2004, ApJ, 610, 920

Rutten R.G.M., Dhillon V.S., 1994, A&A, 288, 773

Rutten R.G.M., van Paradijs J., Tinbergen J., 1992, A&A, 260, 213

Salaris M., García-Berro E., Hernanz M., Isern J., Saumon D., 2000, ApJ, 544, 1036

Saslaw W.C., 1968, MNRAS, 138, 337

Schenker K., King A.R., 2002, in Gänsicke B.T., Beuermann K., Reinsch K., eds, ASP Conf. Ser. Vol. 261, The Physics of Cataclysmic Variables and Related Objects. Astron. Soc. Pac., San Francisco, p. 242

Schenker K., Kolb U., Ritter H., 1998, MNRAS, 297, 633

Schenker K., King A.R., Kolb U., Wynn G.A., Zhang Z., 2002, MNRAS, 337, 1105

Schreiber M.R., Gänsicke B.T., 2003, A&A, 406, 305

Schmidt M., 1968, ApJ, 151, 393

Schmidt G.D., Stockman H.S., 1991, ApJ, 371, 749

Schmidt G.D., Szkody P., Smith P.S., Silber A., Tovmassian G., Hoard D.W., Gänsicke B.T., de Martino D., 1996, ApJ, 473, 483

Schmidt G. D., et al., 2005, ApJ, 630, 1037

Schneider D.P., Young P., 1980, ApJ, 238, 946

Schwope A. D., Schreiber M. R., Szkody P., 2006, A&A, 452, 955

Schwope A.D., Brunner H., Buckley D., Greiner J., Heyden K.v.d., Neizvestny S., Potter S., Schwarz R., 2002, A&A, 396, 895

Schwope A.D., Staude A., Koester D., Vogel J., 2007, A&A, 469, 1027

Shafter A.W., Holland J.N., 2003, PASP, 115, 1105

Shakura N.I., Sunyaev R.A., 1973, A&A, 24, 337

Shara M.M., 1989, PASP, 101, 5

Shara M.M., Hurley J.R., 2006, ApJ, 646, 464

Shara M.M., Prialnik D., 1994, AJ, 107, 1542

Shara M.M., Livio M., Moffat A.F.J., Orio M., 1986, ApJ, 311, 163

Shara M., Moffat A., Potter M., Bode M., Stephenson F.R., 1993, in Regev O., Shaviv G., eds, Annals of the Israel Physical Society, Vol. 10, Cataclysmic Variables and Related Physics. Israel Physical Society, Jerusalem, p. 84

Shaviv G., Starrfield S., 1987, ApJ, 321, L51

Shaviv G., Wehrse R., 1991, A&A, 251, 117

Siegel M.H., Majewski S.R., Reid I.N., Thompson I.B., 2002, ApJ, 578, 151

Sion E.M., 1999, PASP, 111, 532

Skillman D.R., Patterson J., 1988, AJ, 96, 976

Skrutskie M.F., et al., 2006, AJ, 131, 1163

Smak J., 1969, AcA, 19, 155

Smak J., 1970, AcA, 20, 311

Smak J., 1969, AcA, 21, 15

Smak J., 1984, AcA, 34, 317

Smak J., 1986, AcA, 36, 211

Smak J., 1987, Ap&SS, 131, 479

Smak J., 1992, AcA, 42, 323

Smak J., 1994, AcA, 44, 45

Smith D.A., Dhillon V.S., 1998, MNRAS, 301, 767

Smith D.A., Dhillon V.S., Marsh T.R., 1998, MNRAS, 296, 465

Somers M.W., Naylor T., 1999, A&A, 352, 563

Southworth J., Gänsicke B.T., Marsh T.R., de Martino D., Hakala P., Littlefair S., Rodríguez-Gil P., Szkody P., 2006, MNRAS, 373, 687

Southworth J., Gänsicke B. T., Marsh T. R., de Martino D., Aungwerojwit A., 2007a, MNRAS, 378, 635

Southworth J., Marsh T.R., Gänsicke B.T., Aungwerojwit A., Hakala P., de Martino D., Lehto H., 2007b, MNRAS, 382, 1145

Sproats L.N., Howell S.B., Mason K.O., 1996, MNRAS, 282, 1211

Spruit H.C., Ritter H., 1983, A&A, 124, 267

Spruit H.C., Rutten R.G.M., 1998, MNRAS, 299, 768

Spruit H.C., Taam R.E., 2001, ApJ, 548, 900

Starrfield S., Sparks W.M., Shaviv G., 1988, ApJ, 325, L35

Starrfield S., Sparks W.M., Truran J.W., 1985, ApJ, 291, 136

Starrfield S., Timmes F.X., Hix W.R., Sion E.M., Sparks W.M., Dwyer S.J., 2004, ApJ, 612, L53

Steeghs D., Perryman M.A.C., Reynolds A., de Bruijne J.H.J., Marsh T., Dhillon V.S., Peacock A., 2003, MNRAS, 339, 810

Steeghs D., Howell S.B., Knigge C., Gänsicke B.T., Sion E.M., Welsh W.F., 2007, ApJ, 667, 442

Stehle R., Kolb U., Ritter H., 1997, A&A, 320, 136

Stehle R., Ritter H., Kolb U., 1996, MNRAS, 279, 581

Stelzer B., Micela G., Flaccomio E., Neuhäuser R., Jayawardhana R., 2006, A&A, 448, 293

Stockman H.S., Schmidt G.D., Lamb D.Q., 1988, ApJ, 332, 282

Stockman H.S., Berriman G., Liebert J., Moore R.L., Whickramasinghe D.T., 1992, ApJ, 401, 628

Stobie R.S., Ishida K., Peacock J.A., 1989, MNRAS, 238, 709

Stobie R.S., et al., 1997, MNRAS, 287, 848

Stone R.P.S., Baldwin J.A., 1983, MNRAS, 204, 347

Stover R.J., 1981, ApJ, 249, 673

Szkody P., 1987, ApJS, 63, 685

Szkody P., Howell S.B., 1992, ApJS, 78, 537

Szkody P., Gänsicke B.T., Sion E.M., Howell S.B., 2002, ApJ, 574, 950

Szkody P., et al., 2002, AJ, 123, 430

Szkody P., et al., 2003, AJ, 126, 1499

Szkody P., et al., 2004, AJ, 128, 1882

Szkody P., et al., 2005, AJ, 129, 2386

Szkody P., et al., 2006, AJ, 131, 973

Szkody P., et al., 2007, AJ, 134, 185

Taam R.E., Bodenheimer P., 1989, ApJ, 337, 849

Taam R.E., Sandquist E.L., 2000, ARA&A, 38, 113

Taam R.E., Spruit H.C., 1989, ApJ, 345, 972

Taam R.E., Spruit H.C., 2001, ApJ, 561, 329

Tappert C., Augusteijn T., Maza J., 2004, MNRAS, 354, 321

Tassoul J.-P., 1988, ApJ, 324, L71

Thorstensen J.R., Freed I.W., 1985, AJ, 90, 2082

Thorstensen J.R., Lépine S., Shara M., 2006, PASP, 118, 1238

Thorstensen J.R., Ringwald F.A., Wade R.A., Schmidt G.D., Norsworthy J.E., 1991, AJ, 102, 272

Thorstensen J.R., Fenton W.H., Patterson, J.O., Kemp J., Krajci T., Baraffe I., 2002a, ApJ, 567, L49

Thorstensen J.R., Fenton W.H., Patterson J., Kemp J., Halpern J., Baraffe I., 2002b, PASP, 114, 1117

Tinney C.G., Reid I.N., Mould J.R., 1993, ApJ, 414, 254

Tonry J., Davis M., 1979, AJ, 84, 1511

Tout C.A., Hall D.S., 1991, MNRAS, 253, 9

Tout C.A., Pringle J.E., 1992a, MNRAS, 256, 269

Tout C.A., Pringle J.E., 1992b, MNRAS, 259, 604

Townsley D.M., Bildsten L., 2003, ApJ, 596, L227

Townsley D.M., Bildsten L., 2004, ApJ, 600, 390

Townsley D.M., Bildsten L., 2005, ApJ, 628, 395

Tylenda R., 1981a, AcA, 31, 127

Tylenda R., 1981b, AcA, 31, 276

Valdes F., Gupta R., Rose J.A., Singh H.P., Bell D.J., 2004, ApJS, 152, 251

Valtchanov I., Pierre M., 2003, AN, 324, 124

van Paradijs J., Augusteijn T., Stehle R., 1996, A&A, 312, 93

van Teeseling A., Verbunt F., 1994, A&A, 292, 519

van Teeseling A., Beuermann K., Verbunt F., 1996, A&A, 315, 467

van Zyl L., Warner B., O'Donoghue D., Sullivan D., Pritchard J., Kemp J., 2000, BaltA, 9, 231

Verbunt F., 1982, SSRv, 32, 379

Verbunt F., 1984, MNRAS, 209, 227

Verbunt F., van den Heuvel E.P.J., 1995, in Lewin W.H.G., van Paradijs J., van den Heuvel E.P.J., eds, X-ray binaries. Cambridge Univ. Press, Cambridge, p. 457

Verbunt F., Zwaan C., 1981, A&A, 100, L7

Verbunt F., Bunk W.H., Ritter H., Pfeffermann E., 1997, A&A, 327, 602

Voges W., et al., 1999, A&A, 349, 389

Voges W., et al., 2000, IAUC, 7432, 3

Vogt N., 1974, A&A, 36, 369

Vogt N., 1982, ApJ, 252, 653

Vogt N., 1983, A&A, 118, 95

Vrielmann S., Hessman F.V., Horne K., 2002a, MNRAS, 332, 176

Vrielmann S., Stiening R.F., Offutt W., 2002b, MNRAS, 334, 608

Vrtilek S.D., Silber A., Raymond J.C., Patterson J., 1994, ApJ, 425, 787

Wade R.A., Ward M.J., 1985, in Pringle J.E., Wade R.A., eds, Interacting Binary Stars. Cambridge Univ. Press, Cambridge, p. 129

Walker M.F., 1954, PASP, 66, 230

Walker A.R., 2003, Memorie della Societa Astronomica Italiana, Vol. 74, 999

Warner B., 1974, MNRAS, 168, 235

Warner B., 1975, MNRAS, 170, 219

Warner B., 1976, in Eggleton P., Mitton S., Whelan J., eds, IAU Symp. 73, Structure and Evolution of Close Binary Systems. Reidel, Dordrecht, p. 85

Warner B., 1987, MNRAS, 227, 23

Warner B., 1995, Cataclysmic Variable Stars. Cambridge Univ. Press, Cambridge

Warner B., 2001, in Paczynski B., Chen W.-P., Lemme C., eds, ASP Conf. Ser. Vol. 246, Small Telescope Astronomy on Global Scales. Astron. Soc. Pac., San Francisco, p. 159

Warner B., 2004, PASP, 116, 115

Warner B., Nather R.E., 1971, MNRAS, 152, 219

Webbink R.F., Wickramasinghe D.T., 2002, MNRAS, 335, 1

Webbink R.F., Livio M., Truran J.W., Orio M., 1987, ApJ, 314, 653

Wheatley P.J., Burleigh M.R., Watson M.G., 2000, MNRAS, 317, 343

Whelan J., Iben I.J., 1973, ApJ, 186, 1007

Whitehurst R., 1988a, MNRAS, 232, 35

Whitehurst R., 1988b, MNRAS, 233, 529

Wickramasinghe K.W.D., 1993, PASAu, 10, 325

Wickramasinghe D.T., Martin B., 1985, MNRAS, 212, 353

Wickramasinghe D.T., Meggitt S.M.A., 1982, MNRAS, 198, 975

Wickramasinghe D.T., Wu K., 1994, Ap&SS, 211, 61

Wickramasinghe D.T., Wu K., Ferrario L., 1991, MNRAS, 249, 460

Wickramasinghe D.T., Cropper M., Mason K.O., Garlick M., 1991, MNRAS, 250, 692

Willems B., Kolb U., Sandquist E.L., Taam R.E., Dubus G., 2005, ApJ, 635, 1263

Willems B., Taam R.E., Kolb U., Dubus G., Sandquist E.L., 2007, ApJ, 657, 465

Williams D.B., 2000, IBVS, 4994

Williams G.A., Shipman H.L., 1988, ApJ, 326, 738

Williams R.E., 1980, ApJ, 235, 939

Winter L., Sion E.M., 2003, ApJ, 582, 352

Witham A.R., et al., 2006, MNRAS, 369, 581

Witham A.R., et al., 2007, MNRAS, 382, 1158

Witham A.R., Knigge C., Drew J.E., Greimel R., Steeghs D., Gaensicke B.T., Groot P.J., Mampaso A., 2008, MNRAS, in press (arXiv:0712.0988)

Wood J.H., Horne K., Vennes S., 1992, ApJ, 385, 294

Wood J., Horne K., Berriman G., Wade R., O'Donoghue D., Warner B., 1986, MNRAS, 219, 629

Wood J.H., Horne K., Berriman G., Wade R.A., 1989, ApJ, 341, 974

Wood J.H., Naylor T., Hassall B.J.M., Ramseyer T.F., 1995, MNRAS, 273, 772

Woods J.A., Verbunt F., Collier Cameron A., Drew J.E., Piters A., 1992, MNRAS, 255, 237

Woudt P.A., Warner B., 2003, MNRAS, 339, 731

Wu K., Wickramasinghe D.T., 1993, MNRAS, 265, 115

Wu K., Wickramasinghe D.T., Warner B., 1995, PASAu, 12, 60

York D.G., et al., 2000, AJ, 120, 1579

Young P., Schneider D.P., 1980, ApJ, 238, 955

Yungelson L.R., Lasota J.-P., Nelemans G., Dubus G., van den Heuvel E.P.J., Dewi J., Portegies Zwart S., 2006, A&A, 454, 559